Faculty of Science and Engineering

Department of Mechanical Engineering

Single Phase and Boiling Heat Transfer under Steady and Pulsating Confined Jet Impingement

Abishek Sridhar

This thesis is presented for the Degree of

Doctor of Philosophy

of

Curtin University

November 2013

DECLARATION

To the best of my knowledge and belief this thesis contains no material previously published by any other person except where due acknowledgment has been made.

This thesis contains no material which has been accepted for the award of any other degree or diploma in any university.

Signature :

Date   : 28 March 2014

This page is intentionally left blank

ACKNOWLEDGEMENTS

This page is intentionally left blank

ABSTRACT

The need for addressing increasingly higher heat loads at concentrated regions such as in miniaturized high density electronic modules has led to extensive research on techniques to improve traditional thermal management systems as well as development of novel cooling schemes. Jet impingement cooling offers substantially higher heat transfer coefficients as compared to natural or forced convective cooling and has hence been a desired option for several practical applications. Further heat transfer augmentation under jet impingement is achieved by the introduction of phase change through boiling of the impinging jet on the heated module, or by the introduction of mean flow oscillations through pulsating jets.

In the present research, three different types of jet impingement heat transfer problems are investigated: (i) steady, low Reynolds number single phase air jet impingement accounting for effects of buoyancy and surface radiation, (ii) steady state jet impingement boiling, and (iii) pulsating single phase (liquid) and boiling jet impingement.

In single phase (air) impingement cooling systems, employed in miniaturized configurations, heat transfer enhancement through turbulence may not be always possible and sufficiently high surface temperatures could result in substantial radiation interaction between the heated surface and the enclosure. This contribution of surface radiation to the overall heat transfer from the surface could be significantly enhanced to augment heat transfer, by improving the radiation characteristics, such as the surface emissivity of the components. In the first part of the present research, a mathematical model and computational code is developed for the analysis of confined submerged jet impingement flow and heat transfer of a radiatively non-participating gas (air), accounting for the effects of surface radiation and buoyancy. Detailed parametric studies are carried out to study the effects of the dimensionless geometric, flow and thermal controlling parameters on the flow field and thermal characteristics of the surface radiation-coupled mixed convective impingement cooling system, focussing on the relative contributions of surface radiation and convection to the overall heat transfer under different combinations of operating conditions. It is found that the contribution of surface radiation to the overall heat transfer increases from nearly negligible for a surface emissivity of 0.05, to about

23 % in the impingement region and over 50 % in the regions downstream for surface emissivity of 0.85 over the range of parameters studied.

The second study pertains to the analysis of subcooled flow boiling heat transfer under confined and submerged jet impingement. Boiling of impinging jets are characterised by the complex interactions between the ebullition and the thermal hydraulics in the bulk flow, typically involving heat and mass transfer between the phases, lift/ drag and buoyancy forces on the bubbles, bubble coalescence/ collapse, and the associated turbulence contribution to bulk flow. While there are a diverse range of experimental and mechanistic models available for the estimation of boiling parameters such as departure diameter, frequency and nucleation site density, for rather specific configurations and operating parameters, there are no specific models for jet impingement boiling. Nor there is a consensus on a generalized model for the ebullition parameters that could be extended to jet impingement boiling for all fluids. In the present research, a comprehensive modeling philosophy for subcooled confined jet impingement boiling is developed based on a rigorous analysis to ascertain and establish the suitability of different ebullition models as well as multiphase turbulence models, through comparison of the computational predictions against experimental data. Using the comprehensive model, elaborate set of computational simulations are carried out to study the effects of the relevant geometric, flow, thermal parameters and working fluids on the fundamental mechanism of subcooled impingement boiling heat transfer, with particular focus on the partitioning of the total surface heat flux into convection, quenching and evaporation during different regimes of the boiling curve. Results are discussed with spatially averaged as well as local description of the thermo-fluidics (such as distributions of surface temperatures, heat fluxes, liquid-vapor phase change rates on the heated impingement surface, isotherms, streamlines and vapor-phase contours). The relative significance of the partitioned heat transfer mechanisms on the different regimes of the boiling curves are characterized under different parametric conditions.

The third study detailed in this thesis pertains to the experimental analysis of pulsating single phase (liquid) and boiling impingement heat transfer. The literature on pulsating jet impingement heat transfer primarily focus on gas jets, while liquid impingement is the preferred choice for several industrial applications requiring high heat flux removal. Besides, it is also identified that no prior research on the heat transfer characteristics of pulsating boiling impingement is available thus far. The

importance of benchmark experimental results are realized to understand the effects of jet pulsation on the heat transfer characteristics of boiling and single phase liquid jet impingement heat transfer. In the present research, an experimental facility is designed and fabricated for the study of confined submerged liquid jet impingement heat transfer under both boiling and non-boiling conditions, with and without jet pulsations; a novel jet pulsation and monitoring mechanism is developed for the introduction of jet pulsations. Detailed set of experiments are carried out on single phase jet liquid impingement heat transfer (with de-ionized water) with and without jet pulsations, to evaluate the effectiveness of pulsating jets on impingement heat transfer. Further, the effects of jet pulsations on the boiling heat transfer characteristics under pulsating jet impingement is studied using a dielectric fluid FC-72. The isolated effects of jet pulsation frequency, amplitude and Reynolds number are studied under different operating temperatures by comparison of the transient as well as time averaged surface temperatures, heat fluxes and heat transfer coefficients against baseline steady state experimental data. It is found that under both, single phase and boiling conditions, the transient response of the heated surface, quantified in terms of the amplitude of temperature oscillations, decreases with an increase in jet pulsation frequency, indicating that the surface temperature could become insensitive to applied jet pulsations beyond a threshold pulsation frequency. The change in the magnitude of amplitude of temperature oscillations are almost the same as the prescribed change in the amplitude of jet pulsations. While the effect of jet pulsations is negligible for Reynolds numbers upto 1000, a slight decrease (upto 12%) is observed in the Nusselt number for larger Reynolds numbers during single phase experiments. During boiling experiments, a periodic renewal of the boiling process is observed with jet pulsations, where the bubbles on the heater surface are cyclically flushed downstream of the stagnation point in phase with the pulsating jet. A slight deterioration of the heat transfer coefficients is seen for low heat fluxes upto the partial nucleate boiling regime, while no marked influence of jet pulsations is seen in the fully developed nucleate boiling regime for the range of parameters studied. The variation in the critical heat flux between steady and pulsating jet impingement boiling is a maximum of 5% for the range of parameters studied. Considering that pulsating jet impingement boiling has not been investigated before, the present research provides benchmark heat transfer data for further research in the field.

PUBLICATIONS ARISING FROM THE THESIS

JOURNAL PUBLICATIONS (PEER-REVIEWED)

1. S. Abishek, R. Narayanaswamy, V. Narayanan, 2013, Effect of Heater Size and Reynolds Number on the Partitioning of Surface Heat Flux in Subcooled Jet Impingement Boiling, Int. J. Heat and Mass Transfer, Vol. 59, pp. 247-261

2. S. Abishek, R. Narayanaswamy, 2012, Coupled Effects of Surface-Radiation and Buoyancy on Jet-Impingement Heat Transfer, ASME J. Heat Transfer, Vol. 134 (8), pp. 082203-1-14

CONFERENCE PROCEEDINGS (PEER-REVIEWED)

3. S. Abishek, R. Narayanaswamy, V. Narayanan, 2014, Experimental Study of Pulsed and Steady State Confined Submerged Jet Impingement Boiling of FC-72, International Heat Transfer Conference, Aug. 10–15, Kyoto, Japan, Paper number: IHTC15-8439 (accepted; to be presented)

4. S. Abishek, R. Narayanaswamy, V. Narayanan, 2014, Suitability Evaluation of Bubble Departure Diameter and Frequency Models for the Simulation of Subcooled Confined Jet Impingement Boiling, ASME 4th Joint US-European Fluids Engineering Summer Meeting, Aug. 3-7, 2014, Chicago, Illinois, USA, Paper number: FEDSM2014-21498 (accepted; to be presented)

5. S. Abishek, R. Narayanaswamy, V. Narayanan, 2013, Experimental Study of Low Frequency Pulsating Liquid Jet Impingement Cooling in a Confined Planar Geometry, Proc. of the 22th National and 11th ISHMT-ASME Heat and Mass Transfer Conference, Dec. 28-31, IIT Kharagpur, India, Paper number: HMTC1300111

6. S. Abishek, R. Narayanaswamy, V. Narayanan, 2012, Effect of Standoff Distance on the Partitioning of Surface Heat Flux during Subcooled Jet Impingement Boiling, Proc. 18th Australian Fluid Mechanics Conference, Launceston, Australia, Dec. 3-7, Paper number: 302

7. S. Abishek, R. Narayanaswamy, V. Narayanan, 2012, Effect of Heater Size on Confined Subcooled Jet Impingement Boiling, Proc. ASME Summer Heat Transfer Conference, Puerto Rico, USA, July 8-12, Paper number: HT2012-58205, pp. 407–416

8. S. Abishek, R. Narayanaswamy, V. Narayanan, 2011, Transient Characteristics of Confined Submerged Laminar Jet Impingement Heat Transfer from a Vibrating Heater, Proc. 21st National and 10th ISHMT-ASME Heat and Mass Transfer Conference, Chennai, India, pp. 281-290

TABLE OF CONTENTS

LIST OF TABLES

LIST OF FIGURES

NOMENCLATURE

Symbol	Description	Units
A	ratio of jet pulsation amplitude to jet velocity	%
A_b	area fraction of bubbles on the surface	dimensionless
B	hydraulic diameter of slot nozzle	m
c_p	specific heat capacity	J / kg-K
d	width of the slot-nozzle	m
d_b	bubble diameter in free stream	m
d_{bw}	bubble departure diameter	m
D	width of the slot-nozzle	dimensionless
D_h	hydraulic diameter of the slot nozzle	m
f	bubble departure frequency	Hz
	or frequency of jet pulsation	Hz
F	view-factor	dimensionless
	or body force	N
g	acceleration due to gravity = 9.81	m / s^2
h	nozzle-to-heater distance	m
	or heat transfer coefficient	W / m^2-K
H	nozzle-to-heater distance	dimensionless
J	radiosity	W $_/$ m^2
Ja	Jacob number	dimensionless
k	thermal conductivity of fluid	W / m-K
	or turbulence kinetic energy	m^2 / s^2
l_x	length of the impingement surface	m
L	latent heat of vaporization	J / kg
L_x	length of the impingement surface	dimensionless
$\dot{m}$	mass flow rate	kg / s
N_{RF}	radiation-flow interaction parameter	dimensionless
Nu	local Nusselt number	dimensionless
N_w	active nucleation site density	dimensionless
p	local pressure	Pa

Symbol	Description	Units
Pr	Prandtl number	dimensionless
q	heat flux	W/m^2
Ra	average surface roughness	μm
Re	Reynolds number	dimensionless
Ri	Richardson number	dimensionless
R_{RMS}	root mean square surface roughness	μm
t	time	s
T	temperature	K
u, v	component of velocity along x and y-axes	m / s
U, V	component of velocity along x and y-axes	dimensionless
u_{N}	jet-velocity at nozzle-outlet	m / s
v	component of velocity along y-axis	m / s
w	width	m
x, y	distance along x and y-axes	m
X, Y	distance along x and y-axes	dimensionless
z	distance beneath the impingement surface	mm

GREEK SYMBOLS

α	thermal diffusivity	m^2 / s
	or volume fraction	dimensionless
β	thermal expansion coefficient	1 / K
ε	surface-emissivity	dimensionless
	or turbulence dissipation rate	m^2 / s^3
λ	temperature	dimensionless
	or area-averaged normalized temperature	dimensionless
μ	dynamic viscosity	kg / m-s
ρ	density of fluid	kg / m^3
σ	Stefan-Boltzmann constant = 5.67×10^{-8}	W / m^2-K^4
	or surface tension	N m
Ψ	stream function	dimensionless
Ω	vorticity	dimensionless

Symbol	Description	Units
Λ	radiosity	dimensionless

SUBSCRIPTS

C	single phase convective component	
d	based on slot-width	
E	evaporative component	
g	growth component of ebullition cycle	
h	based on standoff distance	
H	based on heater dimensions	
i, j, k	element indices	
	or phase indices (only i and j)	
l	liquid phase	
mean	time averaged	
N	condition at jet nozzle outlet	
Q	quenching component	
CHF	critical heat flux	
R	radiative component	
sat	saturation	
	or degree of superheating	
sub	subcooling	
T	total	
v	vapor phase	
w	wall, solid or impingement surface	
	or waiting component of ebullition cycle	

ACRONYMS

CHF	critical heat flux	
BDD	bubble departure diameter	
BDF	bubble departure frequency	

CHAPTER 1

INTRODUCTION

1.1   NEED FOR JET IMPINGEMENT THERMAL MANAGEMENT

Efficient thermal management is of vital significance in a variety of practical applications across several industries including metal processing, miniature electronics, aerospace, solar and power generation, turbine cooling, lighting, data-centers, drying of textile and photographic films, food processing and refrigeration. In the context of the electronics industry, the reliability of advanced new technologies is strongly related to the cooling efficacy of the waste heat removal technique employed. In recent years, miniaturization in the advanced electronic modules towards efficient and highly functional compact components has led to a significant rise in the rate of heat dissipation over smaller areas (of components). The need for addressing increasingly higher heat loads at concentrated regions has attracted extensive research on techniques to improve traditional thermal management systems as well development of novel cooling schemes. A detailed
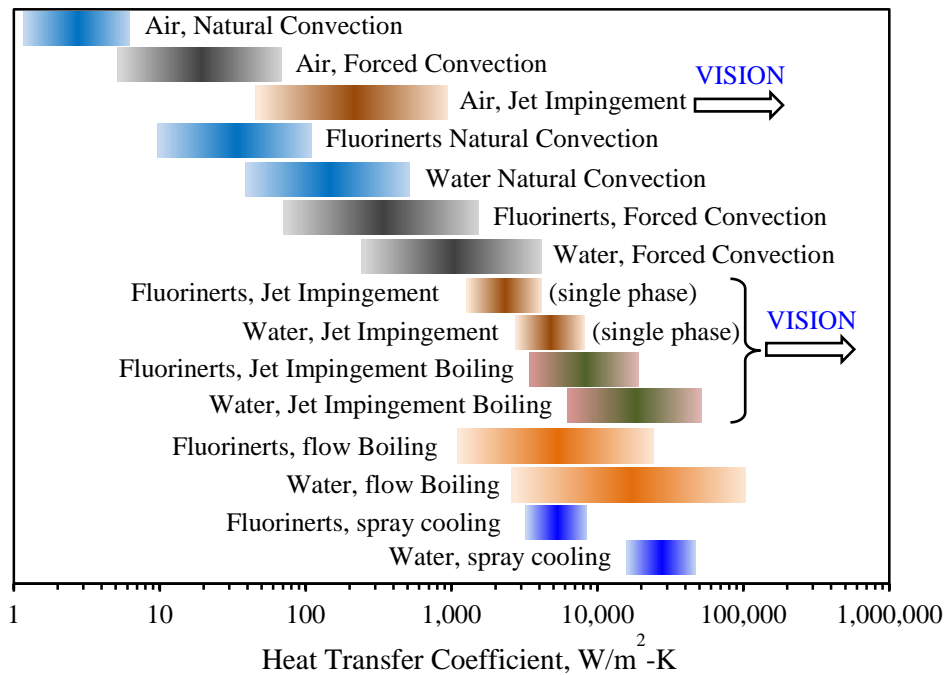
Figure 1.1: Typical ranges of heat transfer coefficients for different cooling techniques

discussion on various advanced cooling technologies employed in the electronics industry is delineated in Lasance [1].

Figure 1.1 illustrates the typical ranges of the heat transfer coefficients obtained from various popular thermal management techniques. Air cooling is the most popular cooling technique used for a variety of applications requiring relatively lower heat removal rates per unit area of upto 10^3 W/m^{2}K. In recent years, several novel enhancements have been proposed for stretching the cooling potentials of air cooled techniques to yield higher heat transfer coefficients, such as piezo-fans introduced by General Electric [2, 3], nanolightning [4] and synthetic jets [5], nevertheless, the enhancements are usually only less than an order of magnitude. While the maximum heat transfer coefficients obtained using traditional fan (forced convective) cooling or duct cooling with air is about 150 W/m^{2}K, much higher (upto 10^3 W/m^{2}K) heat transfer coefficients are obtained by the use of impinging jets on concentrated heat sources.

In comparison to air cooling, the use of liquids such as water and dielectric Fluorinerts offer much higher heat transfer performances as indicated in Fig. 1.1. The several liquid based cooling systems can be broadly classified into direct and indirect schemes based on whether or not the coolant comes in contact with the heated module. Heat pipes [6], cold-plates [7] and microchannel heat sinks [8] are popular indirect cooling systems. With much higher heat dissipation rates (typically over 1–2 MW/m^2) required by advanced power electronics such as integrated-gate-bipolar-transistors, and high density computing devices such as Cray-supercomputers, direct immersion cooling has been sought as a viable cooling technique. Direct cooling systems involving phase change (boiling) yield much higher heat transfer coefficients than traditional single phase cooling systems as a result of additional latent heat removal due to boiling of the coolant on the heated module, and thus have been very effective in addressing the constraints imposed by many sensitive electronic modules on the maximum operating temperatures (typically around 85 $^{\circ}$C). Jet impingement boiling (as well as non-boiling liquid impingement to a certain degree) has been sought as a very efficient cooling technique, particularly due to the relatively significant enhancements obtained in the impingement region (elaborated in Section-1.2.1) in addition to latent heat removal due to boiling of the coolant.

Spray cooling is another impingement cooling technique, where an atomizer breaks up the coolant at the nozzle outlet, and the mixture of several individual drops along with the ambient fluid (air or gas) impinges on the heated surface. Due to high heat transfer coefficients obtained with spray impingement evaporation [9,10] as indicated in Fig. 1.1, the technique has received increased popularity in recent years for high power density applications. Spray cooling and jet impingement are often considered competing options for electronic cooling applications involving high heat fluxes. Jet impingement cooling results in highly concentrated and relatively higher heat transfer coefficients, but with significant non-uniformity in the spatial temperature distribution which could be a concern in terms of thermal stresses generated on the surface. On the contrary, spray cooling offers a relatively larger spatial uniformity of the heat removal performance and significantly delays dry-out on the wall during vigorous boiling conditions, but with a compromise in the peak heat transfer performance. For this reason, jet impingement boiling is a preferred option for several applications involving cooling of concentrated heat sources such as in power electronics, synchrotron x-ray and semiconductor laser systems [11-13].

Water based jet impingement cooling systems result in invariably higher (about half order of magnitude) heat transfer coefficients than flourochemical based systems. However, the latter are a preferred choice for electronic applications, particularly in direct liquid cooled systems due to their dielectric properties that ensure least interference with the electronic circuitry even during failure/ leakage. Besides, the dielectric flourochemical fluids such as FC-72, PF-5060 and FC-77 (from 3M^{TM} Chemicals) have much lower boiling points as compared to water, which make them a better choice for electronic applications requiring phase change cooling at lower temperatures. However, most of the flourochemical coolants are highly volatile and expensive (for operation), making the design of the cooling system more complex than that for water.

1.2   PHYSICS OF JET IMPINGEMENT COOLING

Jet impingement cooling refers to the mechanism of heat removal from a surface due to impingement of a fluid that exits a nozzle placed at a certain distance from the hot surface. Jet impingement boiling (heterogeneous) refers to the condition where the

(a) free surface jet

(b) submerged jet

(c) plunging jet

(d) confined and submerged jet
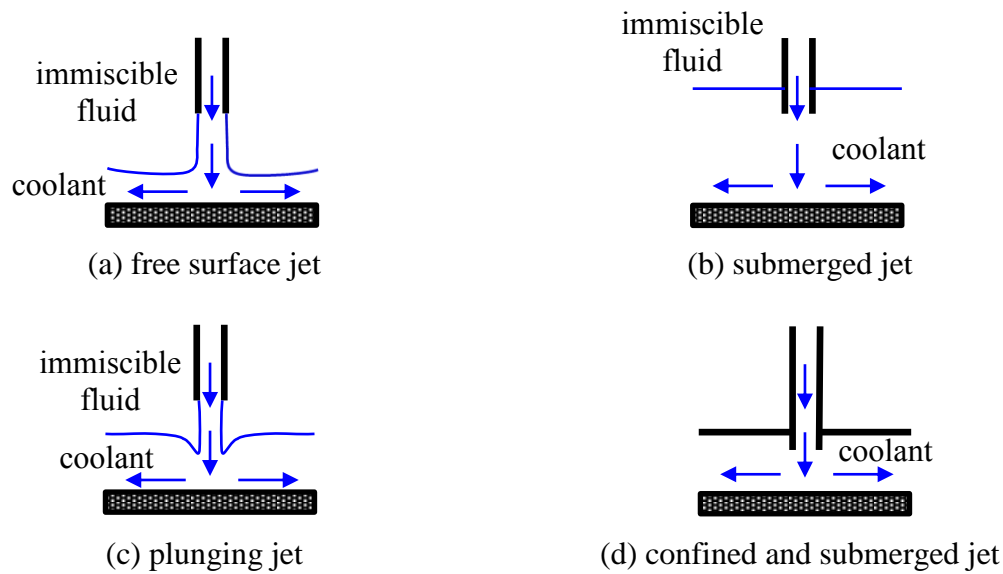
Figure 1.2: Schematics of various jet impingement cooling configurations; ▨▨▨ represents the heated impingement surface and ▬▬ represents solid walls

impinging fluid boils upon impingement on the hot surface when the surface temperature is higher than the saturation temperature of the impinging fluid, at the operating pressure. Depending on the geometry of the application (usually the geometry of the surface to be cooled), jet impingement systems employ circular or rectangular/ slot jet nozzles. Both, circular as well as slot jets are used in several different configurations which are generally classified into (i) free surface, (ii) submerged, (iii) plunging and (iv) confined jet impingement systems. Figure 1.2 illustrates the schematic of the aforementioned configurations. In a free surface configuration (Fig. 1.2 (a)), the coolant exits a nozzle into a medium of a different fluid (usually immiscible) to impinge on the heat transfer surface. In a submerged jet impingement configuration (Fig. 1.2 (b)), the fluid jet exits the nozzle into a quiescent medium of the same fluid before impingement. In a plunging jet configuration (Fig. 1.2 (c)), the coolant exits the nozzle into a medium of a different immiscible fluid (similar to free surface jet impingement) but impinges on the heat transfer surface through a pool of the coolant. In a confined jet impingement configuration (Fig. 1.2 (d)) which in most cases is also a submerged configuration, the fluid exits the nozzle into a quiescent medium of the same fluid which is confined by a solid wall around the nozzle at a certain distance from the heated surface. A special case of a confined and submerged jet impingement configuration is when the

confinement plate lies at the plane of the nozzle exit. As will be discussed in the following sections, the present research focusses on slot jet impingement in a confined and submerged configuration relevant to miniature electronic cooling applications; henceforth, the discussion would pertain to this configuration alone.
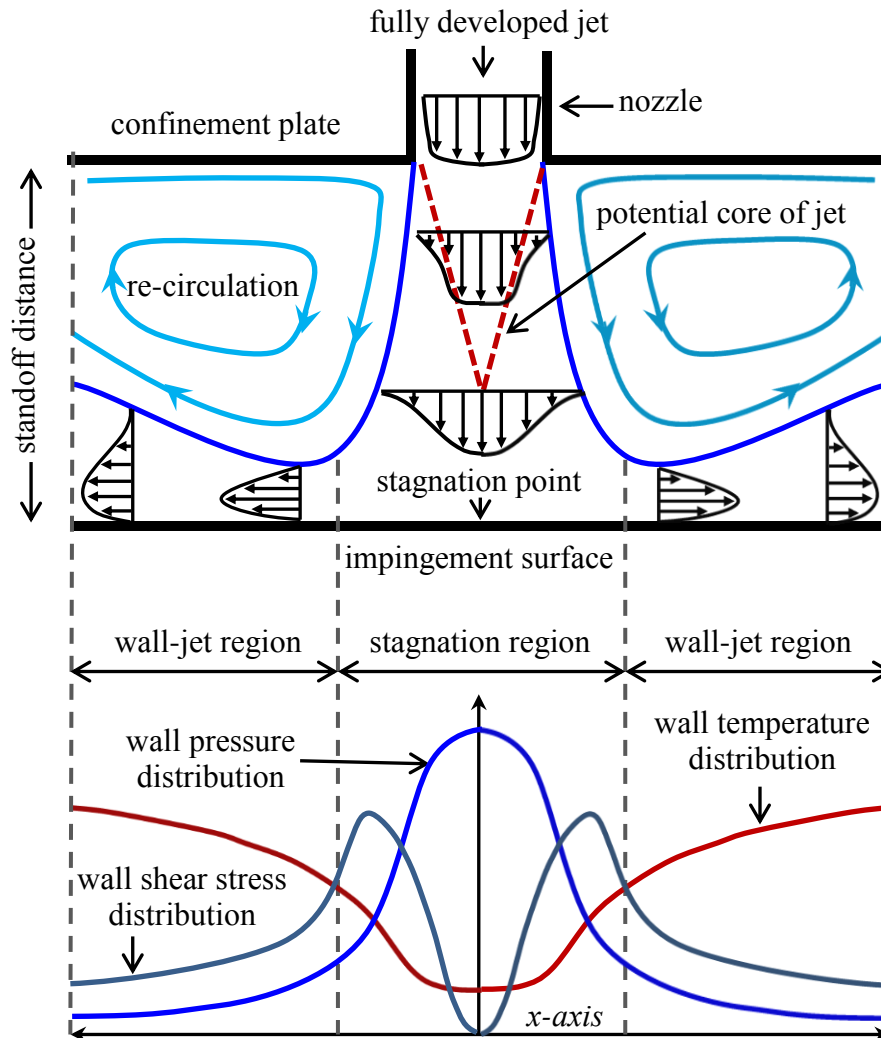
Figure 1.3: Schematic of flow field and associated effects on the impingement surface during confined jet impingement heat transfer

1.2.1 Flow Field and Heat Transfer Characteristics of Single Phase Confined and Submerged Jet Impingement Cooling

Figure 1.3 shows the schematic of the flow field and typical distributions of static pressure, wall shear stress and surface temperature on the impingement surface during confined jet impingement heat transfer on a uniformly heated surface. Under such a configuration, the fluid jet (which could be laminar or turbulent) that issues

into the domain entrains the surrounding fluid through transverse (with reference to the direction of the impinging jet) momentum exchange with the quiescent medium. The major characteristic difference between confined and unconfined jet impingement systems is that, the presence of confinement plate results in circulation cells on either sides of the jet, and thus results in larger momentum exchange between the jet and the surrounding fluid. At sufficiently small (standoff) distances between the nozzle/ confinement plane and the impingement surface, ($\leq 2\times$nozzle hydraulic diameter) the presence of a confinement has been found to be beneficial [14] in improving the heat transfer characteristics on the surface. However, the effect of confinement at higher standoff distances is practically negligible; nevertheless the impingement cooling system becomes more compact and thus more suitable for portable applications. As shown in the figure, the jet spreads in the transverse direction (x-axis) as a result of continual momentum transfer to the surrounding fluid. The region inside the jet where the fluid velocity remains unaffected is known as the potential core (indicated in the figure) and the width of the core reduces with distance downstream due to broadening of the jet. It is to be noted that the length of the potential core could be significantly affected by the impingement plate for sufficiently small standoff distances. Beyond the potential core of the jet, the presence of the impingement surface results in stagnation of the impinging fluid, thereby bringing the fluid completely to rest at what is known as the impingement stagnation point, where the pressure results in a local maximum. In liquid jet impingement systems operating at considerably high velocities (10s of m/s), the pressure rise at the stagnation point could significantly affect the saturation temperature of the fluid, which is of large significance in systems involving phase change (boiling) of the impinging fluid [12,13]. As indicated in Fig. 1.3, the heat transfer coefficient is highest at the stagnation point and thus results in a local minimum for the surface temperature. Beyond the stagnation point, the fluid accelerates in the direction parallel to the impingement surface resulting in a wall jet along the surface on either sides of the stagnation point. The acceleration of the fluid from the stagnation point results in a steep gradient of the wall shear stress in the stagnation region as shown in Figure 1.3. For impingement cooling systems with sufficiently low standoff distances ($\leq 2.5\times$nozzle hydraulic diameter), the fluid acceleration as well as transition to turbulence (in some cases) results in a secondary peak for the heat transfer coefficient at a certain distance downstream of the

stagnation point. With further distance downstream the width of the wall jet increases due to momentum exchange with the surrounding fluid which results in a reduction of the fluid velocity and an associated reduction of the wall shear stress and heat transfer coefficient. It is for this reason that jet impingement is highly desirable for cooling of concentrated targets. However, the presence of the confinement plate for low standoff distance configurations results in a forced parallel flow along the wall jet direction which reduces the spreading rate of the wall jet, thereby retaining relatively higher heat transfer coefficients downstream of the stagnation point, as compared to unconfined impinging jets.

For miniaturized air cooled configurations operating at low jet Reynolds numbers, where the effect of turbulence is relatively low due to large viscous effects that dominate the flow field, sufficiently high surface temperatures could result in substantial radiation interaction between the heated surface and the enclosure. This contribution of surface radiation to the overall heat transfer from the surface could be significantly enhanced to the advantage of augmenting heat transfer, by improving the radiation characteristics, such as surface emissivity of the components in confined configurations. Although not directly related to jet impingement cooling configurations, the influence of surface radiation has been reported [15] to contribute to over 60% of the total heat transfer in many confined electronic cooling applications involving radiatively non-participating coolants (mostly air).

1.2.2   Flow Field and Heat Transfer Characteristics of Confined Subcooled Jet Impingement Boiling

Jet impingement boiling combines the advantages of impingement cooling along with the substantially additional heat transfer rates obtained due to latent heat removal from the surface as a result of liquid to vapor phase change. Boiling of impinging jets are characterised by the complex interactions between the ebullition from numerous sites on the heated surface and the thermal hydraulics in the bulk flow. The interactions typically involve the heat and mass transfer between the phases, lift/ drag and buoyancy forces on the bubbles, bubble coalescence/ collapse, and the associated turbulence contribution to bulk flow particularly near the heated wall. The heat transfer due to boiling of impinging jets depend significantly on the jet

flow rates, degree of subcooling, operating pressures, operating gravity, roughness texture of the heat transfer surface and the geometric configuration. The consequence of the aforementioned conditions are particularly on the ebullition process which is characterised by the bubble diameters during growth and departure, bubble growth time and dwelling time (interval between bubble departure and the occurrence of a subsequent bubble in the void) and active nucleation site density on the superheated surface.
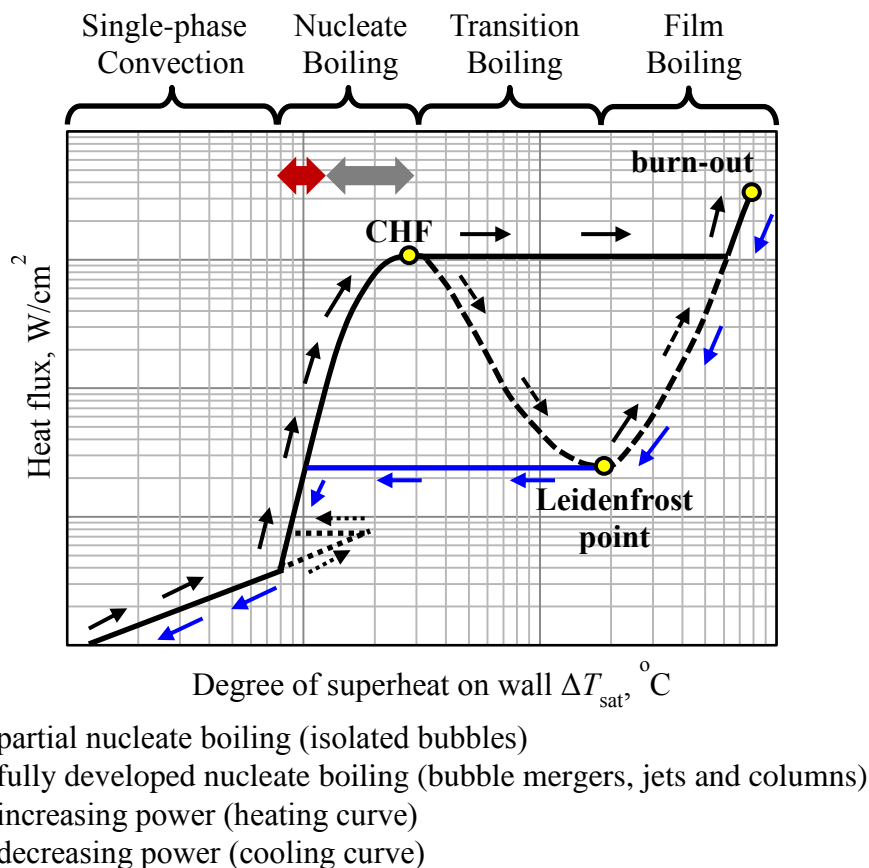
Figure 1.4: Typical boiling curve indicating the various boiling regimes; solid ▬▬ line represents a heat flux controlled system and dashed ▬ ▬ ▪ line represents a temperature controlled system; and dotted ▪▪▪▪▪▪▪ lines represent the temperature excursion in heat flux controlled systems with highly wetting fluids

Heat transfer during boiling is typically expressed in terms of a boiling curve that depicts the variation in the surface heat flux against degree of surface superheat (difference between the surface temperature and the saturation temperature of the fluid). Figure 1.4 illustrates the typical boiling curve, indicating the various regimes for boiling; first introduced by Nukiyama [16] in 1934 from the study of

natural convection pool boiling on a fully submerged heated wire. The boiling curve during jet impingement typically follows the same trend as that for pool boiling, and likewise, depends on whether the heated surface is temperature controlled or heat flux controlled.

(a) single phase convection

(b) partial nucleate boiling

(c) fully developed nucleate boiling

(d) critical heat flux
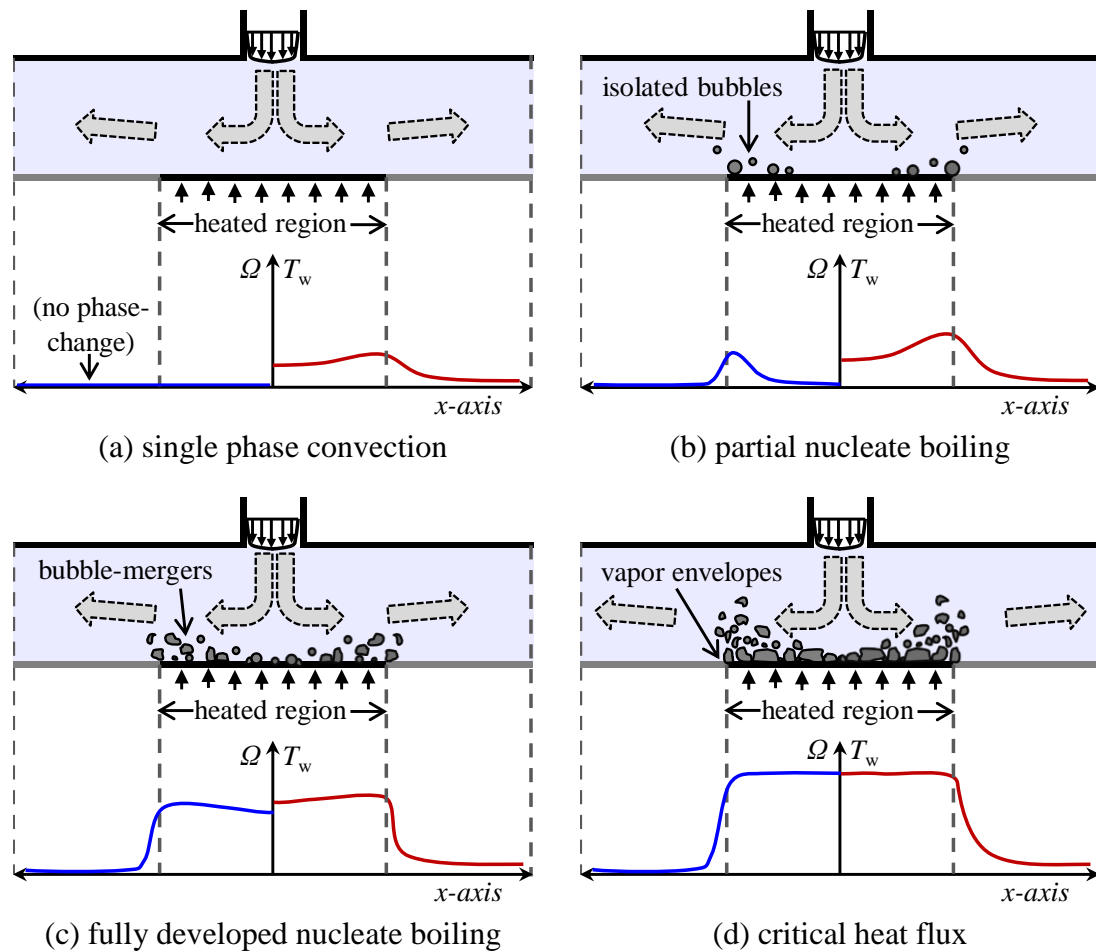
Figure 1.5: Schematic of various regimes of confined and submerged steady state subcooled jet impingement boiling; T_w represents the surface temperature and Ω represents the liquid-vapor phase change rate on the heated impingement surface

For very low heat fluxes, when the surface temperature is below saturation temperature, single phase convection is the only mode of heat transfer. A typical surface temperature distribution (T_w) obtained on a heat flux controlled surface is shown in Fig. 1.5 (a). As indicated in the earlier section (Section 1.2.1), the rate of heat transfer at the stagnation region is highest, and thus the local temperature at the region is significantly lower than that downstream of the stagnation point. As the surface temperature is still below saturation temperature, the liquid-vapor phase

change rate on the hot surface (Ω) is zero during this regime of the boiling curve. With an increase in heat flux, when the surface temperature rises beyond the saturation temperature of the fluid, boiling initiates on the impingement surface, resulting in an increase in the slope of the boiling curve due to the additional latent heat removal as shown in Fig. 1.4. The condition for this combination of heat flux and surface temperature when boiling initiates is referred to as boiling incipience. For some fluids (like Fluorinerts) which highly wet the surface, boiling initiates at relatively higher temperatures and the surface temperature drops immediately after incipience of boiling. This trend is known as temperature overshoot and is indicated in Fig. 1.4. The characteristic difference between boiling incipience in pool boiling and jet impingement boiling is that, nucleation initiates throughout the surface uniformly during pool boiling, while initial nucleation occurs farthest distance downstream (on the superheated area) and traverses towards the stagnation point (at higher heat fluxes) during impingement boiling due to the large convective influence of the jet in the stagnation region. During the initial phase of boiling at relatively low degrees of surface superheat, bubble nucleation occurs at isolated cavities on the heated surface and the effect of forced convection due to the influence of the jet remains the strong mechanism of heat transfer. This initial regime of boiling is termed as partial nucleate boiling or isolated bubble nucleation regime. As indicated in the schematic in Fig. 1.5 (b), the surface temperature in the impingement region remain relatively lower due to the significant influence of the impinging jet and rises steeply towards the periphery of the heated surface (where the influence of the jet has reduced) under the regions where boiling occurs. As a consequence, a peek in the liquid-vapor mass transfer rate is obtained under the region where boiling occurs, as shown in the figure. With further increase in the surface heat flux or surface temperature, boiling spreads through the entirety of the impingement surface resulting in local interaction between the bubbles from neighbouring nucleation sites, and the heat transfer is largely controlled by the mechanism of boiling and lesser due to the influence of convection. The consequence of this vigorous boiling and latent heat removal from the surface in this fully developed nucleate boiling regime is seen in Fig. 1.4 as a steep rise in heat transfer rate for small increases in surface temperature. As shown in the schematic in Fig. 1.5 (c), the surface temperatures and phase change rate on the heat transfer surface are nearly uniform, but could be slightly lower in the stagnation region due to the influence of the jet for conditions of

high jet velocities or degree of subcoolings. With further increase in applied heat flux, the surface becomes enveloped by a film of vapor, which results in a sudden increase in the surface temperature and a deterioration in the boiling process. This condition is known as the critical heat flux (CHF), which dictates the maximum attainable heat flux in most practical applications. While the influence of the jet flow is usually insignificant in influencing the area averaged boiling curves in the fully developed nucleate boiling regime, higher jet velocities invariably result in large values of CHF heat fluxes due to enhanced fluid supply to the heat transfer surface [17]. During and beyond CHF, boiling deteriorates due to insufficient fluid supply to the hot surface, and the temperature distribution becomes entirely uniform throughout the heated area as shown in Fig. 1.5 (d). However, in temperature controlled systems, with increase in surface temperature beyond CHF results in a decrease in the surface heat flux to a local minima (termed as Leidenfrost point) through a regime known as transition boiling. The rate of heat transfer once again increases with further increase in surface temperature due to a significant rise in the contribution from surface-radiation coupled with an increase in vapor phase convection through a regime termed as film boiling, until the component burns out, as indicated in Fig. 1.4.
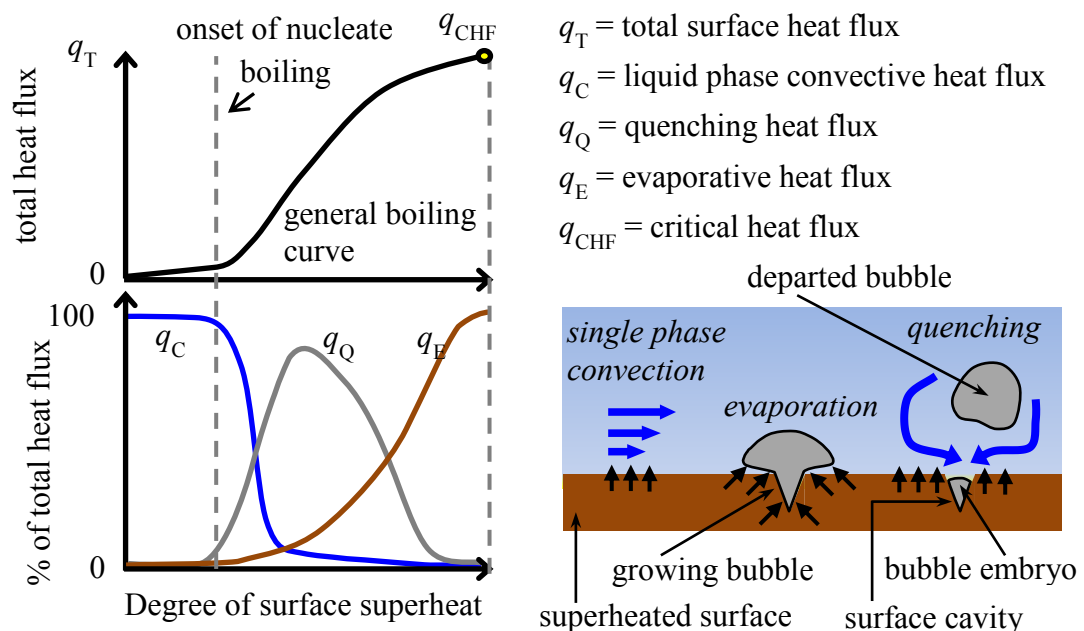
Figure 1.6: Schematic of the three partitioned heat transfer mechanisms and the typical relationships between the partitioned heat fluxes and total heat flux to the surface degree of superheat; note that the cavity on the surface is exaggerated in size

1.2.2.1   Surface Heat Flux Partitioning During Subcooled Flow Boiling

The total heat flux from the hot surface during various regimes of forced convective nucleate boiling (outlined in the preceding paragraph) is typically partitioned into three simultaneous mechanisms namely, (i) liquid phase convection, (ii) quenching, and (iii) evaporation [18]. Figure 1.6 illustrates the schematic of the three partitioned heat transfer processes and the typical relationships between the three partitioned heat fluxes and the total heat flux to the degree of superheat on the heated surface. The single phase convective component accounts for the heat transfer to the liquid phase from the fraction of the surface where boiling does not occur. As shown in the figure, the total heat transfer from the heated surface prior to the onset of nucleate boiling is purely due to convection. After the onset of nucleate boiling (ONB), the total heat from the surface is used partially for liquid-to-vapor phase change (latent heat) and partially for sensible heating of the fluid that occupies the void of a departed bubble (quenching), in addition to single phase convection on the non-nucleating fraction of the surface. The magnitudes of these component heat fluxes are typically determined by the boiling parameters including nucleation site density and the ebullition characteristics, and bulk flow characteristics. The ebullition parameters involve the diameter of the bubble prior to departure (departure could refer to bubble lift-off or sliding on the surface due to the effect of the fluid motion around the bubble), bubble dwelling/ waiting time (interval between the departure of bubble from a nucleation site and the inception of a subsequent bubble at the site) and bubble growth time (time taken for the bubble to grow to the maximum departure size). The frequency of bubble departure cycle is defined as the inverse of the sum of the growth and waiting times. The aforementioned surface heat flux partition mechanism is the basis for the computational studies on jet impingement boiling detailed in this thesis, and is presented in more detail in later chapters.

1.2.3   Flow Field and Heat Transfer Characteristics of Pulsating Jet Impingement Cooling

In a confined pulsating jet impingement cooling system, the mean velocity of the impinging jet is externally forced to oscillate at a certain amplitude, frequency and waveform before issuing into the confined and submerged environment. Pulsations in

(a) 10 % of pulsation cycle

(e) 60 % of pulsation cycle

(b) 30 % of pulsation cycle

(f) 70 % of pulsation cycle

(c) 40 % of pulsation cycle

(g) 80 % of pulsation cycle

(d) 50 % of pulsation cycle

(h) 90 % of pulsation cycle
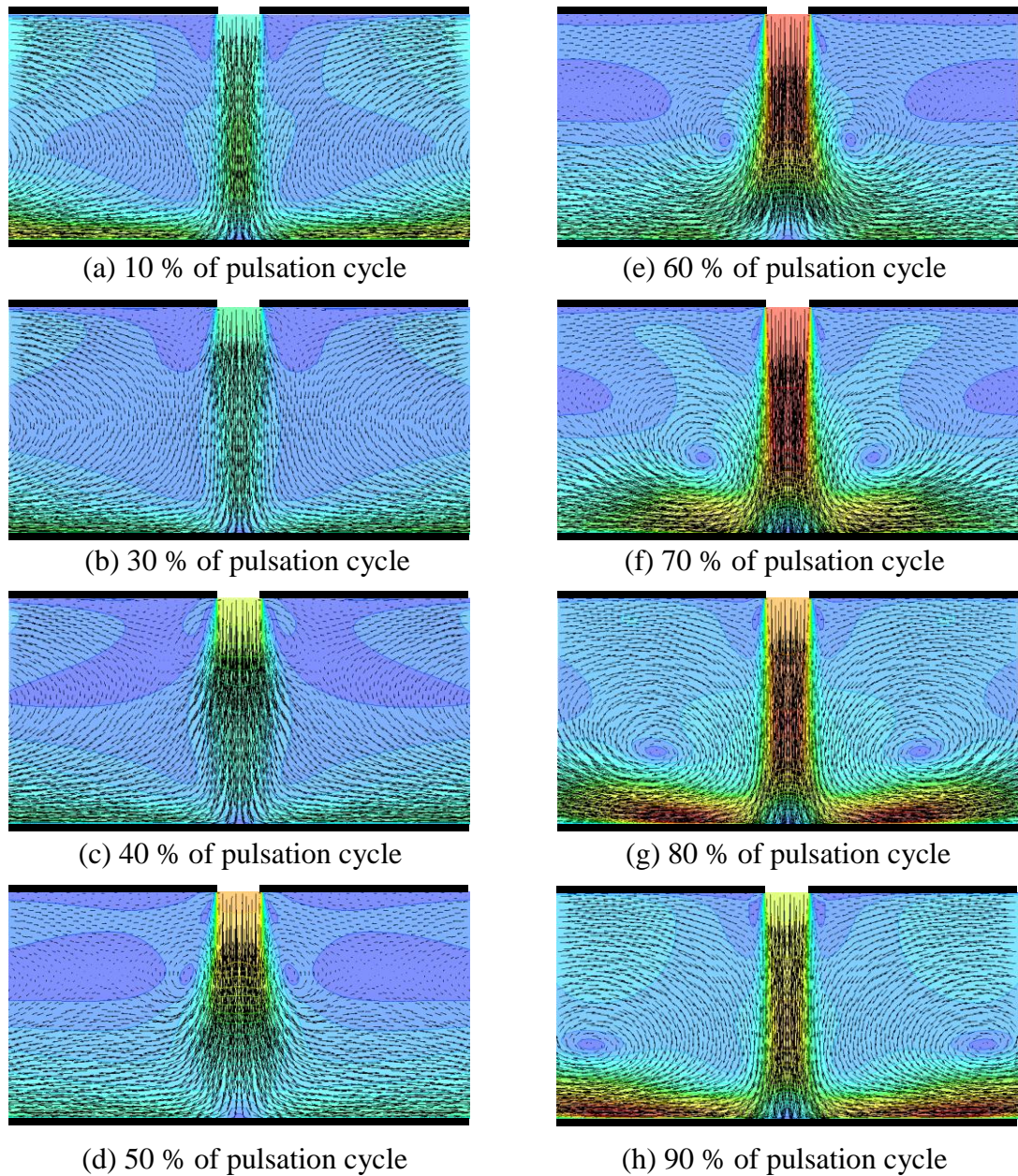
Figure 1.7: Depiction of (a-h) the flow field (velocity vectors superimposed on the contours of velocity magnitude) during various stages of a cycle of single phase pulsating confined and submerged jet impingement, and (g) typical sinusoidal area-averaged instantaneous velocity at the nozzle; data for the figure pertain to simulations from an ongoing research- not presented in the thesis

an imping jet results in disruption of the boundary layer on the heated impingement surface, thereby affecting the wall heat transfer characteristics. Some of the consequences in the flow features due to pulsation of impinging jets are (i) higher turbulence induced by flow instabilities at the interface between the jet and the ambience, (ii) chaotic mixing which promotes entrainment, (ii) change in resistance to boundary layer growth on the impingement surface [19]. Figure 1.7 depicts a typical flow field (velocity vectors superimposed on the contours of velocity magnitude) obtained during various stages of a cycle during single phase pulsating confined and submerged jet impingement. As can be seen, pulsation in the mean jet velocity results in vortices around the jet's shear layer which grow along its path towards the impingement surface due to larger entrainment of the surrounding fluid. Hofmann et al. [20] pointed out that this could be particularly important for large nozzle standoff distance where the free shear layers are large. At sufficiently high pulsation amplitudes, this strongly influences the surface heat transfer characteristics due to a cyclic renewal of the boundary layer on impingement surface. Besides, the cyclically larger entrainment of the fluid results in larger transverse spreading of the issuing jet which could result in the cyclic widening of the stagnation region, as compared to a steady jet. The rolling vortices induced due to the pulsation of the impinging jet particularly result in larger consequences on the thermal characteristics in the parallel flow regime (wall jet). Depending on the combination of pulsation frequencies and amplitudes and the dimensions of the geometric configuration, jet pulsations could result in both enhancement as well as deterioration of the time averaged heat transfer characteristics [20, 21]. Pulsating impinging jets have been employed in many different waveforms including sinusoidal, square wave and triangular for the mean velocity. An interrupted pulsating jet is a special type of pulsating impinging jet where the instantaneous velocity oscillates between 0 (no-flow) and a maximum, resulting in a pulsation amplitude of 100%.

Pulsating impinging jets could also be used as a viable heat transfer augmentation technique in systems involving boiling heat transfer. However, there is no reported study on this study in the open literature. Although not categorized as a pulsating impinging jet system, a recent study [22] pointed out that an oscillating jet of fluid (targeted towards the heated surface) induced under a vibrating metallic diaphragm in an otherwise quiescent pool of liquid, significantly delayed critical heat

flux by forcibly dislodging bubbles that formed on the heated surface during nucleate boiling.

It is pointed out that impingement cooling under both single phase as well as boiling conditions are favourable for a variety of applications involving cooling of localized heated regions. In addition, the introduction of jet pulsations could be a potentially viable technique for heat transfer augmentation in both single phase as well as boiling jet impingement cooling systems. The present research detailed in this thesis delineates the experimental and computational methodologies employed for, and the results thus obtained from the study of heat transfer characteristics under steady state and pulsating impinging jets with and without boiling under different relevant parametric conditions. The following chapter discusses the state of the art on the aforementioned subjects, highlighting the progress in the subject thus far, and identifying areas that require further investigation.

CHAPTER 2

LITERATURE REVIEW

This chapter delineates the present state of knowledge and literature relevant to the different areas of confined and submerged jet impingement heat transfer presented in this thesis, with specific focus on slot (two-dimensional) jet impingement configurations. Much like most of the thesis, this chapter is discussed in three segments:

(i) low velocity air jet impingement, concluding with particular reference to high temperature applications where surface radiation may have a significant role in the overall heat transfer process.

(ii) liquid jet impingement under both single-phase as well as boiling conditions, focusing on average and local heat transfer predictions, and additionally pointing out modeling considerations for jet impingement boiling problems.

(iii) impingement heat transfer under forced jet pulsations for enhancement of steady jet impingement cooling, pointing out vast possibility of exploration in the field of pulsating boiling jet impingement heat transfer, and to a certain extent, pulsating liquid impingement heat transfer as a whole.

2.1 STEADY STATE GAS (AIR) JET IMPINGEMENT HEAT TRANSFER

The earliest studies on two-dimensional jet impingement heat transfer were carried out in the 1960s-70s with specific focus on drying applications, control of heat treatment and enhancement of internal cooling of turbine blades for operation at higher temperatures [23-25]. Gardon and Akfirat [26] made extensive experimental measurements of the heat transfer coefficients produced by the impingement of single and multiple two-dimensional air jets and provided correlations for both local as well as averaged heat transfer coefficients. Their experiments encapsulated a wide range of operating parameters with the jet Reynolds numbers (Re) and standoff distances (H) in the range $450 \leq Re \leq 50000$ and $0.5 \leq H \leq 60$ respectively. For

single slot jets, they identified four regimes for the dependence of heat transfer coefficients with the Reynolds number and standoff distance. Two very important observations were, the presence of an optimum standoff distance (around 4–7 times the hydraulic diameter of the nozzle) for maximum stagnation heat transfer coefficient for any Reynolds number, and the presence of secondary peak for the local Nusselt number for large Reynolds numbers with operation at small standoff distances.

In a subsequent study, Gardon and Akfirat [27] re-examined their previous investigations [26], this time targeting measurements of the velocity and turbulence in the domain to associate their significance to the associated heat transfer characteristics. They pointed out that heat-transfer characteristics of impinging jets cannot be explained in terms of velocity and local boundary-layer thicknesses alone, but the influence of laminar to turbulence transition must be taken into account for the expression of local convection coefficients, particularly with reference to the secondary peaks discussed in [26]. They also explained that, as the turbulence characteristics for both fully turbulent as well as initially laminar jets (that become turbulent due to mixing at the shear layer) can be uniquely determined by the jet Reynolds number and dimensionless jet length alone, all the heat transfer data can be effectively correlated by just the jet Reynolds number without the requirement of any separate parameter characterizing turbulence. The consequence of the maxima in the variation of the stagnation point Nusselt number and the secondary peaks in the lateral distribution of local Nusselt numbers [26] were successfully attributed to the opposing effects of the rising turbulence and the receding velocity magnitude in the wall jet region where turbulence was not fully developed. It was suggested that for slot impingement configurations, confined or unconfined, the transition from laminar to turbulence occurs for Reynolds numbers between 1000-3000.

Sparrow and Wong [28] used the naphthalene-sublimation technique to estimate the mass transfer rates due to orthogonal impingement of a single slot jet on a plane. The measured mass transfer data were extended to heat transfer coefficients using the heat-mass transfer analogy. The experiments employed fully developed initially (at the nozzle outlet) laminar air jets of Reynolds numbers upto 1750 issuing into an unconfined configuration with dimensionless nozzle to heater standoff

distances upto 20. Similar to [26], Sparrow and Wong [28] observed that that the heat and mass transfer coefficients generally tended to decrease with increasing separation distance, but also pointed out evidence of a non-monotonic behaviour and attributed that to the influences of mixing-induced turbulence and diminished jet velocity. It was shown that an increase in the jet Reynolds number tended to increase the transfer coefficients and correlated the stagnation Nusselt number, with 0.6-power dependence.

In contrast to the aforementioned studies which deal with unconfined jet impingement, Lin et al. [29] performed experiments to study the heat transfer characteristics of confined slot jet impingement to evaluate in a parametric fashion, the effects of jet Reynolds numbers and standoff distance on the associated heat transfer characteristics. In line with the observation of Gardon and Akfirat [27], Lin et al. postulated that for initially laminar jets, the effect of entrainment of the quiescent medium into the jet was significant only for jet Reynolds number was greater than about 1300, while the jet impingement configuration could be practically considered as laminar for $Re < 1300$, barring any transition that may occur on the impingement surface. They also pointed out that there could be a threshold cooling length (dimension of the heater) for a given jet configuration, beyond which the single jet impingement cooling system would significantly deteriorate in the heat transfer performance.

Perhaps, the earliest numerical simulations of confined and unconfined laminar jet impingement heat transfer, pertaining to jet Reynolds numbers up to about 1000 dates back to over three decades. Heiningen et al. [30,31] carried out computational analysis of laminar slot jet impingement flow field and heat transfer by modeling the governing partial differential equations to stream function-vorticity form and solved using a variety of finite difference techniques. They pointed out that as the central differencing of the convective terms in the vorticity transport equations induced instability in the convergence over majority of the Reynolds number range, upwind and hybrid differencing schemes proposed by Gosman et al. [32] were implemented. Similar numerical analyses were carried out by several researchers and it was established that parabolic velocity profiles at the nozzle exit have better stagnation region heat transfer characteristics on the impingement surface as

compared to flat velocity profiles [30,31]. They also pointed out that for the simulation of high temperature laminar jet impingement heat transfer, the influence of the variation in thermophysical properties was insignificant upto 450 K in the determination of the local as well as total surface heat transfer coefficients, despite a small difference in the dimensionless temperature gradient on the wall between constant and temperature dependant properties.

Miyazaki and Silberman [33] theoretically studied unconfined laminar jet impingement heat transfer from a slot jet using the potential flow solution, by conformal mapping for the distribution of main-stream velocity over the heater and subsequently solving the energy equations by a finite difference technique to evaluate the Nusselt numbers and friction factors. Graphical data was presented for the Nusselt numbers and friction factors for a dimensionless standoff distance $H \geq 1$ (upto a theoretical limit ∞) and for different fluids with Prandtl numbers between 0.7–100. The analytical study pointed out that the increase of flow friction due to small nozzle standoff distance was much more remarkable than the enhancement of heat transfer rate.

While most of the research on laminar jet impingement heat transfer neglected the effect of buoyancy forces, Yuan et al. [34] and, more recently, Sahoo and Sharif [35] studied the effects of Richardson number (ratio of Grashoff number and the square of the Reynolds number) on the heat transfer from an isothermal surface subjected to an impinging laminar slot-jet. Yuan et al. [34] showed that buoyancy effects contributed to enhancement in the heat transfer coefficient away from the stagnation point for highly buoyant flows, (large Richardson numbers and very low jet-Reynolds numbers) where the influence of the jet was decreased as compared to that at the stagnation region. However, most of their study was restricted to very low jet-Reynolds numbers of less than 100. Sahoo and Sharif [35] studied confined laminar upward as well as downward-facing jet-impingement heat transfer and found that the average Nusselt number at the hot surface increased with increasing jet exit Reynolds numbers. On the other hand, for a given geometric aspect ratio and Reynolds number, they pointed out that the average Nusselt number did not change significantly with change in Richardson number (due to change in orientation of the jet). However, changes in the flow and temperature fields were

noticed with a change in Richardson number, for given values of jet Reynolds number and domain aspect ratio. It was also pointed out that flow separation along the impingement surface occurred for small Richardson numbers, for given values of other parameters. Sahoo and Sharif [35] also indicated that the effect of buoyancy on the flow field and heat transfer was negligible for larger Reynolds numbers (100 - 500), while it was quite significant for lower Reynolds numbers ($\leq$ 100), in line with the predictions of Yuan et al. [34]. Similar results were also obtained by Corcione et al. [36] and Sahoo and Sharif [37].

While highly buoyant jet impingement flows could be related to the large surface temperatures, the effect of surface radiation on the flow and heat transfer could not be ignored, particularly for miniature electronic components where the impingement flows are largely laminar in confined spaces due to a relatively large consequence of viscous forces. Some related literature on the subject of confined flows at moderate Reynolds number are discussed in this regard, although not directly pertaining to jet impingement geometric configurations as dealt with in the present study, but the physical insights are very much applicable. Several studies [38-41] have indicated that under confined flows at moderate Reynolds numbers, the effects of surface-radiation become significant and hence cannot be ignored for a realistic and accurate evaluation of the heat transfer process. The earliest classical analytical study of combined effects of surface-radiation and forced convective heat transfer was carried out by Siegel and Perlmutter [38] for flows in pipes. Subsequently, Keshock and Siegel [40] investigated the augmentation of heat transfer using surface radiation for asymmetrical heating or cooling of flow of radiatively non-participating gasses in two-dimensional and annular ducts. More recently, influence of surface-radiation on heat transfer in channel flow, was studied under mixed convection scenarios by Rao et al. [15,41]. Their analyses focussed on the characteristics of heat transfer with discrete heat sources mounted on the channel walls, relevant to electronic cooling applications. They indicated that the component of convective heat transfer to overall heat transfer decreased when the surface emissivity of the components were increase, due to a consequent rise in the radiation transfer of heat from the surface. A similar trend was also observed with decrease in the spacing between the channel walls. The aforementioned studies on conjugate coupled mixed convective radiation heat transfer pointed out that the effect of

radiation to the overall heat transfer could reach upto 80% under sufficient geometric and operating conditions. This insight on the dependence of the contribution of radiation to the overall heat transfer could be extrapolated to a confined jet impingement configuration with small standoff distance, where the majority of the parallel flow region would be similar to a parallel plate channel as considered in [41].

The above section of the literature review on low Reynolds number air jet impingement cooling applications such as in miniature air cooled electronic systems where the flow field is predominantly laminar, points out that it is possibly imperative that surface radiation could largely influence the overall heat transfer in the system. Based on the afore-reviewed literature on jet impingement, it is found that the studies predominantly focussed on forced convective heat transfer, while recently, the effects of buoyancy on impinging jet heat transfer for laminar flow have also been studied; however, focussing on very low Reynolds numbers (≤ 100) which are practical only to a highly restrictive group of engineering applications. From [15, 39,41] it can be seen that the influence of surface radiation cannot be ignored for accurate prediction of heat transfer in many instances. Hence with a view to explore the relation of surface radiation to low velocity impingement heat transfer, one of the objectives of the research presented in this thesis was to carry out an elaborate parametric investigation to understand the effects of all the relevant controlling parameters on the relative contributions of surface radiation to the overall heat transfer during mixed convective jet impingement heat transfer in a confined geometry.

For air/ gas jet impingement systems operating at larger Reynolds numbers where the flow field is predominantly turbulent, the heat transfer due to convection is very large for surface radiation to play any significant role in the overall heat transfer process. Several reviews of the state of the art on such systems have been published in the literature. Martin [42] presented the first detailed review of the published literature on single as well as array of slot and round jets, encapsulating several empirical correlations for both heat and mass transfer over a wide range of operating conditions with emphasis on their applications to a variety of engineering systems. More recently, Zuckerman and Lior [43,44] presented a similar exhaustive review on the subject extending the focus from just the physics of impingement cooling

systems and empirical predictive tools to the advancements in the computational techniques available for the prediction of single and multiple jet impingement heat transfer, applicable to a variety of engineering systems. On similar lines, Dewan et al. [45] presented a detailed review of the computational techniques for the simulation of flow and heat transfer during single orthogonal jet impingement. The effects of different sub-grid scale models, boundary conditions, numerical schemes, grid distribution, and size of the computational domain adopted in various large eddy simulations were detailed, along with a comment on the direct numerical simulation of the configuration. Besides, a critical review of the advances in the Reynolds-averaged Navier–Stokes modeling of impinging flows was presented and concluded with future directions in the computation of impinging flows. Jambunathan et al. [46] summarized an expansive list of experimental studies on round jet impingement heat transfer for large Reynolds numbers in the range of 5000–124000 pertaining to the turbulent regimes, and dimensionless standoff distances in the range 1.2–16 over a flow region upto 6 times the nozzle diameters in the wall jet region. A new correlation was also derived [46] based on their observation that the Nusselt number must be a function of the Reynolds number raised to a function of the nozzle standoff distance rather than just a constant exponent such as in many of the papers that they reviewed. Other compilations of the impingement heat transfer studies pertaining to specific applications such as food processing [47], turbine cooling [48,49] and flame jet applications [50] are also available.

2.2   STEADY STATE LIQUID JET IMPINGEMENT HEAT TRANSFER

The miniaturization of electronic components and the advances in large scale integration of electronic circuits in the last few decades have resulted in a several fold increase in the heat generation rates per unit area of the chips, demanding more efficient cooling than that offered by traditional natural and forced convective air cooling systems. Heat fluxes of over 200 W/cm^2 have been projected with the requirement of chip temperatures to be maintained under 85-125 ^{o}C [11,51]. Direct immersion cooling with liquids have been shown to be a promising option for such large heat flux applications, particularly with the implementation of impinging jets for cooling localised area due to the several orders of magnitude larger heat transfer coefficients obtained as compared to air cooling techniques [52]. Liquid

impingement systems can be operated in two modes, *viz.* single phase and two-phase (boiling), depending on the thermal requirements of the application. Two-phase boiling impinging jet cooling systems exploit the advantages of latent heat removal from the surface in addition to the intrinsic large cooling potential of impinging jets in the stagnation region. Dielectric liquids such as Fluorinerts have also made it possible for cooling of components without the use of electrically resistive spacers between the electronic modules and the coolant, thereby beneficially reducing the net thermal resistances of the system [53]. Besides, dielectric fluids such as FC-72 (product of 3M) have much lower boiling points ($\approx 56\ ^{\mathrm{o}}\mathrm{C}$) than water, at atmospheric pressure, making them suitable for two phase cooling applications that require to be operated at low temperatures. There have been extensive studies reported in the literature focussing on several aspects of such single phase and boiling liquid impingement cooled systems for engineering applications [43,53-57]. The following sections of the literature review would discuss some of the key reports on single phase liquid impingement heat transfer delineating the difference in the characteristics as compared to gas jet impingement cooling. Subsequently a discussion on the literature on boiling jet impingement heat transfer is presented, where the recent advancements in computational techniques for the simulation of jet impingement boiling are also outlined.

2.2.1 Single Phase Liquid Jet Impingement Cooling

Single phase jet impingement cooling with liquids yield typically much larger cooling potentials at the stagnation as well as the wall jet region of the impingement heat transfer surface as compared gas/ air jets, and this has been attributed to the effect of fluid Prandtl number (*Pr*). Garimella [58] pointed out that there are interesting differences not only in the magnitudes but also in the parametric trends in heat transfer coefficients obtained with FC-77 or water when compared to air, due to large differences in Prandtl numbers. In coherence, Shi et al. [59] showed that the secondary peak in the distribution of local Nusselt number on the surface that did not occur using gas jets with $Pr < 1$ for certain geometric conditions, was obtained using liquid jets such as water, benzene and ethanol with $Pr > 5$. It is also important to note that unlike most gaseous coolants, the thermophysical properties of liquids, particularly dynamic viscosity vary significantly with operating temperature, thus

resulting in a variation in the Prandtl number for a variety of applications, depending on the thermal variations in the domain. This makes it an important design parameter for single phase liquid impingement cooled systems, as the variation in the fluid Prandtl number could significantly influence the heat transfer performance of the cooling system. For example, the *Pr* of water at atmospheric pressure changes from about 8.81 to 1.85 with a change in operating temperature from 10 ^{o}C to 90 ^{o}C; for comparison, *Pr* of air changes from 0.72 to 0.71 for the same range of temperatures.

Shi et al. [59] studied the effect of fluid Prandtl number on the heat transfer characteristics of confined and submerged laminar slot jet impingement for a wide range of Prandtl numbers between 0.7–71, encapsulating a variety of industrial coolants including air, argon, hydrogen, helium, ammonia, ethylene, water, benzene, ethanol, turpentine and isobutyl alcohol. Effect of Prandtl number was studied for a representative case with dimensionless nozzle standoff distance of 6 and Reynolds number of 100. They showed that the stagnation as well as average Nusselt number on the heat transfer surface consistently increased with an increase in fluid Prandtl number. The study also indicated that the increase in the heat transfer coefficients obtained with an increase in the fluid Prandtl number for laminar jet impingement cases were much larger than those obtained under turbulent conditions reported in the literature [60]. They also pointed out that the observed trends in the surface Nusselt number with increase in Prandtl number does not corroborate to the trends in the corresponding trends in the heat transfer coefficients obtained, and this was attributed to the large differences in the thermal conductivity of the fluids which significantly affect the heat transfer rate on the surface for a given flow field. Shi et al. [59] pointed out that water particularly stood out as fluid with the largest heat transfer coefficient for the conditions studied, although its Prandtl number was only about 6, among several other fluids that were considered for comparison with more than an order of magnitude larger Prandtl numbers.

Li and Garimella [60] experimentally investigated the effect of thermophysical properties on confined round liquid jet impingement heat transfer using three different fluids *viz.* air, FC77 and water encapsulating the range of Prandtl numbers between 0.7 and 25.2. The parameter ranges were orifice diameters of 1.59–12.7 mm, turbulent-flow Reynolds numbers of 4000–23 000, and orifice to

heat-source spacings of 1–5 jet diameters. The heat transfer rate in terms of the area averaged and stagnation point Nusselt numbers were characterised by the Prandtl number in addition to the geometric and flow parameters considered. Composite correlations spanning all the fluids were developed, as were separate correlations for individual fluids. With the large data set included in their study that spanned over a wide range of fluids (also including data from other published literature for the purpose of a generalized correlation), Li and Garimella [60] were able to appropriate the Prandtl-number exponent (≈0.452) for a generalised predictive tool for the local and averaged Nusselt numbers.

Wadsworth and Mudawar [53] performed experiments to investigate the heat transfer from confined slot jet impingement on to a simulated electronic module using a dielectric fluid FC-72. They studied the effects of jet width, fluid Prandtl number, channel height, heater sizes and impingement velocity and developed a correlation for the prediction of average Nusselt number for the controlling parameters in the range $8.75 \leq Pr \leq 12.05$, $1000 \leq Re \leq 30000$, $12.5 \leq L \leq 50$, $0.5 \leq H \leq 10$. It was shown that the rectangular slot jets resulted in nearly isothermal chip surface conditions, and that the average Nusselt number was more strongly dependant on the jet velocity and nozzle dimensions and less so on the standoff distance. It was also found that the correlation yielded a vanishing effect of nozzle width on average chip heat transfer coefficient for small values of nozzle width, and thus proposed that the chip cooling rate may be increased by increasing jet velocity alone. Besides, it was pointed out that under such conditions, the cooling flow rate may be minimized by reducing jet width without compromising chip cooling as long as jet velocity is set to the desired value.

Schlunder et al. [61] presented the most general and widely used benchmark correlation for the prediction of heat and mass transfer under a single turbulent slot jet. The correlation was developed based on heat-mass transfer analogy of the experimental Sherwood number data obtained from their own experiments along with those from the literature [26,62]. The generalized correlation was quoted [61] to be valid with 85% confidence for a variety of fluids and controlling parameters including Reynolds numbers (Re), dimensionless standoff distance (H), dimensionless heater size (L) in the range $3000 \leq Re \leq 90000$, $4 \leq L \leq 50$ and $2 \leq H \leq$

10. Martin [42] indicated that the correlation developed by Schlunder et al. [61] could also be applied to the transfer rates corresponding to the impingement stagnation zone for the prediction of stagnation Nusselt and Sherwood numbers with a maximum error 35-40%.

Schafer et al. [51] carried out experiments on submerged and confined slot impingement heat transfer on a series of individual flush mounted heaters of low thermal conductivity mounted along the impingement surface. The first set of experiments were carried out for jet Reynolds numbers (based on heater size) $650 \leq Re \leq 37200$, dimensionless nozzle standoff distances $H = 1.5$ and 3, and dimensionless heater offset distances in the range 0-12 times the slot width, using water, although the dimensionless heat transfer data were extended for generalization including published data for FC77. With this novel investigation using discrete heat sources the location of which was adjustable along the impingement surface, Schafer et al. [51] were able to point out that the heat transfer coefficient was not always maximum when the heater was directly beneath the stagnation point. In fact, for the small standoff distances considered for the study, which are relevant to the miniature electronic components, it was shown that beyond a Reynolds number about 20000 (for their geometric configuration), the Nusselt number under the secondary peak along the impingement surface became increasingly larger than the stagnation Nusselt number, with an increase in the jet Reynolds number upto 37200. In a second set of tests, heaters were placed at five locations from the stagnation point at dimensionless distances of 0, 5, 10, 15 and 20, for a dimensionless standoff distance $H = 1$, and Reynolds numbers upto 120000. In line with their first set of tests, it was shown that the Nusselt number under the secondary peak could reach upto 25% more than the stagnation Nusselt number at the highest Reynolds number studied. It was also pointed out that, the presence of the confinement plate resulted in heat characteristics similar to channel flow at distances farther downstream. Another observation was that the location of the secondary peak in the local Nusselt number occurred at Reynolds numbers much lower than that when the flow transitioned into turbulence, and argued that the reason could be attributed to a strong re-circulation cell in the confined geometry, while it could be attributed to turbulence at larger Reynolds numbers. A maximum Nusselt number value of $Nu/Pr^{0.4}$ 500 was obtained from their study which approximately correspond to heat fluxes of 250 and 40

W/cm^2 for water and FC-72 respectively, at a prescribed surface-to-jet temperature differential of 50°C, indicating the usefulness of single phase impingement cooling for large heat fluxes. Although such large Reynolds numbers (with invariably large velocities) at very small standoff distances may indicate significant cooling potential with single phase jet impingement, it is important to note the associated pressure losses in such systems, which may play a critical aspect for efficient design of cooling systems for miniature electronics.

Several reviews elaborating the state of the knowledge on impingement heat transfer, particularly focussing on liquid jets are available in the literature. Ma et al. [52] presented a detailed summary on the subject including both single phase as well as boiling impinging jets. It was pointed out that the role of turbulence and the geometry of the nozzle on the heat transfer performance was not fully established, and indicated scope for further research in this direction. With reference to engineering applications, Ma et al. [52] mentioned that extrapolation of the vast data on air jets to liquid jets are desirable with appropriate considerations for the effects of fluid Prandtl number, but more studies were suggested for a solid foundation of the fundamental differences. Webb and Ma [54] summarized a large set of analytical and experimental work in the area with the objective of correlating the research findings. Concluding remarks were made on the need and scope for further research in the field of liquid jet array applications, both in submerged and free-surface jet configurations. It was also critically pointed out that cross-flow effects in impingement cooling systems are quite well characterized for submerged jets, but have received only superficial treatment for free-surface jets. It was also suggested that phase change cooling would be essential for large heat flux and large temperature applications, for efficient cooling.

2.2.2 Two-Phase Jet Impingement Cooling: Boiling Heat Transfer

As mentioned in the preface to this section, heterogeneous nucleate boiling of an impinging liquid jet on a heated surface generally result in orders of magnitude larger heat transfer coefficients as compared to single phase impinging jets. In addition, the significantly larger heat fluxes that can be removed for a small rise in the surface temperature (see Fig. 1.4 in Section-1.2.2) make it an attractive option for cooling in

high heat flux applications. Besides the intentional employment of phase change impingement cooling techniques to exploit the large heat transfer coefficients during nucleate boiling (such as in cooling of high power electronic components) several industrial applications like metal processing that involve cooling of sheet metals result in boiling of the coolant on the surface due to the high operating (surface) temperatures. Over the last few decades there has been a multitude of studies on jet impingement boiling in several different configurations and operating conditions.

Wolf et al. [56] has presented, the thus far, most comprehensive review of the literature on experimental studies on jet impingement boiling, comprising of results on free-surface, plunging and submerged (confined and unconfined) jet impingement boiling for both subcooled and saturated conditions. The trends for the boiling curves, conditions controlling the onset of nucleate boiling (ONB), temperature overshoot, critical heat flux (CHF), and the effects of various controlling parameters including jet velocity, nozzle configuration, standoff distance, heater geometry/ size, degree of subcooling, working fluid, operating pressure, etc. were rigorously characterised for each type of jet impingement boiling configuration. In addition, Wolf et al. [56] also pointed out that the heat transfer associated with each mode of boiling is sensitive, in varying degrees, to the experimental conditions of the measurement, such as surface finish [63], surface contamination [64], dissolved gas content [65], heater thickness [66], heater material [67], method of heating (ac or dc powered) [68], and the type of experiment conducted (steady state or transient) [69]. Besides the elaborate comparison of the published data on impingement boiling, several anomalies in the literature with respect to the parametric trends in the controlling variables were also outlined suggesting a need for further investigation in that direction.

While a good deal of literature is available on impingement boiling focussing on free surface jet impingement, and to a certain extent on submerged impingement, the majority of the studies have dealt with round nozzle configurations. Despite that confined planar (slot) jet impingement provides a larger impingement zone than a circular jet while ensuring uniform coolant rejection following impingement [70,71], which is highly beneficial for design of compact electronic cooling systems, the literature on the subject are rather limited.

Mudawar and Wadsworth [71] carried out elaborate experiments to study the heat transfer characteristics of confined and submerged orthogonal jet impingement boiling on a smooth surface using dielectric fluid FC-72 issuing a slot nozzle. The study was performed over a wide range of controlling parameters: velocity $1 \leq u_N \leq 13$ m/s, nozzle width $0.127 \leq w_N \leq 0.508$ mm, standoff distance $0.508 \leq h \leq 5.08$ mm and degree of subcooling $0 \leq \Delta T_{sub} \leq 40$ ^{o}C. General observations in the trends of the effects of controlling parameters included the upward shift of the boiling curve with an increase in jet velocity in the single phase regime and a collapse of the boiling data in the nucleate boiling regime for given subcooling. The critical heat flux was found to higher for relatively larger jet velocities and jet subcoolings. Two regimes for the dependence of CHF on the standoff distance was identified based on the jet velocity, and were classified as the medium velocity regime and high velocity regime. The distinction in the regimes was made based on the observation that the critical heat flux was strongly dependant on the channel height (or the confinement height) for high velocities while the effect of confinement was rather weak for the low velocity regime. It is found that operating in the high velocity regime, especially for the smallest channel height in their experiments, an anomalous reduction in the CHF was obtained with an increase in jet velocity beyond a threshold velocity, and this was attributed to the stream-wise reduction of liquid subcooling within the channel. It was shown that decreasing the nozzle standoff distance promoted the transition into the high velocity regime at lower jet velocities. With a maximum heat flux of about 250 W/cm^2 and the spatial uniformity obtained from their study, it was argued that confined jet geometries were well suited for cooling large arrays of high-power-density heat sources in electronic chips dissipating heat fluxes. It was also suggested that for a given CHF, the cooling requirements of the confined .jet can be reduced by reducing the jet width.

In a subsequent study, Wadsworth and Mudawar [72] investigated the effects fluid subcooling and jet velocity in the range $15 \leq \Delta T_{sub} \leq 40$ ^{o}C and $2 \leq u_N \leq 13$ m/s, respectively on the boiling characteristics of submerged and confined slot jet impingement heat transfer, using dielectric fluid FC-72 on textured impingement surfaces. Two different types of impingement heat transfer surfaces were used for the study, *viz.* smooth and structurally enhanced micro-textured (microgroove and micro-

stud) keeping the plan-form area the same for the different types of heaters. It was pointed out that, the use of a jet-impingement cooling scheme and structurally enhanced surfaces coupled with phase change are capable of removing very high heat fluxes such as those anticipated with microelectronic devices. It was shown that the micro-grooved surfaces outperformed the smooth surface during boiling heat transfer. Critical heat fluxes upto 250 W/cm^2 and over 410 W/cm^2 were achieved with smooth and micro-structured surfaces, respectively in their study. It was also reported that the micro-structured surface provided a virtually isothermal heat source surface under single-phase as well as boiling conditions. While the critical heat flux due to smooth surfaces resulted in a monotonous increase with degree of subcooling, that due to micro-structured surfaces resulted in a non-monotonous relationship; the CHF decreased upto a degree of subcooling of 22 ^{o}C and subsequently increased with increase in subcooling for the micro-grooved surface.

Chang et al. [73] studied the effects of geometric and flow control parameters on the boiling heat transfer characteristics under single and multiple confined jet impingement, using Freon R-113. The effects of jet Reynolds number, standoff distance and inlet fluid quality (in terms of dissolved gas) were studied on the heat transfer characteristics of single jet impingement, while the effects of jet-pitch were included for the study of the multiple jet impingement configuration. They pointed out that while the heat transfer rates obtained during impingement boiling were substantially larger than that obtained using single phase cooling in the same configuration reported in an earlier study [74], the associated pressure drops in the system under boiling conditions were substantially larger for certain geometric conditions. Empirical correlations were presented for confined and submerged two-phase turbulent single and multiple-jet impingement boiling, for subcooled R-113 for the range of controlling parameters studied.

Nakayama et al. [75] carried out submerged and confined impingement boiling experiments using fluorocarbon fluid FX3250 on a simulated electronic chip. The configuration involved a 1 mm wide slot jet issuing into a confined space such that the standoff distance from the heat transfer surface (4 mm long heated chips-array) was 2 mm. The effect of controlling parameters were studied in the range $2 \leq \Delta T_{sub} \leq 21$ ^{o}C and $0.53 \leq u_N \leq 5$ m/s. Experiments were aimed at measuring both, the

average as well as discretized chip by chip heat transfer characteristics to evaluate the local chip-averaged boiling characteristics in the system. It was pointed out that the thermal mass of the heaters could be an important influential factor for determining the critical heat flux of the heater array module. It was also observed that for the geometry considered, the heat transfer behaviour of the central chip under the stagnation point was strongly controlled by impinging flow, while the other chips placed farther downstream exhibited both channel flow or jet impingement modes depending on location or the chip jet Reynolds number. This brings out the significance of the heater size as an important design parameter for two-phase impingement cooling systems. Like most other fluorocarbons, FX3250 was also found to exhibit temperature overshoot prior to boiling incipience due to its large surface wetting characteristics. It was noted that while the general trends in the critical heat flux relationships with the controlling parameters agreed with the literature, the existing correlations consistently overpredicted the magnitudes of CHF. Suggestions for the configurational arrangement of differentially powered chips were also made for cooling under two-phase impingement jets, to exploit the special non-uniformity that may occur under certain flow conditions such as very large jet velocities.

Shin et al. [76] studied the effects of Reynolds number and standoff distance on the nucleate boiling characteristics and CHF of submerged and confined jet impingement boiling of dielectric fluid PF-5060 (which is very similar to FC-72 in thermophysical properties). The controlling parameters were varied in the range $2000 \leq Re \leq 5000$ and $0.5 \leq H \leq 4$. It was shown that the heat flux for boiling incipience was directly proportional to jet Reynolds number and inversely proportional to the nozzle-to-surface spacing. A non-monotonous behaviour was observed for the relationship between the critical heat flux and dimensionless standoff distance, with a local minimum for CHF for each Reynolds number. From the local thermal measurements made using fine thermocouples (spot welded to the underside of the 468 μm thin heated surface), it was shown that during fully developed nucleate boiling, the wall temperature increased with distance from the stagnation point. It was also observed that the variation in the wall temperature with a change in the standoff distance was distinct, particularly in the fully developed boiling regime. It was argued that for smaller standoff distances, nucleating bubbles near the stagnation

point are flushed downstream by the strong momentum of impinging jet, and that the effect of the jet on the fully developed boiling regime was more pronounced with increasing jet velocity and decreasing standoff distance.

Several reports on the state of the art on the employment of two phase impingement cooling systems particular to specific applications are also available in the literature. Ebadin and Lin [55] reviewed the vast literature on high heat flux removal technologies including micro-channels, jet impingements, sprays, surface modification schemes and piezo-electrically driven droplets. They pointed out that although impingement boiling offers very large heat removal capabilities, the associated pressure drops could pose concern particularly for micro-scaled modules. Mudawar [77] discussed the recent research developments in high-heat-flux thermal management schemes such as pool boiling, detachable heat sinks, channel flow boiling, microchannel and mini-channel heat sinks, jet-impingement, and sprays, and compared their corresponding cooling potentials. It was suggested that more research should be directed towards new hardware innovation rather than modification of existing technology through perturbations for enhanced capability. Nakayama [78] pointed out that the heat fluxes on the microprocessor chip are rising only modestly owing to the industry-wide effort to decrease the power bus voltages, although the demands for ever more compact systems will reduce the physical space available for the coolant. It was suggested that more research must be directed towards improving the efficiency of highly compact liquid cooled systems.

2.2.2.1   Computational Approach to Jet Impingement Boiling

Due to the extreme complexity involved in modeling the complete boiling process, most studies on jet impingement boiling (or flow boiling) have been predominantly experimental so far, with very limited but fairly successful attempts at theoretical and computational simulations of specific cases. As outlined in the Chapter-1, jet impingement boiling, which is specific case of flow boiling heat transfer, is characterised by the complex interactions between the ebullition from numerous sites on the heated surface (with a temperature greater than saturation temperature of the fluid), and the thermal hydraulics in the bulk flow. The interactions typically involve the heat and mass transfer between the phases, lift/ drag and buoyancy forces on the

bubbles, bubble coalescence/ collapse, and the associated turbulence contribution to bulk flow particularly near the heated wall. Computational modeling of the phenomenon would require accurate prediction of the interfacial transfer process, along with the estimation of the ebullition process involving the bubble diameters during growth and departure, bubble growth time and dwelling time (interval between bubble departure and the occurrence of a subsequent bubble in the void), active nucleation site density on the superheated surface, to mention a few.

Bubble dynamics in pool boiling have been studied since the 1950s. Several experimental and mechanistic models are available in the literature for estimating the maximum bubble diameter at departure (BDD), bubble departure frequency (BDF) for single bubbles as well as a swarm of bubbles generated on a superheated surface. Jensen and Memmel [79] compared a list of twelve different models for bubble departure diameter against experimental data obtained for a wide range of experimental conditions (for pool boiling) for fifteen different fluids and operating pressures ranging from 4.7 to 13500 kPa. They pointed out that no single model was able to accurately predict the departure diameter for the complete range of conditions investigated, and that a large scatter in results was observed. In addition, Jensen and Memmel [79] proposed two separate correlations where one was dependent and the other independent on the surface superheat, and commented that these two new models had a better agreement with the experimental data.

Tolubinsky and Kostanchuk [80] carried out experiments on subcooled pool boiling of water on a direct-current controlled stainless steel surface to investigate the relationship between the maximum bubble departure diameter, bubble departure frequency and cycle averaged bubble growth time for operating conditions: degree of subcoolings ΔT_{sub} upto 60 ^{o}C and operating pressures upto 1 MPa. In addition the heat transfer coefficients were related to the ebullition parameters in the form of an empirical correlation for the range of operating conditions considered. It was elaborated that the bubble growth rate consistently increased with an increase in degree of subcooling, and decreased with an increase in operating pressure at given values of other controlling parameters. Kocamustafaogullari and Ishii [81] carried out similar experiments on pool boiling, and indicated a possible extension of their predictions from pool boiling to flow boiling problems, particularly with reference to

the estimation of active nucleation site density on the surface. They formulated a differential transport equation for the interfacial area concentration in terms of the active nucleation site density on the heated surface. A constitutive relation for the nucleation site density was developed for pool boiling and extended to nucleate flow boiling.

Unal [82] carried out experiments on flow boiling with water for a wide range of controlling parameters in the range $0.1 \leq p \leq 17.7$ M Pa, $0.47 \leq q_T \leq 10.64$ M W/m^2, $0.08 \leq u_N \leq 9.15$ m/s and $3 \leq \Delta T_{sub} \leq 86$ ^{o}C. Correlations for departure diameter (0.08-1.24 mm) and the maximum bubble growth time (0.175 to 5 ms) were provided. A need for theoretical modeling of the boiling process was pointed out as all the predictive tools that existed then were mostly experimentally developed, which are highly constrained to the operating conditions. Unal [82] developed a heat transfer controlled bubble model to derive a correlation for bubble-growth rate, maximum bubble diameter and maximum bubble-growth time based on the assumption that a spherical or an ellipsoidal bubble grows on a very thin, partially dried liquid film, which forms between the nucleating bubble and the heated surface. It was assumed that during bubble growth, the bubble takes up heat by the evaporation of the very thin liquid film while it dissipates heat by condensation to the surrounding liquid at its upper half, which is true for subcooled boiling. More information on this model, along with the expression for the model itself is presented under Section-4.1.2.

Ivey [83] and Malenkov [84] compiled a detailed list of bubble departure frequency models (in terms of bubble rise velocity) that were developed predominantly from pool boiling data. Ivey [83] indicated that a single relation relationship alone between the frequency and diameter of bubble at departure cannot be correlated for the complete range of fluids and operating conditions, and hence postulated three distinct regimes (hydrodynamic, transition and thermodynamic) based on the magnitude of dominant forces acting on the bubbles. The most popular and widely used model for prediction of bubble departure frequency was deduced by Cole [85] in 1960. The bubble departure frequency was evaluated from a photographic study during saturated pool boiling of water on an electrically heated zirconium ribbon, and measurements of bubble diameters, bubble positions relative

to the heater surface, local bubble departure frequencies and contact angles were obtained at specified time intervals. Cole [85] postulated that the primary forces acting on the bubble during departure under such operating conditions were the drag and buoyancy forces (hydrodynamic regime according to Ivey[83]). It was also shown that for short distances over the heater surface, the surface drag coefficients for the rising bubble were predicted well by the drag coefficient Reynolds number relationship for solid bodies, and for conditions where the bubbles were not spherical, a drag coefficient of unity was reasonable.

Realising that the bubble dynamics is largely influenced by the mean flow field particularly relevant to subcooled flow boiling, in recent years, models for the prediction of bubble departure frequency during flow boiling [86-88] have also been proposed. From experiments on flow boiling of water on a rectangular heater in a vertical channel, Basu et al. [86] experimentally determined the bubble growth and waiting times and correlated the bubble departure frequency on the corresponding Jacob numbers based on the local degree of superheat and subcooling. Podowski et al. [87] carried out an elaborate theoretical analysis and proposed mechanistic models for the prediction of the bubble growth time and waiting times during flow boiling. In contrast to the other BDF models available in the literature (see [88] for details), Podowski et al.'s model includes the effects of surface characteristics (surface finish) on ebullition. Situ et al. [88] carried out experiments for vertical tube boiling of water at atmospheric pressure and correlated a dimensionless bubble departure frequency with heat flux for the partial nucleate boiling regime. They commented that none of the pool boiling correlations or the then existing flow boiling correlations (including Basu et al. [86] and Podowski et al. [87]) correlated with their experimental data well. However, in an earlier investigation, Situ et al. [89] had reported that among the other models that they considered for a computational study of flow boiling in a tube, Podowski et al.'s model resulted in comparatively more realistic prediction of the boiling data.

From the aforementioned discussion, it is seen that there are a diverse range of models available for the prediction of departure frequency, departure diameters, nucleation site density, etc. during pool boiling and subcooled flow boiling, which have each been validated for a rather limited range of fluids, operating conditions

and applications. Realising the essentiality in validating the choice of any such model before performing a computational analysis of the application of interest, one of the aims of the present research presented in this thesis was to carry out a detailed study to ascertain the suitability of different ebullition models for the simulation of submerged and subcooled jet impingement boiling. As will be detailed below, the predictions were compared against both, published experimental data as well as boiling data obtained from the present study.

Although, no such sensitivity analysis validation has been presented in the literature thus far for submerged jet impingement boiling problems, computational studies with rather limited validations of computational approaches for such problems are starting to appear in the recent literature. It could be reasonable to state that computational analysis of jet impingement boiling, or in general flow boiling, commenced started with the development of the Rensselaer-Polytechnic Institute (RPI) wall-boiling model and its variants [90]. In brief, the model partitions the wall heat flux into liquid phase convective, quenching (transient conduction) and evaporative heat fluxes for nucleate boiling, while including an additional partition to accommodate vapor phase convection for problems involving departure-from-nucleate-boiling. RPI wall-partitioning model treats the evaporative heat flux on a macroscopic scale of the entire bubble, instead of considering the evaporation of the liquid-microlayer as suggested by [91]. This partition based wall-function approach is integrated along with other closures for the inter-phase transfer coefficients and solved along with the governing conservation equations. The model is limited to its application in terms of the operating conditions (especially large operating pressures and gravity conditions) and working fluid, especially due to the limited applicability of the included sub-models for bubble diameter, departure frequency and departure diameter; however, a few numerical results have been reported in the literature in recent years [11,92, 93].

Wang et al. [92] undertook one of the earliest computational efforts towards simulating jet impingement boiling of a round impinging jet of FC-72 on a heated silicon chip. The flow and heat transfer were modeled using an Eulerian two-fluid model, assuming the liquid and vapor phases to be co-existent in the domain, defined by volume fraction (interpenetrating continua). They noted that although the trends

of the boiling curves from their numerical simulations were in good agreement with the experimental data, the magnitudes of the predicted surface temperatures deviated by about 30%. Narumanchi et al. [11,93] used the RPI wall-boiling model along with the Eulerian two-fluid model to simulate nucleate boiling in an Insulated-Gate Bipolar Transistor (IGBT) package. They compared their simulations for submerged subcooled unconfined round jet impingement boiling heat transfer, for both vertical and horizontal configurations, with experimental data in the literature and found that the surface averaged values of predicted heat fluxes were about 30% in deviance with experiments, while the stagnation values were in reasonable agreement.

Considering that development of a computational framework benefits in enhanced understanding of any physical problem, besides the advantages over experimental studies in terms of the time and cost involved, it is clear that the complexity involved in a reliable modeling the flow boiling process has been a consistent dilatory factor in the progress in this front. One of the objectives of the present work is to develop a comprehensive modeling philosophy for the computational analysis of subcooled jet impingement boiling and to study the effects of the relevant thermal, flow and geometric control parameters to understand their effects on the fundamental mechanisms of heat transfer in such a system.

In the last decade, efforts have also been made to model jet impingement boiling analytically and also using techniques that combine analytical and empirical techniques. Li and Liu [94] proposed a mechanistic model for the determination of critical heat flux in subcooled impingement boiling on the stagnation zone. The model was based on the combination of the Helmholtz instability theory of macro-layer and the model of bubble induced turbulent heat transfer in subcooled impingement boiling. A semi-theoretical and semi-empirical correlation and its nondimensional form of the CHF for subcooled jet impingement boiling on the stagnation zone were also presented. It was pointed out that under the circumstances of CHF the bubble induced turbulent heat transfer coefficient gets doubled (universally) as compared to the single-phase laminar heat transfer coefficient. Subsequent to successful validation against experimental data, it was reported that the ratio of CHF between the subcooled and saturated jet impingement boiling was dependant on the surface condition of the heater besides the jet velocity.

A few other recent studies have focussed on the theoretical as well as computational analysis of film boiling under an impinging jet, where the flow and thermal characteristics are significantly different from that during nucleate boiling. It is also seen that most of the studies have been based on free surface impinging jets. For further details on these studies, the reader is suggested to refer [95-99]; the related discussion is omitted in this document due to its lesser relevance to the research presented herein.

2.3   PULSATING LIQUID JET IMPINGEMENT HEAT TRANSFER

Since jet impingement boiling or generally turbulent impinging jets readily offer large heat transfer coefficients, the motivation towards of pulsations for enhancement is perhaps diminished. However, such active control of jet characteristics could be of practical interest in single phase cooling systems where the advantages of turbulence cannot be exploited, such as in micro-electronics which primarily operate at low Reynolds numbers [21]. Besides, the characteristics of any simple steady single-phase impingement cooling mechanism is controlled predominantly by the fluid used, the jet Reynolds number, nozzle-standoff distance, operating temperatures and in some instances, the geometry of the nozzle and texture of the heat transfer surface. Hence, the scope for any optimization or enhancement is limited to these few controlling parameters. The demand for enhanced cooling performances in applications outlined earlier have attracted extensive research leading to development of novel actively controlled jet impingement cooling techniques such as synthetic jets [100], self-oscillating jets [101] and pulsating jets [19,21,102- 109].

Extensive literature is available on the fluid dynamics of jet pulsations for non-impingement cases [110- 112]. In brief, the introduction of forced pulsations in a submerged turbulent slot jet results in a cyclic generation of a vortex pairs (or a ring vortex in the case of round jets) on either sides of the jet at the nozzle outlet, which may grow in size due to interaction with other vortices in the domain. As a result of such mean flow pulsations when employed for impingement cooling applications, large enhancements to traditional steady jets are possible due to larger entrainment of the surrounding fluid, which occur more rapidly with large amplitudes [113].

However, flow pulsations have also shown to deteriorate the time averaged heat transfer for certain combination of pulse amplitudes and frequencies [21], which indicate that a detailed understanding of the influence of jet pulsations is required.

Several computational and experimental studies on the influence of jet pulsations on impingement heat transfer have been carried out over the last few decades, mostly focusing on air jets [19,103,104,106-108]. Although liquid impinging jets would invariably have larger heat transfer coefficients as compared to traditional air jets, the literature on pulsating liquid impingement cooling is rather limited [21,102,105,109]. Zumbrunnen and Aziz [105] experimentally investigated the effect of flow intermittency on planar free surface water jet impingement on the associated heat transfer in the range $3300 \leq Re \leq 19600$ and $30 \leq f \leq 130$ Hz. It was reported that enhancements in convective heat transfer coefficients of a factor of two could be achieved with large frequencies due to a sustained reduction in the time averaged thermal boundary layer thickness. Sheriff and Zumbrunnen [21] also studied the effects of flow pulsations on free surface water jets for both square as well as sinusoidal wave forms with jet velocity amplitudes between 0-100% of mean flow, frequencies between 5-280 Hz and Reynolds numbers between 3150 and 15800. They found that for a sinusoidal pulse profile, the time-averaged stagnation region Nusselt numbers were reduced by as much as 17 % when the pulse magnitude was large. Reductions decreased markedly away from the stagnation region and were attributed chiefly to the nonlinear dynamic responses of the hydrodynamic and thermal boundary layers and to a lesser degree to bulges in the jet free surface. For interrupted pulsed jets Nusselt numbers at the stagnation region were enhanced by as much as 33% for Strouhal numbers > 0.26 due to periodic boundary layer renewal. It was also reported that enhancements eventually decreased with increasing frequency beyond a threshold. It is likely that the first study on pulsed submerged liquid jet impingement was carried out by Narumanchi et al. [102]. They computationally investigated the effect of jet pulsations with square and sinusoidal waveforms using a dielectric liquid HFE-8401HT impinging on a heated silicon chip for frequencies in the range $0.3 \leq f \leq 4.0$ Hz and Reynolds numbers up to 100. Their simulations indicated significant oscillations in chip temperatures when the time period of the pulse was larger than the thermal response time of the chip indicating the presence of thermal cycling with unsteady jets. However, no significant difference was observed

between the steady state and pulsed jet impingement Nusselt numbers over the range of parameters investigated. They also pointed out that considering the insignificant enhancement in such a pulsed liquid system, the technique could be undesirable for chip cooling applications as the performance would be significantly deteriorated due to the transient thermal stresses developed as a consequence of the temperature oscillations.

While the focus of the development of enhancement techniques to boiling heat transfer under jet impingement has been predominantly on the modification of surface textures using nanostructed surfaces [114,115] which however result significantly advantageous in considerably reducing the surface superheat (for a given heat flux) as well as significantly increasing critical heat flux (CHF), no investigation has been reported on the effect of forced jet pulsations on boiling heat transfer characteristics. The closest study to such a pulsatile fluid impingement system under boiling conditions was carried out by Tillery et al. [22]. In their study, a brass diaphragm that was placed at a certain distance from the heated surface (both immersed in a pool of liquid) was forced to vibrate at a prescribed amplitude and frequency using a piezoceramic wafer. Tillery et al. [22] showed that the vibration of the spindle induced pressure oscillations near the surface of the diaphragm, resulting in periodic cavitation bubbles that generated a strong liquid jet through entrainment of the surrounding fluid. The induced jet of fluid, when targeted at the heated surface was found to enhance boiling heat transfer by effectively flushing the vapor bubbles that formed on the heated surface, in addition to the enhancement through forced convection. Tillery et al. [22] also reported enhancements upto 280 % using the vibration induced jet in the system with cross-flow. Heat fluxes of over 300 W/cm^2 were achieved in their study using the novel vibration induced jet system.

This section of the literature review on pulsating liquid jet impingement cooling suggests that there have been considerable studies on pulsed air jets and a few on pulsed free surface liquid jets and possibly no experimental report on the effect of jet pulsations in submerged liquid jet impingement cooling configurations. Besides, the heat transfer mechanism under pulsating jet impingement boiling remains unexplored thus far. It is quite possible that besides the control of mean flow vortices by the introduction of jet pulsations, interesting features may arise due to its

effect on the bubble ebullition which could lead to consequences on the associated phase change rate and heat transfer. With this motive, one of the objectives of the present research detailed in this thesis was to carry out an exploratory study on the effects of jet pulsations on single phase and boiling heat transfer under a pulsating liquid slot jet in a confined geometry.

CHAPTER 3

MOTIVATION, OBJECTIVES AND SCOPE OF WORK

In the earlier chapter, a detailed overview of the literature on both single phase and boiling jet impingement heat transfer in a confined slot jet configuration, with and without jet pulsations, was presented. The progress in the understanding of the subject thus far was delineated and the areas where more investigation may be required to gain a deeper insight into the field was outlined. Three different types of jet impingement heat transfer: (i) single phase air jet impingement, accounting for effects of buoyancy and surface radiation, (ii) jet impingement boiling, and (iii) pulsating single phase (liquid) and boiling jet impingement are identified for the present investigation, and the overall objectives for the present research derived from the detailed literature review, along with the motivation and scope, are summarized below:

3.1 CONFINED SINGLE PHASE LAMINAR AIR JET IMPINGEMENT ACCOUNTING FOR BUOYANCY AND SURFACE RADIATION

It is identified that for low Reynolds number air jet impingement cooling applications where the flow field is predominantly laminar, surface radiation could largely influence the overall heat transfer characteristics in the system. The literature review suggests that the previous studies on the subject have focussed mainly on forced convective heat transfer in such configurations, and the effects of buoyancy on the (possibly mixed convective) flow and heat transfer characteristics have been explored only for very low Reynolds numbers (≤ 100). While surface radiation could largely influence the heat transfer, particularly during large surface temperatures or surfaces with high emissivity, the influence on confined jet impingement heat transfer has not been explored thus far. With this motivation, the objectives of the present research are to:

- develop a mathematical model and computational code for the analysis of confined submerged jet impingement flow and heat transfer of a radiatively non-

participating gas (air), accounting for the effects of surface radiation and buoyancy.

- delineate through a parametric investigation, the effects of the controlling parameters such as jet Reynolds number, dimensionless standoff distance, dimensionless surface temperature, dimensionless radiation-flow interaction parameter and Richardson number, on the flow field and thermal characteristics of the surface radiation-coupled mixed convective impingement cooling configuration, with particular focus on the relative contribution of surface radiation and convection to the overall heat transfer.

The research based on the preceding objectives would identify the role of surface radiation and buoyancy assisted fluid movement on the mixed convective heat transfer characteristics in confined laminar slot jet impingement systems. In air cooled miniature electronic systems operating at low Reynolds numbers where enhancement due to turbulence may not be possible, or metal processing applications where the surface temperatures are inevitably high, the significance of the surface radiation properties, such as surface emissivity, in the enhancement of the overall heat transfer would be established over a comprehensive range of realistic operating conditions.

3.2   CONFINED SUBMERGED AND SUBCOOLED TURBULENT JET IMPINGEMENT BOILING

The complexity involved in the reliable modeling of bubble dynamics in flow boiling phenomena has been a consistent dilatory factor for the progress in fully reliable computational analysis of flow boiling problems, particularly turbulent jet impingement boiling. While there are a diverse range of experimental and mechanistic models available for the estimation of the several boiling parameters such as departure diameter, frequency and nucleation site density, for rather specific configurations (such as flow boiling in tubes or over flat plates) and operating parameters (such as fluid/ surfaces used or fluid velocity/ pool boiling), there is no specific comprehensive model for jet impingement boiling. Nor there is a consensus on a generalized model for the ebullition parameters that could be extended to jet

impingement boiling over all fluids. With a motivation to carry out a detailed computational study on the underlying mechanism of heat transfer under confined and subcooled jet impingement boiling, the objectives for the present research are to:

- develop a comprehensive computational framework for the simulation of turbulent jet impingement boiling, and a computer code for the integration of the various recent models for the prediction of ebullition parameters into the finite volume computational solver ANSYS FLUENT 14.0/14.5.

- carry out a rigorous study to ascertain and establish the suitability of different ebullition models, as well as multiphase turbulence models for the simulation of confined and submerged, subcooled jet impingement boiling process by comparison against available experimental data; hence, develop a modeling philosophy for jet impingement boiling problems of the type considered.

- use the comprehensive model to carry out elaborate set of computational simulations and study the effects of the relevant geometric, flow and thermal parameters on the fundamental mechanism of heat transfer, from the perspective of the partitioning of the total surface heat flux into convection, quenching and evaporation during different regimes of the boiling curve. The controlling geometric, flow and thermal parameters are heater and nozzle sizes, nozzle standoff distance, jet Reynolds number and degree of inlet subcooling, working fluids, type of heating (isothermal, isoflux and volumetric heating) and applied heat transfer rate.

The research based on the aforementioned objectives would establish the prediction capability and accuracy of the state-of-the-art comprehensive Eulerian-multiphase computational model for the analysis of confined and submerged subcooled turbulent jet impingement boiling. Spatially averaged as well as local description of the thermo-fluidics of steady state confined and subcooled turbulent jet impingement boiling would be understood for a range of practical operating conditions using different fluids. The relative importance and significance of the various fundamental mechanisms of heat transfer *viz.* liquid phase convection, quenching and evaporation, on the different regimes of the boiling curve would be characterized and their

contribution to the overall heat transfer would be understood under different parametric conditions.

3.3   CONFINED AND SUBMERGED PULSATING SINGLE PHASE AND BOILING JET IMPINGEMENT

The detailed literature review suggests that most of the research on pulsating jet impingement heat transfer is limited to air/ gas jets, while submerged liquid impingement is a preferred choice for several industrial applications requiring high heat flux removal. Besides, it is also identified that no prior research on the heat transfer characteristics of pulsating boiling impingement is available thus far. It is hypothesized that the introduction of jet pulsations could influence the ebullition characteristics during boiling conditions that in turn affect the phase change rate and heat transfer rate on the impingement surface, in addition to the influence on the mean flow vortices that affect single phase heat transfer characteristics. The importance of benchmark experimental results are realized to understand the effects of jet pulsation on the heat transfer characteristics of boiling and single phase liquid jet impingement heat transfer, and hence, the objectives of the present research are to:

- design and fabricate an experimental facility for the study of confined submerged liquid jet impingement heat transfer under both boiling and non-boiling conditions, with and without jet pulsations.

- carry out detailed set of experiments on single phase jet liquid impingement heat transfer with and without jet pulsations, and evaluate the effectiveness of pulsating jets on impingement heat transfer. Identify the isolated effects of pulsation amplitude and frequency on the thermal characteristics of the system at different operating conditions, such as jet velocity and operating temperature.

- carry out a detailed set of experiments on boiling jet impingement heat transfer with and without jet pulsations. Evaluate the effect of jet pulsations on the associated heat transfer characteristics by comparison of the temperatures, heat fluxes and heat transfer coefficients obtained during different regimes of the

boiling curves under pulsating jet impingement against steady state jet impingement boiling.

The research based on the preceding objectives would highlight the usefulness of jet pulsations in liquid (single and multiphase) jet impingement cooling systems from the perspective of heat transfer augmentation. Considering that pulsating jet impingement boiling has not been investigated before, the present research would provide benchmark heat transfer data for further research in the field.

CHAPTER 4

METHODOLOGY

This chapter discusses the methodology adopted for the study of steady state and pulsating, single phase and boiling slot jet impingement heat transfer in a submerged and confined configuration. As will be detailed below, two different approaches *viz.* computational and experimental were employed for the present study. The computational approach was used for the study of both laminar as well as turbulent steady state jet impingement heat transfer with or without boiling, and the experimental approach was used for the study of steady state and pulsating liquid jet impingement with and without boiling. A schematic of the techniques employed for the present investigation is illustrated in Fig. 4.1. As the present study was not limited to just one type of fluid or heater material, a general framework of the computational and experimental technique employed for the study is presented, while the more specific details of materials and their associated thermophysical properties are included where appropriate in the section on results and discussion.
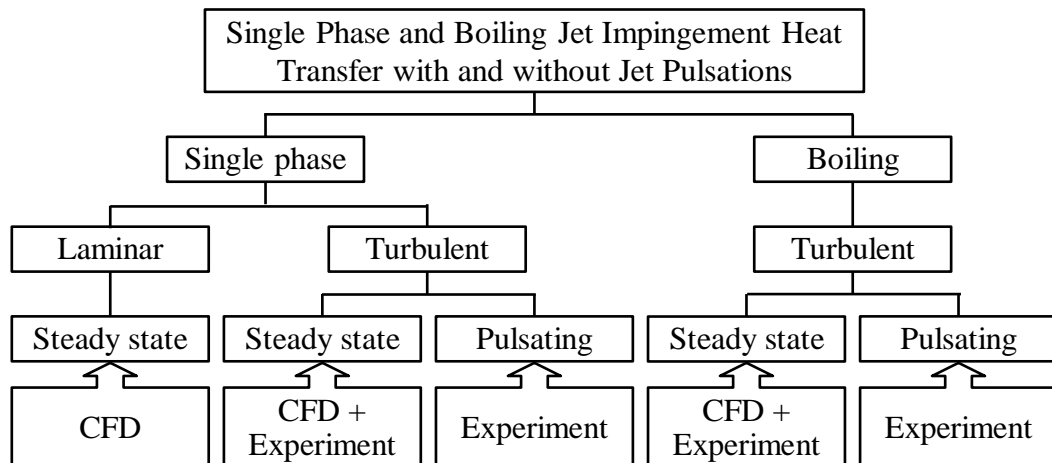
Figure 4.1: Techniques employed for the present research

4.1   COMPUTATIONAL METHODOLOGY

The first computational approach pertains to the study of laminar air jet impingement heat transfer under conditions of high surface temperatures and high surface emissivity where the effects of both buoyancy assisted convection as well as surface

radiation are important. Under such conditions, the attribution of the overall heat transfer due to forced convection alone, as considered in most published literature on the subject, becomes inadequate. With a view to investigate the relative contribution of surface radiation and convection on coupled mixed convective impingement heat transfer, a mathematical model is developed and the governing equations are solved computationally over a substantial practical range of the relevant controlling parameters. The focus of this study is limited to jet impingement heat transfer with air as the working fluid which is a radiatively non-participating media over the range of operating conditions considered.

The second computational approach discussed herein pertains to the study of liquid jet impingement heat transfer at higher Reynolds number (typically larger than 1500) where the flow is predominantly turbulent. The mathematical model and computational approach for both single phase as well as boiling heat transfer heat transfer is discussed along with the detailed set of model closures for turbulence, and inter-phase interactions during boiling heat transfer. Besides, the details of the wall function approach employed for the partition of surface heat flux during boiling jet impingement heat transfer is also delineated in the following sections.
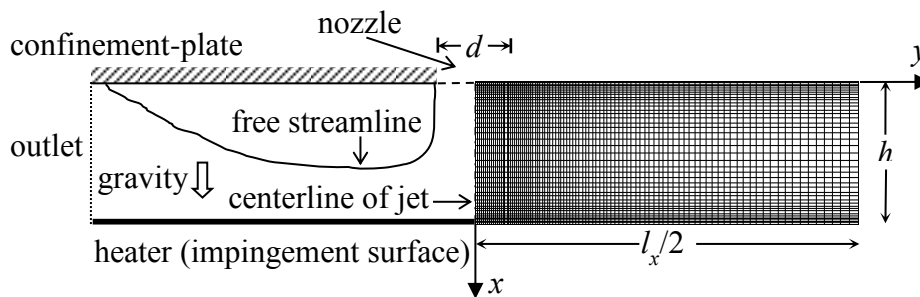
Figure 4.2: Physical geometry and computational domain for convection calculations

4.1.1 Mathematical Model for Steady Laminar Air Jet Impingement Heat Transfer Accounting Surface Radiation and Buoyancy

4.1.1.1 Geometry, Computational Domain and Model Assumptions

A schematic of the confined and submerged slot jet impingement geometry used for the study of low to moderate Reynolds numbers pertaining to the laminar regime is illustrated in Fig. 4.2. The computational domain with the description of the

boundaries are indicated on the left hand side of the centerline of jet, and a typical computational mesh (for convection calculations) is indicated on the right side of the centerline of jet, in the figure. A laminar air-jet issues from a slot nozzle of width d, through a quiescent medium of air at the same temperature, resulting in submerged jet impingement, on an isothermal heater. The confinement-plate is insulated from the outside, making it an adiabatic surface. Both, the impingement surface as well as the confinement plate are assumed to be radiatively opaque and diffuse grey surfaces with emissivity ε. Symmetry about the centerline of the jet is exploited to carryout numerical simulations on one half of the domain alone for the flow field.
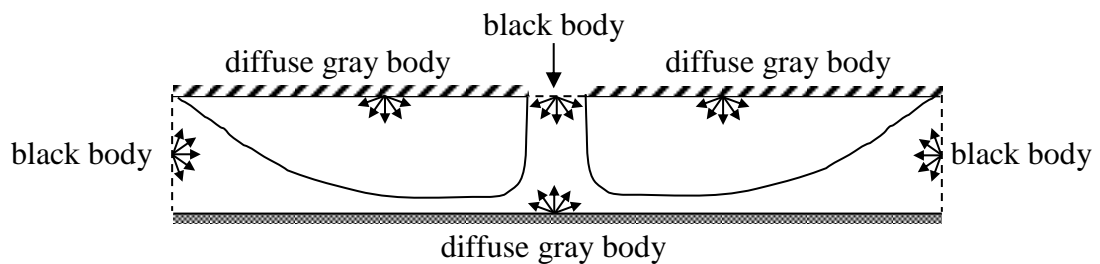
Figure 4.3: Domain for surface-radiation calculations (radiation-domain)

While symmetry about the centerline of jet is exploited for the prediction of the flow field, it is impossible to evaluate temperatures by considering just one half of the domain, as surface radiation has to be modeled for all surface elements in the complete physical domain to obtain radiosities. For this reason, the full domain extending to both sides of the symmetry (centerline of jet) as illustrated in Fig. 4.3 is considered for the evaluation of view factors and radiosities. The nozzle-outlet and the two outlets at the sides of the domain are assumed to be radiatively black surfaces at ambient temperature. The general assumptions for the mathematical model developed are as follows:

(i)   The length scale of the geometry in the direction perpendicular to the plane of the paper in Fig. 4.2 and Fig. 4.3 is much larger than the other length scales in the domain, and hence the flow and heat transfer are two-dimensional in the plane of the paper.

(ii)   For the same reason, the radiative heat losses to the ends of the geometry in the directions perpendicular to the plane of the paper are negligible.

(iii) The fluid properties are invariant with changes in temperature, and density

variations in the domain due to buoyancy are modeled with the validity of Boussinesq-approximation.

(iv) The Prandtl number of air is assumed to be constant = 0.71, which is valid [116] for operating temperatures between 220 and 450 K, with a maximum error of about 3 % for the assumed temperature independence of Prandtl number. This also limits the range of operating temperatures T_{w} and T_{N} for the present dimensionless study.

(v) The working fluid, air, is assumed to be radiatively non-participating, which is reasonable in the aforementioned range of operating temperatures [41].

(vi) No-slip boundary conditions are valid on all the wall/ surfaces.

4.1.1.2 Mathematical Formulation

The non-dimensionalized governing partial differential equations for incompressible laminar flow for a radiatively non-participating fluid with constant thermo-physical properties are reduced to the stream function-vorticity form, and solved simultaneously with the energy equation. Following Heiningen et al. [30] and Gosman et al. [32], the non-dimensionalized general partial differential equations for vorticity transport, stream function and temperature, in two-dimensional Cartesian coordinates is written for the fluid domain as:

$$a_\phi \left\{ \frac{\partial}{\partial X}\left(\phi \frac{\partial \psi}{\partial Y} \right) - \frac{\partial}{\partial Y}\left(\phi \frac{\partial \psi}{\partial X} \right) \right\} - \frac{\partial}{\partial X}\left(b_\phi \frac{\partial \phi}{\partial X} \right) - \frac{\partial}{\partial Y}\left(b_\phi \frac{\partial \phi}{\partial Y} \right) + c_\phi = 0 \qquad (4.1)$$

The coefficients a_Φ, b_Φ and c_Φ that correspond to $\phi = \Psi$, Ω and λ are listed in Table 4.1.

Table 4.1: Coefficients appearing in the general governing equation

ϕ	a_ϕ	b_ϕ	c_ϕ
Ψ	1	$1/Re_{\mathrm{h}}$	$-\Omega$
Ω	0	1	$-Ri_{\mathrm{h}} \times \partial\lambda/\partial Y$
λ	1	$1/(Re_{\mathrm{h}}\,Pr)$	0

For the evaluation of surface radiation interaction in the radiation-domain (Fig. 4.3), all the boundary surfaces are spatially discretized into finite elements and the radiosity-irradiation formulation is employed for the calculation of local

radiosities. The general radiosity equation for the jth element of an enclosure is:

$$J_j = \varepsilon_j \sigma T_j^4 + \left(1 - \varepsilon_j\right) \sum_{k=1}^{N_{SE}} F_{j \to k} J_k \tag{4.2}$$

where $F_{j \to k}$ is the view factor from the jth element to the kth element in the radiation-domain and N_{SE} is the total number of discretized surface-elements in the radiation-domain. View factors between elements on parallel planes are evaluated using Hottel's crossed-string method [117], while those on perpendicular planes are evaluated using formulations of Siegel and Howell [117], in conjunction with view factor algebra.

As the confinement plate is adiabatic, from conservation of energy, the net internal radiation heat transfer to the confinement plate is balanced by the heat convection to the fluid. With the assumption that the confinement plate (as is the impingement plate) is thin, and thus neglecting conduction through the plate, the thermal energy balance of the confinement plate is evaluated as:

$$\left(\frac{\varepsilon}{1-\varepsilon}\right)\left(\sigma T_j^4 - J_j\right) - k \left.\frac{\partial T}{\partial x}\right|_j = 0 \tag{4.3}$$

where, T_j and J_j are the local temperature and radiosities on the jth element on the confinement plate, respectively. The boundary conditions considered for the simulations are listed in Table 4.2. The dimensionless stream function and vorticity are defined in their usual form, as

$$U = \partial \psi / \partial Y \; ; \; V = -\partial \psi / \partial X \quad \text{and} \quad \Omega = \partial V / \partial X - \partial U / \partial Y \tag{4.4}$$

Table 4.2: Boundary conditions for convection calculations

centerline of jet $0 \le X \le 1$; $Y = 0$	$\Psi = 0$	$\Omega = 0$	$\dfrac{\partial \lambda}{\partial Y} = 0$
outlet $0 \le X \le 1$; $Y = L_x$	$\dfrac{\partial \psi}{\partial Y} = 0$	$\dfrac{\partial \Omega}{\partial Y} = 0$	$\dfrac{\partial \lambda}{\partial Y} = 0$
confinement-plate $X = 0$; $D/2 \le Y \le L_x$	$\Psi = D/2$	$\Omega = -\dfrac{\partial^2 \psi}{\partial X^2}$	$\dfrac{\partial \lambda}{\partial X} = N_{RF,h}\left(\dfrac{\varepsilon}{1-\varepsilon}\right)\left[(\lambda + \lambda_N)^4 - \Lambda\right]$
heater surface $X = 1$; $0 \le Y \le L_x$	$\Psi = 0$	$\Omega = -\dfrac{\partial^2 \psi}{\partial X^2}$	$\lambda = 1$
nozzle-outlet $X = 0$; $0 \le Y \le D/2$	$\Psi = Y$	$\Omega = 0$	$\lambda = 0$

The non-dimensional parameters used in Eq. (4.1) to (4.4) and in Table 4.2 are defined as follows;

$$
\begin{aligned}
X &= x/h & U &= u/u_N & \lambda &= (T-T_N)/(T_w-T_N) \\
Y &= y/h & V &= v/u_N & Ri_h &= g\,\beta\,(T_w-T_N)/(u_N h)^2 \\
D &= d/h & Pr &= \mu/\rho\alpha & N_{RF,h} &= \sigma\,h\,(T_w-T_N)^3/k \\
L_x &= l_x/h & Re_h &= \rho\,u_N h/\mu & \Lambda &= J/\sigma\,(T_w-T_N)^4
\end{aligned}
\tag{4.5}
$$

For the purpose of discussion of results, some of the preceding dimensionless parameters are also represented in terms of the length scale of the slot-width d as:

$$
\begin{aligned}
H &= h/d & Ri_d &= g\,\beta\,(T_w-T_N)/(u_N d)^2 & Re_d &= \rho\,u_N d/\mu \\
\Psi_d &= \Psi H & N_{RF,d} &= \sigma\,(T_w-T_N)^3/k
\end{aligned}
\tag{4.6}
$$

4.1.1.3   Convective and Radiative Nusselt numbers

The heat transfer due to convection from the heater is calculated by the application of Fourier-law on the impingement surface, as the velocities are zero due to the no-slip boundary condition. After appropriate non-dimensionalization of the convective heat flux, the local convective Nusselt number is,

$$
Nu_C = \frac{q_C}{k(T_w-T_N)/d} = \frac{1}{H}\frac{\partial\lambda}{\partial X}\bigg|_{X=1}
\tag{4.7}
$$

The net local radiation per unit area from the heater is expressed as:

$$
q_R = \frac{\varepsilon}{1-\varepsilon}\left(\sigma T_w^4 - J_w\right) \quad ; \quad \text{where } J_w \text{ is the local radiosity on the wall}
\tag{4.8}
$$

After non-dimensionalization of the radiative heat flux, the radiative Nusselt number is expressed as:

$$
Nu_R = \frac{q_R}{k(T_w-T_N)/d} = \frac{N_{RF,d}}{H^2}\left(\frac{\varepsilon}{1-\varepsilon}\right)\left[(\lambda_w+\lambda_N)^4 - \Lambda_w\right]
\tag{4.9}
$$

As the convective and the radiative heat fluxes are both non-dimensionalized with respect to the same reference heat flux scale, the total Nusselt number becomes the arithmetic sum of the convective and radiative Nusselt numbers. Hence,

$$Nu_{\mathrm{T}} = Nu_{\mathrm{C}} + Nu_{\mathrm{R}} \qquad\qquad 4.10)$$

4.1.1.4   Solution Technique

The computational half-domain for convection calculations is discretized with a set of structured rectangular non-uniform mesh with $N_{\mathrm{X}} \times N_{\mathrm{Y}}$ divisions along x and y axes respectively with a denser mesh in the regions near the centerline of jet and the walls, where N_{Y} includes N_{N} divisions along the nozzle-outlet (in the half-domain). The divisions on the nozzle-outlet, confinement-plate and the isothermal impingement surface are assumed symmetric on either sides of the jet's centerline for the evaluation of view factors and radiosities. The coupled general partial differential equation in Eq. (4.1) for dimensionless stream function, vorticity and temperature are converted to finite difference equations and are solved simultaneously using a computer code written using Fortran 95. A hybrid of central-difference and flow oriented upwind-scheme according to Heiningen et al. [30] and Gosman et al. [32] is employed for discretization of Eq. (4.1) for all the solved variables, such that the numerical scheme is consistently second-order-accurate. In the numerical scheme, the non-linear convective terms are approximated by central differences when the magnitudes of convective terms are smaller than the corresponding diffusion terms, otherwise the upwind scheme is employed for the convective terms while neglecting the diffusion terms. This hybrid scheme has been reported to be more accurate than the fully upwind scheme, while the convergence stabilities are not significantly different [30]. The finite difference equations along with the boundary conditions were solved using Gauss-Siedel iterations with relaxation, until the local stream functions, vorticities, temperatures and radiosities converge within a relative error of 10^{-4} at every computational grid. The solution algorithm adopted for the calculations involve the following steps:

Step-1: Read input parameters, and assume values for stream function, vorticity and temperature for all internal nodes of the convection half-domain. Assume values for radiosities for all nodes in the radiation-domain.

Step-2: Evaluate the view factors between all elements in the full radiation-domain.

Step-3: Update the values of dimensionless stream function and vorticity at all nodes in the convection half-domain after applying boundary conditions, with values of temperature obtained from previous iteration (or assumed values for first iteration).

Step-4: Update the values of radiosity in the full radiation-domain using the values of temperatures from the previous iteration (or assumed values, for first iteration). The values of temperature on the confinement-plate in the other side of the half-domain are calculated assuming symmetry about centerline of jet.

Step-5: Update the values of temperature at all nodal points in the convection half-domain.

Step-6: Repeat *Steps-3 to 5* until convergence is obtained with a relative error of less than 10^{-4} at every computational grid.

Step-7: Evaluate the steady state convective, radiative and total Nusselt numbers.

4.1.2 Mathematical Model for Turbulent Boiling and Single-phase Jet Impingement Heat Transfer

The computational framework for the simulation for turbulent single phase jet impingement heat transfer is predominantly the same as that employed for boiling jet impingement heat transfer, while the conservation equations for phasic volume fraction and interphase heat, mass and momentum transfer were not included in the calculations during the simulations. Hence, the more general governing equations of flow and heat transfer pertaining to boiling impinging jets, involving the interactions between both phases are detailed herein.
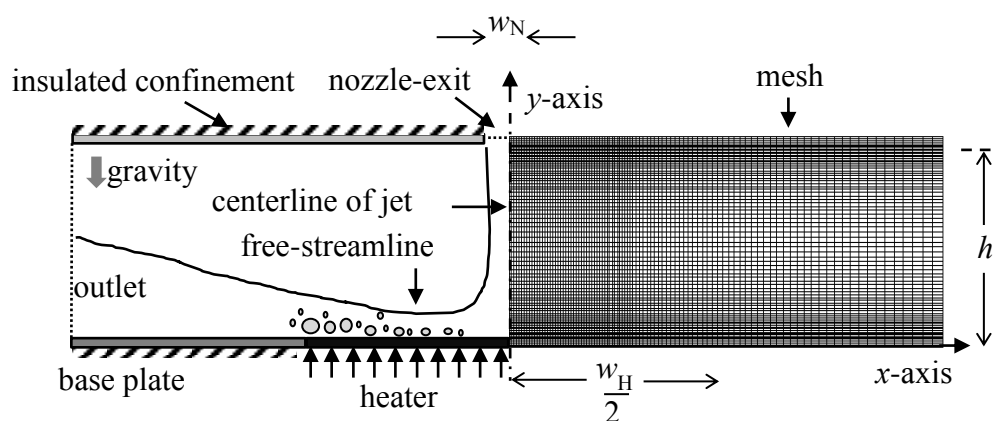
Figure 4.4: Geometry and mesh for confined slot jet impingement boiling

4.1.2.1 Geometry and Computational Domain and Model Assumptions

A schematic of the confined and submerged slot jet impingement geometry used for

the study of turbulent jet impingement heat transfer with and without boiling is illustrated in Fig. 4.4, wherein the computational domain and mesh are indicated on the right side of the centerline of jet. A fully developed turbulent liquid-jet at a specified inlet temperature (or ΔT_{sub}) and a known velocity exits a slot-nozzle of width w_N into a quiescent medium of the same liquid at the same temperature and at atmospheric pressure, resulting in submerged jet impingement. The impingement surface comprises of a heated (isothermal or isoflux) metallic plate surrounded by an unheated base-plate insulated from outside, placed at a specified standoff distance h from the plane of the nozzle outlet. The heated region of the impingement plate extends to a length $w_H/2$ on either sides of the centerline of jet. The flow passage is sandwiched between the impingement plate and externally insulated confinement blocks placed at the plane of the nozzle outlet to facilitate a confined configuration, as shown in the figure. Subsequent to impingement, the fluid exits through the outlets indicated in Fig. 4.4, to a quiescent medium of the liquid phase at atmospheric pressure. To ensure a realistic representation of the physical problem, a conjugate heat transfer analysis is carried out by considering two-dimensional conduction along the entire length of the impingement plate (even beyond the heated region).
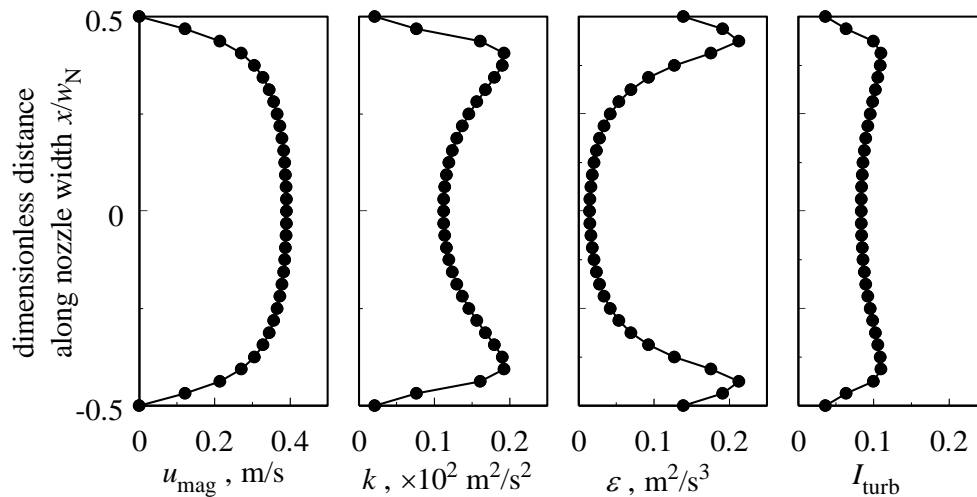
Figure 4.5: Typical distribution of velocity (u_{mag}), turbulence kinetic energy (k), dissipation rate (ε) and intensity (I_{turb}) at the outlet of the two-dimensional duct which is applied at the nozzle for jet impingement simulations; the data corresponds water at 80 ^{o}C, mean Reynolds number (based on hydraulic diameter) = 4000, and nozzle width (w_N) = 2 mm

An isothermal and hydrodynamically fully developed flow condition is

imposed at the exit of the nozzle in the jet impingement geometry. For this, a separate simulation is carried for turbulent flow inside a two-dimensional duct, and the velocity profile and the distribution of turbulence characteristics (turbulence kinetic energy and dissipation rate) obtained at the outlet of the duct are prescribed as the boundary conditions at the nozzle of the jet impingement domain shown in Fig. 4.4. The width of the duct is the same as that of the nozzle (w_N) and the length of the duct is $50 \times w_N$. The fully developed flow conditions at the outlet of the duct is validated by imposing the obtained outlet flow conditions to the inlet to the duct, and re-performing the simulation until the flow features cease to change inside the duct. The fluid properties and mean velocity for the duct-flow simulation are based on each of the thermophysical conditions and jet Reynolds number of jet impingement study. A typical distribution of velocity profile, turbulence kinetic energy, turbulence dissipation rate and turbulence intensity at the outlet of the duct obtained using this technique, is shown in Fig. 4.5 for a representative case: working fluid = water, T_N = 80 ^oC, Re (based on hydraulic diameter) = 4000 and w_N = 2 mm.

A spatially varying non-uniform rectangular mesh is used for the simulations, where the mesh is fine near the walls and centerline of jet, and relatively coarser near the outlet of the domain as shown on the right hand side of the illustration in Fig. 4.4. It was ensured that the mesh in the near wall region was resolved such that the wall $y^+ \leq 4$ on the impingement surface, as the viscous sublayer of the turbulent boundary layer was modeled in the simulation (without using standard turbulent wall functions) for increased prediction accuracy. This is particularly important in the cases with boiling occurring on the surface, to avoid overprediction of surface temperature or inaccurate determination of local surface heat flux. The symmetry about the centerline of the jet was exploited to carryout simulations on one-half of the domain alone, thereby significantly reducing the computational time involved, particularly for those cases involving boiling. The general assumptions for the mathematical model are as follows:

(i)   The length scale of the geometry in the direction perpendicular to the plane of the paper in Fig. 4.4 is much larger than the other length scales in the domain, and hence the flow and heat transfer are two-dimensional in the plane of the paper.

(ii) The fluid properties of both the liquid and vapor phases are invariant with changes in temperature, and density variations in the liquid phase due to buoyancy are modeled with the validity of Boussinesq-approximation.

(iii) The vapor phase remains at saturation temperature until condensation, which is acceptable for subcooled flow boiling for heat fluxes below critical heat flux.

(iv) No-slip boundary conditions are valid on all the wall/ surfaces for both, the liquid as well as the vapor phase.

(v) Boiling occurs only due to heterogeneous nucleation.

4.1.2.2   Mathematical Formulation

The complete set of governing equations for the turbulent flow, heat and mass transfer in the domain, assuming the two phases (during boiling jet impingement heat transfer) to be Euler-Euler interpenetrating continua are solved in conjunction with the *Rensselaer-Polytechnic Institute* (RPI) wall-boiling model. This section presents the basic conservation equations of mass, momentum, energy and volume fraction for the multiphase system, and the closures for the interphase heat, mass, momentum transfer, turbulence, ebullition/ bubble dynamics and wall heat flux partitioning scheme. The subscripts i and j in the following equations denote the phase (liquid or vapor) for which the equation is written and the other phase, respectively.

(i) *Volume fraction*: The phasic volume of each phase V is determined using the volume fractions of each phase (α) as

$$V_i = \int_V \alpha_i \, dV \quad \text{where} \quad \alpha_i + \alpha_j = 1 \tag{4.11}$$

(ii) *Conservation of mass* for each phase is determined as

$$\nabla \cdot \left(\alpha_i \rho_i \vec{v}_i \right) = \dot{m}_{j,i} \tag{4.12}$$

where $\dot{m}_{j,i}$ is the rate of mass transfer from phases i→j. If i represents the liquid phase, the mass transfer corresponds to evaporation and if i represents the vapor phase, then the mass transfer corresponds to condensation. The interphase mass transfer (rate of vapor formation in this case) per unit volume in Eq. (4.12) is given by

$$\dot{m}_{i,j} = -\dot{m}_{j,i} = \frac{h_{RM} A_{int}(T_l - T_w)}{L} + \frac{q_E A_w}{L + c_{p_l}(T_w - T_l)}$$

(4.13)

In Eq. (4.13), the interfacial area density is given by $A_{int} = 6\alpha_{sv}(1-\alpha_v)/d_b$, where α_{sv} is min(α_v, 0.25) according to Kurul and Podowski [118], L is the latent heat per unit mass, $A_w = \delta(\vec{x} - \vec{x}_w)$ is the interfacial area density on the wall surface; T_w and T_l are the surface (wall) temperature and liquid phase temperatures, respectively; and q_E is the evaporation heat flux described under *RPI wall-boiling model* section. The liquid side heat transfer coefficient h_{RM} (for heat transfer between the liquid and vapor bubble) is given by Ranz-Marshall correlation [119] as:

$$h_{RM} = \frac{k_l}{d_b}\left(2 + 0.6 Re_b^{0.5} Pr_l^{0.33}\right)$$

(4.14)

The bubble diameter in the stream (not departure diameter) d_b (in meters) is given by Kurul and Podowski [18] as

$$d_b = \begin{cases} d_b^{max} + \theta \times \Delta T_{sub} & \text{...if } 0 \leq \Delta T_{sub} \leq \Delta T_{sub}^{max} \\ \max\left(d_b^{min} \times \exp\left[\left(\Delta T_{sub} - \Delta T_{sub}^{max}\right)\theta/d_b^{min}\right], 10^{-5}\right) & \text{...if } \Delta T_{sub} > \Delta T_{sub}^{max} \\ 10^{-3} & \text{...if } \Delta T_{sub} \leq 0 \end{cases}$$

(4.15)

In the preceding equation, $\Delta T_{sub} = T_{sat} - T_l$, $\Delta T_{sub}^{max} = 13.5$ °C, $d_b^{min} = 1.5 \times 10^{-4}$ m and $d_b^{max} = 10^{-3}$ m following [18].

(iii) *Conservation of momentum* for each phase is determined as

$$\nabla \cdot \left(\alpha_i \rho_i \vec{v}_i \vec{v}_i\right) = -\alpha_i \nabla p + \nabla \overline{\overline{\tau}}_i + \alpha_i \rho_i \vec{g} + \left(\vec{R}_{j,i} + \dot{m}_{j,i} \vec{v}_{j,i}\right) + \vec{F}_{turb,i} + \vec{F}_{lift,i}$$

(4.16)

where $\overline{\overline{\tau}}_i$ is the phase stress-tensor for the ith phase given by

$$\overline{\overline{\tau}}_i = \alpha_i \mu_i\left(\nabla \vec{v}_i + \nabla v_m^T\right) + \alpha_i \mu_i\left(\lambda_i - \frac{2}{3}\mu_i\right)\nabla \vec{v}_i \overline{I}$$

(4.17)

where $\vec{v}_{i,j}$ and $\vec{v}_{i,j}$ are the interphase velocities defined by

$$\vec{v}_{i,j} = \begin{cases} \vec{v}_i & \text{;if } m_{i,j} > 0 \\ \vec{v}_j & \text{;if } m_{i,j} < 0 \end{cases} \quad \text{and} \quad \vec{v}_{j,i} = \begin{cases} \vec{v}_j & \text{;if } m_{j,i} > 0 \\ \vec{v}_i & \text{;if } m_{j,i} < 0 \end{cases}$$

(4.18)

where ∇v_m^T is the turbulent diffusion tensor (expanded in detail under Turbulence

Modeling). In Eq. (4.16) $\vec{R}_{j,i}$ represents the interphase force (predominantly interphase drag force) defined as

$$\vec{R}_{j,i} = -\vec{R}_{i,j} = K_{j,i}(\vec{v}_j - \vec{v}_i) \quad \text{and} \quad \vec{R}_{i,i} = \vec{R}_{j,j} = 0 \tag{4.19}$$

where $K_{j,i}$ is the momentum exchange coefficient given by

$$K_{j,i} = K_{i,j} = \alpha_l \alpha_v \rho_v f / \eta_v \tag{4.20}$$

where η_j is the relaxation time for bubbles given by

$$\eta_v = \rho_v d_v^2 / 18 \mu_l \tag{4.21}$$

The variable f in Eq. (4.20) is the drag function given by

$$f = \frac{C_{drag} \rho_l d_b}{24 \mu_l} |\vec{v}_v - \vec{v}_l| \tag{4.22}$$

where the drag coefficient C_{drag} is obtained based on a modified version of the coefficient defined by Ishii and Zuber [120] as

$$C_{drag} = \min\left(C_{drag}^{visc}, C_{drag}^{disp}\right) \tag{4.23}$$

In Eq. (4.23) C_{drag}^{visc} and C_{drag}^{disp} are the drag coefficients during the dispersed and viscous regimes flow regimes identified by Ishii and Zuber [120], accounting for the effects of high vapor phase concentration, and are defined as

$$C_{drag}^{visc} = \frac{24\left(1 + 0.1 Re_b^{0.75}\right)}{Re_b \sqrt{\max(\alpha_l, 0.5)}} \tag{4.24}$$

$$C_{drag}^{disp} = \frac{2 d_b \sqrt{g(\rho_l - \rho_v)/\sigma}}{3 \times \max(\alpha_l, 0.5)} \tag{4.25}$$

The lift force $\vec{F}_{lift,i}$ used in Eq. (4.16) is given by Moraga et al. [121] as

$$\vec{F}_{lift,l} = -\vec{F}_{lift,v} = C_{lift} \rho_l \alpha_v (\vec{v}_v - \vec{v}_l) \times (\nabla \times \vec{v}_l) \tag{4.26}$$

where,

$$C_{lift} = \begin{cases} 0.0767 & \text{... if } \phi \leq 6 \times 10^3 \\ \left[0.12 - 0.2 \exp\left[\dfrac{-\phi}{3.6 \times 10^5}\right]\right] \times \exp\left[\dfrac{\phi}{3 \times 10^7}\right] & \text{... if } 6 \times 10^3 < \phi < 1.9 \times 10^5 \\ -0.002 & \text{...if } \phi \geq 1.9 \times 10^5 \end{cases}$$

$$\tag{4.27}$$

where $\phi = Re_b Re_\nabla$. Here, the bubble Reynolds number is $Re_b = d_b \rho_l |v_l - v_v| / \mu_l$

and the bubble shear Reynolds number is $Re_\nabla = d_b^2 \rho_l |\nabla \times \vec{v}_l| / \mu_l$ respectively

(subscripts l, v and b refer to liquid, vapor and bubble respectively). As can be seen

from the preceding equation, the lift coefficient C_{lift} combines the opposing actions

of both, the classical aerodynamic lift that results from the interaction of the bubble

with the liquid, and the force that results from the interaction between the bubbles

and the vortices shed by the bubble wake. The induced turbulence in the flow field

due to the interaction of the numerous bubbles with the primary fluid phase, denoted

as the dispersion force $\vec{F}_{turb,i}$ is given according to Kurul and Podowski [118] as

$$\vec{F}_{turb,l} = -\vec{F}_{turb,v} = C_{turb} \rho_l k \nabla \alpha_v \tag{4.28}$$

where turbulent dispersion coefficient $C_{turb} = 1$. Other variations of the turbulent

dispersion force are available in the literature [122-128].

(iv) *Turbulence* for the multiphase flow is modeled using the RNG-*k*-*ε* model for the

mixture domain in the following way. The turbulent diffusion tensor ∇v_m^T in Eq.

(4.17) is defined as

$$\nabla v_m^T = \frac{\partial}{\partial x_p} \overline{v'_{m,q} v'_{m,q}} + \frac{\partial}{\partial x_q} \overline{v'_{m,q} v'_{m,q}} \quad \text{where} \quad \overline{v'_{m,p} v'_{m,p}} = -\frac{\mu_{T,m}}{\rho_m} \left(\frac{\partial v_{m,q}}{\partial x_p} + \frac{\partial v_{m,p}}{\partial x_q} \right)$$

$$\tag{4.29}$$

The subscripts p and q in Eq. (4.29) are the coordinate directions for the tensor, *v'*

represents the fluctuating component of the velocity and $\vec{v}_m = \sum_{i=1}^{2} \alpha_i \rho_i \vec{v}_i \Big/ \sum_{i=1}^{2} \alpha_i \rho_i$

represents the mean mixture phase velocity. The turbulent viscosity of the mixture is

defined as per the usual definition for RNG-*k*-*ε* model as

$$\mu_{T,m} = \rho_m C_\mu \frac{k^2}{\varepsilon} \quad \text{where the mixture-density is} \quad \rho_m = \sum_{i=1}^{2} \alpha_i \rho_i \tag{4.30}$$

In the preceding equations, *k* is the turbulent kinetic energy and *ε* is turbulent

dissipation rate.

The equations that govern the RNG-*k*-*ε* turbulence model for the mixture are

$$\nabla \cdot (\rho_m \vec{v}_m k) = \nabla \cdot (\mu_{T,m} \nabla k / \sigma_k) + G_{k,m} - \rho_m \varepsilon + S_k \tag{4.31}$$

$$\nabla \cdot \left(\rho_{\mathrm{m}} \vec{v}_{\mathrm{m}} \varepsilon \right) = -\nabla \cdot \left(\mu_{\mathrm{T,m}} \nabla \varepsilon / Pr_{\varepsilon} \right) + \left(C_{1\varepsilon} G_{k,m} - C_{2\varepsilon} \rho_{\mathrm{m}} \varepsilon \right) \varepsilon / k + S_{\varepsilon} - R_{\varepsilon} \qquad (4.32)$$

where the production of turbulence kinetic energy $G_{k,m}$ is defined as

$$G_{k,m} = \mu_{\mathrm{T,m}} \left\{ \nabla \vec{v}_{\mathrm{m}} + \left(\nabla \vec{v}_{\mathrm{m}} \right)^{\mathrm{T}} \right\} : \nabla \vec{v}_{\mathrm{m}} \qquad (4.33)$$

The constants in the above equations are $C_{1\varepsilon} = 1.42$, $C_{2\varepsilon} = 1.68$, $C_{\mu} = 0.0845$, $\sigma_{k} = \sigma_{\varepsilon} = 0.7194$ and $Pr_{\varepsilon} = 0.75$. in Eq. (4.32), R_{ε} accounts for the production of dissipation in the ε equation; it was first derived by Yakhot et al. [129-131] and later modified by Yahkot and Smith [132] after the inclusion of an additional expansion parameter η based on the ratio of the turbulent and mean strain time scales as given as:

$$R_{\varepsilon} = v_{\mathrm{T}} S^{3} \left(1 - \eta / \eta_{o} \right) / \left(1 + \beta \eta^{3} \right) \qquad (4.34)$$

where $\eta = S \bar{k} / \bar{\varepsilon}$, $S = \sqrt{2 S_{\mathrm{i,j}} S_{\mathrm{i,j}}}$ and $\eta_{o} \approx 4.38$. The constant $\beta = 0.012$ is chosen such that it results in a value of 0.4187 for the Von Karman constant [133].

The terms S_{k} and S_{ε} in Eqs. (4.31,4.32) represent the bubble induced turbulence kinetic energy and dissipation rates, defined according to Troshko and Hassan [134]:

$$S_{\mathrm{k}} = 0.75 \, C_{\mathrm{drag}} \left(\rho_{\mathrm{l}} \, \alpha_{\mathrm{v}} / d_{\mathrm{b}} \right) \left| \vec{v}_{\mathrm{v}} - \vec{v}_{\mathrm{l}} \right|^{2} \qquad (4.35)$$

and $S_{\varepsilon} = 1.35 \, C_{\mathrm{drag}} \left(S_{\mathrm{k}} / d_{\mathrm{b}} \right) \left| \vec{v}_{\mathrm{v}} - \vec{v}_{\mathrm{l}} \right| \qquad (4.36)$

(v) *Conservation of energy* for each phase is determined as

$$\nabla \cdot \left(\alpha_{\mathrm{i}} \rho_{\mathrm{i}} \vec{v}_{\mathrm{i}} h_{\mathrm{i}} \right) = \overline{\overline{\tau}}_{\mathrm{i}} : \nabla \vec{v}_{\mathrm{i}} - \nabla \vec{q}_{\mathrm{i}} + \left(Q_{\mathrm{j,i}} + \dot{m}_{\mathrm{j,i}} h_{\mathrm{j,i}} \right) \qquad (4.37)$$

where $\vec{q}_{\mathrm{i}}$ is the heat flux vector, $Q_{\mathrm{j,i}}$ is the energy exchange between the two phases and $h_{\mathrm{j,i}}$ is the difference in the enthalpy of formation between the phases. In all the above equations, $\dot{m}_{\mathrm{i,j}} = -\dot{m}_{\mathrm{j,i}}$ and $\dot{m}_{\mathrm{i,i}} = \dot{m}_{\mathrm{j,j}} = 0$, and similarly, $Q_{\mathrm{i,j}} = -Q_{\mathrm{j,i}}$ and $Q_{\mathrm{i,i}} = Q_{\mathrm{j,j}} = 0$. The conservation of energy in the solid domain (impingement plate and confinement block) is typically the same as Eq. 4.37, where the fluid properties are replaced with that of the solid, the convective and interphase exchange terms are zero, and where the energy source term $Q\mathrm{j,i}$ is replaced with the volumetric heat generation rate (for cases when the heating on the impingement plate is through volumetric heat generation).

4.1.2.3   Wall Heat Flux Partitioning

During forced convective turbulent single phase jet impingement, the rate of heat transfer on the impingement surface is purely attributed to convection. However, during impingement heat transfer with phase change, the overall heat transfer rate due to nucleate boiling is attributed to several simultaneous mechanisms including liquid and vapor phase convection, quenching or cyclic cooling by the fluid occupying the void of a departed bubble (transient convection) and evaporation. The total heat flux at the solid-fluid interface is thus evaluated as the sum of these individual partitioned heat fluxes according to the *RPI wall-boiling model* as

$$q_T = q_C + q_Q + q_E \tag{4.38}$$

It is to be noted that the vapor phase convective component is ignored in the above equation, as the contribution is expected to be insignificant during subcooled nucleate boiling. The three components of the heat flux are evaluated as follows.

(i) *Liquid phase convective heat flux*: At any instant of time during nucleate boiling, the surface over which boiling is expected to occur is divided into two areas: A_b , covered by the vapor bubbles; and $(1-A_b)$, covered by the liquid. Hence, the convective heat flux resulting from the heat removal on the portion of the heater not occupied by bubbles is defined as

$$q_C = h_C \left(1 - A_b\right)\left(T_w - T_l\right) \tag{4.39}$$

where, T_w and T_l are the local wall and liquid phase temperature respectively, and h_C is the liquid phase turbulent convective heat transfer coefficient defined by Egorov and Menter [135] using the near wall velocity field. This form of the heat transfer coefficient is practically more suitable for problems of the type in the present research, as compared to Kurul and Podowski's [18] Stanton number based correlation which is highly mesh dependant. The effective area occupied by the bubbles (A_b) is as

$$A_b = \min \left[1 , \left((\pi/4)\xi N_w \, d_{bw}^2\right)\right] \tag{4.40}$$

where the area influence coefficient is defined according to De Valle and Kenning [136] as

$$\xi = 4.8 e^{-0.0125 \, Ja_{sub}} \tag{4.41}$$

In the preceding equation, the Jacob number based on fluid subcooling is defined as

$$Ja_{sub} = \rho_l c_{p_1} \Delta T_{sub} / \rho_v L \tag{4.42}$$

and the nucleation site density is defined according to Lemmert and Chawla [137] as

$$N_w = 210^{1.8} \Delta T_{sat}^{1.8} \tag{4.43}$$

In the preceding equations, ρ_l, c_{pl}, ΔT_{sub}, ρ_v, L, ΔT_{sat} and d_{bw} represent the density of liquid, specific heat of liquid, local degree of subcooling, vapor density, latent heat, local degree of surface superheat and the bubble departure diameter (explained in detail in section 4.1.2.4), respectively.

(ii) *Quenching heat flux*: The quenching component of the total heat flux is modeled as the cyclic averaged transient energy transfer related to the liquid filling the vicinity of the wall in the void of the bubble subsequent to its detachment. Similar to the liquid phase convective heat flux, the quenching heat flux is given by,

$$q_Q = h_Q A_b \left(T_w - T_1^* \right) \tag{4.44}$$

where T_1^* is a characteristic liquid temperature (explained in detail in section 4.1.2.4) and h_Q is the quenching heat transfer coefficient defined as

$$h_Q = 2f \sqrt{\tau k_1 \rho_1 c_{p_1} / \pi} \tag{4.45}$$

where τ is the fraction of bubble dwelling/ waiting time.

(iii) *Evaporation heat flux*: The evaporative component of the total heat flux of the initially subcooled liquid, resulting from the change of phase is defined as

$$q_E = \left(\pi/6 \right) d_{bw}^3 f N_w \rho_v L \tag{4.46}$$

where d_{bw}, N_w, ρ_v, L and f are bubble departure diameter, nucleation site density, density of vapor, latent heat and bubble departure frequency respectively. The details of the models employed for the estimation of bubble departure diameter, departure frequency and the characteristic liquid temperature (Eq. 4.44) are provided in the following section.

4.1.2.4 Bubble Departure Diameter and Frequency

Although there are several models available for the estimation of the numerous ebullition parameters including departure diameter, nucleation site density,

frequency, etc., there is no definite consensus on a generalized model for any of these parameters for flow boiling applications. Accurate modeling of these parameters depending on the thermo-hydraulic realistic conditions particular to the problem investigated is intrinsically important for a realistic simulation of such problems. Besides, most of the experimental models for these ebullition parameters are constrained to the specific conditions, and particularly, the fluid which was used for the experiment and flow configuration (duct flow or annular flow, etc.), and hence their applicability to analyses are constrained to the conditions in which the experiments were conducted. Thus, it is realised that a problem based analysis is absolutely essential before implementation of these models to jet impingement boiling problems and while using fluids that were not primarily used in the development of the various models. Two different models for estimation of bubble departure diameter and three different models for the evaluation of bubble departure frequency are compared in the present computational framework and as will be shown in the section discussing the results. The predictions using each of these models are compared to check their validity of the present computations against experimental data obtained in the present research using FC-72 as the working fluid, as well published experimental data of Shin et al. [76] for a similar fluid (PF-5060) and geometric configuration, but different range of operating parameters such as jet Reynolds number, fluid subcooling and jet standoff distance. The choice of bubble departure diameter and frequency models included in the simulations encompass both pool boiling as well as flow boiling based models, developed from both experimental as well as mechanistic approaches. The reason for including pool boiling based models for the present simulation which is classified as flow boiling is that, it has been widely accepted for jet impingement boiling configurations that boiling curves due to different Reynolds numbers collapse into a single curve during the fully developed nucleate boiling regime, rendering the effect of jet flow velocity (or Reynolds number) insignificant in the regime, although the critical heat flux is significantly influenced by fluid velocity [56,138-140]. This has been attributed to the vigorous fluid motion induced in the vicinity of the superheated surface due to the large number of activated nucleation cavities resulting in substantial boiling activity that consequently overshadows any effect of the jet induced fluid motion in the region.

(i) *Bubble departure diameter*: Several models for the estimation of maximum diameter of bubble at departure (d_{bw}) obtained by mechanistic as well as experimental techniques have been proposed in the literature [80-82,86,141]. Some of these models [81,86] require the knowledge of the parameters such as liquid contact angle on the surface at different operating temperatures and pressures that vary substantially with the surface characteristics (roughness), which are not readily available for any general system making their implementation into the already complex computational framework more difficult. In the present research, two different bubble departure diameter models, one due to Unal [82] and the other due to Tolubinsky and Kostanchuk [80], which essentially encompass both pool boiling and flow boiling based models, are included for comparison purposes. Both these models have been reported to provide reasonable predictions for tube boiling simulations when compared against experimental data [142,143]. The description of Unal's, and Tolubinsky and Kostanchuk's models for bubble departure diameter as implemented in the computational simulations is delineated hereunder.

Unal [82] correlated the bubble departure diameter during the heat flux controlled regime of ebullition using water as the working fluid for operating conditions in the range $0.1 \leq p \leq 17.7$ M Pa, $0.47 \leq q_T \leq 10.64$ M W/m^2, $0.08 \leq u_l \leq 9.15$ m/s, $3 \leq \Delta T_{sub} \leq 86$ ^{o}C resulting in bubble departure diameters in the range $0.08 \leq d_{bw} \leq 1.24$ mm. The bubble departure diameter from Unal [82] integrated into the present framework of ANSYS-FLUENT is given as:

$$d_{bw} = 2.42 \times 10^{-5} P^{0.709} \, \xi_1 \big/ \sqrt{\xi_2 \, \xi_3} \tag{4.47}$$

where p is the local pressure; and the parameters ξ_1 ξ_1 and ξ_1 are defined as

$$\xi_1 = \frac{k_w \, \Delta T_{sat}}{2 L \rho_v \sqrt{\pi \alpha_w}} \tag{4.48}$$

$$\xi_2 = \begin{cases} \dfrac{\Delta T^*_{sub}}{2\left(1 - \rho_v/\rho_l\right)} & \text{... if } \Delta T^*_{sub} > 3\,^o\text{C} \\[4mm] \dfrac{\Delta T^*_{sub}}{2\left(1 - \rho_v/\rho_l\right)} \exp\left(\dfrac{\Delta T^*_{sub}}{3} - 1\right) & \text{... if } \Delta T^*_{sub} \leq 3\,^o\text{C} \end{cases} \tag{4.49}$$

and $\xi_3 = \max\left[\left(\dfrac{u^*}{0.61}\right)^{0.47}, 1\right]$ \hfill (4.50)

In Eq. (4.49), the degree of subcooling based on the characteristics liquid temperature is $\Delta T_{sub}^* = T_{sat} - T_1^*$. As pointed out in Krepper et al. [144], the values of T_1^* and u^* in Eqs. (4.49-4.50) were originally formulated for one-dimensional thermo-hydraulic models, in terms of the mean-flow temperature and velocity of the bulk fluid. Implementation of such models in a representative computational framework would impose limitations on the near wall mesh to be undesirably coarse (to avoid under-prediction of velocity due to no-slip boundary condition, and over-prediction of the liquid temperature as the model also includes the thin superheated layer near the wall). Consequently, the vapor generation would be anomalously over-estimated. Thus, following Krepper et al. [144], the characteristic temperature and velocity, T_1^* and u^*, are evaluated at a constant $y^+ = 250$ based on locally re-constructed temperature and velocity log-law profiles, as follows:

$$T_1^* = \max\left[\min\left[\left(T_W - \frac{q_{liq}}{\rho_1 c_{p1} u_\tau} T^+ \right), T_{sat} \right], T_N \right] \tag{4.51}$$

and $u^* = u^+ / u_\tau$ $\tag{4.52}$

where, $q_{liq} = q_T - q_E$ is the heat flux used for sensible heating of the liquid phase.

$$T^+ = Pr_\tau \left[u^+ + 9.24 \left\{ \left(Pr / Pr_\tau \right)^{0.75} - 1 \right\} \left(1 + 0.28 e^{-0.007 Pr / Pr_\tau} \right) \right] \tag{4.53}$$

$$u^+ = \frac{1}{\kappa} \ln\left(9.793 \, y^+ \right) \tag{4.54}$$

In the preceding equations, the turbulent Prandtl number $Pr_\tau = 0.85$ and the Von Karman constant $\kappa = 0.4187$. As the understanding of the boundary layer flow/ heat transfer on a surface over which boiling occurs is still sparse, the aforementioned values are evaluated based on liquid phase velocity and temperature rather than that of the bulk fluid. A further investigation into the theory of multiphase boundary layers involving phase change is required for an improved closure to the model that would include the bulk velocity and temperature.

The second model used for the estimation of the bubble departure diameter is due to Tolubinsky and Kostanchuk [80]. They carried out subcooled pool boiling experiments using water at different pressures to ascertain the relationship between the bubble departure diameter and frequency. The expression for bubble departure

diameter was given as:

$$d_{bw} = \min\left[0.0014, 0.0006 \times e^{\left(\frac{-\Delta T_{sat}}{45}\right)}\right]$$ (4.55)

In the preceding equation, ΔT_{sat} is the local degree of superheat on the heater surface, and the expression was developed [145] from the experimental data of Tolubinsky and Kostanchuk [80] in the range of degree of subcoolings ΔT_{sub} upto 60 ^{o}C and operating pressures upto 1 M Pa.

The implementation of two different models for the estimation of bubble departure diameter into the present computational framework was discussed in the preceding section; the different models employed for the estimation of bubble departure frequency follows.

(ii) *Bubble departure frequency*: The most popular and widely used model for prediction of bubble departure frequency is that deduced by Cole [85] in 1960. The bubble departure frequency was evaluated from a study of pool boiling in water, by balancing the buoyancy forces to the drag forces for a rising bubble, under high heat flux conditions. This model was also reported to agree with the experimental data of both Perkins and Westwater [146] (nucleate boiling of methanol under conditions below as well as during CHF) and Deissler [147] (heat fluxes during CHF) with an average error of $\pm$ 52.2%. The model for departure frequency (in Hz) according to Cole was defined as:

$$f = \sqrt{\frac{4g}{3d_{bw}}\left(1 - \frac{\rho_v}{\rho_l}\right)}$$ (4.56)

where g, ρ_v, ρ_l and d_{bw} represent the acceleration due to gravity, density of vapor, density of liquid and the bubble departure diameter (see Eq. (4.47)), respectively. It is to be noted that Eq. (4.56) considers only the bubble rise velocity, and hence the bubble waiting time (during which, heat transfer takes place to the liquid that fills the vacant space of the departed bubble) is not included. In the present study, the bubble waiting time was modeled based on the suggestion of Kurul and Podowski [18] as 80% of the departure period, as follows:

$$t_w = 0.8/f$$ (4.57)

The second model for bubble departure frequency included in the computational analysis is due to Basu et al. [86]. They measured the bubble growth and waiting times from flow boiling (of water) experiments performed for a range of mass fluxes (124-926 kg/m²s), heat fluxes (2.5-90 W/cm²), pressures (1.03 to 3.2 bar), bubble contact angles (30°-90°) and inlet subcoolings (7.7-46.5 °C). The bubble departure frequency was evaluated as the inverse sum of the bubble growth time and waiting time, as follows:

$$f = 1/(t_{\mathrm{w}} + t_{\mathrm{g}})$$
(4.58)

From their experimental data, Basu et al. [86] observed that the bubble waiting time decreased with increase in ΔT_{sat}, but had no clear relationship with ΔT_{sub}. The bubble waiting was correlated with a prediction accuracy of $\pm$ 23.2% as

$$t_{\mathrm{w}} = 139.1(\Delta T_{\mathrm{sat}})^{-4.1}$$
(4.59)

Based on an analysis that during the bubble growth period, the net heat flux from the superheated liquid layer to the bubble contributes to growth of the bubble and further evaporation, Basu et al. [86] correlated the bubble growth time with a prediction accuracy of $\pm$ 10% as

$$t_{\mathrm{g}} = \frac{d_{\mathrm{bw}}^2}{45\,\alpha_{\mathrm{l}}\,Ja_{\mathrm{sat}}}\,e^{0.02\,Ja_{\mathrm{sub}}}$$
(4.60)

where, α_{l} is the thermal diffusivity of the liquid phase. The Jacob numbers based on degree of superheat and subcooling are defined as

$$Ja_{\mathrm{sat}} = \frac{\rho_{\mathrm{l}}\,c_{p\mathrm{l}}}{\rho_{\mathrm{v}}\,L}\,\Delta T_{\mathrm{sat}} \qquad \text{and} \qquad Ja_{\mathrm{sub}} = \frac{\rho_{\mathrm{l}}\,c_{p\mathrm{l}}}{\rho_{\mathrm{v}}\,L}\,\Delta T_{\mathrm{sub}}^*$$
(4.61)

As mentioned earlier, the liquid subcooling $\Delta T_{\mathrm{sub}}^*$ in the preceding equation is evaluated based on the characteristic temperature (T_{l}^*) defined in Eq. (4.51) for the present research.

The third model used for the estimation of bubble departure frequency employed in the present research is due to Podowski et al. [87]. Using a rigorous analytical approach, Podowski et al. [87] deduced a mechanistic model for the ebullition characteristics during forced convective subcooled boiling, by combining the transient heat transfer solutions for a heated wall and the liquid filling the space of a departed bubble (quenching). The closed-form solution for the bubble departure

frequency (determined for a critical diameter of bubble before departure) involved several controlling parameters including transient heat flux, subcooling, pressure, mass flux and critical cavity radius. Similar to Basu et al. [86], the bubble departure frequency was defined as shown in Eq. (4.58), where t_w and t_g were evaluated to be

$$t_w = \left\{ \frac{1}{2\xi_1} \left(-\xi_2 + \sqrt{\xi_2^2 - 4\xi_1\xi_3} \right) \right\}^2 \tag{4.62}$$

where, $\quad \xi_1 = \dfrac{2q_T}{\Re\pi} \tag{4.63}$

$$\xi_2 = \frac{T_W\sqrt{k_w\rho_w c_{pw}} + T_1^*\sqrt{k_1\rho_1 c_{pl}}}{\sqrt{k_w\rho_w c_{pw}} + \sqrt{k_1\rho_1 c_{pl}}} - T_{sat} - \frac{q_T r_c}{\Re\sqrt{\pi\alpha_1}} - \frac{2\sigma T_{sat}}{r_c L}\left(\frac{1}{\rho_v} - \frac{1}{\rho_1}\right) \tag{4.64}$$

$$\xi_3 = \frac{r_c}{\sqrt{\pi\alpha_1}}\left(T_1^* - \frac{T_W\sqrt{k_w\rho_w c_{pw}} + T_1^*\sqrt{k_1\rho_1 c_{pl}}}{\sqrt{k_w\rho_w c_{pw}} + \sqrt{k_1\rho_1 c_{pl}}} \right) \tag{4.65}$$

and $\quad t_g = \left\{ \dfrac{1}{2\xi_4}\left(-\xi_5 + \sqrt{\xi_4^2 - 4\xi_4\xi_6} \right) \right\}^2 \tag{4.66}$

where,

$$\xi_4 = q_T / k_w \tag{4.67}$$

$$\xi_5 = \frac{2}{\sqrt{\pi\alpha_w}}\left(\frac{T_W\sqrt{k_w\rho_w c_{pw}} + T_1^*\sqrt{k_1\rho_1 c_{pl}}}{\sqrt{k_w\rho_w c_{pw}} + \sqrt{k_1\rho_1 c_{pl}}} + \frac{2q_T\sqrt{t_w}}{\pi\Re} - T_{sat} \right) \tag{4.68}$$

$$\xi_6 = \frac{d_{bw}\rho_v L}{2k_w} \tag{4.69}$$

In the preceding equations,

$$\Re = k_w\big/\sqrt{\pi\alpha_w} + k_1\big/\sqrt{\pi\alpha_1} \tag{4.70}$$

In line with the suggestions in [87] and [88], the above model is implemented into the present numerical framework with the assumption of critical cavity radius $r_c = 10^{-5}$ m.

4.1.2.4   Solution Technique

The computational framework employed for the simulations of boiling jet impingement heat transfer is illustrated in Fig. 4.6. The governing equations of mass,

Conservation Equations	Closures	RPI model Closures
		Wall-Heat-Flux partitioning
		Bubble diameter in stream
		Bubble departure diameter
	Turbulence (*RNG-k-ε* + EWT)	Bubble departure frequency
Continuity	Interphase Heat Transfer	Bubble growth time
Volume fraction (for vapor phase)	Interphase Mass Transfer	Bubble waiting time
Momentum (for each phase)	Interphase Lift and Drag Forces	Interfacial area concentration
Energy (for liquid phase)	Bubble induced turbulence	Active nucleation site density

Multiphase model	Eulerian-Euler two-fluid model (liquid-vapor phase interpenetrating continua)
Solver	Finite-Volume (ANSYS-FLUENT 14.0/14.5)

Figure 4.6: Computational framework for boiling jet impingement heat transfer

momentum, energy, turbulence along with the closures for wall heat flux partitioning, interphase mass, momentum and heat transfer and turbulence with *Re-Normalization Group* (RNG) *k-ε* model, simultaneously and iteratively using the finite volume based solver ANSYS-FLUENT 14.0/ 14.5. The *Quadratic Upstream Interpolation for Convective Kinematics* (QUICK) numerical scheme is employed for the governing equations of continuity, momentum and energy, while a modified *High Resolution Interface Capturing* (HRIC) scheme is employed for conservation equations of volume fraction. For single phase studies, the conservation equations of volume fraction and those pertaining to interphase transfer are omitted, thus rendering the flow regime to consist of just the primary fluid.

4.2   EXPERIMENTAL METHODOLOGY

Single phase experiments for both steady state and pulsating impinging jets are carried out with de-ionized water, while boiling experiments for steady state and

pulsating impinging jets are carried out with FC-72. The experimental facility used for both the investigations are predominantly the same with minor changes, as will be indicated in the following sections of this chapter. The experimental methodology described hereunder is employed for the measurement of surface heat flux and impingement surface temperature for different inlet jet velocities, jet temperatures and different jet pulsation characteristics, under both single phase and boiling conditions.

4.2.1   Design and Fabrication of Jet Impingement Experimental Facility

An experimental facility comprising of the flow loop, thermal and flow control equipments, thermal and flow monitoring and measurement instrumentations, test cell to accommodate confined and submerged jet impingement, heater block to facilitate heat input to the impinging jet, is designed and fabricated for the present study. The general philosophy employed for the design and fabrication of the experimental setup involves the following stages:

(i)   Identification of desired experimental variables and conditions to accomplish objectives of the present research;

(ii)   Identification of suitable process equipments, flow and thermal control components, and measuring and monitoring instrumentation;

(iii) Design of flow loop, jet impingement test cell, and structural frame for housing the equipments, instrumentation, fluid piping and test cell;

(iv) Design of pulsating jet mechanism and in-line degassing system (to control dissolved gas content during impingement boiling experiments);

(v)   Design of electrical circuitry for power supply for components as well as data transfer;

(vi) Procurement of materials and components;

(vii) Fabrication of sub-components and integration into the experimental facility using designed and identified pipe fittings, adhesives or brazed/ welded connections.
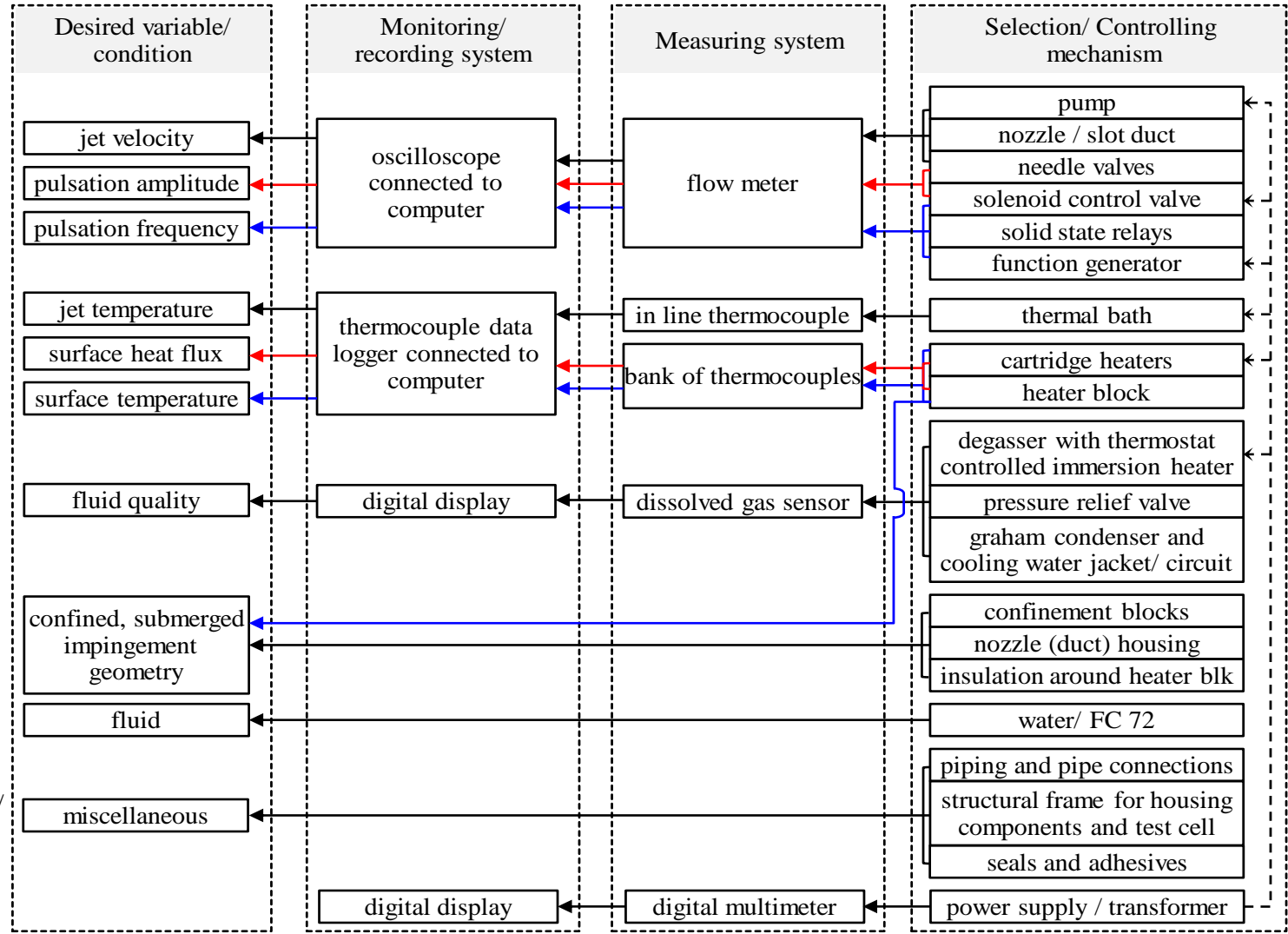
Figure 4.7: Identification of experimental variables/ conditions, and the archetype process equipment and instrumentation to control measure and monitor/ record the desired experimental variables or operating condition; note: coloured arrows represent the selection/ controlling mechanism for a particular desired variable/ condition
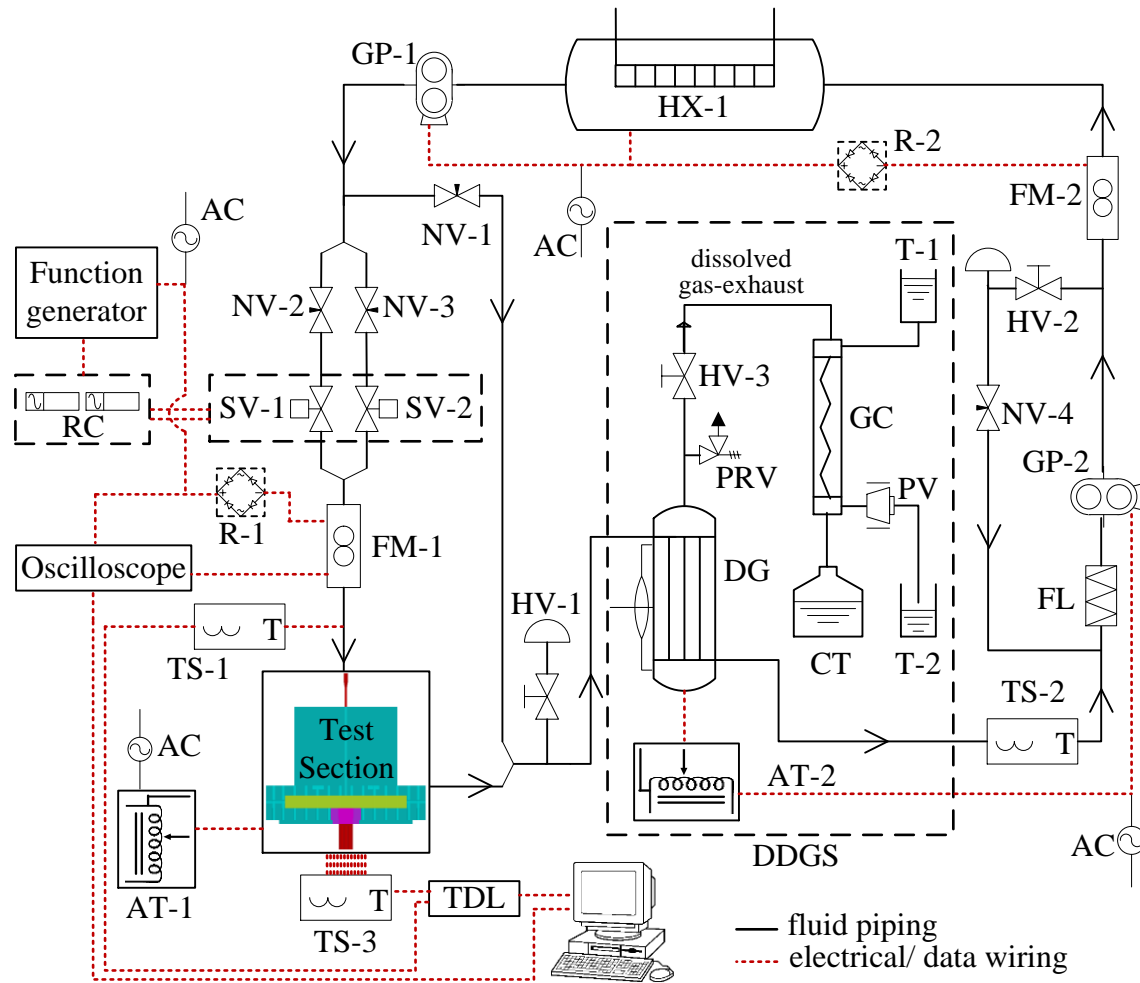
Key	
AC	alternating current power supply
AT-1,2	auto-transformers
CT	collecting tank for condensed fluid
DDGS	degassing/ dissolved gas exhaust system
DG	degasser with thermostat control
FL	inline filter
FM-1,2	flow-meters
GC	graham condenser
GP-1,2	gear pumps
HV-1,2,3	hand valves
HX-1	heat exchanger (thermal bath)
NV-1,2,3,4	needle valves
PRV	pressure relief valve
PV	plug valve
R-1,2	rectifier (ac/dc converter)
RC	relay circuit
SV-1,2	solenoid control valves
T-1,2	tank (for condenser coolant-water)
TDL	thermocouple data logger
TS-1,2	in-line thermocouples
TS-3	thermocouples from heater-block

Figure 4.8: Schematic of jet impingement experimental facility

Figure 4.7 illustrates the schematic of the first two stages of the aforementioned general philosophy employed, indicating the identified experimental variables/ conditions, and the archetype process equipment and instrumentation to control, measure and monitor/ record the desired experimental variables. The experimental facility is designed based on the identified experimental conditions, variables and components, by considering several critical and interrelated governing parameters as outlined in Appendix A-1. Computational simulations are carried out to infer the suitable materials and sizes of the elements in the jet impingement test cell comprising of the heater block, nozzle slot duct, confinement blocks and insulations around the heater block. The components for the experimental facility, the number and type of measuring tools (such as number and locations of thermocouples in the test cell), are chosen based on design calculations made for compatibility with the desired ranges of flow rates, fluid temperatures, dissolved gas content in fluid, heat fluxes, heater surface temperatures, and so on. The experimental setup including the flow loop, electrical network, data acquisition system and jet impingement test cell hence developed for the present research, along with the working mechanism is described in the following section. A photograph of the experimental facility is shown in Appendix A-2.

4.2.2   Description of Jet Impingement Experimental Facility

Figure 4.8 illustrates the schematic of the experimental setup and flow loops constructed for the study of steady and pulsating liquid jet impingement cooling with and without boiling. The temperature of the liquid jet (T_N) is controlled using an internally re-circulating constant temperature thermal bath (DC30, HAAKE), from where the liquid is pumped into the test section (filled with the working fluid) using a magnetic drive gear pump (MG213XPS17, Clark Sol.). The flow rate of the working fluid is controlled using three needle valves (two for the jet and the other for the bleed). Two solenoid control valves (a normally open and a normally closed) which are powered using two solid-state relays are used to control the pulsation characteristics (frequency and amplitude) of the liquid jet. A square-waveform from a function generator (MFG-8216A, Matrix)that is fed to the solid state relays is used to determine the frequency of operation of the solenoid valves (and the pulsating jet),

and the two needle valves (placed before the solid state relays) control the amplitude and mean flow rate of the pulsating jet. A schematic of the jet pulsation generation
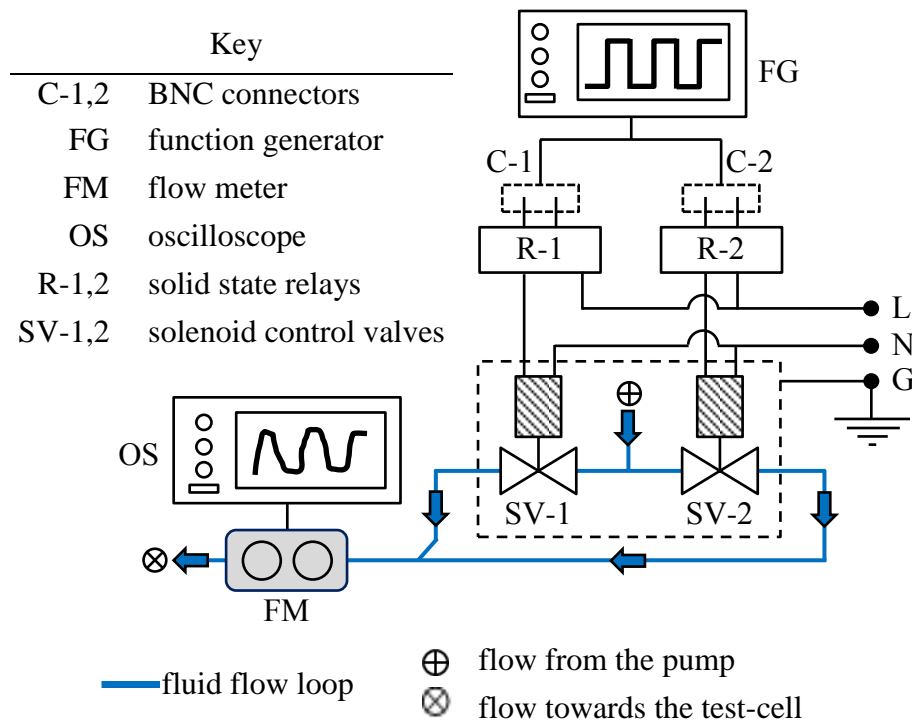
Figure 4.9: Jet pulsation generating and monitoring system

and monitoring mechanism is illustrated in Fig. 4.9. As indicated in the figure, the instantaneous volumetric flow rate is measured using a digital flow meter (PF3W704, SMC Pneumatics) by continuously monitoring an analogue output from the flow meter in an oscilloscope (DS4014, RIGOL). As both the solenoid valves are controlled using a single signal from the function generator, and as the time scale for operation of the solid state relays is several orders of magnitude smaller than the time scale of pulsations (or controlling signal's waveform) it is ensured that the solenoid valves operated precisely in-phase. A K-type thermocouple (OMEGA) is used for inline measurement of the instantaneous temperature just before the jet nozzle. During steady state jet experiments, the function generator is turned off to ensure that just the normally-open solenoid valve permits the flow to pass through. The fluid leaving the test section flows into a settling chamber and is subsequently pumped back for recycling into the thermal bath, resulting in a closed flow-loop system. During boiling jet impingement experiments, this settling tank is replaced with a combined de-aeration and dissolved gas exhaust system comprising of a degasser (with thermostatic control), a graham condenser and a collecting tank for condensed

vapor. The degasser is operated continuously for most of the duration of the experiment to ensure the liquid is sufficiently free of dissolved gases. The quantity of dissolved gas in the working fluid is measured using a (HI9142, Hanna Inst.) dissolved oxygen sensor a few times during and after the completion of each experimental run.
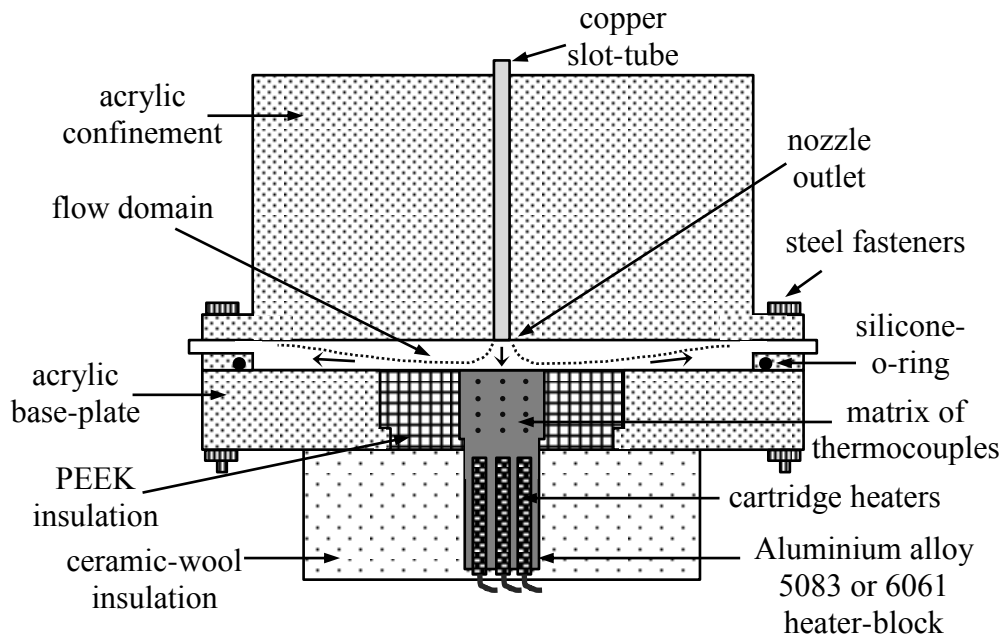
Figure 4.10: Schematic of the test cell

Figure 4.10 shows the schematic of the test cell. The outlet of the flow meter is connected to a round-to-rectangular reducer through which the working fluid enters the rectangular passage (4 mm × 25 mm) that leads to the slot nozzle of the same dimensions (jet-width = 4 mm). The rectangular passage is made of copper and is of sufficient length ($\approx 70 \times$ nozzle width) to ensure a fully developed flow profile at the nozzle outlet. A block of acrylic around the slot nozzle is designed to facilitate the confinement for the submerged jet impingement geometry. The impingement plate is made of three sections, *viz.* aluminium alloy (heater block), PEEK (insulation) and acrylic base-plate as shown in the figure. Two different materials aluminium alloy-5083 and 6061 are used for the construction of the heater block. As the heat fluxes obtained during single phase experiments are expected to be much lower than those during boiling experiments, the heater block fabricated with aluminium alloy-5083 (which has a thermal conductivity lower than alloy 6061) is used for experiments with de-ionized water to reduce the uncertainty in the estimation of surface heat flux and the calculated surface temperature. For the boiling

experiments with FC-72, the alloy 6061 which has a relatively larger thermal conductivity and which is suitable for continuous operation at larger temperatures (unlike alloy 5083) is used for the construction of the heater block. The heater block (40 mm × 10 mm cross-sectional area) is impregnated with three 200 W cartridge heaters (Helios), which are powered by a voltage-controlled AC input. The section of the heater block between the cartridge heaters and the impingement surface (55 mm) consists of a matrix of twelve K-type thermocouples (OMEGA) in three equidistant (10 mm spacing) columns of four thermocouples each as shown in Fig. 4.10, where the central column is directly under the stagnation point of the impinging jet. The first row of three thermocouples was positioned at a distance of 3 mm from the impingement surface. The complete dimensions of the test cell are indicated in Appendix A-3. While the sides of the upper part of the aluminium heater block are insulated with an insulating polymeric thermoplastic Polyether-ether-ketone (PEEK), the lower part is thoroughly insulated with ceramic wool to ensure minimal heat losses. The fluid is contained in the confined geometry of the test cell, with a silicone O-ring between the acrylic confinement blocks and the acrylic base plate as shown in the figure. The room-temperature-vulcanizing (RTV, Selleys) silicone adhesive is used for arresting fluid leakage between the aluminium heater block and the PEEK insulation, and another type of wet-area Silicone (for submerged applications) is used for joints between the PEEK and acrylic. It is pointed out that most common epoxies and adhesives are incompatible with acrylic, particularly for prolonged submerged applications.

In summary, a fully developed turbulent (pulsating or steady) liquid jet (de-ionized water or FC-72) at atmospheric pressure and a temperature of T_N exits a slot nozzle of width $w_N = 4$ mm into a quiescent medium of the same liquid at the same temperature to impinge on a heated aluminium surface of width $L = 40$ mm (and depth of 10 mm into the plane of the paper in Fig. 4.10). The flow passage is sandwiched between the impingement surface and acrylic blocks placed at the plane of the nozzle-exit, resulting in confined and submerged jet impingement. The detailed list of components, equipments, measurement systems and instrumentation used in the experimental facility, along with their specifications and uncertainties are tabulated in Table-4.3.

Table 4.3: List of equipment used in the experimental facility

Description	Quantity	Manufacturer / Model and	Specifications	Uncertainty
Auto-transformer	2	METREL/ HSN 0303	0 - 3.38 kW, 0 – 260 V; 13A	-
Cartridge heater	3	Helios/ RHR/250/50/200	¼"×50mm 200 W	-
Computer	1	Dell Precision/ T1600	Intel Xeon E3-1200 series	-
Digital multimeter	1	Digitech/ QM1535	-	0.01 V (<40 V) 0.1 V (>40 V)
Dissolved gas sensor	1	Hanna Instr./ HI9142	0-19 mg/L	+/- 0.1 mg/L; 1.5% (20 ^{o}C)
Flow meter	2	SMC Pneumatics/ PF3W704	0.5 - 4 lit/m viscosity upto 3 mPa-s	+/- 3 %
Function generator	1	Matrix/ MFG-8216A	0.3-3 M Hz	$\leq$ 1%
Gear pump	2	Clark Sol./ MG213XPS17	SS, 13mm PEEK gears, 160-180 LPH	-
Graham condenser	1	Lab Supply Aus./ CC 22	450 cm^2; eff. length 0.3 m	-
Hand valves	6	Actrol	⅜" BSP	-
Isothermal bath	1	Thermo Haake/ DC30	230V, 50 Hz A/C 17 LPM max -50°C - 200°C	+/- 0.01 ^{o}C
Magnetic drive motor for gear pumps	2	Clark Sol./ Lafert motor 6910470	230V, 50Hz A/C	-
Needle valves	3	Clark Sol./ CVSB3S	brass,1/8" FNPT, S-T-Std. 0-3.55 LPM max	-
Oscilloscope	1	RIGOL/ DS4014	100MHz band/ 4 GSa/s real-time	-
Pipe fittings	-	steel/ brass	⅜" or ¼" BSP	-
Pressure relief valve	1	NEFA/ PTR1000	Pressure limiting 600 k Pa	-
Scanning electron microscope	1	ZEISS/ EVO Neon 40 EsB	5 kV EHT	-
Solid state relay	2	Altronics/ RSR2ND-A24003	4-32V in/ 3A-240VAC out SPST	-
Solenoid Valve	2	Clark Sol./ 1393BS083T	2-way N/C and 2-way N/O	-
Surface roughness measurement	1	MITUTOYO/ SURFTEST SJ-201R/ 178-955-4A	x-axis: 12.5mm z-axis: -200- $+150\mu$m	+/- 5%

Table 4.3 *continued....*

Description	Quantity	Manufacturer / Model and	Specifications	Uncertainty
Thermocouples	15	Omega	K-type −200 - 1250°C	1.1^{o}C or 0.4%
Thermocouple calibration	1	Armfield/ TH1	PT100 with 5point NAMAS calibration certificate	-
Thermocouple data logger module	2	Pico Technology/ TC-08	8 channels 10 Hz data rate -270 ^{o}C - 1820 ^{o}C	+/- 0.2 % or +/- 0.5 ^{o}C
Thermostat controlled immersion heater	1	Helios/ TXM/30	2" boss×305 mm 3000 W 0 - 150 ^{o}C	+/- 2 ^{o}C for controls
Tubing	-	copper and silicone rubber	⅜" lines	-

4.2.3   Characteristics of Heater/ Impingement Surface

The characteristics of the heat transfer surface have been reported in the literature [148-151] to significantly influence the characteristics of associated heat transfer, particularly during boiling. Kandlikar and Spiesman [152] showed that the effect of roughness was very complex but the heat transfer performance particularly depends on the number of nucleation site cavities and the cavity size distributions and not just the average roughness. However, considering surfaces with sufficiently statistically homogeneous roughness, several studies have characterised the associated boiling heat transfer during both pool as well as flow boiling conditions based on the average Roughness index (*Ra*). Cardenas and Narayanan [153] also showed from experiments on submerged jet impingement boiling with water as working fluid, that the surface roughness also significantly influences the magnitude of critical heat flux irrespective of the jet Reynolds number for any given operating condition.

In the present research, the surface was prepared by hand polishing the machined impingement surface of the heater block using successively finer emery sheets (grit size # 320, # 400 and # 800). To the best possible extent it was ensured that the motion of the emery sheet relative to the heater surface was always unidirectional along the *x*-axis (see Fig. 4.11). Subsequent to polishing, the surface

was cleaned with acetone and isopropyl alcohol before conducting the single phase and boiling experiments. The impingement heater surface was further aged with FC-72 (or de-ionized water for single phase experiments) at room temperature for over 24 hours and flushed with the same fluid for 1-1.5 hours before recording data for each experimental run.

As the heater block is too large to fit into surface roughness measuring and imaging systems, a sample was prepared using an identical technique employed for the heater block. Figure 4.11 shows the surface roughness measured using a surface roughness tester (SURFTEST SJ-201R, MITUTOYO) for three typical samples. As
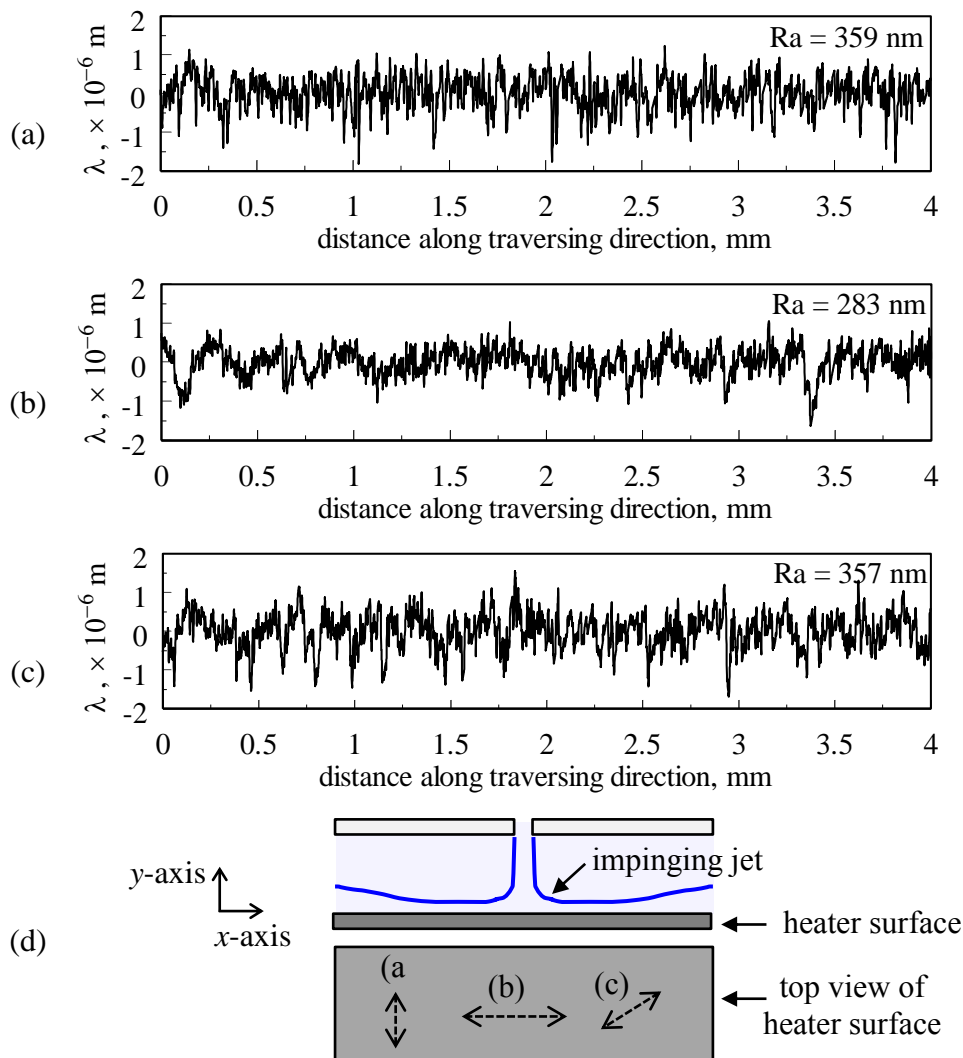
Figure 4.11: (a,b,c) Measured surface roughness profile for three test cases, and (d) indicates the direction with reference to the heater surface in which the measurement sensor was traversed; the quantity λ is the local roughness height/ depth on the sample surface

(a)

(b)
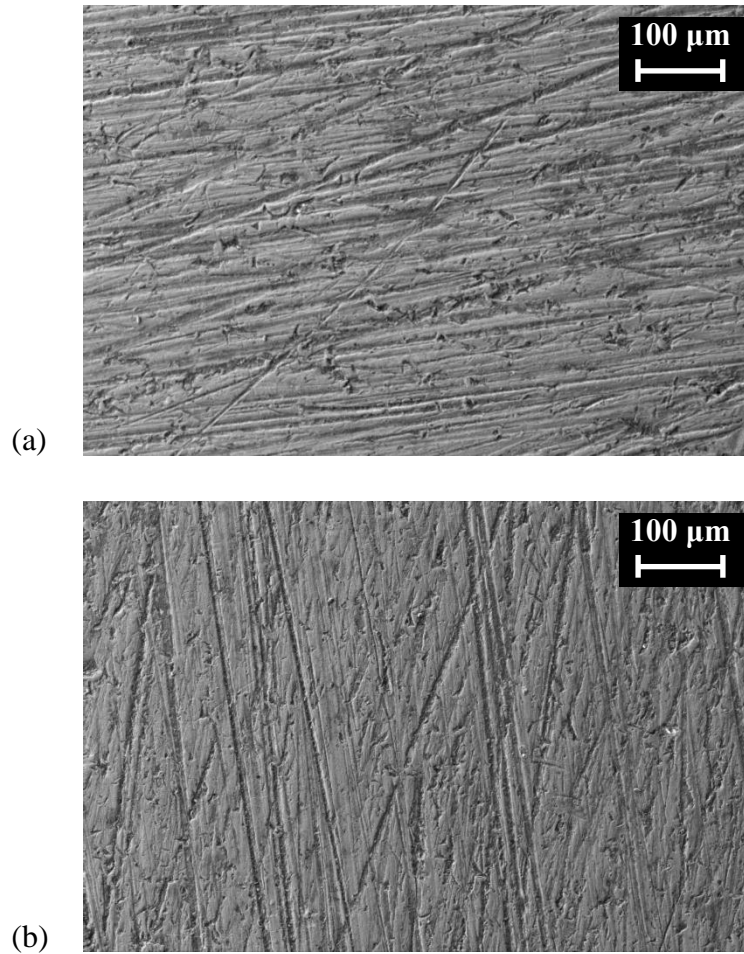
Figure 4.12: Scanning Electron Microscope (SEM) images of the surface texture on the sample alloy-6061 prepared in the same way as the heater block at two representative locations; working distance = 4.7 mm, accelerating voltage = 5 kV, aperture size = 30 μm

mentioned in the earlier paragraph, the heater surface was polished unidirectionally and hence the roughness measured in any one direction would not be representative of the overall surface roughness. Hence the roughness along, transverse and diagonal to polishing directions were measured and averaged to obtain the average roughness. As expected, it is seen from comparison of Fig. 4.11 (b) with Fig. 4.11 (a) and Fig. 4.11 (c) that the roughness's peak-valley distance for the measurements along the polishing directions are clearly lower than those in the transverse and diagonal directions. The statistics of the surface roughness thus measured from the sample pieces, which are indicative of the roughness on the heater surface are listed in Table-4.4. The surface texture on the samples used for surface roughness measurement was photographed using a scanning electron microscope (Neon-40 EsB

FIB-SEM, Zeiss), and the images at two typical locations are illustrated in Fig. 4.12. The parallel streaks (or scratches) on the surface indicate the unidirectional polishing described in the earlier paragraph.

Table 4.4: Statistics of surface roughness

	Unit	Direction as per Fig. 4.11		
		(a)	(b)	(c)
Number of tests	-	2	2	2
Length of sample measured	mm	4	4	4
Number of data points	-	8000	8000	8000
Average roughness (Ra)	μm	0.359	0.283	0.357
RMS roughness	μm	0.426	0.361	0.455
Maximum height of profile	μm	1.237	1.059	1.554
Maximum depth of profile	μm	1.811	1.625	1.691
Maximum profile peak	μm	3.048	2.684	3.245

4.2.4 Data Extraction, Calibration and Uncertainty Analysis

Using the experimental methodology described in the preceding section, the surface texture, the jet fluid quality, jet flow rate, jet temperature, jet pulsation amplitude, jet pulsation frequency, applied power (heat) and temperatures at the twelve locations in the heater block are measured. The parameters calculated from these measured quantities are the jet velocity, jet Reynolds number, jet subcooling (for boiling experiments), pulsation frequency, pulsation amplitude (%), average surface heat flux, average surface temperature and average temperature at different locations beneath the impingement surface.

The average surface heat flux is obtained by considering steady state (or oscillating-steady state in the case of pulsed jet impingement) one-dimensional conduction along the direction perpendicular to the impingement surface in the heater block (along the 3×columns of 4×thermocouples each). As mentioned earlier, the first row of thermocouples is 3 mm below the impingement surface, and hence, the surface temperature is evaluated by extrapolation of the one-dimensional temperature distribution to the impingement surface location. It is to be noted that the surface temperature is not measured directly as the placement of thermocouples on
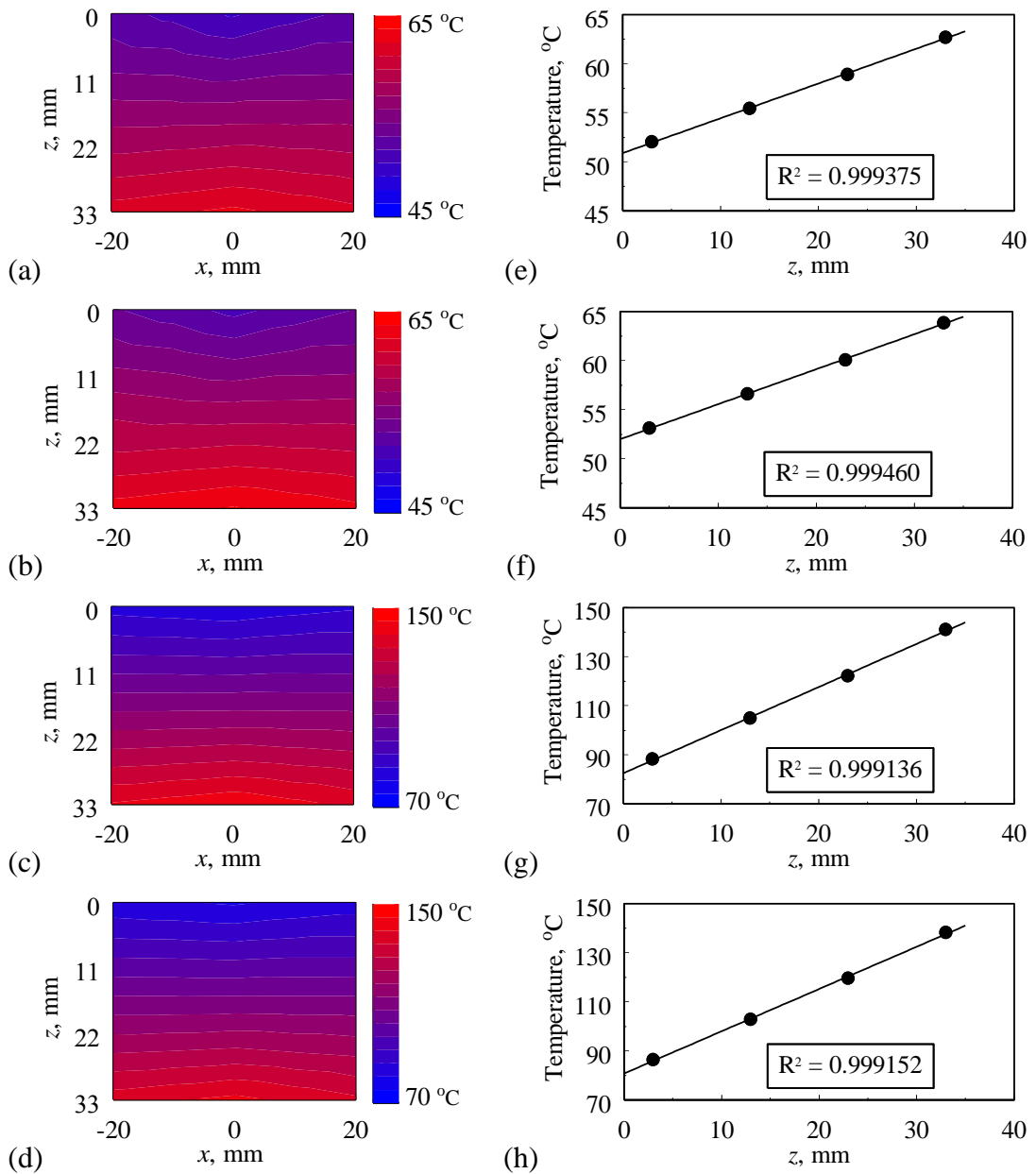
Figure	q_T W/cm^2	T_N $^\circ$C	Re -	amplitude %	frequency Hz	Fluid	Boiling/ Single phase
(a) and (e)	4.397	39.76	3399.7	steady	steady	DI water	single phase
(b) and (f)	4.432	39.85	3645.3	50	0.5	DI water	single phase
(c) and (g)	33.986	39.26	9046.4	steady	steady	FC-72	boiling
(d) and (h)	33.238	39.00	3390.3	63	0.5	FC-72	boiling

Figure 4.13: Typical temperature contours and reconstructed 1D temperature distribution in the heater block during steady state and pulsating jet impingement experiments with and without boiling

the surface would alter the surface texture which would significantly influence the heat transfer characteristics, particular during the boiling experiments. The thermal

conductivity of the aluminium alloys-5083 and 6061 used for the estimation of average surface heat flux was based on the mean temperature of the one-dimensional domain. The values of temperatures used for the calculation of heat flux were evaluated as the average over the last two minutes during steady state (or oscillating-steady state in the case of pulsed jet impingement) for each experimental run.

Figure 4.13 (a-d) shows the typical contours of temperature in the section of the heater block from where the average surface heat flux is deduced, and Figs. 4.13 (e-h) show the reconstructed one-dimensional temperature distribution in the domain. As the temperature just beneath the impingement stagnation zone is expected to be slightly lower than the regions farther downstream, a linear averaging of the temperatures at plane (indicated as z) beneath the impingement surface would result in overpredicted surface temperatures due to bias introduced by the two thermocouples used in the downstream locations (in every plane). Hence, for a more realistic estimate of the surface temperature and the heat flux, the average temperature at every plane at a given plane at a distance z beneath the heater block is averaged by using polynomial curve fit for the three temperatures in every plane and assuming that the temperature gradient at the extremities of the heater block (represented by x = -20 mm and 20 mm) are zero. This approximation for the temperature gradient at the boundaries is also validated by the fact that the PEEK that surrounds the heater block has a much lower thermal conductivity ($\approx$ 0.25 W/m-K) than the aluminium alloys. The polynomial curve fit for each location z beneath the impingement surface is given as:

$$T\left(0 \leq x \leq 0.02 , z\right) = a\,x^4 + b\,x^2 + c \tag{4.71}$$

where, (x = 0, z) indicates the locus of locations aligned with the centerline of jet. In Eq. (4.71) x and z are are represented in meters and T is represented in $^{\mathrm{o}}$C. The temperature profile for -0.02 $\leq$ x $\leq$ 0 is identical due to symmetry. As indicated earlier, the boundary conditions at the heater-PEEK interface are given as

$$\left.\frac{\partial T}{\partial x}\right|_{x=-0.02,\,0.02} = 0 \tag{4.72}$$

The average temperature at any location z is thus obtained by integration of the polynomial temperature profile over the length of the heater in the x-direction as:

$$T_{\text{avg}}(z) = \frac{1}{0.02} \int\limits_{x=0}^{x=0.02} T(x,z)\, dx = \frac{a}{5} \times 0.02^4 + \frac{b}{3} \times 0.02^2 + c \tag{4.73}$$

where the polynomial coefficients a, b and c were evaluated as

$$a = \frac{250000}{7}\left[399 T_{x=0} - 200\left(T_{x=-0.01} + T_{x=0.01}\right)\right]$$

$$b = \frac{80000}{7}\left(T_{x=-0.01} + T_{x=0.01}\right) - 11425 T_{x=0} \tag{4.74}$$

$$c = T_{x=0}$$

It is seen from Figs. 4.13 (e-h) that average temperatures obtained by the above technique follow the one-dimensional temperature profile along the z-direction, thus validating the assumptions herein. It was also observed that the R-squared for the linear one-dimensional curve fit along z-direction for all the data obtained in the experiments carried out for the present studies was greater than 0.999, as shown in the examples in Fig. 4.13.

The surface-averaged total surface heat flux is thus evaluated from the aforementioned validated assumption of 1D conduction assumption as

$$q_{\text{T}} = k_{\text{w}} \frac{d}{d z} T_{\text{avg}}(z) \tag{4.75}$$

In the preceding equation, k_{w} is the thermal conductivity of the heater block based on the average temperature of the 1D domain. As outlined earlier, the average impingement surface temperature is evaluated by the extrapolation of this linear temperature profile to $z = 0$ from

$$T_{\text{w}} = T(z) - q_{\text{T}} \frac{z}{k_{\text{w}}} \tag{4.76}$$

While the results of average heat fluxes from the experiments on boiling jet impingement heat transfer are discussed in terms of their dimensional units under in the following chapters of this thesis, the corresponding results for single phase experiments are expressed in terms of the non-dimensional Nusselt numbers. The Nusselt number is this defined as

$$Nu_{\text{avg}} = h_{\text{C}}\, B / k_{\text{l}} \tag{4.77}$$

where B is the hydraulic diameter of the slot nozzle ($2 \times w_{\text{N}}$) and the heat transfer coefficient is given as

$$h_C = q_T / (T_w - T_N) \tag{4.78}$$

While the Reynolds number for the discussion of boiling experimental results are calculated with fluid properties based on the conditions at jet inlet, the fluid properties used for the calculation of Nusselt number and Reynolds numbers for single phase experiments are based on the bulk temperature defined as

$$T_{bulk} = (T_w + T_N) / 2 \tag{4.79}$$
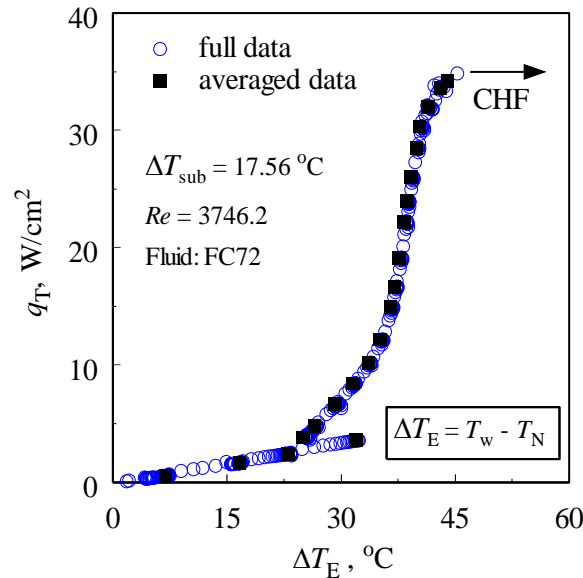
Figure 4.14: Comparison of the raw data set collected throughout the course of the experiment with the averaged data (over the last 120 seconds of the steady state process) for a representative steady jet impingement boiling case

For steady state experiments using both water and FC-72 the temperatures are recorded at intervals of one second using a thermocouple data logger (TC-08, PICO Tech.). For pulsating jet impingement experiments, the measured temperatures are recorded at 0.1 to 0.2 second intervals to ensure at least data 10 points for each cycle of jet pulsations. On an average, any prescribed power increment took about 30-75 minutes to reach sufficiently steady state (or oscillating steady state during pulsed jet impingement). Boiling jet impingement experiments are carried out for the full nucleate boiling regime of the boiling curve including single phase convection, partial nucleate boiling and fully developed boiling until critical heat flux (CHF) by controlling the heat input, for any given set of operating conditions. The heat inputs are incrementally changed from zero to CHF ensuring at least 20 equally distributed

Table 4.5: Uncertainty estimates for area averaged quantities

Single phase experiments with de-ionized water and aluminium alloy-5083 heater block		
Variable	Maximum ($\pm$)	Average ($\pm$)
T_N	0.3 ^{o}C	0.3 ^{o}C
Re	3.03 %	3.03 %
T_S	0.90 %	0.76 %
T_S-T_N (^{o}C)	6.88 %	3.93 %
q_T	7.84 %	6.52 %
Nu_{avg}	9.52 %	7.38 %
A	5.8 %	4.3 %
f	0.8 %	0.6 %

Boiling experiments with FC-72 and aluminium alloy-6061 heater block		
Variable	Maximum ($\pm$)	Average ($\pm$)
T_N	0.3 ^{o}C	0.3 ^{o}C
Re	3.03 %	3.03 %
T_S	0.71 %	0.62 %
T_S-T_N (^{o}C)	4.76 %	1.81 %
A	4.7 %	3.5 %
f	0.8 %	0.6 %
Uncertainty in Heat Flux (q_T)		
1 W/cm^2 $\rightarrow$ 5 W/cm^2	33.2 % $\rightarrow$ 8.0 %	
5 W/cm^2 $\rightarrow$ 10 W/cm^2	8.0 % $\rightarrow$ 4.5 %	
10 W/cm^2 $\rightarrow$ 15 W/cm^2	4.5 % $\rightarrow$ 3.1 %	
15 W/cm^2 $\rightarrow$ 20 W/cm^2	3.1 % $\rightarrow$ 2.5 %	
20 W/cm^2 $\rightarrow$ 25 W/cm^2	2.5 % $\rightarrow$ 2.2 %	
25 W/cm^2 $\rightarrow$ 30 W/cm^2	2.2 % $\rightarrow$ 1.9 %	
30 W/cm^2 $\rightarrow$ 35 W/cm^2	1.9 % $\rightarrow$ 1.7 %	
35 W/cm^2 $\rightarrow$ 40 W/cm^2	1.7% $\rightarrow$ 1.6 %	

steady state (or oscillating steady state) data points are experimentally determined for each boiling curve. It was interesting to note that as the power increments to the heater was small, all the data collected during the full course of the boiling experiments for each operating condition followed the general trend of the boiling curve; an example is shown in Fig. 4.14. Considering it useful to represent a continuous boiling curve instead of the intermediate averaged values, all the boiling

curves shown following sections discussing the results were plotted for the full data set (corrected with any bias errors determined from instrument calibration).

The thermocouples used for measurement of the temperature of the inlet jet as well as at the various locations in the heater block were calibrated in the range 20-100 ^{o}C using an industrial grade platinum resistance thermometer (PT100 with five-point NAMAS calibration certificate), in a stirred pool of water. It was found that the thermocouples used in the present experimental facility had an average positive bias error of 0.3463 ^{o}C as compared to the reference thermometer. The flow meter used for the measurement instantaneous flow rate was factory calibrated for the range 0.5 to 4 LPM which encompasses the flow rates used in the present studies. Following Kline and McKlintock [154], and Moffat [155], an uncertainty analysis was carried out for the calculated parameters. The individual maximum and average uncertainty estimates hence evaluated are shown in Table-4.5. The uncertainty in the calculated Reynolds number, temperatures of the surface and inlet jet, heat flux, Nusselt number (for single phase experiments with water), pulsation amplitude and frequencies were determined based on thermocouple bias and precision errors, flow rate precision error, temperature difference linear curve fit error including error in predicted slope and intercepts, distance (spacing and geometric) errors, and oscilloscope noise. From a data repeatability check, the critical heat fluxes during boiling experiments were found to vary upto 3.5 %, and the Nusselt numbers during single phase experiments were found to vary upto 5 %.

CHAPTER 5

RESULTS AND DISCUSSION

This chapter discusses the results obtained from the computational and experimental studies on steady state and pulsating, single phase and boiling slot jet impingement heat transfer in the submerged and confined configurations. The focus of the discussion on the steady state results would be on relative contributions of the fundamental heat transfer mechanisms resulting in the overall heat transfer from the heated impingement surface for various combinations of controlling parameters. As outlined in the preceding chapter (Section-4.1.1), the total heat transfer during laminar jet impingement at high surface temperature and emissivity is partitioned into convective and radiative heat fluxes where the fluid used is air- assumed to be a radiatively non-participating media for the range of operating conditions considered for the present research. During jet impingement heat transfer with phase change, the total heat flux from the surface over which boiling occurs is partitioned into convective, quenching and evaporative heat fluxes following the RPI wall-boiling model, as described in Section-4.1.2. To evaluate the effectiveness of jet pulsations on single phase impingement heat transfer, base line steady state experiments were carried out, while detailed parametric analysis of the controlling parameters on single phase impinging liquid jets are not in the scope of this work. However, a detailed review of the literature on the subject has been provided in Section-2.2.1. Subsequently, the results from the experimental investigation of pulsating impinging jet boiling will be described. It is pointed out that while there is substantial literature on steady state jet impingement boiling as described in Section-2.2.2, there is no reported literature on the investigation of jet pulsations on impingement boiling.

The fluid properties considered for the calculation of dimensionless parameters, computational analysis or discussion of results in the following sections of this chapter are according to Appendix A-4, unless otherwise stated in the text.

5.1   COMPUTATIONAL STUDY OF CONFINED STEADY LAMINAR AIR JET IMPINGEMENT HEAT TRANSFER ACCOUNTING FOR SURFACE RADIATION AND BUOYANCY

The results and discussion presented hereunder pertain to the analysis on the geometry illustrated in Fig. 4.2 and Fig. 4.3 in Section 4.1. The dimensionless parametric analysis carried out for combinations of jet Reynolds number (Re), dimensionless standoff distance (H), radiation-flow interaction parameter ($N_{RF,d}$), Richardson number (Ri_d) and surface-emissivity (ε), on the convective, radiative and total Nusselt numbers, are presented for the controlling parameters in the range $100 \leq Re_d \leq 900$, $1 \leq H \leq 8$, $0.1 \leq N_{RF,d} \leq 2$, $0.01 \leq Ri_d \leq 10$ and $0.05 \leq \varepsilon \leq 0.85$. It is pointed out that the exhaustive ranges of the non-dimensional parameters also include relatively large values of ΔT (about 80-120 ^{o}C) for some combinations of physical quantities encapsulated in the relevant non-dimensional parameters, but the influence temperature difference on the thermo-physical properties is not modeled in the present study. From a detailed computational analysis using air in a similar geometric configuration, Heiningen et al. [30] established that the inclusion of the effect of temperature dependant fluid properties in the analysis resulted in insignificant difference in the predicted thermo-hydraulics as compared to that obtained using constant properties upto surface temperatures of 170 ^{o}C (or $\Delta T = T_w$-$T_N = 150$ ^{o}C). The range for ε is based on the spectrum of diffuse gray surfaces, that fall between polished wall ($\varepsilon = 0.05$) and black paint ($\varepsilon = 0.85$), while the ranges for other parameters are based on realistic values of the dimensional parameters involved, for problems of the type considered in the present research. All the results for streamlines, isotherms and Nusselt numbers presented in the following sections are given for one side of the centerline of jet alone, exploiting the symmetry.

5.1.1   Grid Sensitivity Analysis and Validation

A rigorous grid sensitivity analysis is carried out with 48 different structured non-uniform rectangular mesh configurations, with $N_X \times N_Y$ varying from 40×140 to 120×240, for a given set of other controlling parameters, for each value of $H = 1, 2, 4$ and 8. After careful observation of the variations in distribution and magnitudes of local Nu_C and Nu_R on the heater, over the range of mesh configurations, it is found
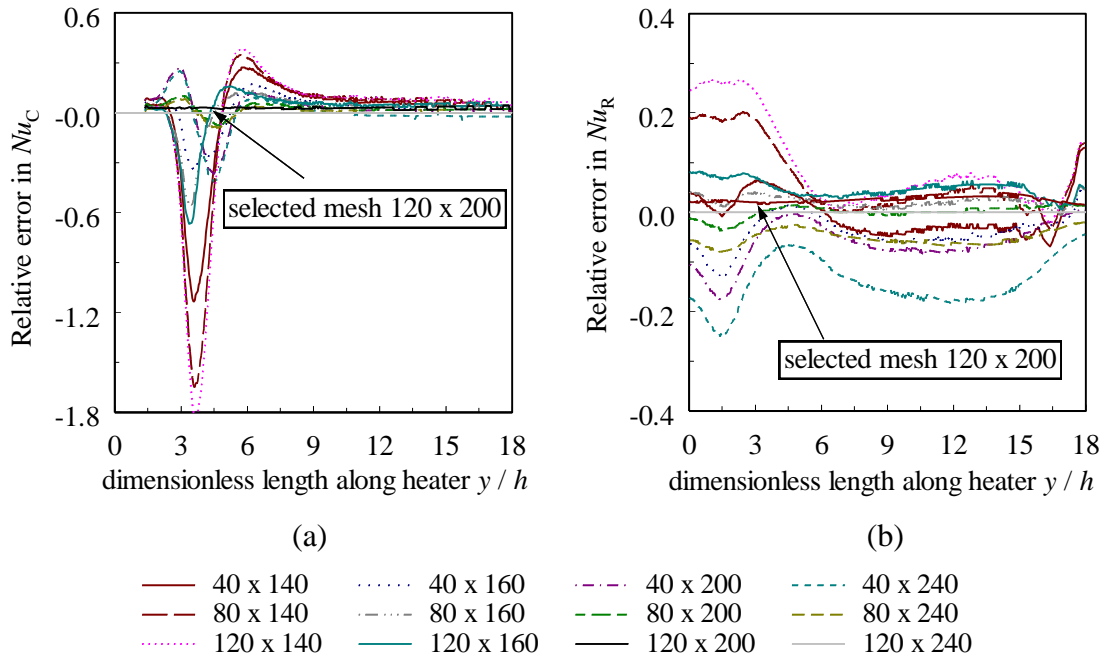
Figure 5.1: Relative error in the convective and radiative Nusselt numbers with
change in mesh size as compared to that obtained for the finest 120×240
mesh configuration; the data is for a typical case $H = 8$, $Re_d = 300$, $Ri_d = 0.01$,
$N_{RF,d} = 0.5$ and $\varepsilon = 0.5$
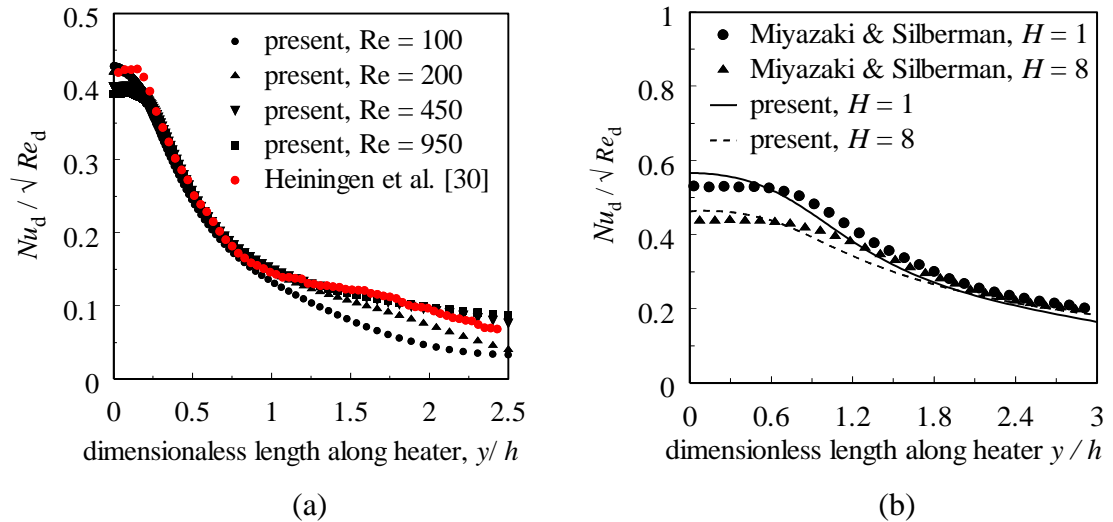
Figure 5.2: Comparison of predicted Nu_C for forced convective jet impingement
neglecting the effects of surface radiation against (a) Heiningen et al. [30] for
$H = 4$, and (b) Miyazaki and Silberman [33] for $Re_d = 500$

that 80×160, 80×200, 80×200 and 120×200 mesh sizes are the best compromise
between accuracy (maximum error less than 2% as compared to 120×240) and
computational time for values of $H = 1$, 2, 4 and 8 respectively. A typical variation in

the predicted deviances for the convective and radiative Nusselt numbers with change in mesh size is illustrated in Fig. 5.1 for $H = 8$, $Re_d = 300$, $Ri_d = 0.01$, $N_{RF,d} = 0.5$, $\varepsilon = 0.5$. Case-by-case grid independence graphs are not presented here for brevity. The typical mesh configuration is illustrated in Fig. 4.2 of Section 4.1.

(a) $Re_d = 100$

(d) $Re_d = 100$

(b) $Re_d = 400$

(e) $Re_d = 400$

(c) $Re_d = 900$

(f) $Re_d = 900$

Nu_C for $\varepsilon = 0.05$ Nu_C / Nu_T for $\varepsilon = 0.05$
Nu_R for $\varepsilon = 0.05$ Nu_R / Nu_T for $\varepsilon = 0.05$
Nu_C for $\varepsilon = 0.85$ Nu_C / Nu_T for $\varepsilon = 0.85$
Nu_R for $\varepsilon = 0.85$ Nu_R / Nu_T for $\varepsilon = 0.85$
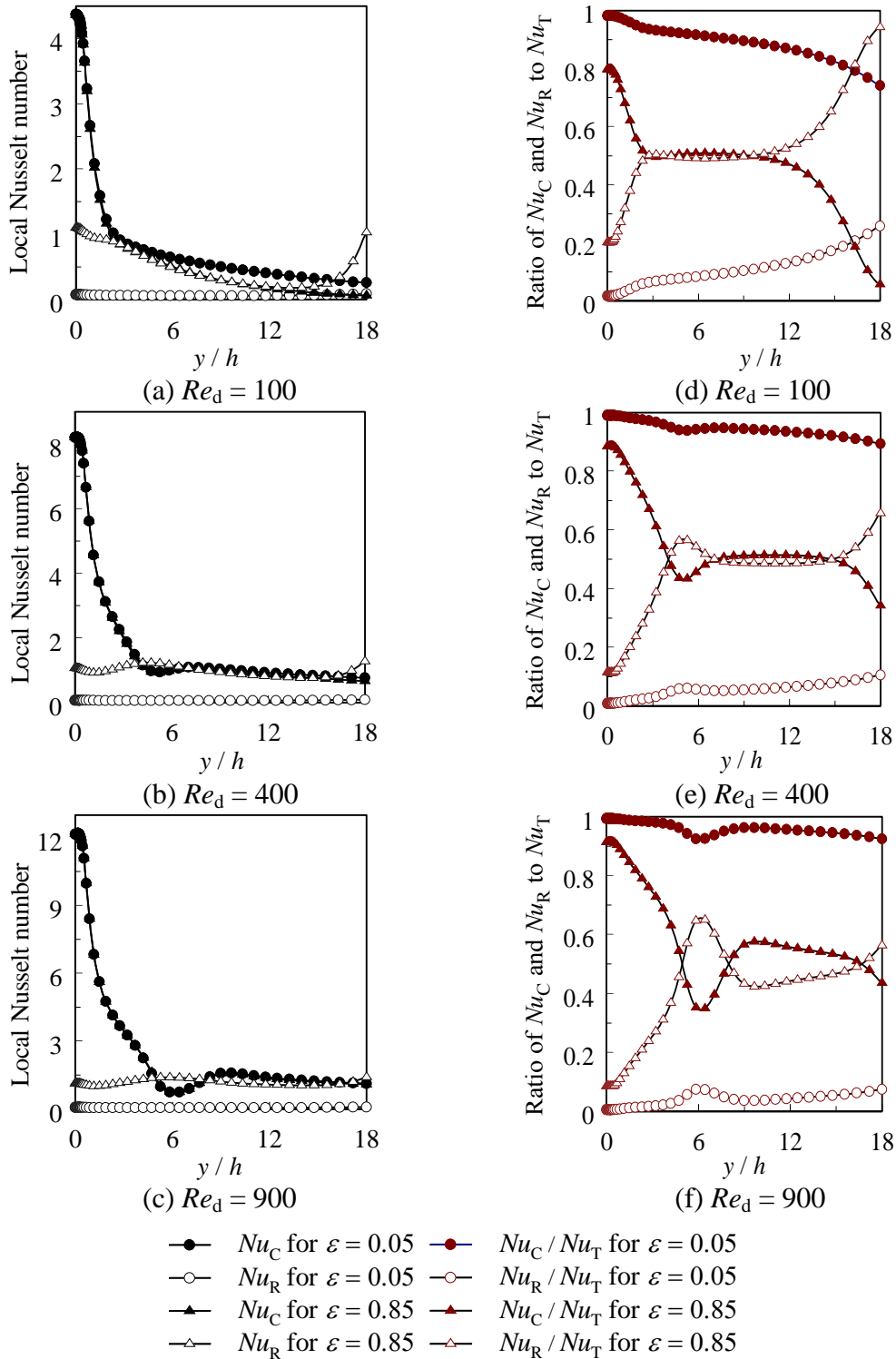
Figure 5.3: Comparison of the distribution of Nu_C, Nu_R, Nu_C/Nu_T and Nu_R/Nu_T along the heater between $\varepsilon = 0.05$ and 0.85 for $H = 2$, $Ri_d = 1$ and $N_{RF,d} = 2$

Following the grid sensitivity analysis, the computational code is validated by comparing the distribution of local Nusselt numbers calculated by the present methodology during forced convective heat transfer in the absence of radiative effects (in lieu of published data including effects of surface radiation) against Heiningen et al. [30] and Miyazaki and Silberman [33]. Figure 5.2 (a) shows the comparison against Heiningen et al. [30] for a given standoff distance $H = 4$ and three different Reynolds numbers $Re_d = 100, 200, 450$ and 950 (for which the data is expected to collapse into a single curve when scaled by $Re^{1/2}$), and Figure 5.2 (b) illustrates the comparison against Miyazaki and Silberman [33] for a given Reynolds numbers $Re_d = 500$, and two different dimensionless standoff distances of $H = 1$ and 8. It is seen from the figures that the predicted values are in good agreement with the results available in the literature, thereby validating the present numerical model.
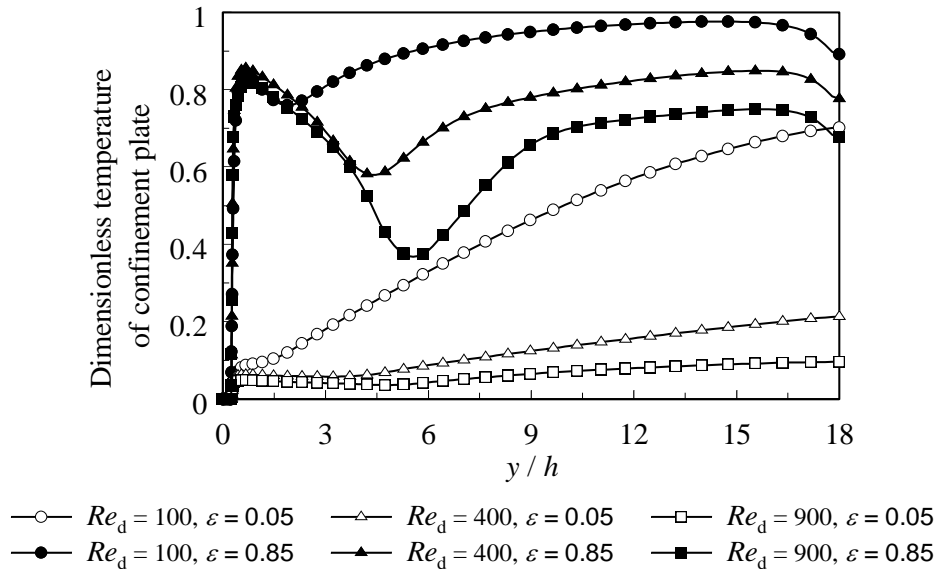
Figure 5.4: Distribution of normalized temperature on the nozzle-outlet and confinement-plate for $H = 2$, $Ri_d = 1$, $N_{RF,d} = 2$

5.1.2 Relative Contributions of Convection and Radiation to the Total Heat Transfer

Figures 5.3 (a-c) show the distributions of convective Nusselt number (Nu_C) and radiative Nusselt number (Nu_R) along the heater for $H = 2$, $N_{RF,d} = 2$, $Ri_d = 1$, $Re_d = 100, 400$ and 800 and for $\varepsilon = 0.05$ and 0.85. Figures 5.3 (d-f) show the corresponding distributions of Nu_C/Nu_T and Nu_R/Nu_T along the heater. It is seen from the figures that the magnitude of local radiative Nusselt number increases

substantially with change in the surface-emissivity from $\varepsilon = 0.05$ to 0.85 for given values of other controlling parameters. The contribution of radiation to the overall heat transfer is nearly negligible for $\varepsilon = 0.05$, while it is found to be as large as about 23 % of the total heat transfer in the stagnation region and over 50% in the regions downstream for $\varepsilon = 0.85$. With an increase in ε from 0.05 to 0.85, the emissive power of the heater increases. However, as the confinement plate is an adiabatic gray surface with the same emissivity ε, the surface temperature of the confinement-plate also increases, as can be seen from Fig. 5.4. The presence of the confinement plate, in a way, suppresses the net radiation from the heater due to the decrease in the effective temperature differential available for radiation exchange, which would have otherwise been relatively larger in the absence of the confinement-plate. However, the net radiative heat transfer between the heater and the outlets (that are radiatively black bodies at a lower temperature) increase substantially with a prescribed increase in ε. Hence, the local as well as net radiative Nusselt numbers increase with an increase in ε. However, the relatively larger temperature of the confinement-plate for $\varepsilon = 0.85$ as compared to $\varepsilon = 0.05$ heats the fluid region near the confinement-plate, thereby thickening the thermal boundary layer near the confinement plate, for given values of other controlling parameters. From comparison of the dotted (....... $\varepsilon = 0.05$) and straight (━━ $\varepsilon = 0.85$) streamline profiles shown in Figs. 5.5 (a-c), it is seen that flow field (or streamlines) are nearly unaffected in the regions near the confinement-plate, and hence the change in thermal boundary layer thickness in those regions is entirely due to the temperatures rise on the confinement-plate due to increased radiation. As the thermal boundary layer on the heater is thicker for $Re_d = 100$ as compared to the $Re_d = 400$ and 900 irrespective of the values of ε, the increase in the temperature of the confinement-plate due to an increase in ε, adversely affects the temperature gradient on the heater, in some cases by making the flow thermally fully developed in the domain, thereby reducing Nu_C, especially in the wall-jet region. From Figs. 5.5 (d-f), it is seen that the density of the isotherms in the regions near the heater decreases with a change in ε from 0.05 to 0.85. While this effect is large for $Re_d = 100$, it is found to be lower for relatively larger values of Re_d, to the extent that it is almost negligible for $Re_d = 900$. This change in the density of isotherms in the region near the heater is manifested as a decrease in the temperature gradient on the wall. Hence, a slight decrease in the magnitude of convective Nusselt number is seen in the regions downstream of the stagnation point for $Re_d = 100$.
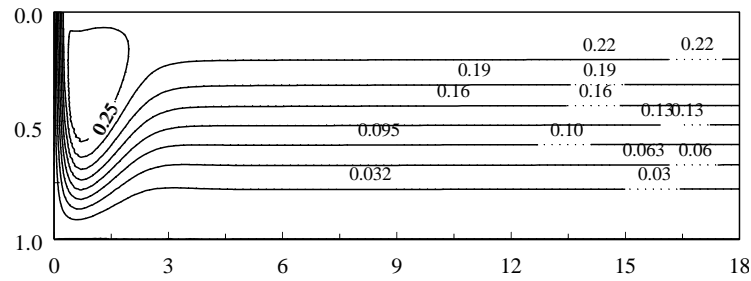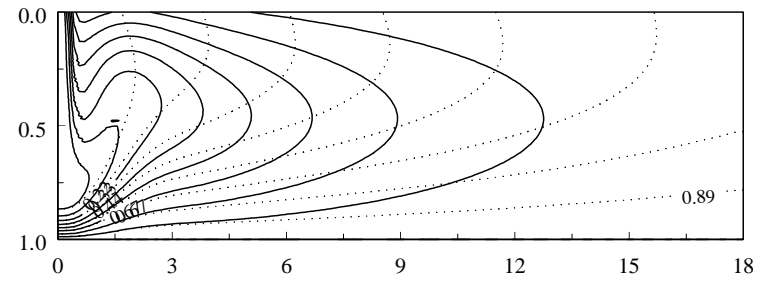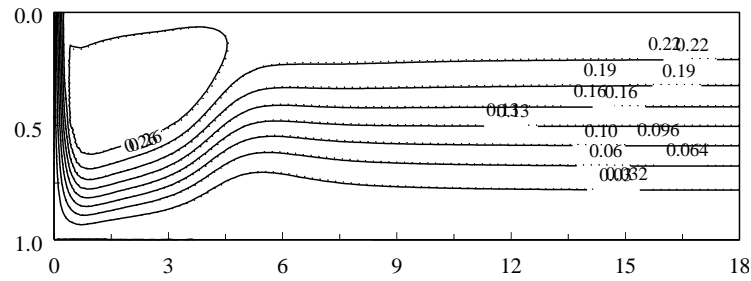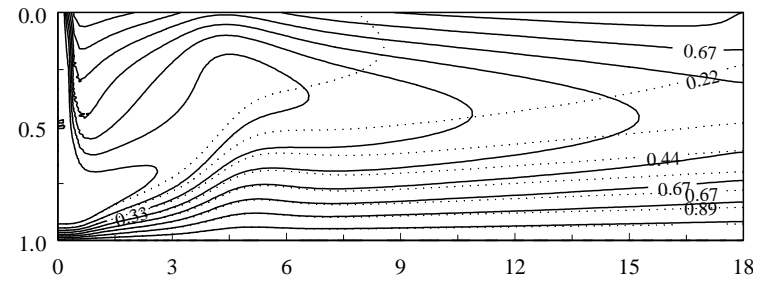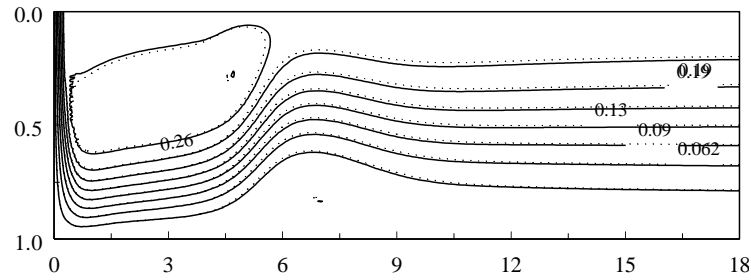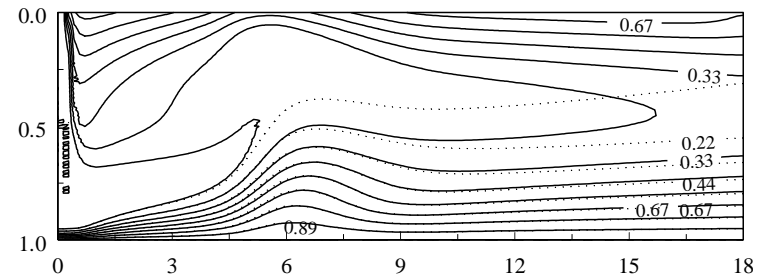
Figure 5.5: Comparison of (a-c) contours of streamlines and (d-f) normalized isotherms between $\varepsilon = 0.05$ and 0.85,

for $H = 2$, $Ri_d = 1$ and $N_{RF,d} = 2$ (....... $\varepsilon = 0.05$; —— $\varepsilon = 0.85$)

(a) $Ri_d = 0.01$, $N_{RF,d} = 0.1$

(b) $Ri_d = 0.01$, $N_{RF,d} = 0.8$

(c) $Ri_d = 0.01$, $N_{RF,d} = 2$

(d) $Ri_d = 10$, $N_{RF,d} = 0.1$

(e) $Ri_d = 10$, $N_{RF,d} = 0.8$

(f) $Ri_d = 10$, $N_{RF,d} = 2$
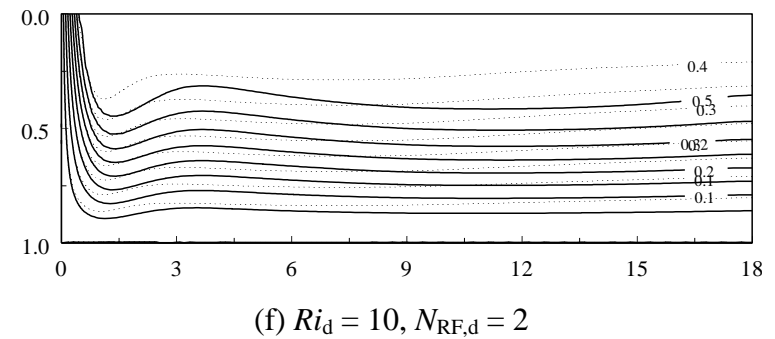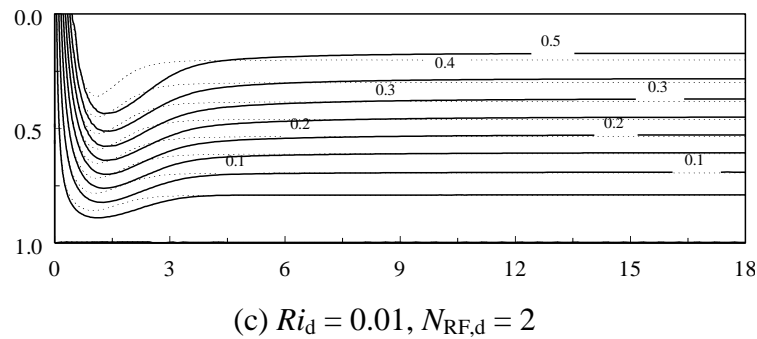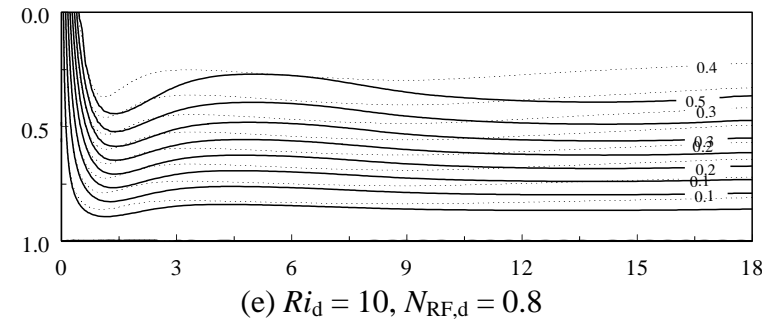
Figure 5.6: Comparison of streamlines between $Ri_d = 0.01$ and 10, for $\varepsilon = 0.85$ and $H = 1$; (....... $Re_d = 100$; ▬ $Re_d = 400$)

As larger values of Re_d can be interpreted as larger fluid velocities *ceteris paribus*, the heat transfer due to convection from confinement-plate is relatively larger, thereby resulting in lower temperatures on the confinement-plate in the regions downstream of the nozzle-outlet. The increase in the temperature differential between the heater and the confinement-plate results in the relatively larger potential for radiative heat transfer from the heater for $\varepsilon = 0.85$ as compared to $\varepsilon = 0.05$, (for a prescribed geometry and other controlling parameters), due to which, the magnitudes of local radiative Nusselt number in the wall-jet region are consistently larger for larger values of Re_d, as seen in the Figs.5.3 (a-c). It is seen from Figs. 5.3 (d-f) that, with a change in Reynolds number from $Re_d = 100$ to 900 (covering an exhaustive range of Reynolds numbers for laminar jet impingement [28,29,43]), the contribution of radiation to total heat transfer at the stagnation point decreases from about 23% to about 10%, for the given set of other controlling parameters. A similar qualitative trend is also observed in the regions over the heater, farther downstream. This is because, although the magnitude of local radiative Nusselt number increases with an increase in Re_d, the convective heat transfer from the surface of the heater also increases with increase in Re_d, seemingly at a relatively larger rate, thereby resulting in the percentage contribution of radiation to overall heat transfer from the impingement-surface decrease for any given increase in Re_d, as shown in Figs. 5.3 (d-f). It is also notable from Figs. 5.3 (a-c), the value of Nu_R increases near the outlet of the domain, due to the fact that the outlet is assumed to be a radiative black body at ambient temperature (same as the temperature of the jet at nozzle-outlet), which is a reasonable assumption for problems of the type studied in the present research [38,40].

To study the extent of influence of surface radiation, all further results discussed in the following sections are with the assumption that the surfaces of the heater and confinement-plate are both coated with black-paint ($\varepsilon = 0.85$).

Figures 5.6 (a-c) and Figs. 5.6 (d-f) show the contours of streamlines for $Ri_d = 0.01$ and 10 respectively, for $H = 1$, $\varepsilon = 0.85$, $Re_d = 100$ and 400, and $N_{RF,d} = 0.1$, 0.8 and 2. The corresponding contours of isotherms for the set of parameters are illustrated in Figs. 5.7 (a-c) and Figs. 5.7 (d-f). It is seen from Figs. 5.6 (a-f) that while the change in Ri_d from 0.01 to 10 has negligible effect on the flow field in the
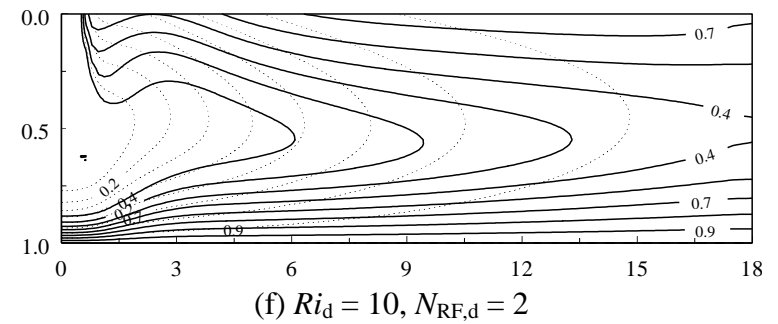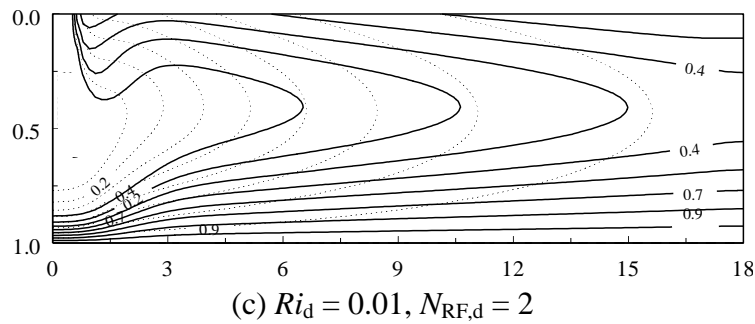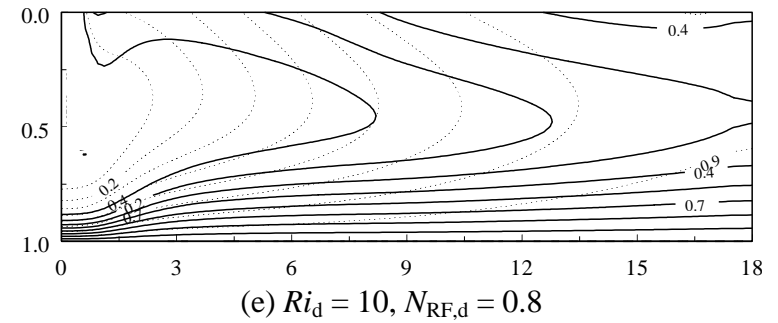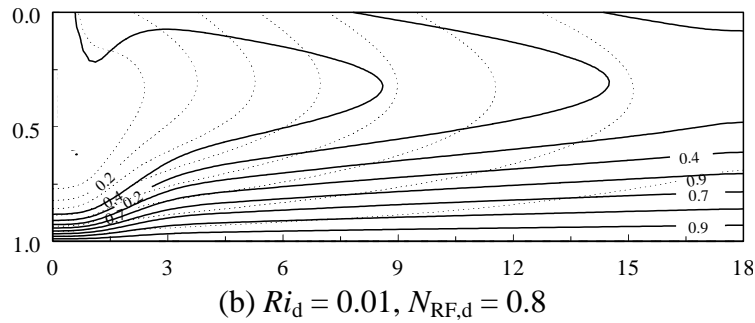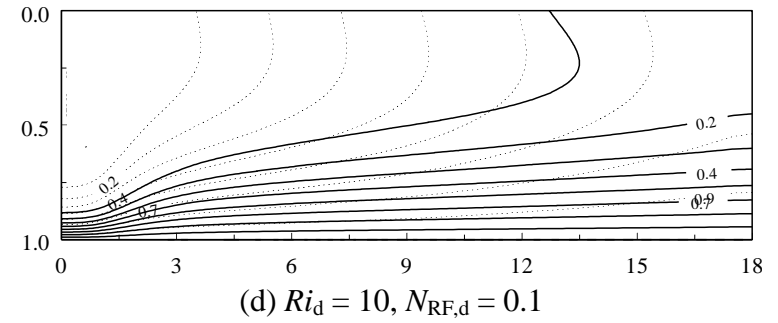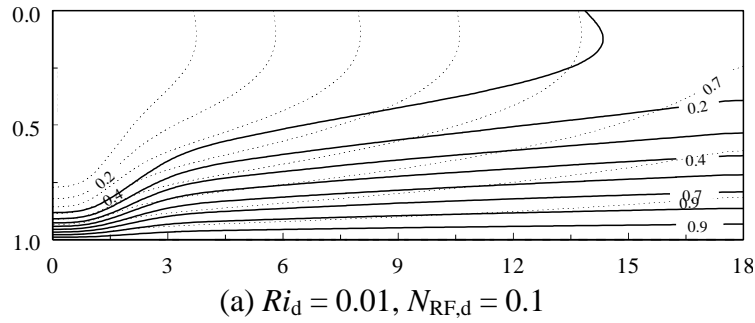
Figure 5.7: Comparison of contours of normalized isotherms between $Ri_d = 0.01$ and 10 for $\varepsilon = 0.85$ and $H = 1$ (....... $Re_d = 100$; —— $Re_d = 400$)

(a) $Re_d = 100$

(b) $Re_d = 400$

(c) $Re_d = 100$

(d) $Re_d = 400$

- $N_{RF,d} = 0.1$, $Ri_d = 0.01$ - $N_{RF,d} = 0.1$, $Ri_d = 10$
- $N_{RF,d} = 0.8$, $Ri_d = 0.01$ - $N_{RF,d} = 0.8$, $Ri_d = 10$
- $N_{RF,d} = 2$, $Ri_d = 0.01$ - $N_{RF,d} = 2$, $Ri_d = 10$
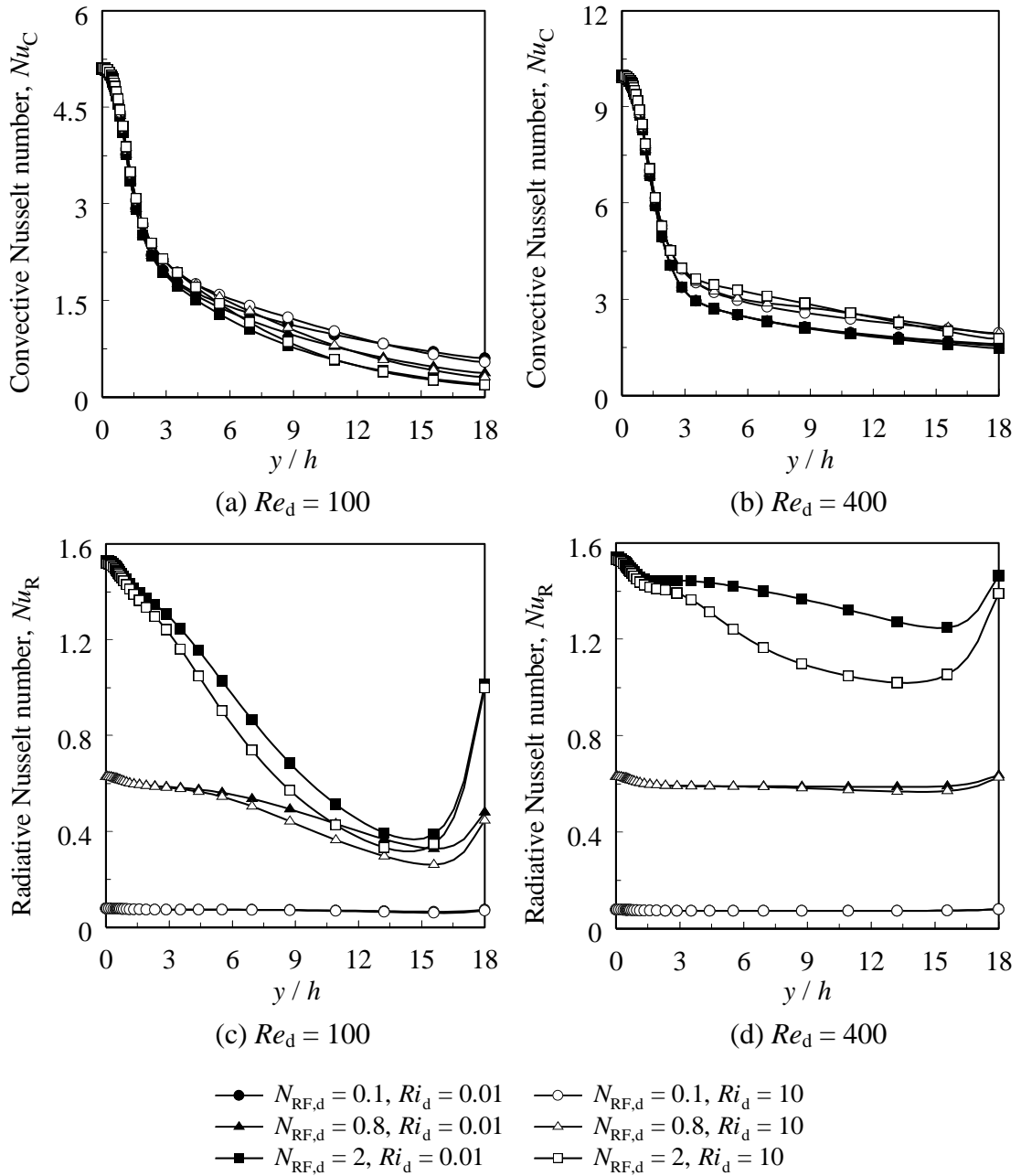
Figure 5.8: Comparison of distribution of Nu_C and Nu_R over the heater between $Ri_d =$ 0.01 and 10, for $H = 1$ for $\varepsilon = 0.85$ and $N_{RF,d} = 0.1$, 0.8 and 2

stagnation region, as reported in the literature [34,35], the effect is pronounced on the flow field farther downstream for all combinations of controlling parameters considered in the figures. The increase in congestion of the streamlines near the heater, due to the increase in Ri_d consequently results in an increase in the density of isotherms, particularly in the regions downstream of the stagnation point. This is in turn manifested as an increase in the convective Nusselt number, although not very substantial, as seen Figs. 5.8 (a-b). It is also seen from the Figs. 5.7 (a-f) that the

(a) $H = 1$ and $Ri_d = 0.01$

(c) $H = 1$ and $Ri_d = 10$

(b) $H = 4$ and $Ri_d = 0.01$

(d) $H = 4$ and $Ri_d = 10$

- $N_{RF,d} = 0.1$, $Re_d = 100$
- $N_{RF,d} = 0.8$, $Re_d = 100$
- $N_{RF,d} = 2$, $Re_d = 100$
- $N_{RF,d} = 0.1$, $Re_d = 400$
- $N_{RF,d} = 0.8$, $Re_d = 400$
- $N_{RF,d} = 2$, $Re_d = 400$
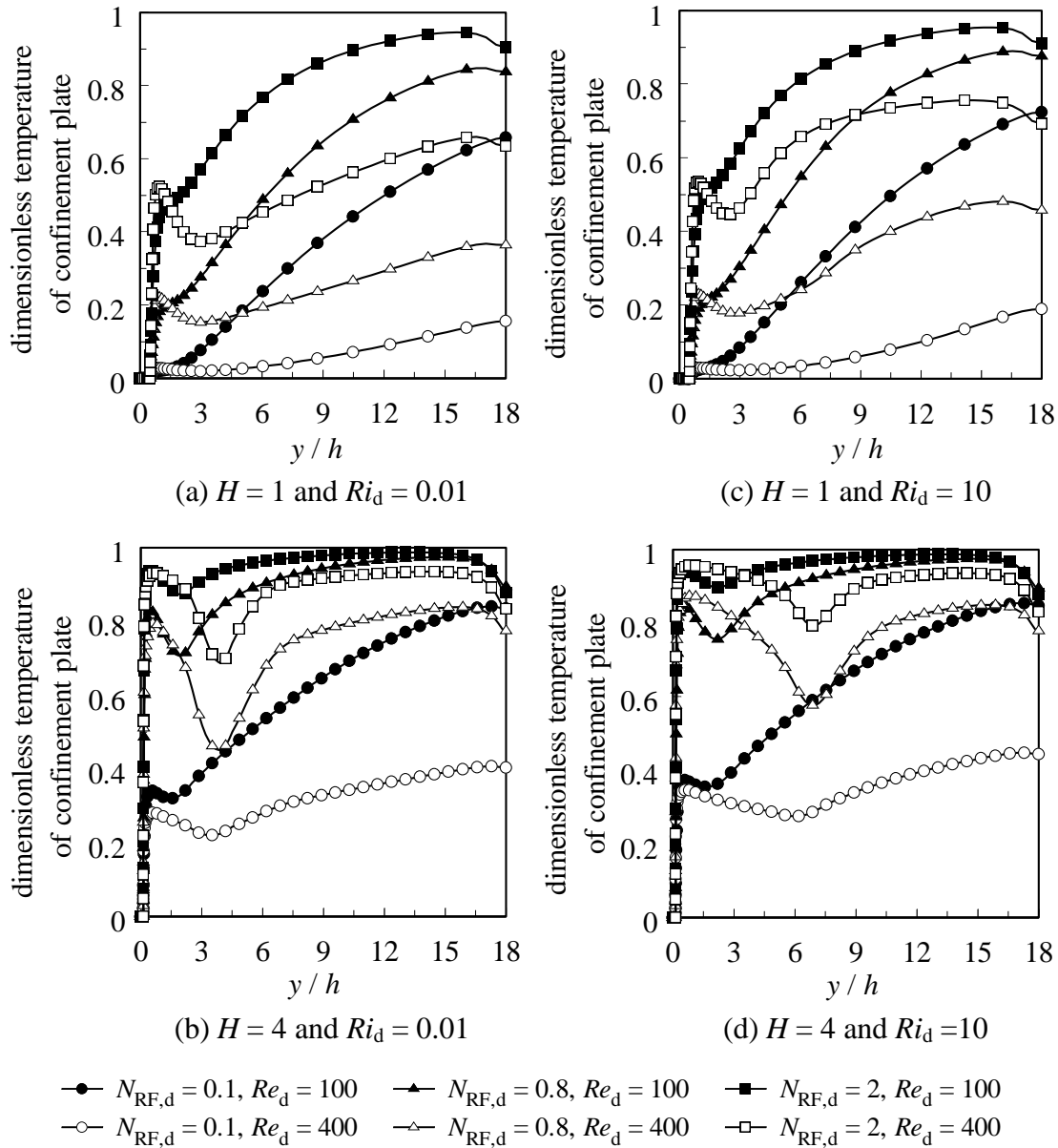
Figure 5.9: Distribution of normalized temperature on the nozzle-outlet and confinement-plate for $\varepsilon = 0.85$, $Re_d = 100$ and 400 and $N_{RF,d} = 0.1$, 0.8 and 2

density of the streamlines and isotherms in the region near the confinement-plate reduce with an increase in Ri_d from 0.01 to 10, indicating a reduction in the convective heat removal from the confinement plate. It is recalled that the confinement-plate is an adiabatic gray surface, and hence energy balance on any elemental area on the confinement-plate requires the net radiation heat transfer 'in' to be equal to the net convective heat transfer 'out' to the fluid. Hence, the reduction in the convective heat transfer from the confinement-plate consequently results in a decrease in net radiative heat transfer to the confinement-plate with change in Ri_d.
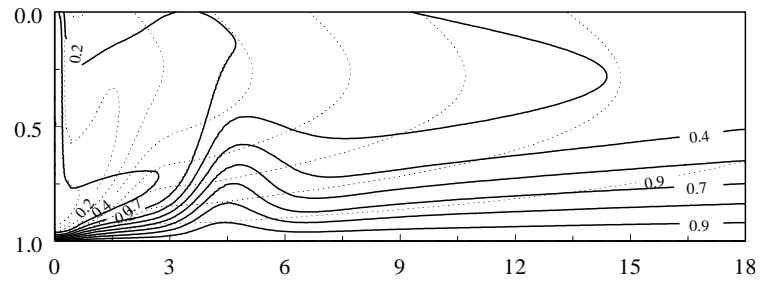
(a) $Ri_d = 0.01$, $N_{RF,d} = 0.1$
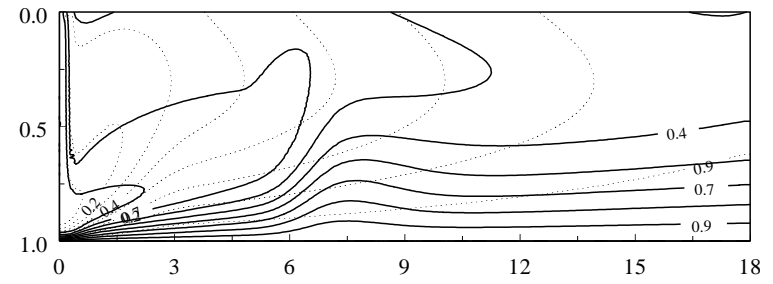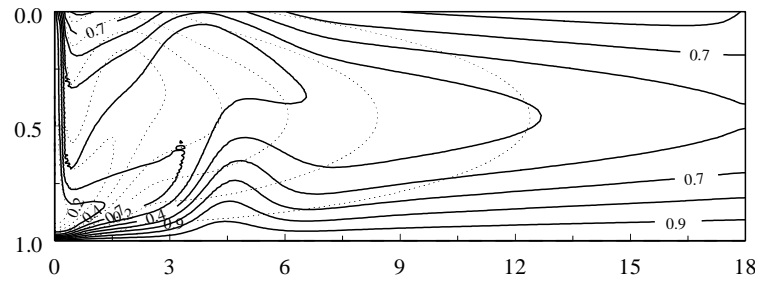
(b) $Ri_d = 0.01$, $N_{RF,d} = 0.8$
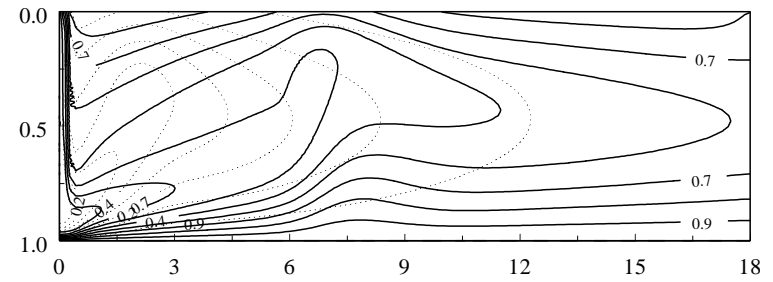
(c) $Ri_d = 0.01$, $N_{RF,d} = 2$
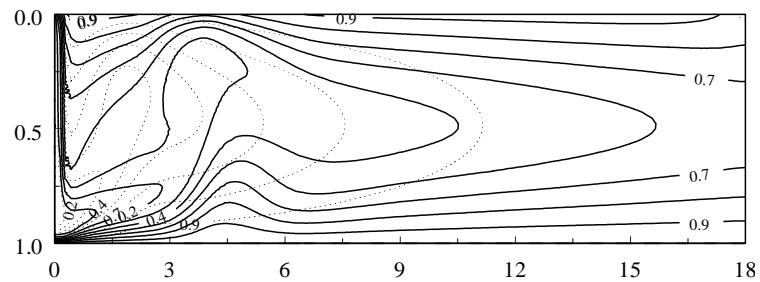
(d) $Ri_d = 10$, $N_{RF,d} = 0.1$
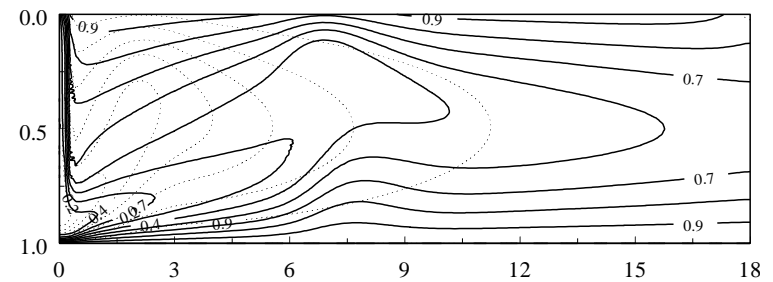
(e) $Ri_d = 10$, $N_{RF,d} = 0.8$

(f) $Ri_d = 10$, $N_{RF,d} = 2$

Figure 5.10: Comparison of normalized isotherms between $Ri_d = 0.01$ and 10, for $\varepsilon = 0.85$ and $H = 4$ (....... $Re_d = 100$; ⎯⎯ $Re_d = 400$)
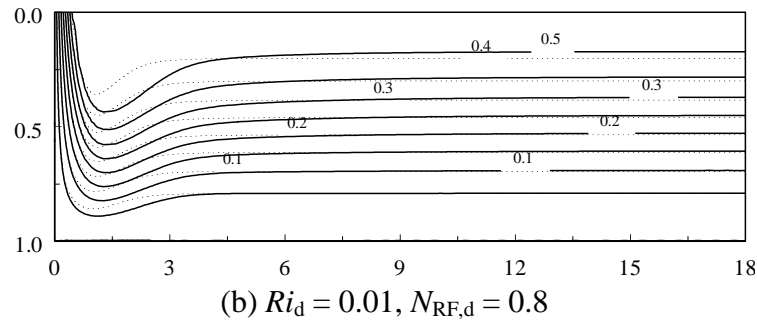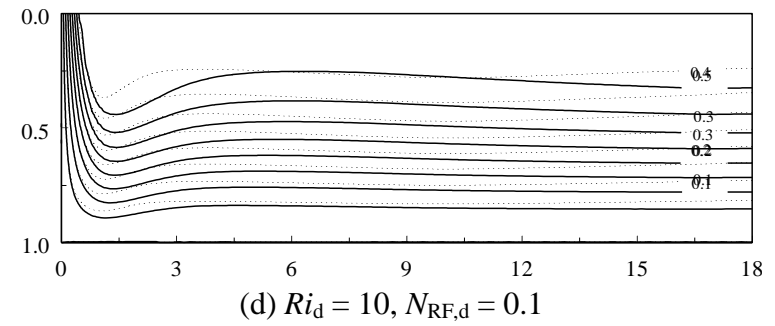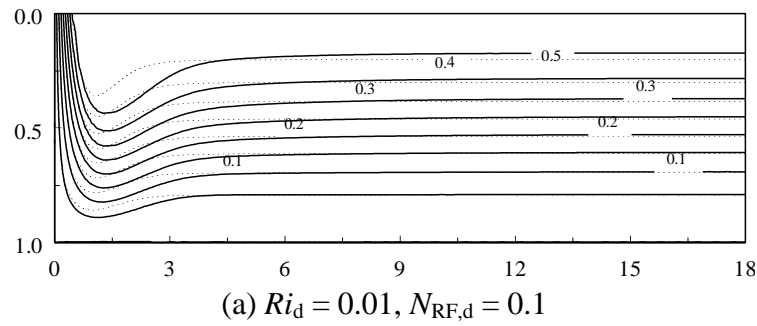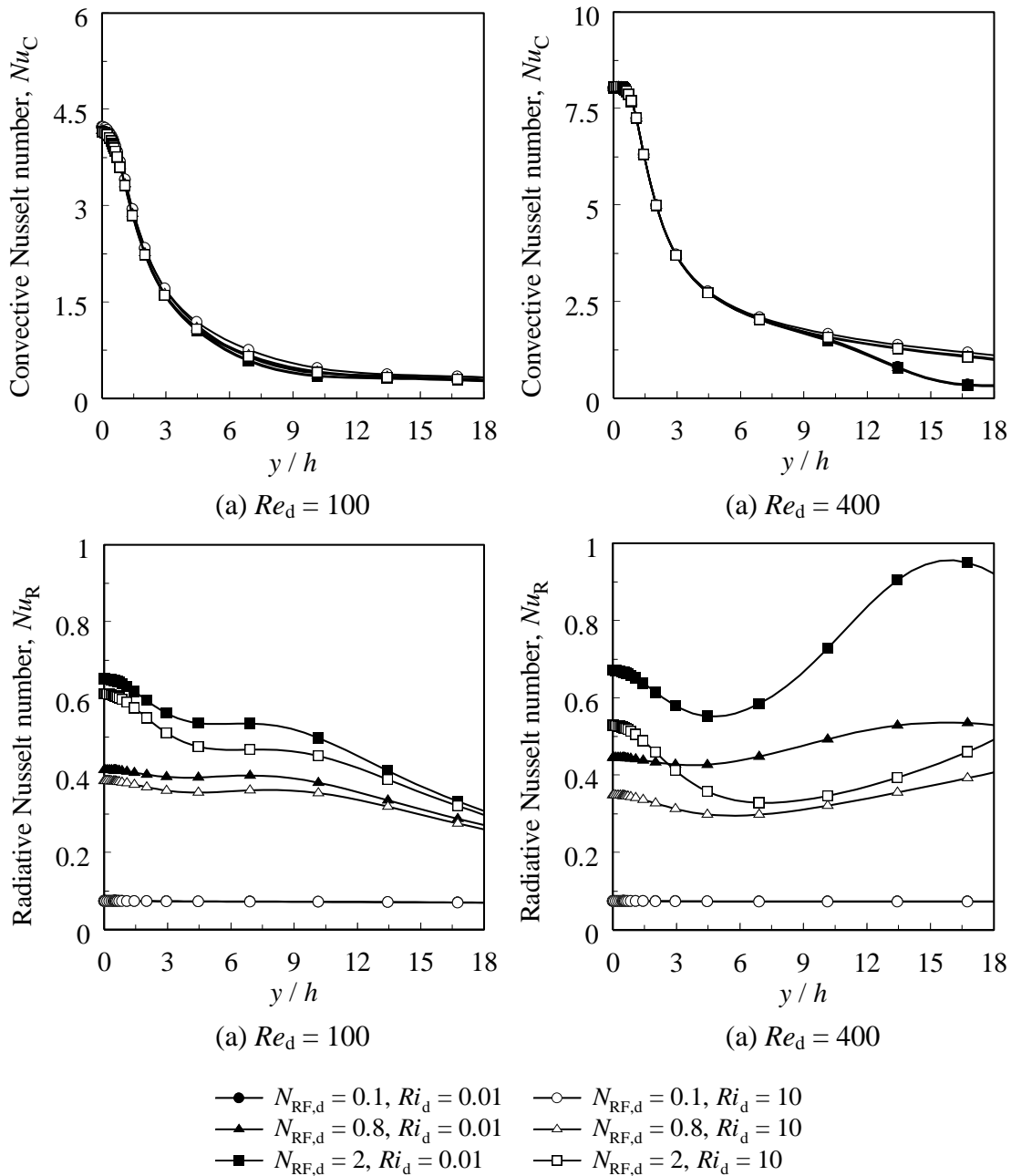
Figure 5.11: Comparison of distribution of Nu_C and Nu_R over the heater between $Ri_d = 0.01$ and 10, for $H = 4$ for $\varepsilon = 0.85$ and $N_{RF,d} = 0.1$, 0.8 and 2

While the radiative heat exchange between the heater, and the outlets and the nozzle-outlet is constant for any given value of ε, irrespective of the other controlling parameters, this reduction in the radiative heat exchange between the heater and the confinement-plate results in the suppression of net radiation from the heater. The larger normalized temperatures on the confinement-plate for $Ri_d = 10$, as compared to $Ri_d = 0.01$, as seen from comparison of Fig. 5.9 (a) and Fig. 5.9 (c) also indicate the lower potential for radiative heat transfer from the heater during operation at such
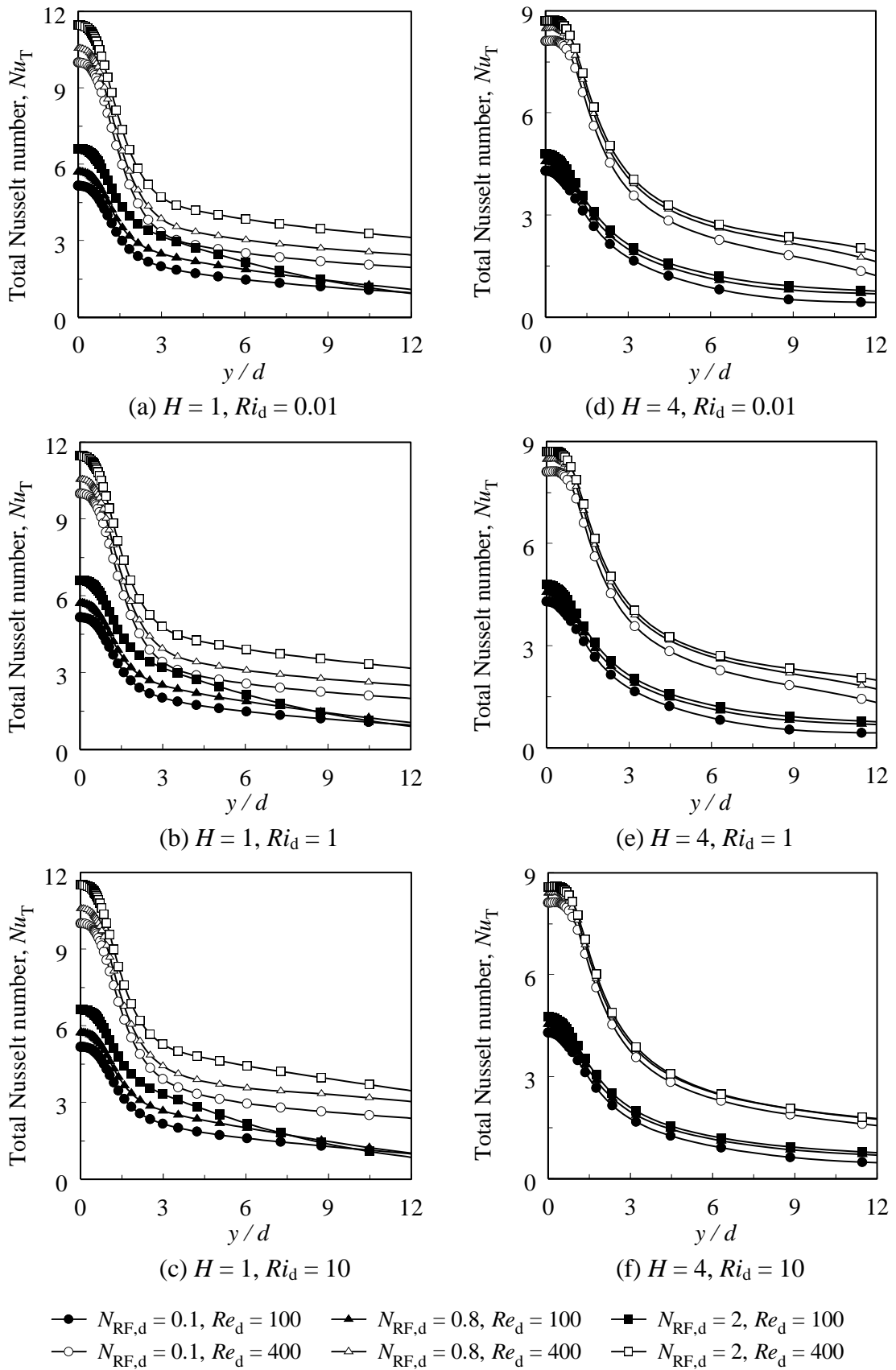
Figure 5.12: Local distributions of Nu_T over the heater for $H = 1$ and 4, for $\varepsilon = 0.85$, $Re_d = 100$ and 400, and $N_{RF,d} = 0.1$, 0.8 and 2

large Richardson numbers. In line with the discussion, the magnitude of local radiative Nusselt number on any point on the heater is consistently lower for $Ri_d = 10$ as compared to $Ri_d = 0.01$ as illustrated in Figs. 5.8 (c-d).

(a)   (b)

(c)
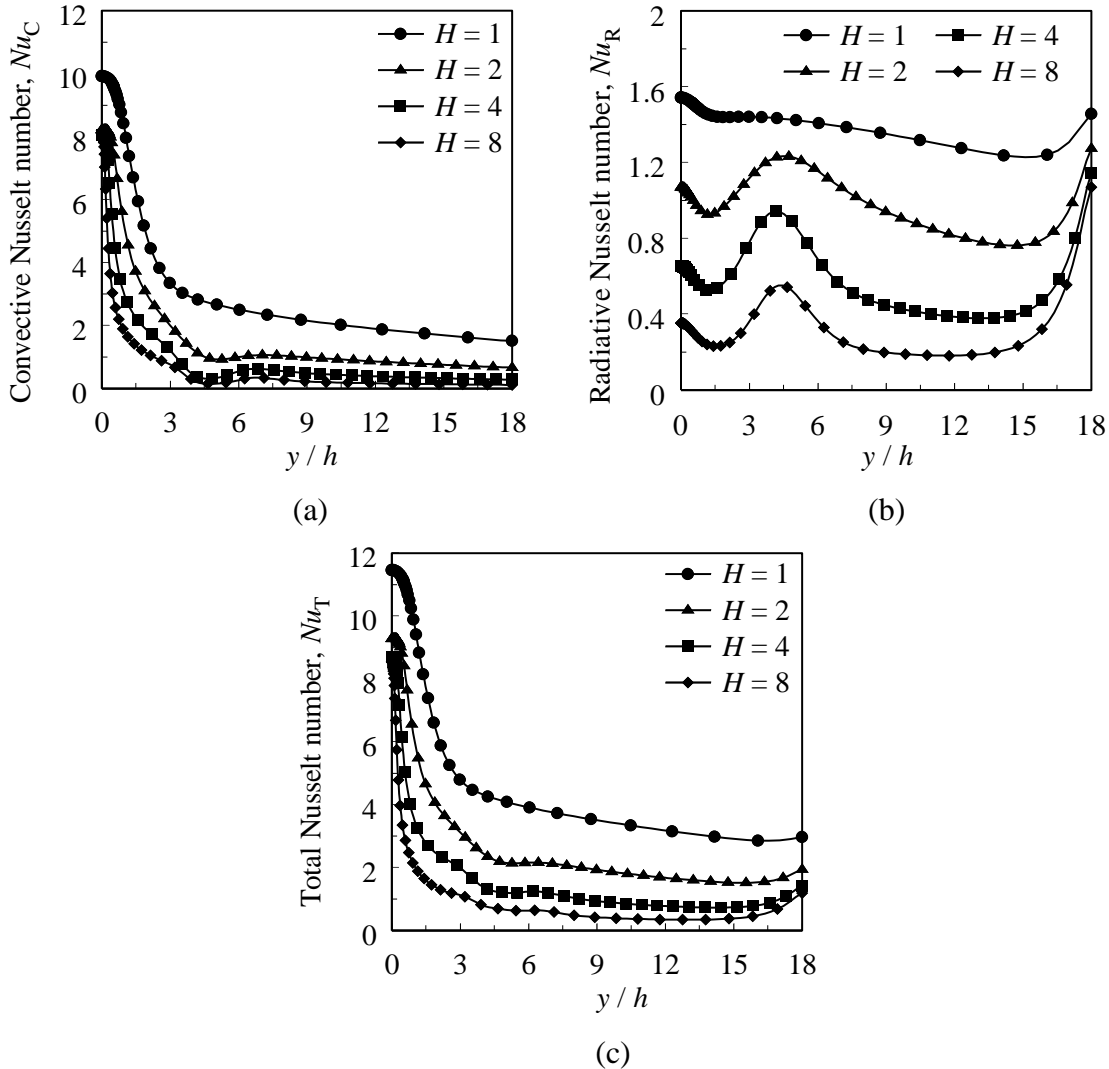
Figure 5.13: Comparison of the distribution of Nu_C, Nu_R and Nu_T for different values of $H = 1, 2, 4$ and 8, for $\varepsilon = 0.85$, $Re_d = 400$, $N_{RF,d} = 2$, and $Ri_d = 1$

Figures 5.10 (a-c) and Figs. 5.10 (d-f) show the contours of isotherms for $Ri_d = 0.01$ and 10 respectively, for $H = 4$, $\varepsilon = 0.85$, $Re_d = 100$ and 400, and $N_{RF,d} = 0.1$, 0.8 and 2. The corresponding contours of streamlines are omitted for brevity. From the figures, it is seen that the trends for $H = 4$ are similar to that observed for $H = 1$ with change in Ri_d, *ceteris paribus*. The local radiative Nusselt numbers on the heater are found to be substantially attenuated for $Ri_d = 10$ as compared to $Ri_d = 0.01$, while there is no significant change in the convective counterpart as seen in Figs.

5.11 (a-d). The consistently larger values of normalized temperature on the confinement plate for $Ri_d = 10$, as compared to $Ri_d = 0.01$, irrespective of all other controlling parameters, in Figs. 5.9 (b) and Fig. 5.9 (d), are indicative of the lower potential for radiative heat transfer from the heater for larger values of Ri_d.

From Figs. 5.8 (a-b) and Figs. 5.11 (a-b) it is seen that for given values of controlling parameters, any change in dimensionless radiation flow interaction parameter $N_{RF,d}$ within the range considered, causes very little change in the magnitude of convective Nusselt number on heater in the stagnation region. However, a slight decrease in the magnitude of local convective Nusselt number is observed in the regions farther downstream with an increase in $N_{RF,d}$ for low values of H. On the contrary, it is seen from Figs. 5.8 (c-d) and Figs. 5.11 (c-d) that a substantial increase in the magnitude of local radiative Nusselt number is accompanied with an increase in $N_{RF,d}$ within the range considered, thereby resulting in consequent rise in the total Nusselt number, as illustrated in Figs. 5.12 (a-f) for $H = 1$ and 4, $\varepsilon = 0.85$, $Re_d = 100$ and 400, $N_{RF,d} = 0.1$, 0.8 and 2; and $Ri_d = 0.01$, 1 and 10. For a given raise in $N_{RF,d}$ from 0.1 to 2, the total heat transfer rate, quantified in terms of the total Nusselt number, increases to about 25% in the stagnation region and over 40% in the wall jet region for a value of $H = 1$, while to about 15 % in the stagnation region and over 50 % in the wall-jet region for $H = 4$.

Figures 5.13 (a-c) illustrate the magnitudes of local convective, radiative and total Nusselt numbers on the heater, respectively, for different values of dimensionless nozzle standoff distances $H = 1$, 2, 4 and 8, and for typical set of other parameters $\varepsilon = 0.85$, $Re_d = 400$, $N_{RF,d} = 2$, and $Ri_d = 1$. It is seen from the figures that the magnitude of both convective as well as radiative Nusselt numbers decrease with an increase in H, over the range considered. With an increase in the nozzle standoff distance from $H = 1$ to 8, effect of the impinging jet is reduced due to reduction in the kinetic energy (true for submerged jets) which is consequently seen as an adverse reduction in the convective Nusselt number on the surface [30,31]. However the radiative Nusselt numbers are also seen to decrease with an increase in the dimensionless standoff distance. A given increment in the value of H for any given values of other controlling parameters, can be interpreted as an increase in standoff distance h for a given value of d. Consequently, the total area of the outlet of the

(a) H=1, Ri_d = 0.01

(d) H=4, Ri_d = 0.01

(b) H=1, Ri_d = 1

(e) H=4, Ri_d = 1

(c) H=1, Ri_d = 10

(f) H=4, Ri_d = 10

$\cdots\bullet\cdots$ Nu_C/Nu_T for Re_d = 100, NRF_d = 0.1 $\cdots\blacktriangle\cdots$ Nu_C/Nu_T for Re_d = 100, NRF_d = 0.8

$\cdots\circ\cdots$ Nu_R/Nu_T for Re_d = 100, NRF_d = 0.1 $\cdots\triangle\cdots$ Nu_R/Nu_T for Re_d = 100, NRF_d = 0.8

$\!-\!\bullet\!-$ Nu_C/Nu_T for Re_d = 400, NRF_d = 0.1 $\!-\!\blacktriangle\!-$ Nu_C/Nu_T for Re_d = 400, NRF_d = 0.8

$\!-\!\circ\!-$ Nu_R/Nu_T for Re_d = 400, NRF_d = 0.1 $\!-\!\triangle\!-$ Nu_R/Nu_T for Re_d = 400, NRF_d = 0.8

$\cdots\blacksquare\cdots$ Nu_C/Nu_T for Re_d = 100, NRF_d = 2

$\cdots\square\cdots$ Nu_R/Nu_T for Re_d = 100, NRF_d = 2

$\!-\!\blacksquare\!-$ Nu_C/Nu_T for Re_d = 400, NRF_d = 2

$\!-\!\square\!-$ Nu_R/Nu_T for Re_d = 400, NRF_d = 2
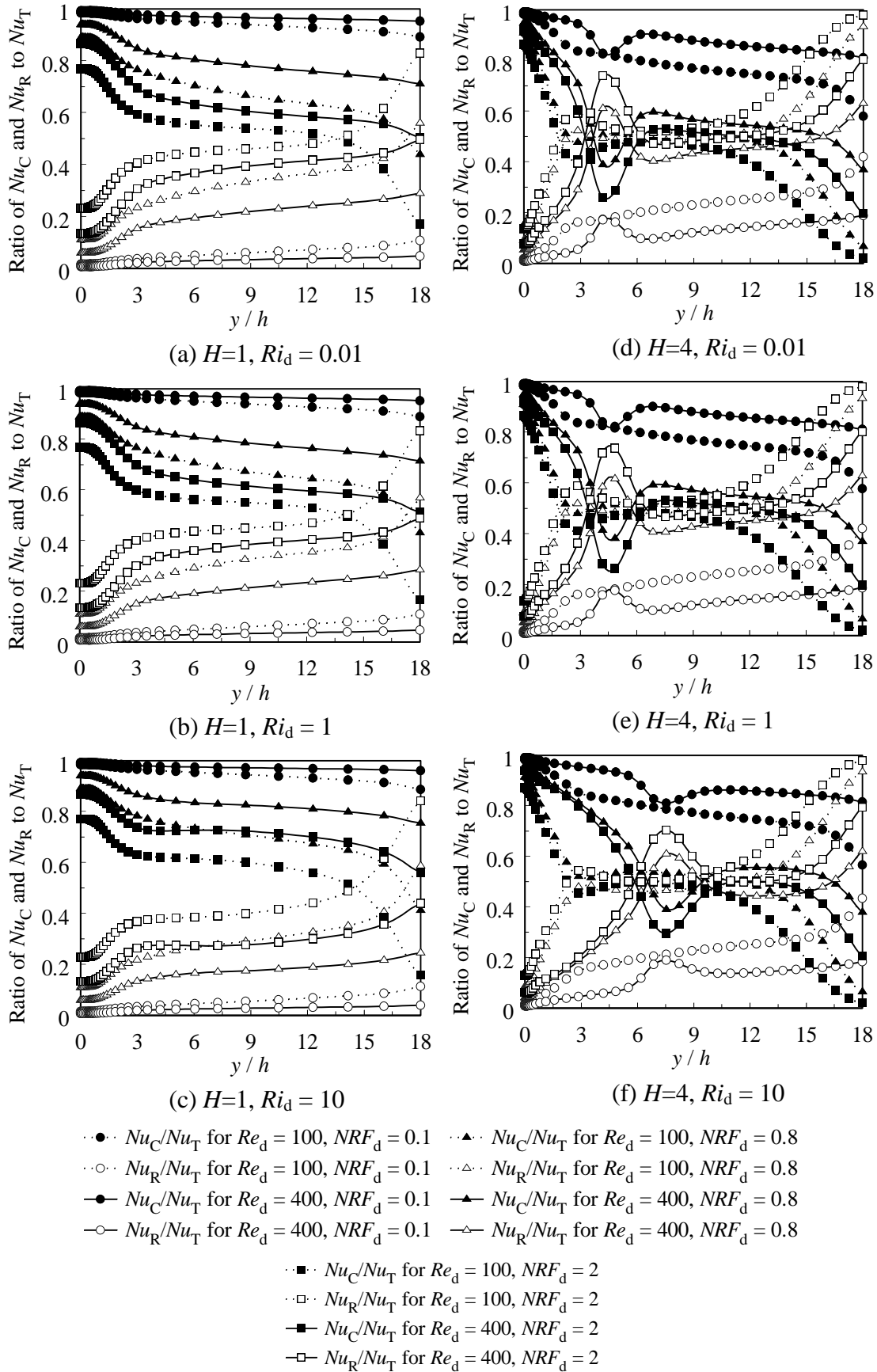
Figure 5.14: Distribution of Nu_C/Nu_T and Nu_R/Nu_T along the heater for H=1 and 4,

for Re_d = 100 and 400, ε = 0.85 and $N_{RF,d}$ = 0.1, 0.8 and 2

domain also increases proportionally to any specified change in h, thereby increasing the potential for larger radiative heat loss thorough these regions for larger standoff distances. However, from the comparison of Fig. 5.9 (a) and Fig. 5.9 (b) with Fig.5.9 (c) and Fig.5.9 (d) respectively, it is seen that the values of the normalized temperatures over the confinement-plate are consistently larger for $H = 4$ as compared to $H = 1$. This results in larger irradiation to the heater from the confinement-plate, for any given value of other controlling parameters. As the length of the heater is always maintained as $36 \times h$, any increase in H results in a proportional increase in L_x for any given value of d. Hence, the increase in L_x implies that the geometry of channel is elongated in the direction downstream of the wall-jet proportional to the increase in H (on either sides of the centerline of jet). Hence, the view-factor between most of the internal surface elements on the heater to the outlet is reduced due to decrease in proximity with the outlet, thereby decreasing the net radiation exchange between most of the upstream surface elements on the heater and outlet. The higher temperatures on the confinement plate for larger values of H implicitly result in larger irradiation to the heater on those surface elements thereby reducing the net radiation from the heater and consequently reducing the magnitude of local radiative Nusselt numbers with an increase in H as shown in Fig. 5.13 (b). As the total Nusselt number is, simply, the arithmetic sum of the radiative and convective Nusselt numbers, the effect of increase in H on Nu_T is summative of the two modes.

Figures 5.14 (a-f) illustrate variation of the distribution of the relative contributions of convection and surface radiation to total heat transfer, over the surface of the heater, for various values of $Ri_d = 0.01$, 1 and 10, $N_{RF,d} = 0.1$, 0.8 and 2, $H = 1$ and 4, $Re_d = 100$ and 400 and $\varepsilon = 0.85$. For any given value of Ri_d, it is seen that the relative contribution of radiation to total heat transfer from the heater consistently decreases with increase in the jet-Reynolds number. Also, in coherence with the discussion presented in the preceding paragraphs of this section, it is seen that for any given increase in $N_{RF,d}$ and for given set of other controlling parameters, the relative contribution of radiative heat transfer from the heated surface also increases. From the comparison of Figs. 5.14 (a-c) with Figs. 5.14 (d-f), it is seen that the contribution of radiation to overall heat transfer is larger for $H = 4$ as compared to $H = 1$, in the wall-jet region, while it is larger for $H = 1$ as compared to $H = 4$ in

the stagnation region.

For sufficiently large values of jet-Reynolds numbers or large values of dimensionless nozzle-to-heater distance, a small recirculation region is formed over the heater a certain distance downstream of the stagnation point. At this region, the local convective Nusselt number drops in magnitude and consequently rises at the end of this recirculation region. It is also observed that the upstream end of this recirculation cell on the impingement surface occurs directly below the downstream end of the recirculation cell that occurs near the confinement-plate. As is true for the impingement surface, the convective heat removal from the confinement plate again follows the same trend around the recirculation cell. Consequently, the normalized temperature of the confinement plate drops near the downstream end of this recirculation cell that occurs near the confinement-plate, due to increased heat removal, as seen in Figs. 5.9 (a-d) for large values of Re_d and/ or large values of H. As convective heat transfer from these regions on the confinement-plate is large, from energy balance on the confinement-plate, the potential for absorption of radiative heat into those sections of the confinement-plate is also large. Hence, the regions on the heater directly beneath those regions of the confinement-plate are directly benefitted due to their closer proximity in these regions with higher temperature differential, and a consequent increase in the magnitude of local radiative Nusselt number is observed around the recirculation cells. Consequently, the relative contribution of radiation to overall heat transfer from the heater peaks around this recirculation region, as seen in Figs. 5.14 (d-f). In fact, the contribution of radiation to the overall heat transfer from the impingement surface reaches about 60% to 80% in these regions, as seen in the figures. From Fig. 5.13 (b) it is seen that the rise in radiative Nusselt numbers in these local peaks increase with increase in H up to a value of $H = 4$, but decreases relatively, with further increase in H from $H = 4$ to 8. The rise in radiative heat transfer in these regions of the heater compensates for the drop in local convective Nusselt number (Fig. 5.13 (a)), resulting in the elevation of total Nusselt number as can be seen from Fig 5.13 (c). It can also be seen from the figures that, the location of this recirculation region moves downstream with an increase in Ri_d. However, the change in this location from that obtained for $Ri_d = 0.01$ is significant only for $Ri_d = 10$, as compared to $Ri_d = 1$.

5.1.3   Summary of Key Findings

The aforementioned discussion reveals some interesting insights into the thermal transport associated with mixed convective laminar air jet impingement heat transfer at high surface temperature and/ or high surface emissivity. With a view to understand the relative strengths of the underlying heat transfer mechanisms in such configurations, a detailed study is carried out for a wide range of controlling parameters ranges $1 \leq H \leq 8$, $0.01 \leq Ri_d \leq 10$, $0.1 \leq N_{RF,d} \leq 2$, $100 \leq Re_d \leq 900$ and $0.05 \leq \varepsilon \leq 0.85$, with specific focus on the simultaneous effects of buoyancy and surface-radiation. The key findings are listed below:

- For given values of other controlling parameters, increase in ε increases the contribution of radiation to the overall heat transfer from the heater, from nearly negligible for $\varepsilon = 0.05$ to about 23 % in the stagnation region and over 50 % in the regions downstream for $\varepsilon = 0.85$.

- Increase in emissivity also causes a slight decrease in the convective Nusselt number distribution in the regions far downstream of the stagnation point for low Reynolds ($Re_d = 100$) numbers due to the relatively larger temperatures of the confinement plate.

- For a given variation in jet-Reynolds numbers, the change in the magnitude of Nu_C is relatively larger as compared to Nu_R on the heater, resulting in the percentage contribution of radiation to overall heat transfer from the surface decrease with increase in Re_d.

- The effect of variation in Ri_d, on the flow and heat transfer in the stagnation region is negligible; however, a slight increase in the magnitude of the local Nu_C over the regions of the heater farther downstream is observed for all combinations of controlling parameters.

- For a given increase in Ri_d, the magnitude of local radiative Nusselt number decreases, for all prescribed combinations of other controlling parameters.

- Any variation in $N_{RF,d}$ within the range considered, causes very little change in the magnitudes of local Nu_C along the heater in the stagnation region, however, a slight decrease in the magnitudes is observed in the regions downstream. It is also seen that a substantial increase in the magnitudes of local Nu_R is also

accompanied with an increase in $N_{RF,d}$.

- The rise in the total Nusselt number, increases to about 25% in the stagnation region, while over 40% in the wall jet region with a change in $N_{RF,d}$ from 0.1 to 2 for a value of $H = 1$, and to about 15 % in the stagnation region to over 50 % in the wall-jet region for $H = 4$.

- Similar to the magnitude of local convective Nusselt number, the magnitude of local radiative Nusselt number at any point over the heater also decreases with increase in H. However, the change in magnitude of local Nu_C with change in H decreases with increase in H beyond about $H = 4$, while the magnitude of Nu_R continue to decrease monotonically with increase in H.

- For sufficiently large value of Re_d or large values of H, a small recirculation region is formed over the heater at a certain distance downstream of the stagnation point. The upstream end of this recirculation cell on the heater occurs directly below the downstream end of the recirculation cell that occurs near the confinement-plate. The relative contribution of radiation to overall heat transfer from the heater peaks around this recirculation region to reach about 60% to 80% for specific combinations of controlling parameters.

- The increase in magnitude of local Nu_R at any point in these local peaks increase with increase in H up to a value of $H = 4$, but decreases relatively, with further increase in H from $H = 4$ to 8.

- The location of these recirculation cells move downstream with an increase in Ri_d. However, the change in the locations is relatively larger between $Ri_d = 0.01$ and 10 as compared to that between $Ri_d = 0.01$ and 1.

5.2 COMPUTATIONAL STUDY OF CONFINED, SUBMERGED, SUBCOOLED AND STEADY TURBULENT JET IMPINGEMENT BOILING

5.2.1 Grid Sensitivity Analysis

A grid independence test is carried out for each geometric configuration studied by successive refinement of an initial mesh, particularly in the regions near the wall, and comparison of the change in magnitudes of various predicted parameters such as the

(a)

(b)

(c)

(d)

(e) size of first cell from the wall

(f) mesh distribution along y-axis
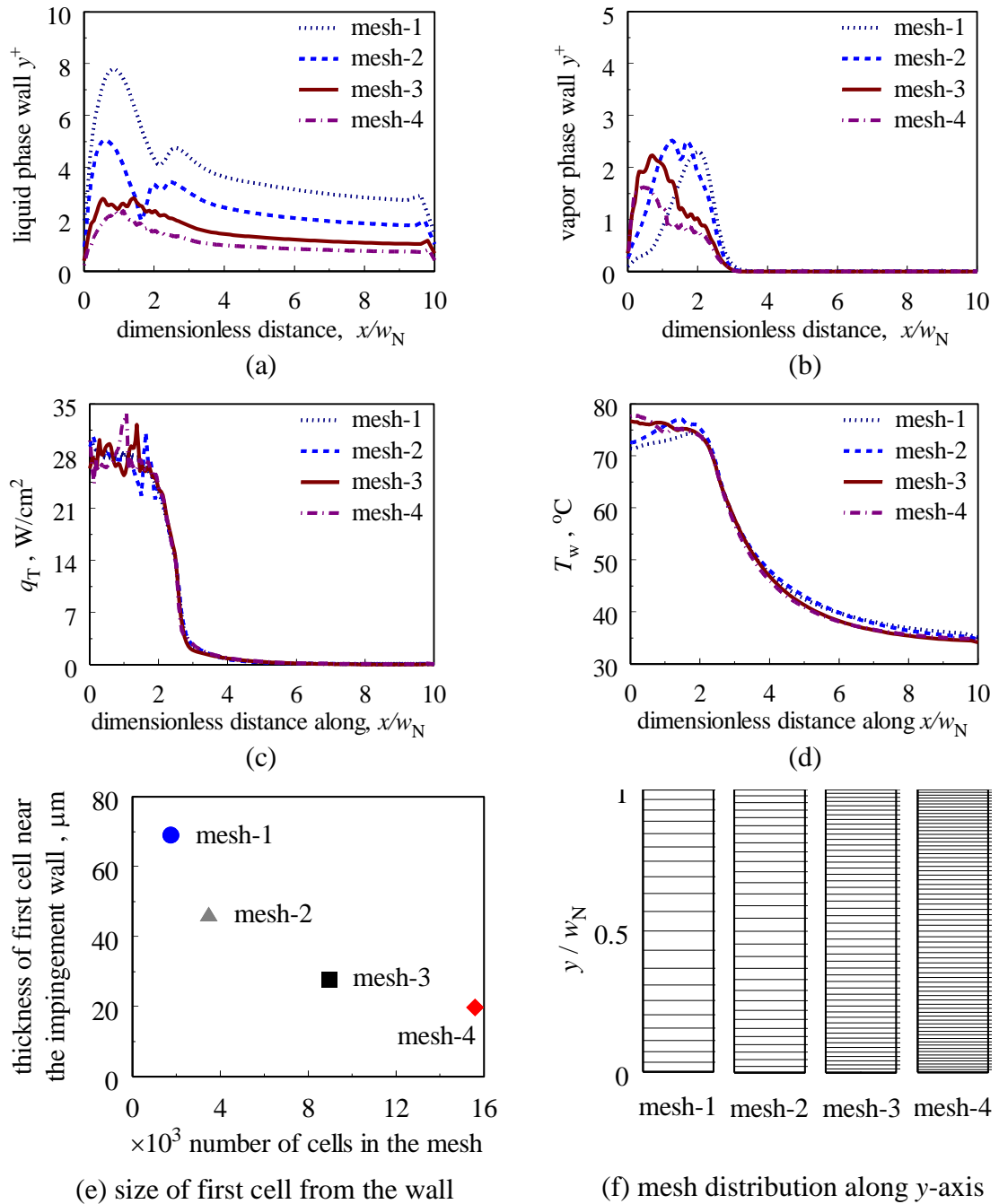
Figure 5.15: (a-d) Variation in local quantities with successive mesh refinement for a typical submerged and confined jet impingement boiling case; fluid = FC-72, $\Delta T_{sub} =$ 25 $^{\circ}$C, $Re = 4916$, $H = 1$, $w_H/w_N = 5$, and (e-f) typical variation in mesh-distribution along y-axis; mesh-1 = 1764 cells, mesh-2 = 3480 cells, mesh-3 = 8970 cells and mesh-4 = 15600 cells

wall-y^+, temperature and heat fluxes on the impingement surface. As for most problems involving heat transfer (or large temperature gradients) as in the present study, the resolution of the near wall mesh plays a very critical role in the successful

simulation of the flow field and associated heat transfer. It is identified as an intrinsic necessity that the mesh in the regions near the impingement surface, particularly around the heater is fine enough to capture the thermal gradients accurately. In addition, as the flow field is turbulent, the choice of turbulence models also impose strict requirements on the near wall mesh configuration (or wall-y^+). As the prediction of the associated multiphase heat transfer requires a sufficiently fine mesh near the wall, the turbulence models involving standard wall functions, which invariably demand a coarse near-wall mesh, are deemed unsuitable for the present research detailed in this thesis. For example, the k-ε turbulence model with standard wall-functions imposes a constraint on the near wall mesh to satisfy wall-$y^+ > 30$, which would undesirably result in only a few cells in the direction perpendicular to the wall for the range of Reynolds numbers considered in the present study. The choice of turbulence model used for the present studies taking into consideration the mesh requirement is delineated in Section 5.2.2 subsequent to the following discussion on mesh refinement.

Figure 5.15 (a-d) shows the variation in the local magnitudes of liquid phase $y+$, vapor phase $y+$, total surface heat flux and wall temperature with successive refinement of mesh for four different structured non-uniform mesh configurations with sizes (number of cells) 1764 (mesh-1), 3480 (mesh-2), 8970 (mesh-3) and 15600 (mesh-4) respectively for a typical case. Figures 5.15 (e,f) show the variation in the mesh distribution along the y-axis (direction perpendicular to the impingement surface) for the four mesh configurations. The data illustrated in the figure pertains to a typical case of confined and submerged impingement boiling where a dielectric fluid FC-72 at an inlet subcooling $\Delta T_{sub} = 25$ ^{o}C issues from a slot nozzle of width 2 mm with a jet Reynolds number $Re = 4916$ and impinges on a 0.467 mm thick Inconel-600 plate of length $w_H = 10$ mm that was heated uniformly volumetrically such that the average surface heat flux $q_T = 28$ W/cm^2. An insulating confinement plate is placed at a height of 2 mm from the impingement surface (also the plane of the nozzle-outlet), such that the dimensionless standoff distance is $H = 1$. It is seen that from the figure that the wall-y^+ based on the liquid and vapor phase velocities vary considerably with successive refinement of mesh. Although it is intuitive that the wall y^+ would continue to decrease with refinement of the mesh and a decrease in the distance of the first cell with reference to the wall, the purpose of this comparison
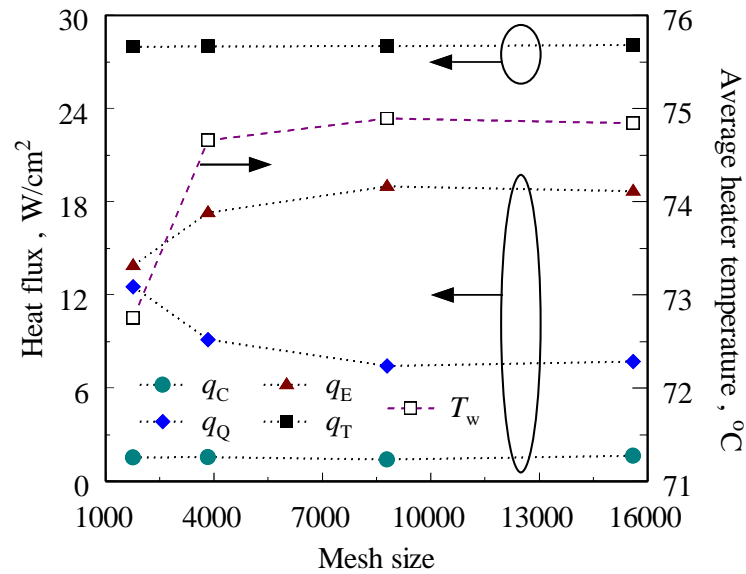
Figure 5.16: Variation in surface averaged component heat fluxes, total heat flux and surface temperature with successive mesh refinement; the operating conditions are same as that for Fig. 5.15

of wall y^+ with the change in mesh was to determine of the chosen mesh satisfies the near wall mesh requirements imposed by the turbulence model. The multiphase RNG-k-ε turbulence model is used for the simulations included in Fig. 5.15 (a-d) which requires a near wall $y+ < 5$ to accurately resolve the viscous sublayer of the turbulent boundary layer. It is seen from Figs. 5.15 (a,b) that only mesh-3 and mesh-4 satisfy this criterion indicating a suitability for the simulations from the perspective of accurate turbulence modeling. It is also seen from Figs. 5.15 (c,d) that the imposed change in mesh sizes has a significant effect on the stagnation region heat transfer. The change in the surface averaged liquid phase convective, quenching and evaporative components of the total heat transfer, along with the total heat transfer and average surface temperature, against mesh size is illustrated in Fig. 5.16 for the sample operating conditions detailed earlier. It is seen from the figure that the range of mesh sizes considered for the typical case are sufficient as the averaged quantities seem to converge with the relative error in each quantity decreasing with successive mesh refinement. Similar grid sensitivity analyses were carried out for the studies presented hereunder for appropriate range of mesh sizes, and the mesh configuration was chosen such that the change in the averaged quantities were less than 4 % considering the substantial increase in the computational effort that would be required for any further improvement in prediction accuracy. For the example

illustrated in Fig. 5.16, the maximum relative error between the averaged quantities using mesh-3 as compared to mesh-4 is 3.7%. The typical mesh configuration used for the simulations is illustrated in Fig. 4.4 of Section-4.1.2.

(a) Boiling Curve   (b) Local distribution of heat fluxes
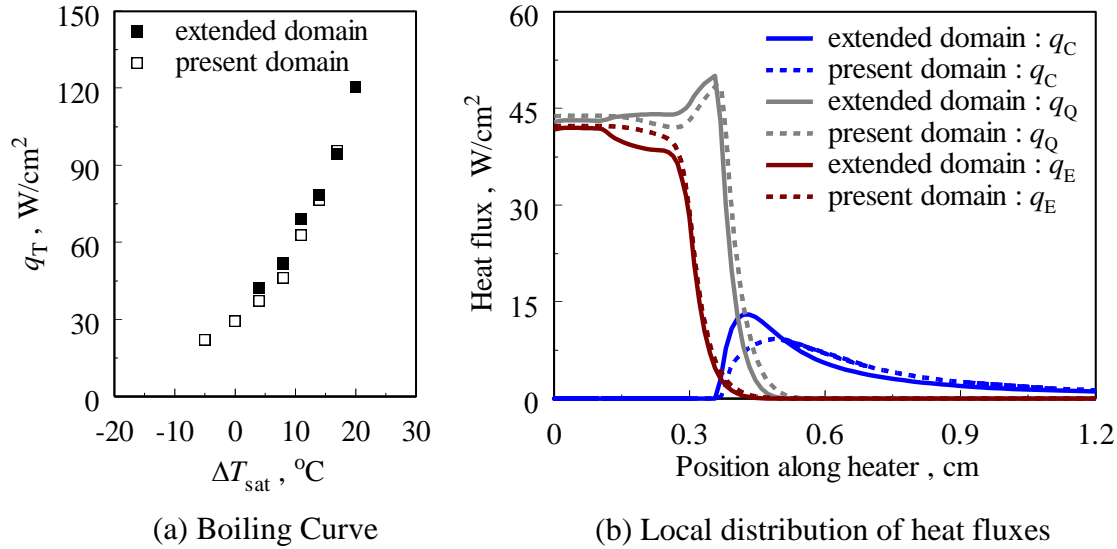
Figure 5.17: Comparison of local and surface averaged heat fluxes from an isothermal heater with $\Delta T_{sat} = 20$ ^{o}C, between present domain and an extended domain for $Re = 3750$, $w_H/w_N = 3$ and $H = 4$, using de-ionized water

As the geometry for the problem considered involves a confined outflow, which partially consists of a wall-jet and partially reverse flow (re-circulation), any specified outlet pressure would not represent the real geometry and would introduce numerical anomalies due to the superficially imposed pressure at the outlet of the domain. Hence, the length of the domain beyond the heater was determined (purely for computational correctness and accuracy) by using successively longer sections of the confined region far from heater, to ensure that the outlet boundary condition does not affect the flow features in the region of interest. The results from a typical test carried out for a given set of input parameters is presented in Figure 5.17 were the dimensionless nozzle standoff distance was $H = 4$, and the working fluid de-ionized water at an inlet subcooling $\Delta T_{sub} = 20$ ^{o}C and atmospheric pressure impinges on a copper plate of thickness 0.2 mm heated isothermally from below. Figure 5.17 (a) shows the comparison of boiling curves obtained between the present domain and an extended domain with a length of $120 \times w_N$, for a representative case: jet Reynolds number $Re = 3750$ and heater-nozzle size ratio $w_H/w_N = 3$. Figure 5.17 (b) illustrates

the comparison of the corresponding local magnitudes of liquid-phase convective, quenching and evaporative heat fluxes in the region of interest for a specified surface temperature with $\Delta T_{sat} = 20$ °C. It is seen from the figures that the predictions from the present domain compare very well with that from the extended domain, with deviations of less than 4 % for heat flux for both, local values and averaged boiling curves; thus, reinforcing confidence in the present numerical predictions, particularly, with respect to the extent of the computational domain considered.
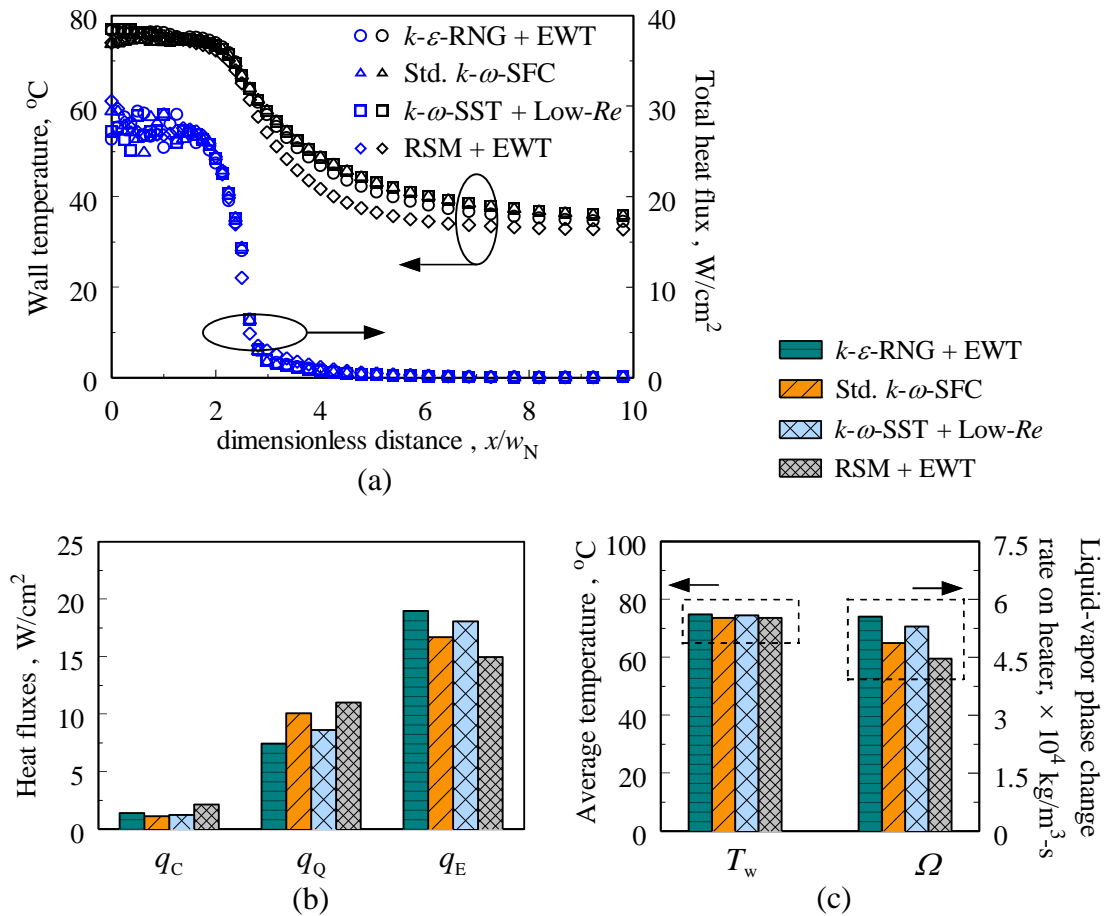
Figure 5.18: Change in (a) local, and (b, c) area averaged magnitudes of quantities on the heated impingement surface with choice of turbulence model for a typical case of submerged and confined jet impingement boiling using FC-72, for $\Delta T_{sub} = 25$ °C, Re = 4916, $H = 1$ and $w_H/w_N = 5$

5.2.2   Effect of Multiphase Turbulence Models on Predictions

In line with the discussion on the requirements on the mesh size imposed by the turbulence models outlined in the previous section, four different types of Reynolds-Averaged-Navier-Stokes (RANS) turbulence models available in ANSYS-FLUENT

pertaining to Eulerian multiphase flows were explored for their suitability in terms of computational accuracy and convergence stability for the simulation of the present multiphase heat transfer/ fluid flow problem under investigation. The multiphase turbulence models considered are: (i) Re-normalization-Group (RNG)-k-ε with enhanced wall treatment (EWT) [129], (ii) Standard k-ω with Shear flow corrections [156,157], (iii) k-ω with Shear stress transport (SST) and low-Reynolds number corrections [158,159], and (iv) Reynolds stress model (RSM) with linear pressure strain and EWT [160]. The choice of these four turbulence schemes encompasses both the linear (Boussinesq hypothesis) as well as the non-linear formulates of mixture eddy/ turbulence viscosity. It is to be noted that all the four models chosen are best accurate when the wall $y^+ \leq 5$, i.e., the mesh must be fine enough to resolve the viscous sublayer. The complete formulations and incorporation of the aforementioned turbulence models into the Eulerian multiphase framework is detailed in the ANSYS FLUENT-Theory guide [145], and hence omitted here for brevity. However, the details of the k-ε- RNG + EWT model are presented in the Section-4.1.2.2.

Figure 5.18 (a) illustrates the predicted magnitudes of local surface temperature and total heat flux on the impingement surface with the choice the turbulence model for a typical case: same as that used for the discussion of grid sensitivity analysis in Section-5.2.1. It is seen from the figure that the trends as well as the magnitudes of predictions from all the four different turbulence models are very similar, with a maximum difference of about $\pm$ 8 % in the magnitudes for the local heat flux and about $\pm$ 0.8 ^{o}C for the local surface temperature. It is also seen from the comparison of the area averaged component heat fluxes in Fig. 5.18 (b), and heater temperature and liquid vapor phase change rate on the heater in Fig. 5.18 (c) that the effect of the choice of turbulence model is not very substantial on the predictions, particularly on the predicted average heater temperatures where the difference is only $\pm$ 0.6 ^{o}C, although the difference in the predicted component heat fluxes and the liquid-vapor phase change rate vary upto $\pm$ 10 %. The heater-area weighted phase-change rate on the heater-fluid interface shown in the figure is defined as

$$\Omega = \frac{1}{A_H} \int_{A_S} \phi . dA \tag{5.1}$$

where A_H, A_S and ϕ are the area of the heater, area of the impingement surface and the liquid-vapor phase-change rate per unit volume of the mixture, respectively. It is also notable that the maximum deviations in the local or the averaged quantities are largest when using the RSM model as compared to the counterparts listed above. Considering the small differences obtained between different turbulence models used, and in lieu of any experimental or DNS data for the turbulence parameters during jet impingement boiling against which the present computational approach could be compared, the k-ε-RNG+EWT is chosen for all simulations carried out for the present research. The choice was based on the relatively better characteristics of convergence stability and computational time obtained as compared to its counterparts explored.

5.2.3   Validation and Effect of Boiling Sub-models on Prediction Capability

As is the case for any subcooled flow boiling problem, impingement boiling heat transfer is characterised by the complex interactions between the ebullition from numerous sites on the heated surface (with a temperature greater than saturation temperature of the fluid), and the thermal hydraulics in the bulk flow. The interactions typically involve the heat and mass transfer between the phases, lift/ drag and buoyancy forces on the bubbles, bubble coalescence/ collapse, and the associated turbulence contribution to bulk flow particularly near the heated wall. Computational modeling of the phenomenon would require accurate prediction of the ebullition process involving the bubble diameters during growth and departure, bubble growth time and dwelling time (interval between bubble departure and the occurrence of a subsequent bubble in the void), active nucleation site density on the superheated surface, to mention a few. Although a diverse range of models have been proposed in the literature for modeling the various ebullition parameters that have each been validated for a rather limited range of fluids, operating conditions and applications, there is no definite consensus on generalized models for these parameters for the variety of flow boiling applications of interest. Thus, a thorough problem-based evaluation of the available models to conform to experimental data is often required to ensure a realistic simulation of the complex physics. Realising this essentiality in validating the suitability of any such model for the present studies, a sensitivity analysis is carried out for two different bubble departure diameter models

(represented as BDD from hereon) and three different models for bubble departure frequency (represented as BDF from hereon), for the simulation of submerged and subcooled jet impingement boiling by comparison against experimental data obtained in the present research, as well as published experimental data of Shin et al. [76]. The choice of models encompass both pool boiling as well as flow boiling based models, developed from both experimental as well as mechanistic approaches. The details of the geometry and operating conditions of Shin et al. [76] against which the present computational results are compared, along with the material properties assumed for the simulation are presented in Table-5.1. The geometric configuration pertaining to the experimental data of the present research (used for validation in this section) are detailed Section-4.2, while the relevant operating conditions for the data are indicated wherever required in the discussion.

Table 5.1: Experimental operating conditions of Shin et al. [76] and corresponding material properties used in the present simulations

Schematic of jet impingement configuration					
Working fluid	Degassed dielectric fluid PF-5060 (3M)				
Operating Pressure	101.325 k Pa (atmospheric pressure)				
Power/ heating	6.4 to 32 W ; uniform volumetric heat generation				
Heater plate	467 μm thick; polished Inconel^{TM}-600 alloy				
Subcooling	$\approx 25^{o}$C				
Reynolds number	$2000 \leq Re \leq 5000$; based on hydraulic diameter of nozzle				
Standoff distance	$h = 2$ mm and 8 mm, corresponding to $H = 1$ and 4				
Heater size	$w_H = 10$ mm, corresponding $w_H/w_N = 5$				
Experimental uncertainty	$q_T \rightarrow \pm 2.64$ % and $\Delta T_E \rightarrow \pm 2.8$ ^{o}C				
Property	Units	liquid	vapor	Inconel^{TM}-600	Polycarbonate
ρ	kg/m^3	1658.836	13.4	8470	1210
k	W/m-K	0.05658	0.02	14.9	0.22
c_p	J/kg-K	1062.347	500	444.0	1250
μ	Pa-s	5.65×10^{-4}	1.81×10^{-5}		
T_{sat}	K	329.15			
σ	N/m	0.00827			
L	J/kg	88000			

(a) Comparison against

present experimental data

(b) Comparison against data

of Shin et al. [76]

Figure	ΔT_{sub} ^{o}C	Re -	H -	w_H/w_N -	Fluid
(a)	7.45	9836	7	10	FC-72
(b)	25.10	2995	1	5	PF-5060

○ Shin et al. [76] experiment

● Present experiment

● Unal

▲ Tolubinsky & Kostanchuk

■ Tolubinsky & Kostanchuk with high-VF$_2$-corrections

Figure 5.19: Comparison of surface-averaged boiling curves obtained using various

models for bubble departure diameter against experimental data from the present

research and that of Shin et al. [76]; ⟶ indicates CHF

5.2.3.1   Choice of Bubble Departure Diameter

Figure 5.19 illustrates the comparison of boiling curves obtained using the present

numerical framework with the bubble departure diameter modelled according to two

different models, due to Unal [82] and Tolubinsky and Kostanchuk [80] against

experimental data obtained in the present research using FC-72 as well as the

experimental data of Shin et al. [76] where the working fluid was PF-5060 (a fluid

very similar in thermophysical properties to FC-72). The other operating conditions

pertaining to the boiling curves shown are listed in the figure caption. It is seen from

the figures that irrespective of the Reynolds number or the standoff distance or

degree of subcooling considered, the surface temperature predicted due to the use of

Tolubinsky and Kostanchuk's model are consistently and substantially higher as

compared to the experimental data, while that due to the use of Unal's model are in

reasonable agreement with the experimental data. The consistent overprediction of surface temperatures due to Tolubinsky and Kostanchuk's model throughout the

(a) Unal

(b) Tolubinsky and Kostanchuk

(c) Tolubinsky and Kostanchuk with high-VF_2 corrections
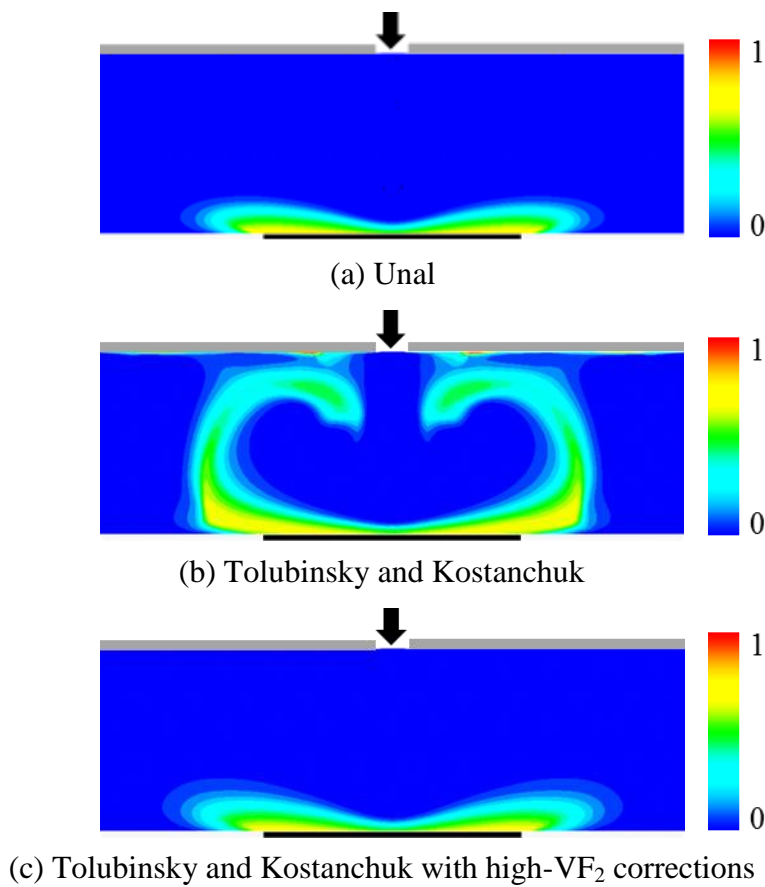
Figure 5.20: Comparison of vapor phase volume fraction in the domain obtained from simulations using various models for bubble departure diameter, for jet impingement boiling of FC-72 at $\Delta T_{sub} = 7.45\ ^{o}$C, $H = 7$ and $Re = 9836$

boiling curve could be attributed to the weak relationship between the model and the pertinent flow conditions existing in the domain. From comparison of Figs. 5.20 (a) and (b) it is also evident that the vapor phase volume fraction in the domain is substantially larger from the use of Tolubinsky and Kostanchuk's model as compared to that obtained from the use of Unal's model in the simulations. It is seen that the maximum magnitude of local vapor phase volume fraction in the domain is close to 1.0 with the use of Tolubinsky and Kostanchuk's model for BDD, for the case considered. Under conditions of such high vapor fraction, the interphase drag coefficients under the Eulerian multiphase model must be suitably altered (when the vapor fraction rises beyond a threshold of about 0.8) [145] to account for the change in the multiphase flow regime from vapor-in-liquid to droplet-in-vapor. Besides, due

to the large concentration of the vapor near the heated surface, the non-isothermal behaviour of the vapor phase must be accounted for, unlike the assumption in the RPI framework. Hence, the simulations are repeated with the so called Wall-Boiling-CHF model [145] in FLUENT 14.5 for the same operating conditions. It is to be noted that the name of the model is a *misnomer* as it is not "only" applicable to CHF conditions, but also conditions below to CHF where vapor phase volume fractions are large. The model is henceforth referred to in this thesis as the RPI-model-with-VF_2 corrections. As seen from Figs. 5.19 (a) and (b), this modification of the RPI wall boiling model results in more reasonable prediction in the boiling curve although the departure diameter was still modeled using Tolubinsky and Kostanchuk's model. It is also seen from comparison of Figs. 5.20 (b) and (c) that the vapor phase volume fraction in the domain are also now substantially reduced. However, no such change in the boiling curves was obtained from the use of non-
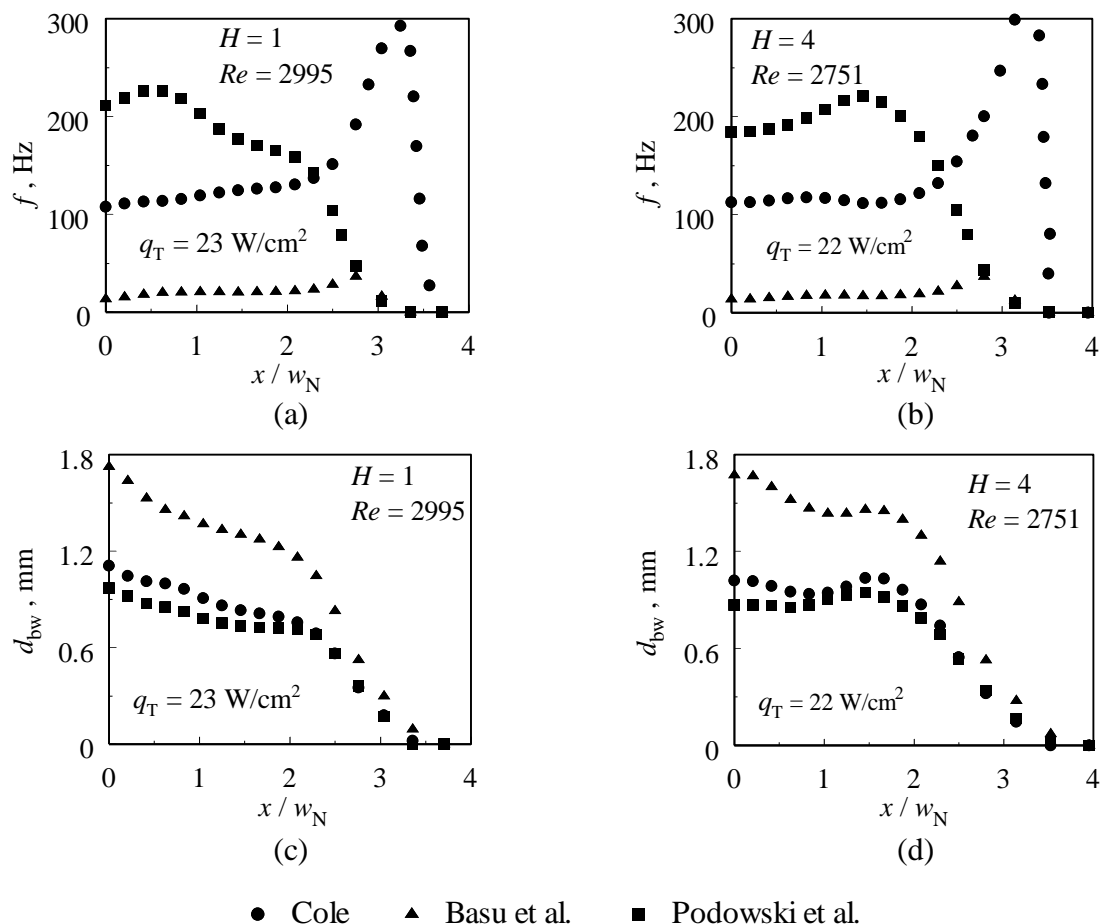
Figure 5.21: Distribution of bubble departure frequency and diameter on the impingement surface, obtained using various BDF models, for two representative cases; working fluid = FC-72

isothermal vapor phase in the domain with Unal's model for BDD. In lieu of any general model for the wide range of operating conditions that could prevail for subcooled jet impingement boiling, or particular to the fluids used for the investigation (FC-72 or PF-5060), Unal's model for the prediction of bubble departure diameter was deemed more suitable for the simulations. The other factor leading to this conclusion was the operating flow conditions where the model was empirically correlated, which encompasses the flow conditions considered in the present computational studies. It is however, interesting to note that Tolubinsky and Kostanchuk's model for bubble departure diameter has been reported to yield good predictions of both, surface averaged as well as local the surface heat transfer characteristics for tube boiling applications when compared against experimental data [142,143]. Thus, all the further computational data from the present research discussed hereon pertain to simulations using Unal's model for the prediction of bubble departure diameter.

5.2.3.2   Choice of Bubble Departure Frequency

Figures 5.21 (a,b) and Figs. 5.21 (c,d) illustrate the local distribution of bubble departure frequency and diameter, respectively, on the impingement surface for two representative cases *viz.* (i) $H = 1$, $Re = 2995$, $q_T = 23$ W/cm^2 (82 % of CHF); and (ii) $H = 4$, $Re = 2751$, $q_T = 22$ W/cm^2 (76% of CHF). It is seen from the figures that
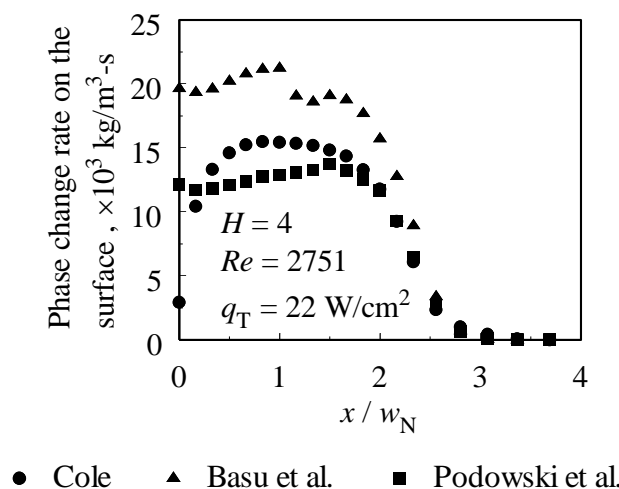
Figure 5.22: Distribution of liquid-vapor phase change rate on the impingement surface for $H = 4$, $Re = 2751$ and $q_T = 22$ W/cm^2

Basu et al.'s model, as compared to Cole and Podowski et al.'s models consistently relatively underpredicted the magnitude of BDF. As a lower value of bubble departure frequency would imply that the bubble spends a longer time on the surface before departing, the energy transferred to the bubble for growth is also larger. Consistently the magnitudes of predicted bubble departure diameters are also relatively larger when Basu et al.'s model is used, as seen in Figs. 5.21 (c,d). This is also evident from the magnitude of liquid-vapor phase change rate on the surface in Fig. 5.22 for $H = 4$, $Re = 2751$ and $q_T = 22$ W/cm^2. As the discussion for the other heat fluxes and Reynolds numbers considered herein is qualitatively the same, the data is omitted for brevity. It is also seen from Figs. 5.21 (a, b) that the magnitude of BDF predicted by Cole's model seem to anomalously peak near the extremity of the heater ($x/w_N = 2.5$). This is due to the exclusory (neglecting the other thermo-hydraulic conditions) inverse dependence of BDF on the bubble departure diameter (which is smaller near the extremity of the heater due to lower thermal energy transfer from the surface) assumed in Cole [85], unlike the other models[86,87] analysed herein.

Figures 5.23 (a-c) and Figs. 5.23 (d-f) illustrate the comparison of average (on the heater region, i.e. upto $x/w_N = 2.5$ representing the heated area) values of bubble departure diameter and frequency, respectively, against total heat flux, predicted by use of the three BDF models, for $H = 1$, $Re = 1967$, 2995 and 4916. Figures 5.24 (a-c) and Figs. 5.24 (d-f) illustrate the corresponding values for $H = 4$, $Re = 1999$, 2751 and 4998. In line with the discussion in the earlier paragraph, irrespective of the values of heat flux, Reynolds number or standoff distance, the magnitude of bubble departure diameter predicted from the use of Basu et al.'s model is seen to be consistently larger as compared to the two other models investigated herein. In coherence, the predicted value of bubble departure frequency from Basu et al.'s model is consistently relatively lower (in some cases upto an order of magnitude), over the complete range of parameters studied. Interestingly, while the magnitudes of average bubble departure diameters due to the implementation of Cole's and Podowski et al.'s models seem to fall in the same range and follow the same qualitative trend with increase in surface heat flux, the values of BDF predicted by Podowski's model increases with increase in heat flux, while that due to Cole decreases with increase in heat flux. It is also of interest to note that although

● Cole ▲ Basu et al. ■ Podowski et al.
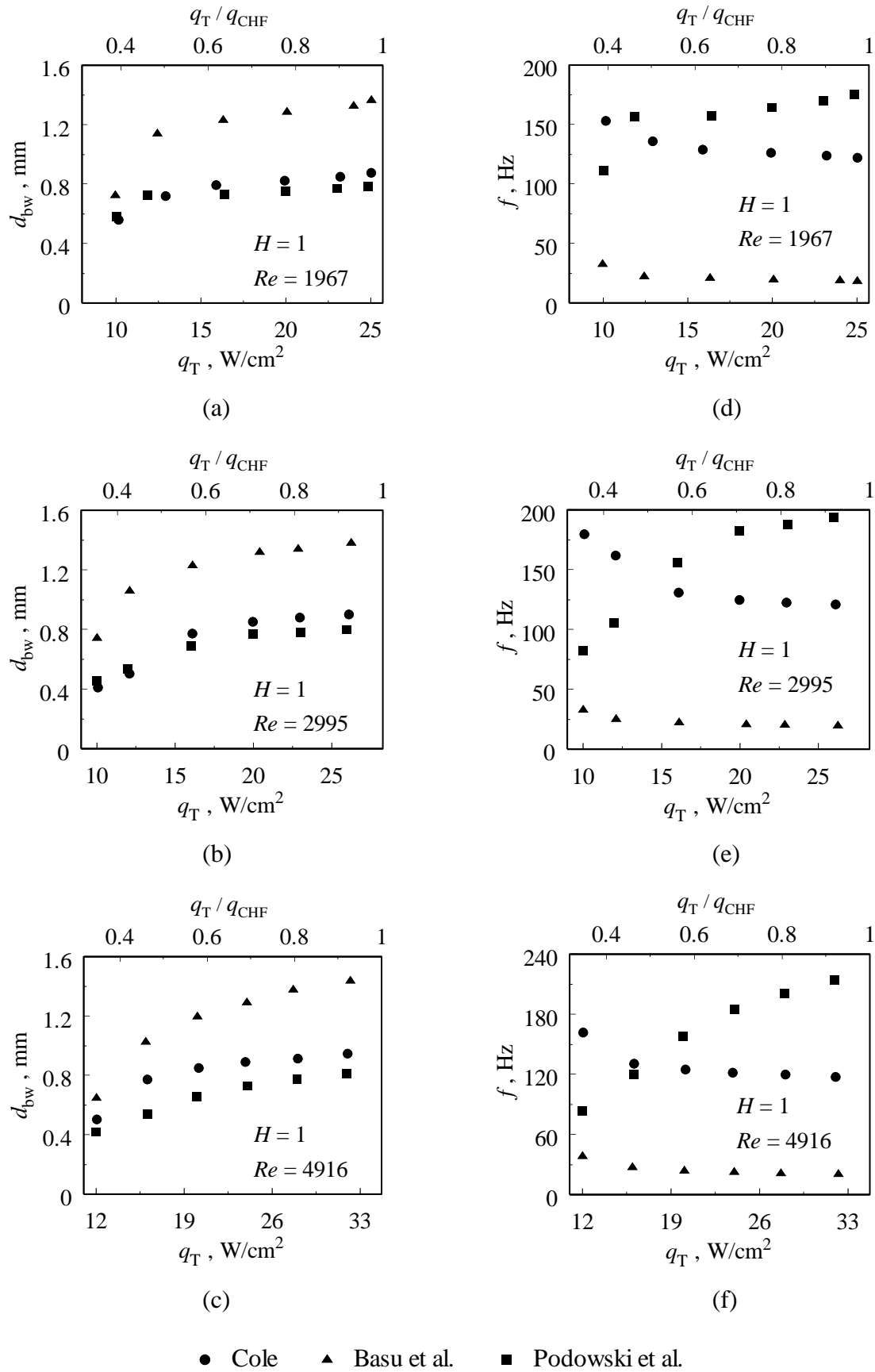
Figure 5.23: Variation in bubble departure diameter and frequency with average

surface heat flux for $H = 1$, and $Re = 1967$, 2995 and 4916

(a)

(b)

(c)

(d)

(e)

(f)

● Cole   ▲ Basu et al.   ■ Podowski et al.
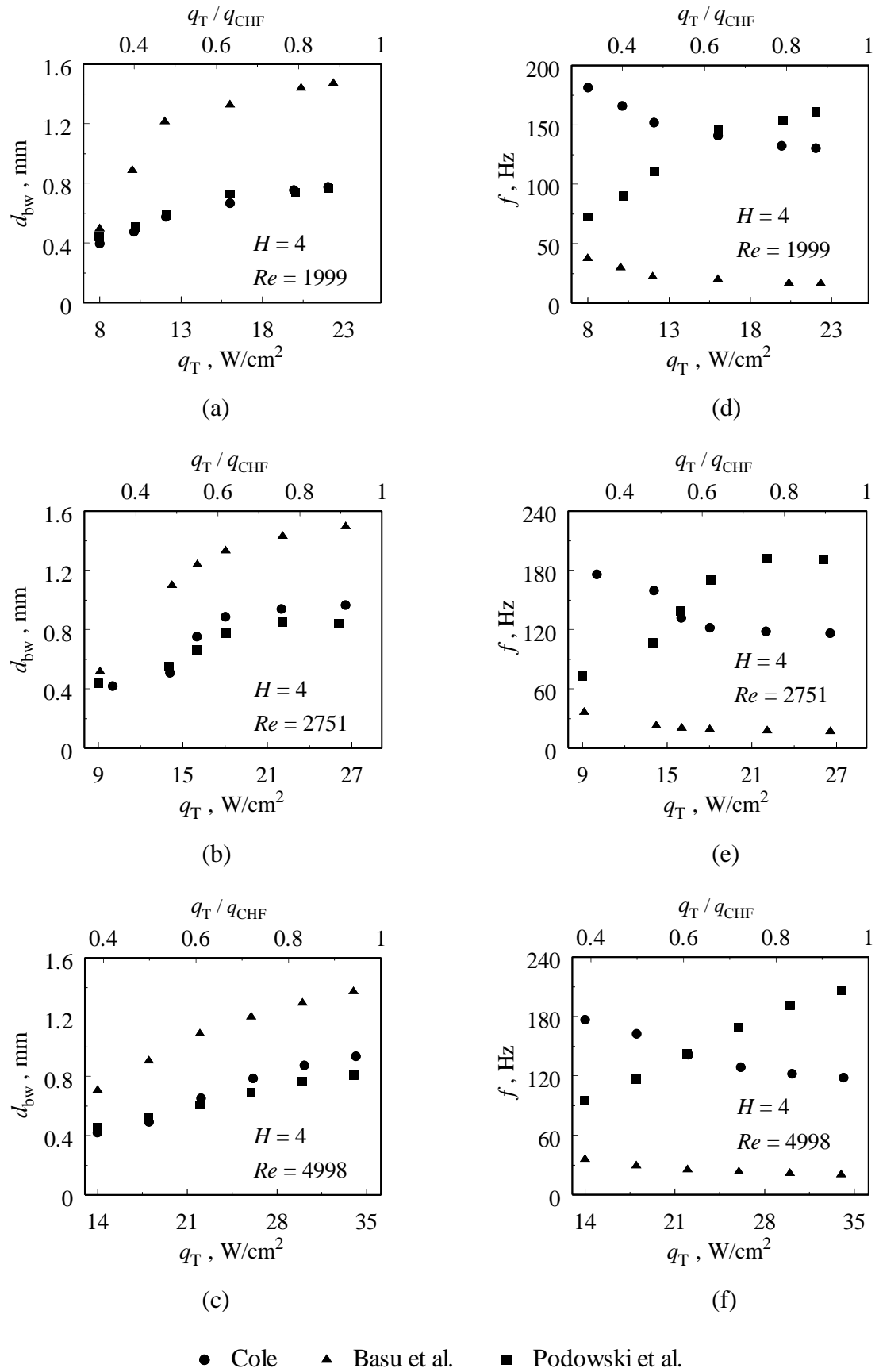
Figure 5.24: Variation in bubble departure diameter and frequency with average

surface heat flux for $H = 4$, and Re = 1999, 2751 and 4998

Basu al.'s model which was developed particularly for flow boiling following a physical basis similar to that of Podowski et al.'s model, their corresponding relationships between BDF and the surface heat flux show contrary trends, as seen in Figs. 5.23 (d-f) and Figs. 5.24 (d-f). This is evidently corroborated from the variation in the bubble departure frequency with bubble departure diameter illustrated in Fig. 5.25 for the range of parameters studied. It is also seen from the figure that the predicted magnitudes of bubble departure frequency and diameters from the use of Podowski's model distinctly indicate a variation with change in Reynolds number and standoff distance, while the same is not very prominent from the use of the other two models.
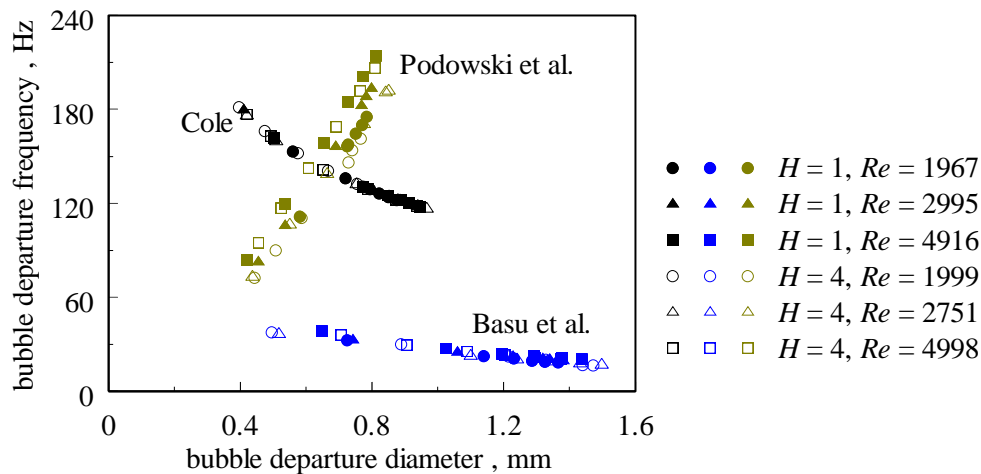
Figure 5.25: Relationship between the predicted values of surface averaged bubble departure diameter and frequency, obtained using various models for bubble departure frequency

As seen in the present computational results using Podowski et al.'s model, Podowski et al. [87] also demonstrated in their paper that the bubble departure frequency increased with increase in surface heat flux, for a given set of other parameters such as subcooling, pressure, fluid velocity and surface conditions. In a more recent paper, Chang et al. [161] observed from flow boiling experiments in a horizontal channel using FC-72 (which is very similar in all respects of thermo-fluid properties as the fluid used for the present discussion: PF-5060), that the bubble departure frequency increased with increase in surface heat flux ceteris paribus, for both smooth as well as micro-pin-finned surfaces. Several other experimental studies in the literature on pool as well as flow boiling of FC-72 [162-166] also reported the
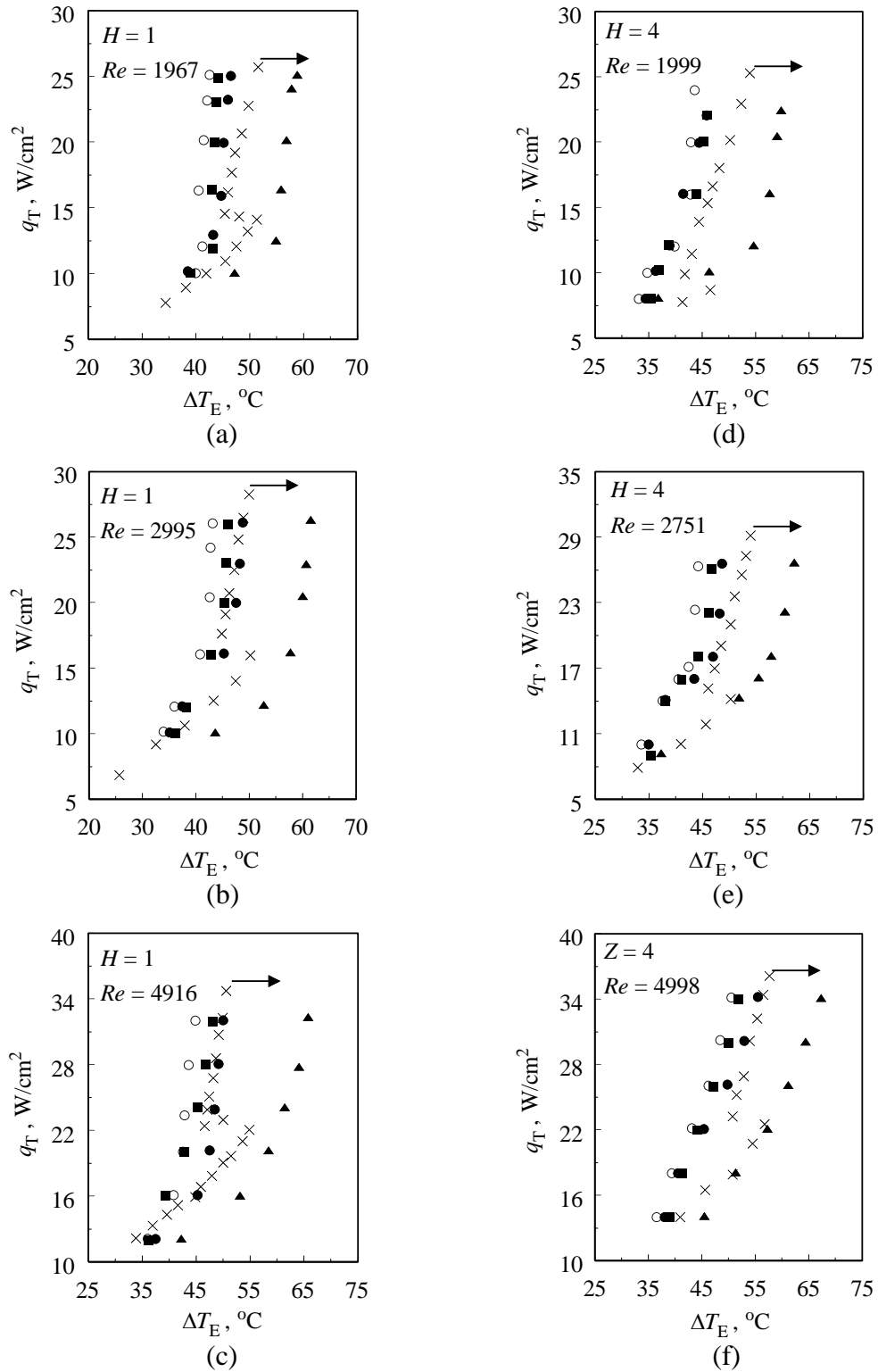
Figure 5.26: Comparison of surface-averaged boiling curves obtained using various models for bubble departure frequency; $\longrightarrow$ indicates CHF

directly proportional relationship between the total surface heat flux and the bubble departure frequency, thereby reassuring confidence in the trends observed in the

simulations using Podowski et al.'s model for BDF. On the contrary, several experimental studies including the detailed list of models summarised in Ivey [83] and Carey [167] present an inverse relationship between the bubble departure frequency and diameter. Ivey [83] postulated that there are three distinct regimes (hydrodynamic, transition and thermodynamic) for ebullition during nucleate boiling, and the relationship between bubble departure frequency and diameter was correlated as:

$$f \times d_{\mathrm{bw}}^{\mathrm{n}} = \mathrm{constant} = F(\text{thermophysical properties}) \tag{5.2}$$

where the exponent ($n > 0$) depended on the regime and the fluid. As mentioned earlier, this inversely proportional relationship between the bubble departure frequency and diameter is obtained when using Cole's model for BDF in the simulations. In the hydrodynamically controlled regime (which is the basis for Cole's BDF model), ebullition is assumed to purely depend on buoyancy and drag forces, thus neglecting the influence of inertia, surface tension and viscous forces. In the transition regime [83], the bubble departure diameter and frequency depended on all the three forces: buoyancy, drag and surface tension that are equal in order of magnitude. In the thermodynamically controlled ebullition regime [83], the influence of heat transfer rate through the region near the liquid vapor boundary was considered most influential. In summary, there has been experimental evidence for both, a directly proportional as well as an inversely proportional relationship between bubble departure frequency and departure diameter (or total heat flux, as the d_{bw} increases with increase in q_{T}). It is pointed out that the lack of sufficient experimental bubble dynamics data for submerged jet impingement boiling presents a constraint on a conclusive comment on the validity of the exact physical dependence of the departure frequency on surface heat flux and departure diameter.

Figures 5.26 (a-f) illustrate the boiling curves obtained in the present simulations using the three BDF models against experimental data of Shin et al. [76]. In addition to boiling curves obtained due to the three BDF models, those obtained from using FLUENT's inbuilt version are also included. This is because, although the BDF model in FLUENT is based on Cole [85], there is some ambiguity in how some of the wall-boiling model closures such as the characteristic temperature and velocities (see Eqs. (4.51-4.54) of Section-4.1.2.3) are evaluated therein, which in turn influence the flow and thermal characteristics in the domain. It is seen from the

figures that irrespective of the standoff distance or the Reynolds number (in the range considered) the average surface temperature is consistently overestimated by use of Basu et al.'s model for BDF, while the predictions from the use of Cole and Podowski et al.'s models are in better agreement with the experimental boiling curves. The consistent overestimation of the surface temperature due to Basu et al.'s model is a consequence of the overestimation of the liquid to vapor phase change rate explained earlier (discussion on Fig. 5.22) which results in larger vapor volume fraction near the heater surface. Situ et al. [89] carried out similar simulations on subcooled flow boiling in a tube for a range of subcoolings, pressures, mass flow rates and heat fluxes, and observed a similar poor relationship between the predictions using Basu et al.'s model against their experimental data. As Basu et al. [86, 168] reported their model to conform well with their experimental flow boiling data within an error of ± 30 %, it would only be reasonable to mention that the choice of models are extremely problem dependant.

It is interesting to note that, although the predicted relationship between the bubble departure frequency and heat flux obtained due to Podowski et al.'s and Cole's models are completely different (see Fig. 5.25), the corresponding boiling curves are not as much in deviance. This is possibly due to: (i) the fact that the evaporative heat flux is related strongly to the cubic power of the departure diameter while only a linear relationship with the departure frequency (defined as $q_{\mathrm{E}} = (\pi/6) d_{\mathrm{bw}}^3 f N_{\mathrm{w}} \rho_{\mathrm{v}} L$); (ii) the magnitude of BDF obtained from use of Podowski et al.'s and Cole's models are similar. It is thus identified that although Cole's model was not particularly developed for flow boiling, the predicted surface-averaged heat transfer data are in good agreement with experiments. Of the three models considered for the present analysis, Podowski et al.'s model for bubble departure frequency seems to be most suitable considering the relatively greater physical justification behind the model as compared to that of Cole's, for particular application to jet impingement boiling problems.

It is however pointed out that due to the enormous complexity of the computational framework involving several interrelated mechanistic as well as empirical closures that are solved in conjunction with the governing conservation equations, a more thorough sensitivity analysis may be required to isolate the effects

of each of the model parameters for any conclusive comment on their validity for jet impingement boiling.
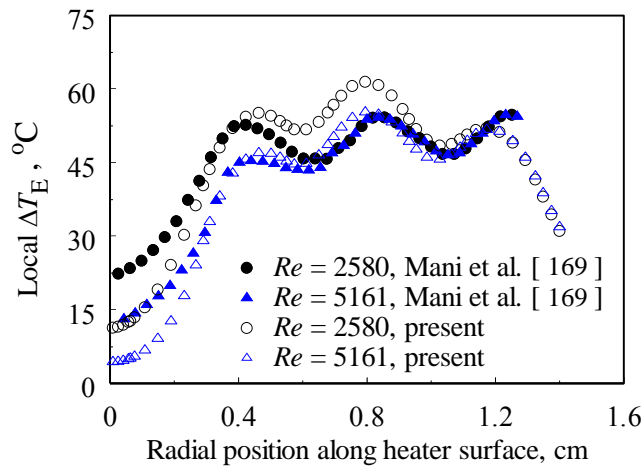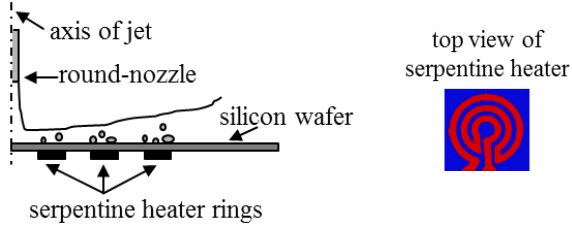
Figure 5.27: Comparison of predicted local surface temperature during subcooled submerged and unconfined jet impingement boiling against experimental data of Mani et al. [169]

An exercise was also carried out to check the validity of the present computational technique for subcooled submerged round/ axisymmetric jet impingement boiling in an unconfined configuration. The experimental conditions of Mani et al. [169] from where the experimental data are used to compare the present computational predictions are illustrated in Table-5.2. While the earlier discussions in this section were based on comparison of the present computational predictions against area averaged experimental boiling curves, this study was particularly useful and insightful as local heat transfer data was available, unlike most papers on slot jet impingement boiling. Figure 5.27 shows the surface temperature on the heater obtained from the present numerical simulations with water for two different jet Reynolds numbers $Re = 2580$ and 5161 for a heater power of 442 W, superimposed on the experimentally obtained temperature distribution of Mani et al. [169]. It is seen from the figure that the predicted numerical results for the local temperature distribution on the silicon (impingement) surface are in good agreement with the experiments of Mani et al. [169]. The maximum absolute error in the local surface temperature (in K), defined as $Error = 1 - T_{pred}/T_{expt}$, is found to be about $\pm$ 2 %, while the magnitude of the maximum deviation in the surface temperature is about $\pm$ 7 ^{o}C in the stagnation region and less than about $\pm$ 4 ^{o}C on the rest of the heated

impingement surface. It is also seen that the local peaks in the temperature distribution due to the radially discrete rings of the serpentine heater elements are captured accurately in the numerical simulations. This exercise reiterates that the present computational model is suitable for the simulation of jet impingement boiling with reasonable accuracy despite the various modelling constraints that underlie.

Table 5.2: Experimental operating conditions of Mani et al. [169] and corresponding material properties used in the present simulations

Schematic of jet impingement configuration	
Working fluid	De-ionized and degassed water
Operating Pressure	101.325 k Pa (atmospheric pressure)
Power/ heating	442 W ; discretized-uniform volumetric heat generation (serpentine heater)
Heater surface	380 µm thick; polished silicon
Subcooling	$\approx 20^{\circ}$C
Reynolds number	2580 and 5161; based on nozzle diameter
Standoff distance	$h = 4.176$ mm, corresponding to $H = 3.6$
Heater size (total diameter)	$d_H = 25.4$ mm, corresponding $d_H/d_N = 22.76$
Experimental uncertainty	$q_T \rightarrow$ average :±3.8 %, maximum: 10.9 % $\Delta T_E \rightarrow$ average :±3.2 %, maximum: 6.9 %

Property	Units	liquid	vapor	Copper
ρ	kg/m^3	965.23	0.5976	8978
k	W/m-K	0.675	0.02512	387.6
c_p	J/kg-K	4205.54	2078.18	381.0
μ	Pa-s	3.156×10^{-4}	1.227×10^{-5}	
T_{sat}	K	373.12		
σ	N/m	0.059		
L	J/kg	2257000		

5.2.4   Surface Heat Flux Partitioning during Subcooled Confined and Submerged Jet Impingement Boiling

The discussion presented hereunder on the effects of geometry and thermophysical conditions of the impinging jet on the partitioning of surface heat flux are based on

simulations carried out with subcooled water as the working fluid that impinges on a heated copper surface resulting in submerged jet impingement. The impingement surface comprises of a copper plate of length $w_H = 50$ mm and thickness of 200 µm, and is at a dimensionless standoff distance of H from the plane of the nozzle exit. The copper plate is heated from below upto a length $w_H/2$ on either sides of the centerline of jet, while the rest of the plate is thermally insulated from outside the flow domain. Two types of heating to the impingement surface are considered *viz.* (i) *isothermal-heater*, where the bottom surface of the heater is maintained at a constant temperature, and (ii) *isoflux-heater*, where uniform heat flux is applied at the bottom surface of the heater. The flow passage is sandwiched between the copper plate and
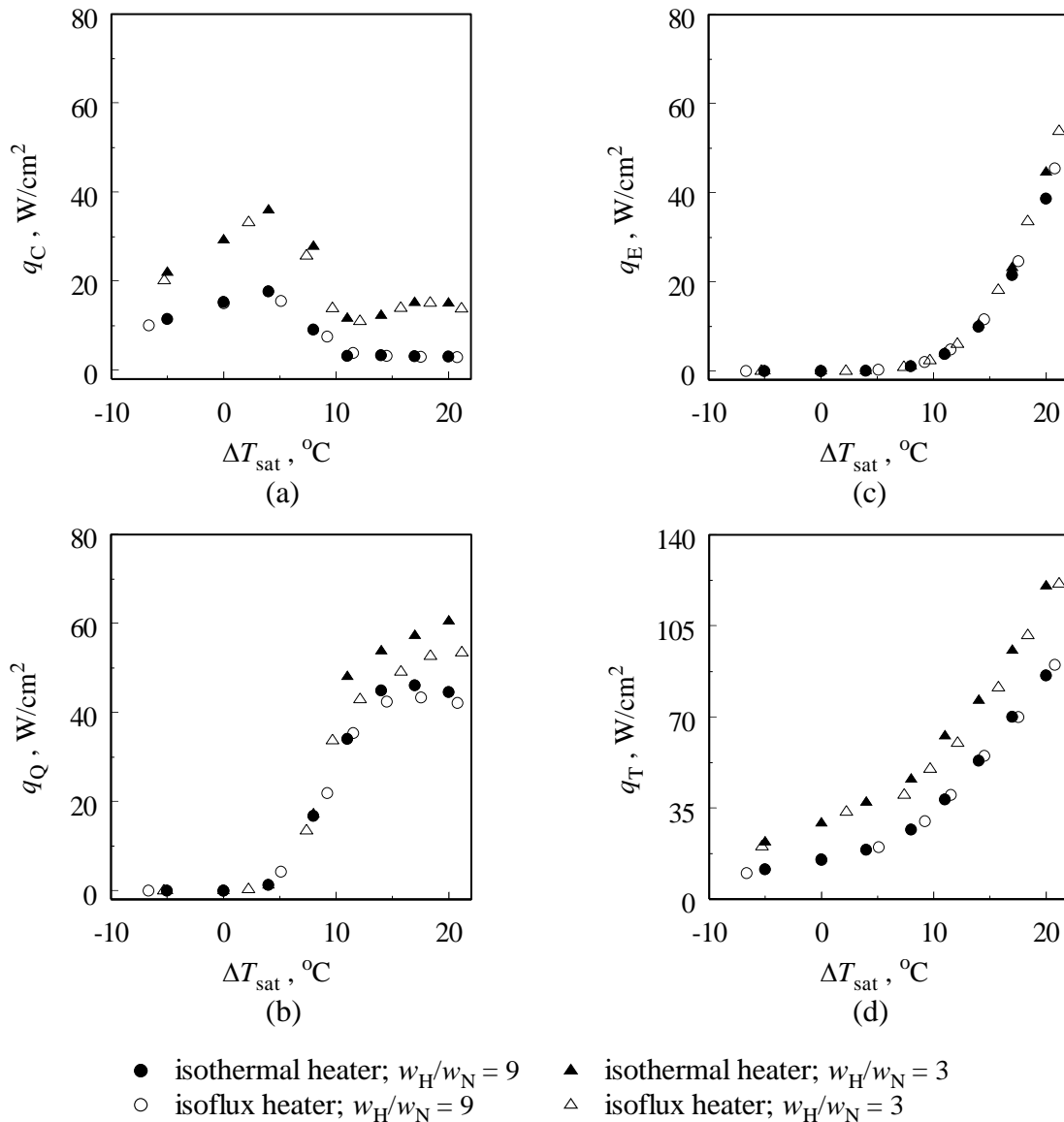
Figure 5.28: Comparison of boiling curves between isothermal and iso-flux heaters of various sizes for $Re = 2500$; $\Delta T_{sub} = 20$ ^{o}C and $H = 4$

2 mm thick polycarbonate confinement blocks on either sides of the centerline of jet, that are thermally insulated from the outside, as shown in the Fig. 4.4 of Section-4.1.2.

5.2.4.1   Comparison of Temperature Controlled and Heat Flux Controlled Boiling Curves

Figures 5.28 (a-d) show the area averaged boiling curves of the liquid phase convective, quenching, evaporation and total heat fluxes for isothermal and iso-flux heaters for two sample heater sizes of $w_H/w_N = 3$ and 9, and a jet Reynolds number of

- ● isothermal heater; $w_H/w_N = 9$ ▲ isothermal heater; $w_H/w_N = 3$
- ○ isoflux heater; $w_H/w_N = 9$ △ isoflux heater; $w_H/w_N = 3$
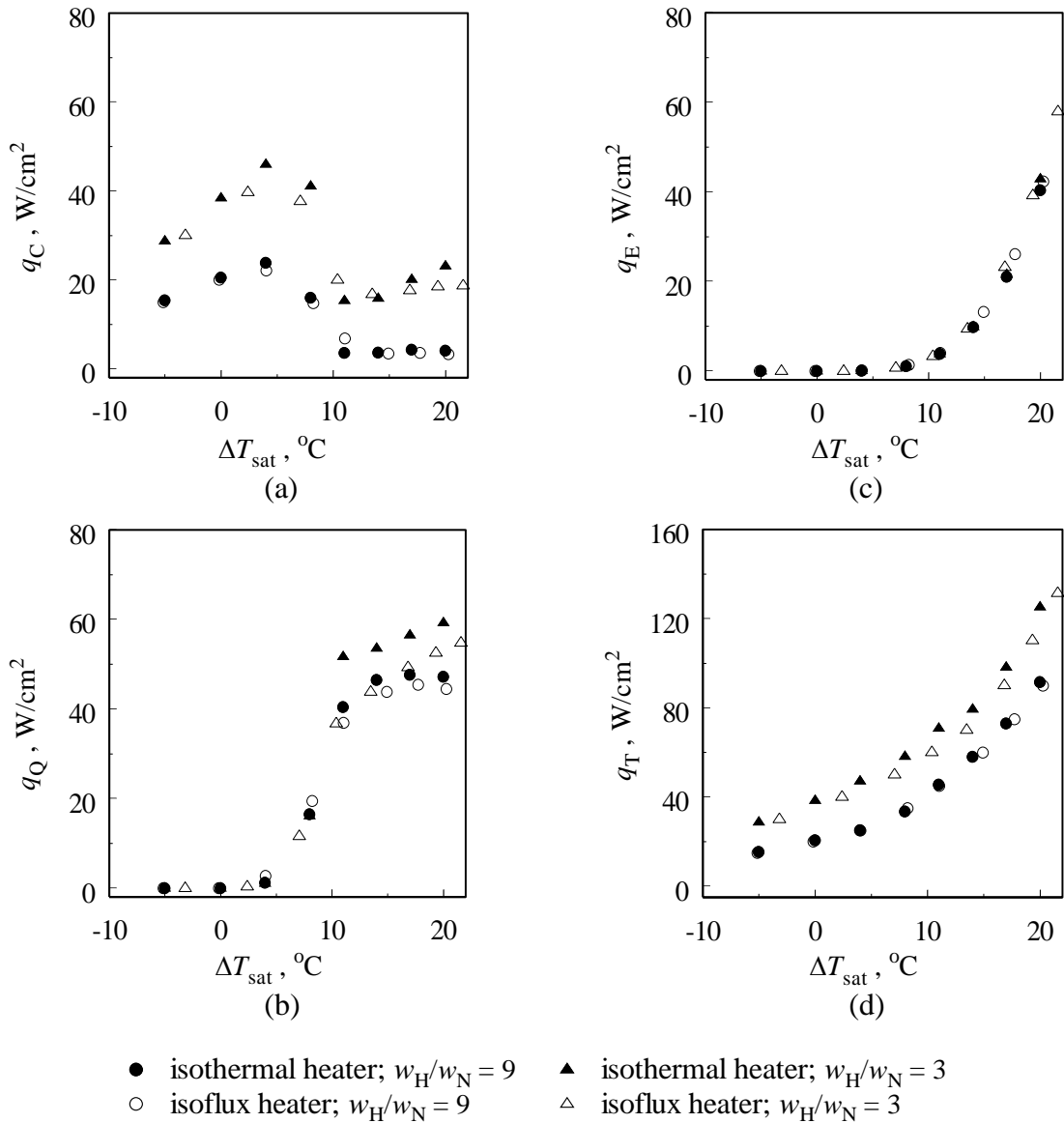
Figure 5.29: Comparison of boiling curves between isothermal and iso-flux heaters of various sizes for $Re = 3750$; $\Delta T_{sub} = 20\ ^oC$ and $H = 4$

Re = 2500. Figures 5.29 (a-d) show the corresponding plots for a jet Reynolds number of *Re* = 3750. It is seen from comparison of Figs. 5.28 (a-d) and Figs. 5.29 (a-d) that the steady state characteristics of boiling exhibited by the two types of heaters *viz.* isothermal and isoflux are nearly equivalent, irrespective of the heater size or Reynolds number, for the range of parameters considered. This predicted trend is congruent with the fact that the boiling curves due to the two types of heating employed start to deviate [170] from each other only beyond CHF, and considering that the applied heat fluxes/ wall temperatures for the present discussion are considerably below CHF. The slight variation between the predictions with isothermal and isoflux heaters is attributed to the conjugate conduction in the impingement (copper) surface beyond the heater. This exercise of comparison of the characteristics of boiling from the two types of heaters also reinforces the consistency in the numerical predictions for this conjugate multiphase heat transfer problem.
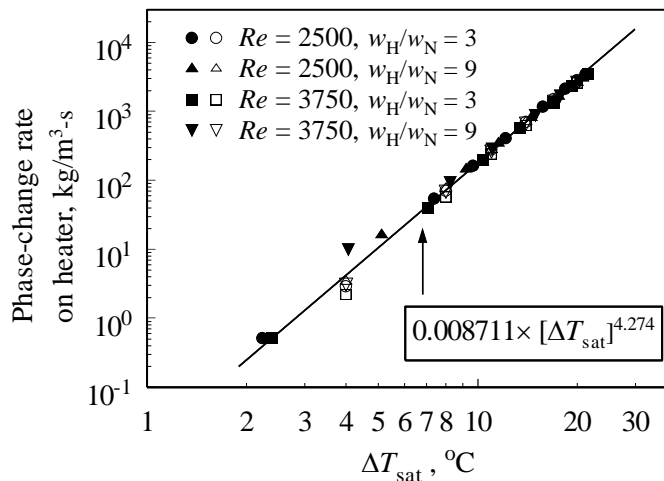
Figure 5.30: Comparison of the variation in liquid-vapor phase-change rate on the surface with average surface temperature, between isothermal (open symbols) and iso-flux (filled symbols) heaters, for *Re* = 2500 and 3750; $\Delta T_{sub} = 20\ ^{o}C$ and *H* = 4

It is seen from Fig. 5.28 (a) and Fig. 5.29 (a) that, for isothermal as well as isoflux heaters, the liquid phase convective heat flux increases linearly to a maximum of about 4 to 6°C and subsequently decreases with increase in average surface temperature of the heater over the range considered. Figures 5.28 (b-c) and Figs 5.29 (b-c) also indicate a rise in the quenching and evaporative heat fluxes from zero, with increase in surface temperature beyond a threshold, indicating the onset of

nucleate boiling for degree of superheats typically in the range of about 2 to 6°C. Figure 5.30 illustrates the variation in the heater-area weighted phase-change rate on the heater-fluid interface (Eq. (5.1)) with change in degree of surface superheat for Re = 2500 and 3750, and w_{H}/w_{N} = 3 and 9. In coherence with Figs. 5.28 (a-c) and Figs. 5.29 (a-c) it is seen from the Fig. 5.30 that the phase-change rate also increases exponentially from zero beyond this threshold value of surface superheat, vindicating the onset of nucleate boiling. As is known, the dimensionless heat transfer coefficient for forced convective single-phase jet-impingement heat transfer in any geometry is independent of the surface temperature (or applied heat flux), for a given jet Reynolds number. Hence, until the onset of nucleate boiling, the single phase convective component of the heat flux as shown in Fig. 5.28 (a) and Fig. 5.29 (a) shows a linear increase in heat flux with surface temperature (other components of the heat flux, *viz.* quenching and evaporation are zero during single phase convection, i.e. before onset of nucleate boiling). However, for any increase in the surface temperature (or increase in surface heat flux in the case of isoflux heaters) beyond this threshold degree of surface superheat, as nucleate boiling sets in, the total area of the impingement surface available for single phase convection reduces due to the presence of the vapor bubbles on the surface. The exponential rise in the liquid-vapor phase-change rate on the surface in Fig. 5.30 also indicates a proportional rise in the concentration (or the area density) of the vapor-phase on the surface (see Eq. (4.40) of Section-4.1.2.3). Consequently in this regime of the boiling curve, the liquid phase convective component of the heat flux decreases initially with a steep descent with any further increase in applied surface temperature (or surface heat flux). The liquid phase convective component of the heat flux is not completely eliminated with subsequent increase in heater temperature due to the conjugate conduction in the impingement surface beyond the length of the heater, that results in considerable convection (without boiling) at large temperatures of the heater.

Interestingly, upto a certain degree of surface superheat in the boiling regime immediately after onset of nucleate boiling, it is seen from Figs. 5.28 (a-b) and Figs. 5.29 (a-b) that the liquid phase convective heat flux decreases and the quenching heat flux increases, rather steeply, with increase in surface superheat. In this interval of the surface superheats, typically of about 4 to 10°C, the rate of increase of the evaporative heat flux (Fig. 5.28 (c) and Fig. 5.29 (c)) and the

evaporative phase-change rate on the heater (Fig. 5.30), with increase in surface temperature are lower, as compared to the intervals at relatively higher degrees of surface superheats. As the population of the vapor phase on the surface is still expected to be low in this interval of surface superheats immediately after the onset of nucleate boiling (indicating the isolated bubble regime), the temperature of the liquid region inside the thermal boundary layer is also lower due to lower bubble condensation (averaged in time; as the present analysis is steady state). Consequently, colder fluid occupies the region occupied by the bubble after detachment, resulting in large quenching (transient conduction). Besides, the increase in quenching heat flux can also be attributed to the relatively larger frequency of bubble departure with increase in applied surface temperature in this range of superheats. However, further increase in the surface temperature results in a consequent increase in the liquid phase temperature due to convective heat transfer, as well as due to interphase heat transfer from the vapor bubbles (as the fluid is subcooled) that are relatively larger in population as compared to that at lower surface temperatures. This adversely affects the quenching heat flux, resulting in a drop in the rate of increase of quenching heat flux with increase in surface degree of superheat despite rapid increase in vapor-phase volume fraction (implying an
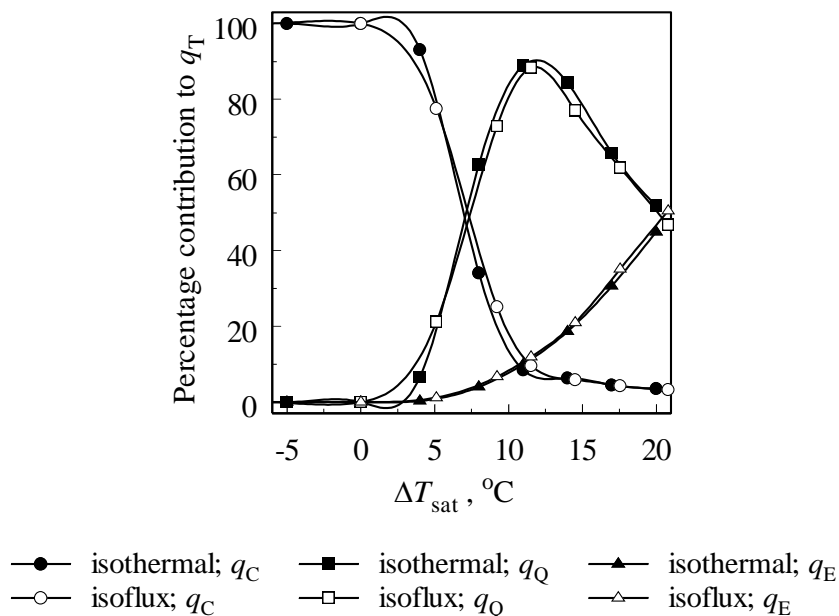
Figure 5.31: Variation in the percentage contribution of q_C, q_Q and q_E to q_T with average surface-superheat for isothermal and iso-flux heaters; $Re = 2500$, $w_H/w_N = 9$; $\Delta T_{sub} = 20\ ^oC$ and $H = 4$

increase in the nucleation sites for the range of heat fluxes considered). If this trend were to be extrapolated to high surface superheats, it would imply that as the surface is completely enveloped by vapor, the liquid phase and quenching components of the heat fluxes would become negligible [168]. As the volume fraction of the vapor near the surface of the heater becomes substantial at such large degrees of surface superheat, the RPI wall-boiling model deteriorates in accuracy (and hence not attempted in the present research). This is due to the assumption of isothermal properties of the vapor and the exclusion of the vapor phase convective heat flux in the partitioning of surface heat.

(a) $w_H/w_N = 1$

(b) $w_H/w_N = 3$

(c) $w_H/w_N = 11$
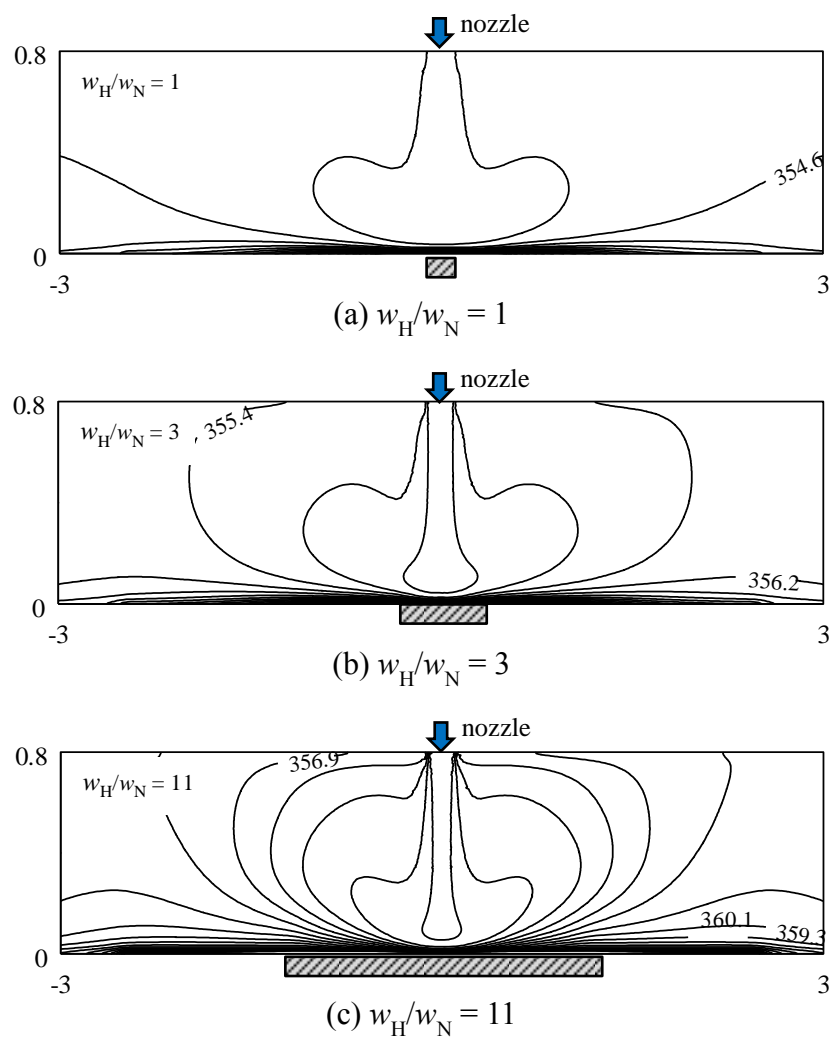
Figure 5.32: Contours of isotherms in the fluid domain for $Re = 2500$, $\Delta T_{sat} = 14\ ^{o}C$, for $w_H/w_N = 1$, 3 and 11 (isothermal heater), $\Delta T_{sub} = 20\ ^{o}C$ and $H = 4$; ▨ denotes the length of the heater; lengths are shown in cm; 20 isotherms are shown in the range $353 \leq T_l \leq 368$ K with $\Delta T_{l,\ isotherms} \approx 0.71$ K

Figure 5.31 illustrates the percentage contribution of liquid phase, quenching and evaporative heat fluxes to the total heat flux for a jet Reynolds number of 2500 for both isothermal and isoflux heaters of $w_H/w_N = 9$. In line with the earlier discussion, it is seen that the percentage contribution of the liquid phase convective heat flux monotonically reduces from 100% prior to the onset of nucleate boiling. On the contrary, the percentage contribution of quenching heat flux increases initially until the vapor fraction on the surface of the heater reaches a threshold, and consequently attenuates with further increase in the degree of surface superheat. The percentage contribution of the evaporative heat flux is seen to increase monotonically with increase in degree of wall superheat resulting in larger phase change from liquid to vapor.

5.2.4.2   Effect of Heater Size on Heat Flux Partitioning

Figures 5.32 (a-c) illustrate the contours of liquid phase temperature in the domain for typical case with dimensionless heater sizes of $w_H/w_N = 1$, 3 and 11, isothermal heater temperature at 387.12 K ($\Delta T_{sat} = 14^{\circ}$C) and jet Reynolds number of 2500. Figure 5.33 illustrates the comparison between the rates of liquid-to-vapor phase change on the heater-fluid interface for $T_{sat} = 14^{\circ}$C, $Re = 2500$ for $w_H/w_N = 1,3,7$ and 11. As can be seen from Figs. 5.32 (a-c), in the region near the impingement surface,
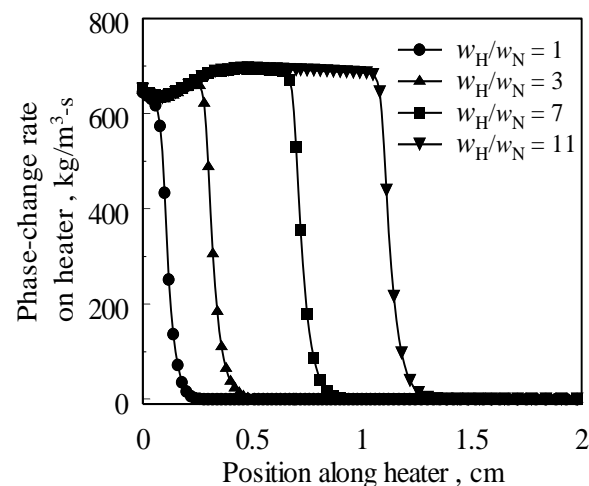
Figure 5.33: Comparison of liquid to vapor mass transfer rates on the heater-fluid interface between $w_H/w_N = 1$, 3, 7 and 11, for $Re = 2500$, $\Delta T_{sat} = 14\ ^{\circ}$C, $\Delta T_{sub} = 20\ ^{\circ}$C and $H = 4$
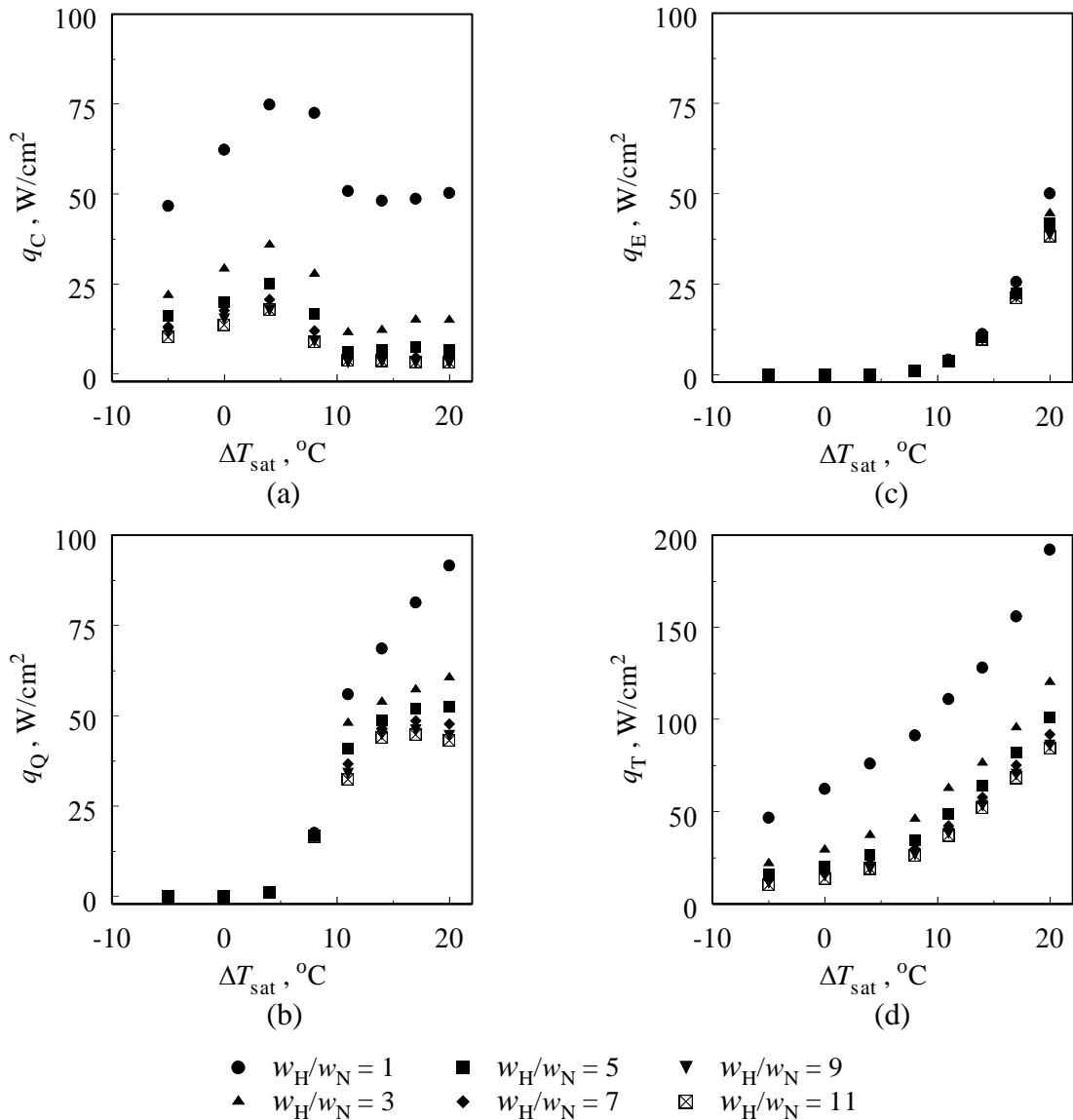
Figure 5.34: Boiling curves for isothermal heater; for $Re = 2500$, $\Delta T_{sub} = 20\ ^{o}C$
and $H = 4$

the isotherms are denser for $w_H/w_N = 1$ as compared to $w_H/w_N = 3$ and denser for $w_H/w_N = 3$ as compared to $w_H/w_N = 11$, indicating a larger temperature gradient on the impingement surface for relatively smaller heaters. Consequently, the liquid phase convective heat flux is larger for relatively smaller values of w_H/w_N, *ceteris paribus*. This trend is also evident from the surface averaged boiling curve for liquid phase convective component of the total heat flux illustrated in Fig. 5.34 (a). Due to the relatively thinner boundary layer for relatively smaller values of w_H/w_N (for any specified value of surface temperature or surface heat flux), relatively cooler fluid occupies the vicinity of the wall after bubble detachment, resulting in larger transient conduction or quenching [86,171]. In line with the preceding argument, it can be

seen from Fig. 5.34(b) that the magnitude of quenching heat flux (after the onset of nucleate boiling) is relatively larger for smaller heaters, for the range of heater sizes considered ($1 \leq w_H/w_N \leq 11$), and for any given heater temperature and jet Reynolds number. It is also seen from Fig. 5.33 that the total rate of phase change from liquid to vapor is clearly larger for larger heaters. Although it would be intuitive for the evaporative component of the total heat flux to follow the same trend, an opposite trend is seen from Fig. 5.34 (c) for smaller heaters, and almost negligible difference between any of the relatively larger heaters ($w_H/w_N \geq 3$). This is because, quite a

(a) $\Delta T_{sat} = 14\ ^oC$

(b)
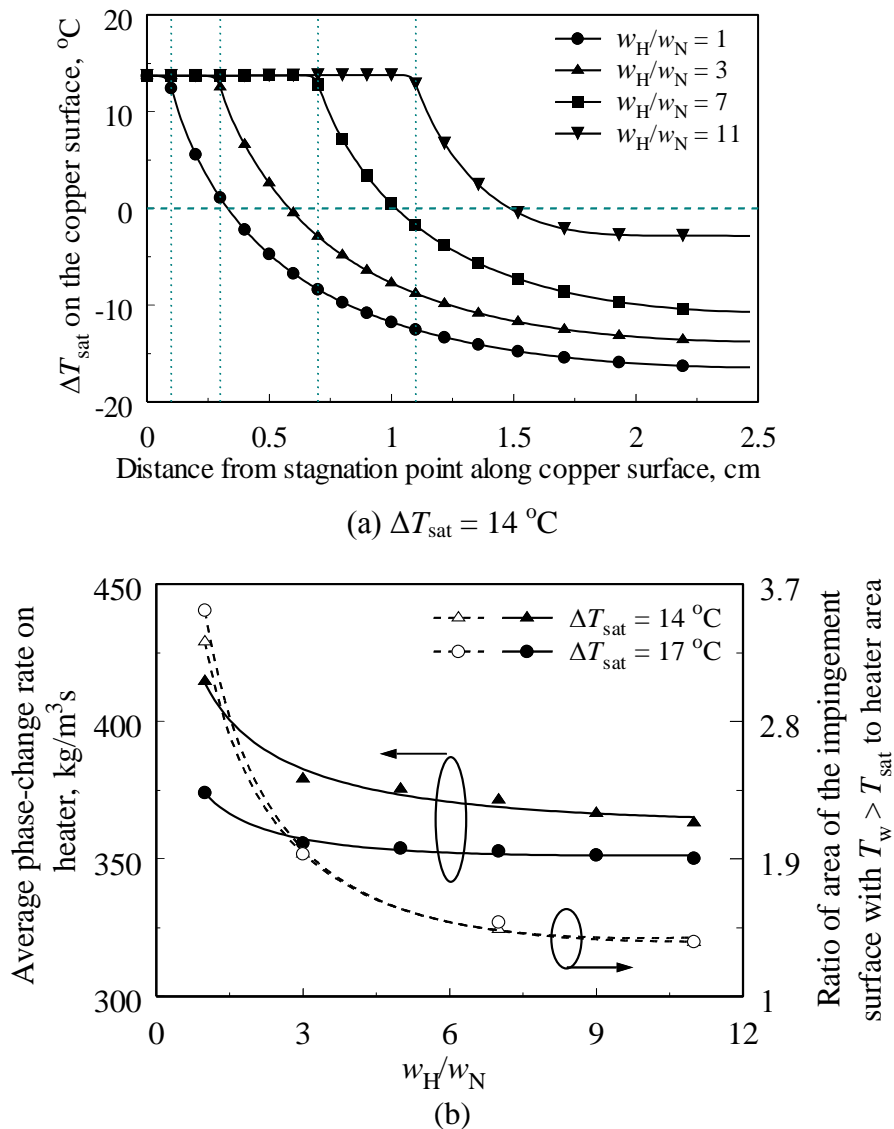
Figure 5.35: Comparison of (a) local surface temperature, and (b) average phase-change rate on the heater and ratio of dimensionless area of the impingement surface above saturation temperature, among isothermal heater of different sizes, for $Re = 2500$, $\Delta T_{sub} = 20\ ^oC$ and $H = 4$

considerable portion of the impingement surface on either sides of the heater is above saturation temperature (due to transverse conduction in the heater) for smaller heaters sizes (say, $w_H/w_N \leq 3$), unlike that for relatively larger heaters, as seen in Fig. 5.35 (a,b). Hence, the ratio of the area available for nucleation to area of the heater is larger for smaller heaters as compared to relatively larger heaters (see Fig. 5.35 (b)), implying a concomitant increase in the evaporative heat flux (although the total magnitude of evaporative heat transfer is obviously more for larger heaters). The preceding argument is corroborated by Fig. 5.35 (b) where it is found that with increase in heater size, the variation in the liquid-vapor phase-change rate on the heater is found to decrease substantially for smaller heaters, while the change is almost negligible for larger heaters, for given values of other controlling parameters. It is seen from the boiling curve for the total surface averaged heat flux in Fig. 5.34 (d) that for any prescribed wall superheat, the total heat flux is consistently larger for smaller heaters. This is indicative of the effectiveness of jet impingement boiling, or in general, jet impingement cooling for applications involving localised heat sources. Leinhard and others [12,13] have shown that heat fluxes of over 40 kW/cm^2 could be obtained without reaching CHF for such localized cooling in the stagnation zones, with large velocity (over 50 m/s) free-surface jets, focussing on applications involving cooling of high-heat-load components in synchrotron x-ray, fusion, and semiconductor laser systems [12].

It is also seen from Fig. 5.33 that, unlike for $w_H/w_N = 1$, the rate of phase change from liquid to vapor on the heater-fluid interface is relatively slightly larger near the regions of the heater downstream of the stagnation region for $w_H/w_N = 3$ and 11, for any prescribed value of jet Reynolds number and surface superheat. This is possibly because the effect of the jet (or the wall-jet) is lowered downstream thereby enhancing boiling and elevating the bubble diameters. This observation is in line with the results of Shin et al. [76], where the larger diameters of the bubbles at the downstream region as compared to the stagnation regions were photographically captured in the experiments with confined slot jets.

Figures 5.36 (a-d) illustrate the percentage contribution of the three heat fluxes partitions, *viz*. liquid phase convective, quenching and evaporative, to the total heat flux from the surface, for isothermal heaters, for a given jet Reynolds number of
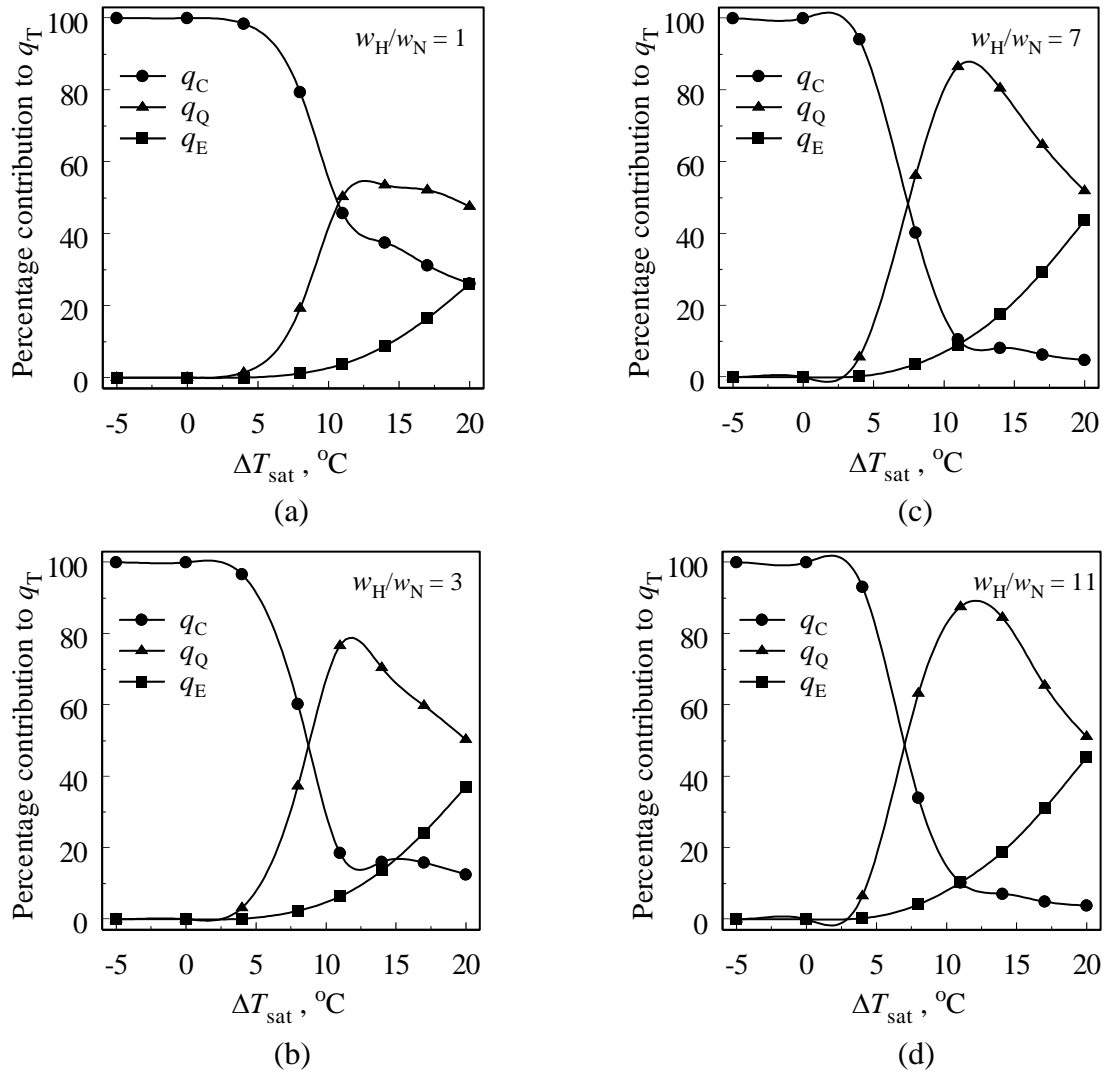
Figure 5.36: Variation in the percentage contribution of q_C, q_Q and q_E to q_T with change in average surface temperature, for isothermal heaters of various sizes, and for $Re = 2500$, $\Delta T_{sub} = 20\ ^{o}C$ and $H = 4$

$Re = 2500$, $\Delta T_{sub} = 20\ ^{o}C$ and $H = 4$ and four different heater sizes defined by $w_H/w_N = 1, 3, 7$ and 11. As can be seen, the contribution of liquid phase convection decreases with increase in surface temperature, while that of evaporation increases monotonically with increase in temperature. It is also seen, especially from Figs. 5.36 (b-d) that the contribution of quenching to the total heat flux increases upto a certain value and decreases with further increase in surface temperature, due to the increase in evaporation. It is interesting to see from the figures that transient conduction (quenching component) becomes the dominant mode of heat transfer for surface temperatures beyond a certain threshold value. Basu et al. [86,168] pointed out that if the quenching heat flux is modelled appropriately (as in the present numerical

model), it would be possible to accurately predict that its contribution to the total heat flux is distinctively the dominant mode of heat transfer at sufficiently large wall superheats, especially during (subcooled) fully developed nucleate boiling. As the area density of the bubbles on the surface A_b is a function of the surface temperature (see (4.40)) the temperature at which the quenching component of the heat flux would become the dominant mode can be deduced by evaluation of the area density for that surface temperature. Solving Eq. (4.39) and Eq. (4.44), the corresponding area density A_b, is evaluated to be

$$A_b = \frac{h_C}{h_C + h_Q}$$ (5.3)

It is also seen from Fig. 5.37 that this threshold value of surface superheat decreases almost exponentially with increase in heater size, for any typical value of jet Reynolds number (the representative values used are 2500 and 3750) for the range of controlling parameters considered in for discussion in this section. Recalling the discussion on Figs. 5.36 (a-d) and Fig. 5.33 as the phase-change rate on the heater surface is relatively larger near the ends of the heaters, for heaters with sizes sufficiently larger than the stagnation region, the area fractions are also large, presumably due to the larger sizes of the bubbles in those outer regions of the heaters. As a consequence of the larger area fraction (A_b) for the larger heaters, for any prescribed value of surface temperature, and as the quenching heat flux component is directly proportional to A_b, the threshold value of temperature is lower for relatively larger heaters.
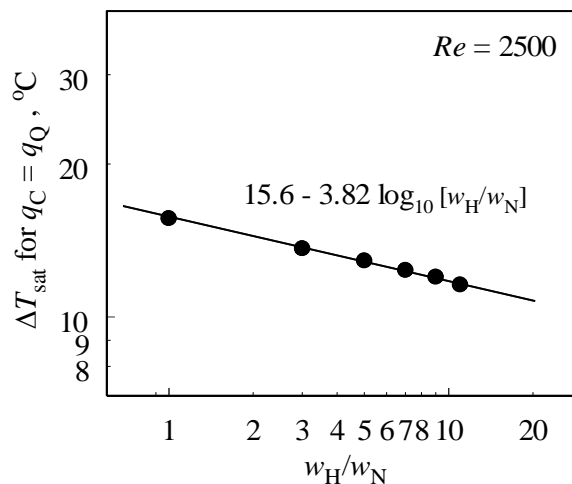
Figure 5.37: Relationship between the threshold value of ΔT_{sat} beyond which q_Q exceeds q_C with w_H/w_N, for $Re = 2500$, $\Delta T_{sub} = 20$ ^{o}C and $H = 4$

(a) $Re = 2500$

(b) $Re = 3750$
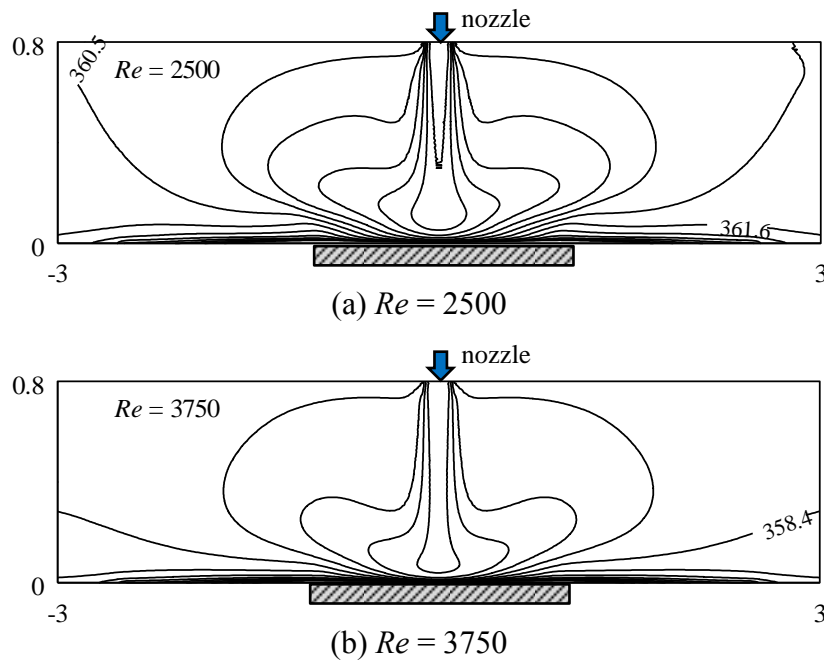
Figure 5.38: Contours of isotherms in the fluid domain for $Re = 2500$ and 3750, ΔT_{sat} = 17 ^{o}C, $w_H/w_N = 9$ (isothermal heater), $\Delta T_{sub} = 20$ ^{o}C and $H = 4$; ▨ denotes the length of the heater; lengths are shown in cm; 15 isotherms are shown in the range $353 \leq T_l \leq 368$ K with $\Delta T_{l,\,isotherms} \approx 1.07$ K

5.2.4.3   Effect of Reynolds Number on Heat Flux Partitioning

Figures 5.38 (a-b) show the contours of liquid phase temperature in the domain for an isothermal heater with a prescribed degree of superheat of $\Delta T_{sat} = 17^{o}$C, $w_H/w_N =$ 9 and for two different Reynolds numbers of 2500 and 3750 for a representative case with $\Delta T_{sub}=20^{o}$C and $H = 4$. As is the case for all impinging jet heat transfer problems, it is seen from the figures that the isotherms are denser for $Re = 3750$, as compared to $Re = 2500$, implying a relatively larger temperature gradient on the impingement surface for $Re = 3750$. Consequently, the liquid phase convective component of the total heat flux is relatively larger for $Re = 3750$ as compared to Re = 2500. As explained in the preceding Section-5.2.4.2, the thinner boundary layer thickness also facilitates cooler liquid to occupy the location of the detached bubbles, thereby resulting in larger quenching for larger Reynolds numbers. It is seen from Fig. 5.39 that the magnitude of the local liquid-to-vapor mass transfer rate on the heater-fluid interface is almost the same for both Reynolds numbers considered. This implies that the Reynolds number has a negligible influence on the evaporative heat transfer in the range of parameters considered. The slight variation between the plots
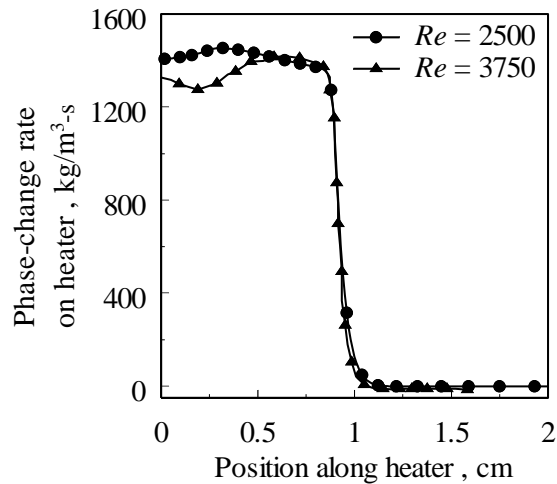
Figure 5.39: Comparison of liquid to vapor mass-transfer rates on the heater-fluid interface between Re = 2500 and 3750, for w_H/w_N = 9, ΔT_{sat} = 17 ^{o}C, ΔT_{sub} = 20°C and H = 4

in the near the stagnation point could be due to the relatively more pronounced effect of the subcooled jet for Re=3750 as compared to Re=2500 in the impingement stagnation region.

Figures 5.40 (a-d) compare the boiling curves for the liquid phase convective, quenching, evaporative and total heat fluxes, between two different jet Reynolds numbers of Re = 2500 and 3750, for isothermal heaters of sizes w_H/w_N = 3 and 9, and ΔT_{sub}=20°C and H = 4. It is seen that irrespective of the heater size, the liquid phase convective heat flux is consistently larger for Re = 3750 as compared to Re = 2500, while the quenching component of the heat flux is not affected by change in Reynolds number in the fully developed nucleate boiling regime, typically for T_{sat}>12°C. It is also seen from Fig. 5.40 (c) that the evaporative heat flux is also negligibly affected by the Reynolds number over the range considered; this in-line with the discussion on Fig. 5.39 presented in the earlier paragraph. Consequently, it is seen from Fig. 5.40 (d) that the total heat flux is larger for Re = 3750 as compared to 2500, for the range of surface superheats in the partial nucleate boiling regime, while the curves for the two Reynolds numbers seem to nearly merge in the fully developed nucleate boiling regime. This observed trend of the nucleate boiling data falling on a single line was previously demonstrated by McAdams et al. [172] and Bergles and Rohsenow [173], and elaborated by Mudawar and Wadsworth [71]. Wang et al. [92] found that significant reduction of the surface temperature can be
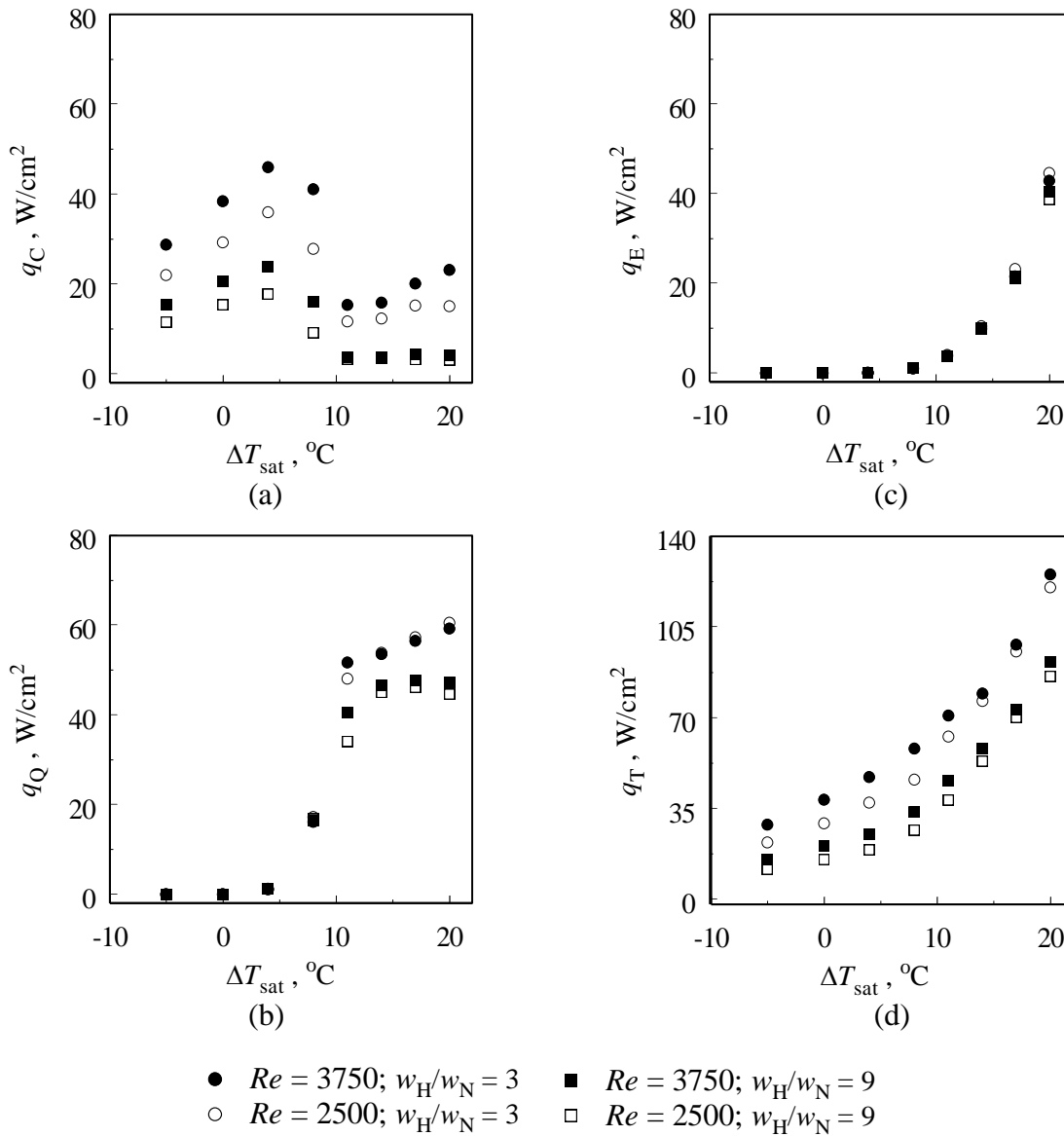
Figure 5.40: Comparison of boiling curves between $Re = 2500$ and 3750 for isothermal heaters of various sizes, and $\Delta T_{sub} = 20$ ^{o}C and $H = 4$

achieved for nozzle-outlet velocity upto about 4.4 m/s beyond which there was no prominent improvement of cooling performance. They also suggested that there could be an optimized flow rate for maximum cooling.

To reiterate the effect of Reynolds number on the partitioning of surface heat flux during confined jet impingement boiling, results pertaining to operating conditions listed in Table-5.1 are also included hereunder, as the boiling curves were already validated against experimental data in the literature as detailed earlier. Figure 5.41 illustrates the variation in the surface averaged boiling curves of the single phase convective, quenching and evaporative heat fluxes between two different
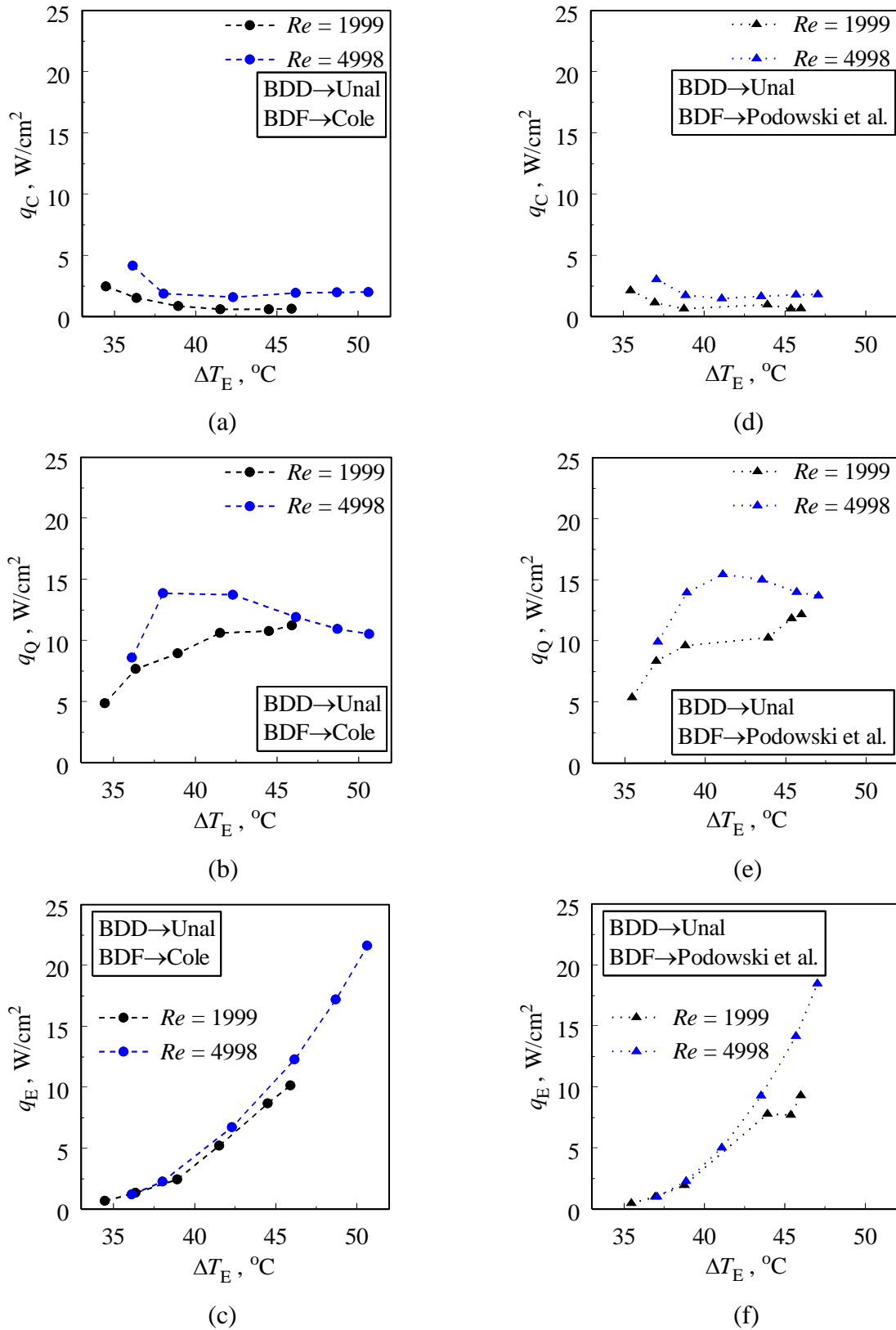
Figure 5.41: Comparison of heat flux partitioning obtained between $Re = 1999$ and 4998, during jet impingement boiling of PF-5060 on an Inconel heate, $\Delta T_{sub} = 25\ ^{o}C$ and $H = 4$

Reynolds numbers $Re = 1999$ and 4998, for $\Delta T_{sub} = 25\ ^{o}C$ and $H = 4$. To avoid any error in judgement in the trends of the boiling curves due to the modelling of bubble departure frequency (which is expected to depend on flow/ jet Reynolds number; see Section-5.2.3.2), the results from simulations using both, Cole's as well as Podowski et al.'s models for BDF are included in the figure. In line with the earlier discussion, irrespective of the BDF model used, the single phase convective heat fluxes are consistently larger for $Re = 4998$ as compared to $Re = 1999$ over the full range of the boiling curve, and the evaporative heat fluxes are consistently unresponsive to the change in Reynolds number over the range considered. However, it is interesting to note from the comparisons shown in Figs. 5.41 (b) and (e) that the quenching heat fluxes are to a certain extent larger for $Re = 4998$ as compared to $Re = 1999$. This was not brought about in the discussion on Fig. 5.40 presented in the earlier paragraph, perhaps due to relatively lower difference in the Reynolds numbers used for the comparison therein ($Re = 2500$ and 3750). This could be attributed to the fact that besides the fact that relatively colder fluid occupies the void of bubble departure during $Re = 4998$ as compared to $Re = 1999$, due to the relatively thinner thermal boundary layer, the bubble waiting time is also relatively larger for $Re = 4998$. From the averaged magnitudes of bubble departure diameters and frequencies obtained during the various regimes of the boiling curve shown in Fig. 5.42 it is seen that the
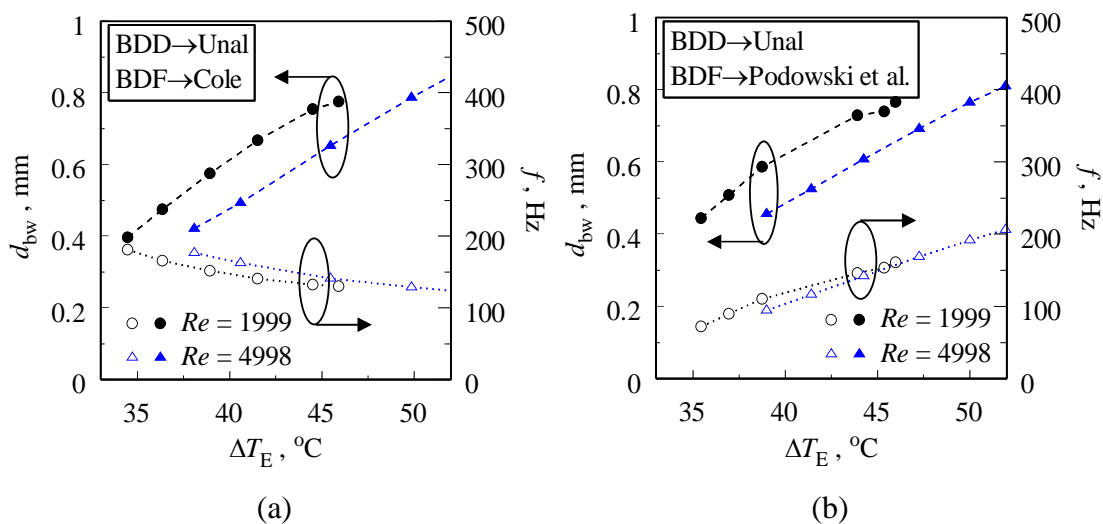
Figure 5.42: Comparison of averaged bubble departure diameter and frequency between $Re = 1999$ and 4998, during jet impingement boiling of PF-5060 on an Inconel heater, for $\Delta T_{sub} = 25\ ^{o}C$ and $H = 4$, obtained using Cole and Podowski et al.'s model for BDF

(a)   (b)
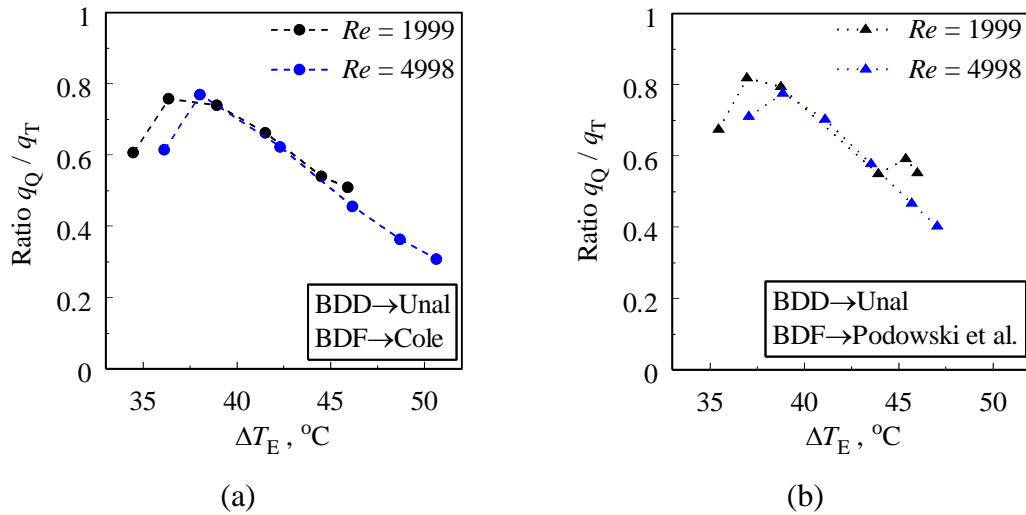
Figure 5.43: Comparison of relative contribution of quenching to the total heat flux between $Re = 1999$ and 4998, during jet impingement boiling of PF-5060 on an Inconel heater, for $\Delta T_{sub} = 25\ ^{o}C$ and $H = 4$, obtained using Cole and Podowski et al.'s model for BDF

bubble departure diameter is consistently larger for $Re = 1999$ as compared to $Re = 4998$, for any specified degree of surface superheat (or heat flux). For any given heat flux, *ceteris paribus*, this would imply that the bubble growth time for $Re = 1999$ is relatively larger than that during $Re = 4998$, due to the larger wall shear stress imposed due to larger velocities during $Re = 4998$, and conversely, the waiting time for $Re = 4998$ is comparatively larger, given that the magnitude of bubble departure frequencies are seen to be nearly equal between the two Reynolds numbers, for the parameters considered for the comparison. Thus the two factors, (i) relatively cooler fluid occupying the void of bubble departure, and (ii) the waiting time being larger, both for $Re = 4998$ as compared to $Re = 1999$, results in a relatively larger magnitude of the transient conduction heat flux (or quenching component) as seen in Fig. 5.41. Nevertheless, the relative contribution of quenching heat flux to the total heat flux remain unchanged between the two Reynolds numbers compared, during most of the boiling regime, as seen in Fig. 5.43.

5.2.4.4   Effect of Nozzle Standoff Distance on Heat Flux Partitioning

The influence of change in the nozzle heater spacing in terms of the dimensionless standoff distance in the range $2 \leq H \leq 8$ is delineated with water as the working fluid,

(a)

(b)

(c)
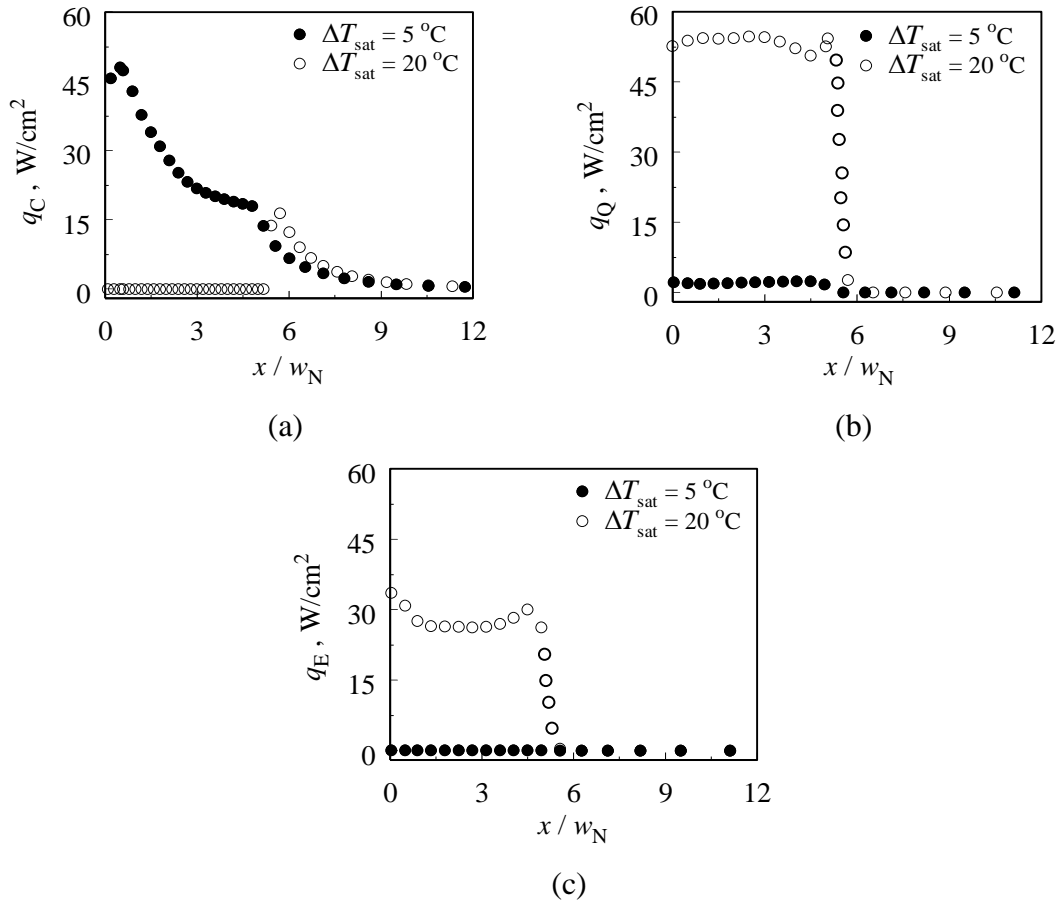
Figure 5.44: Comparison of local distribution of q_C, q_Q and q_E between $\Delta T_{sat} = 5$ ^{o}C

and 20 ^{o}C, for $w_H/w_N = 10$, $H = 6$, $\Delta T_{sub} = 25$ ^{o}C and $Re = 5400$

for a representative jet Reynolds number $Re = 5400$, $\Delta T_{sub} = 25$ ^{o}C, two different dimensionless heater sizes $w_H/w_N = 3$ and 10.

Figures 5.44 (a-c) compare the distribution of local liquid phase convective, quenching and evaporative heat fluxes over the copper impingement surface (heated isothermally) between $\Delta T_{sat} = 5$ ^{o}C and 20 ^{o}C for $w_H/w_N = 10$ and $H = 6$. It is seen from the figures that the liquid phase convective heat flux is the largest contributor to the total heat flux, with insignificant magnitudes of quenching and evaporative heat flux for $\Delta T_{sat} = 5$ ^{o}C. On the contrary, the liquid phase convective heat flux is almost zero on the surface for $\Delta T_{sat} = 20$ ^{o}C where the quenching and evaporative components contribute to the majority of the total heat flux. The reason for the convective component of the total heat flux not reducing to zero with at large surface superheats is because of the conduction in the impingement surface from the heated region to regions beyond the length of the heater, which results in single phase (non-

(a)

(b)

(c)

(d)

$-\bullet-\ H = 2,\ w_H/w_N = 3$ $-\blacktriangle-\ H = 6,\ w_H/w_N = 3$ $-\blacksquare-\ H = 8,\ w_H/w_N = 3$

$-\circ-\ H = 2,\ w_H/w_N = 10$ $-\triangle-\ H = 6,\ w_H/w_N = 10$ $-\square-\ H = 8,\ w_H/w_N = 10$
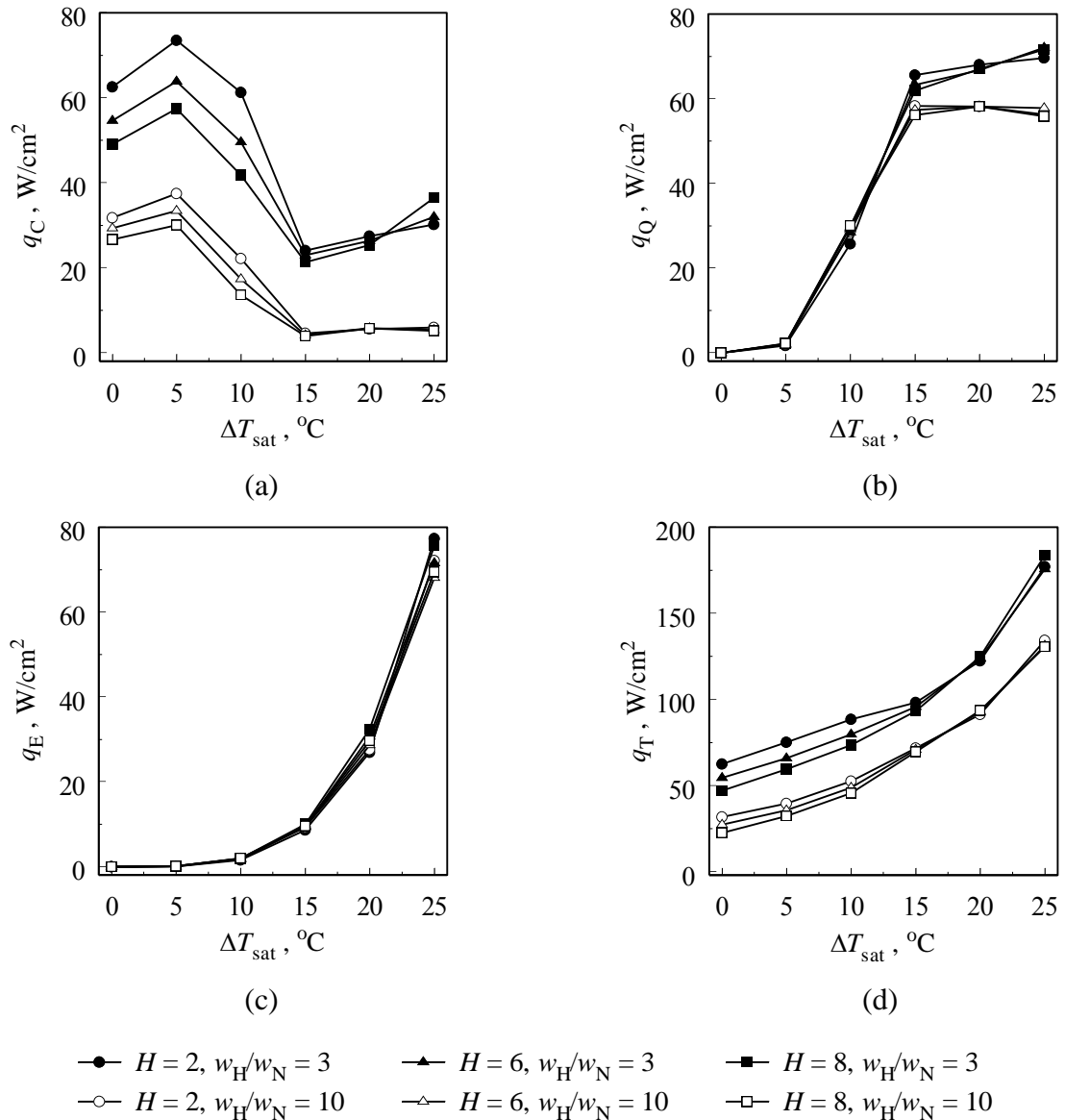
Figure 5.45: Comparison of boiling curves between three different standoff distances H = 2, 6 and 8, for two different heater sizes w_H/w_N = 3 and 10, and for ΔT_{sub} = 25 ^{o}C and Re = 5400

boiling) convective heat transfer. As discussed in an earlier Section-(5.3.4.1, this comparison of the local heat flux distribution can be correlated to mean that the flow and heat transfer regime is partial nucleate boiling for ΔT_{sat} = 5 ^{o}C while it is fully developed nucleate boiling for ΔT_{sat} = 20 ^{o}C. Hence, it is evident that the transition from partial to fully developed nucleate boiling occurs in an interim value of 5 ^{o}C $\leq$ $\Delta T_{sat} \leq$ 20 ^{o}C, for the examples discussed. It is seen from Figs. 5.45 (a-c) that beyond a threshold value, typically in the range 10 ^{o}C $\leq \Delta T_{sat} \leq$ 15 ^{o}C there is a steep drop in the liquid phase convective heat flux, associated with a concomitant steep rise in the

quenching and the evaporative heat fluxes with any prescribed increase in the average surface superheat. As shown in the earlier Section-5.2.4.1 and as indicated by Basu et al. [86,168], this trend can be correlated to the transition from partial nucleate boiling to fully developed nucleate boiling. It is also seen from Fig. 5.45 (d) that the onset of fully developed nucleate boiling results in a subsequent rise in the total surface heat flux removed per unit change in heater temperature (note the increase in the slope of the curve).
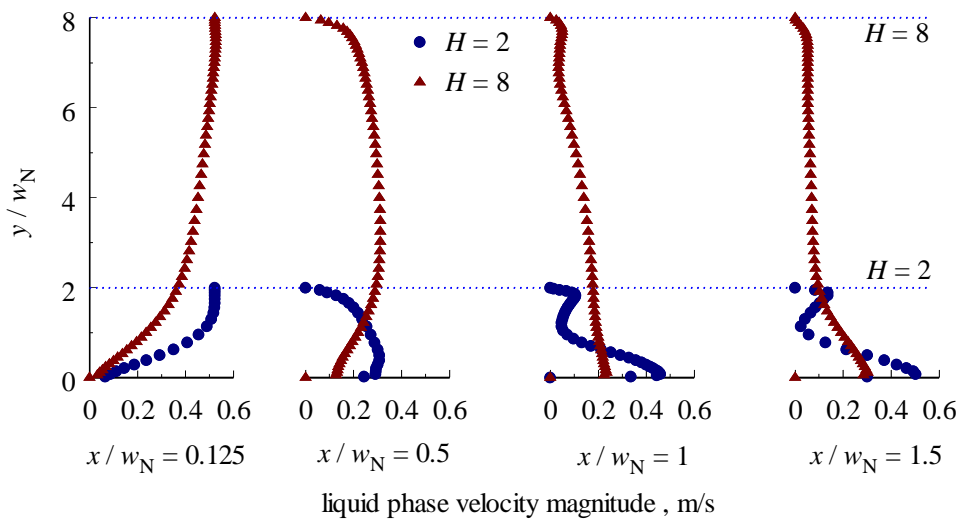
Figure 5.46: Comparison of the predicted liquid phase velocity magnitudes along the y-axis at different locations downstream from the stagnation point between $H = 2$ and 8, for $\Delta T_{sat} = 10\ ^{o}C$, $\Delta T_{sub} = 25\ ^{o}C$, $Re = 5400$ and $w_H/w_N = 3$

It is seen from Figs. 5.45 (a-d) that the surface averaged values of the liquid phase convective heat flux and the total heat flux are consistently larger for relatively smaller standoff distances while there is negligible change in the quenching and evaporative counterparts with change in standoff distance. As the total heat flux is modeled as the sum of the component heat fluxes in the current numerical model, the observed trend for q_T with change in the dimensionless standoff distance in the partial nucleate boiling regime can be perceived as a direct consequence of q_C. Recalling the discussion on Fig. 5.44 (a-c) and that liquid phase convection is the dominant mode of heat transfer in the range of surface temperatures until the transition of the boiling to fully developed nucleate boiling (or a large number of bubbles on the surface), the average heat transfer is larger for relatively smaller standoff distances, as is the case for single phase jet impingement cooling. This is a

direct consequence of the larger effectiveness of the turbulent forced convective velocity gradient on the heater surface. The magnitudes of liquid phase velocity perpendicular to the impingement surface obtained for two representative cases $H = 2$ and 8 for a typical set of operating conditions in the partial nucleate boiling regime: $\Delta T_{sat} = 10\ ^{\circ}\text{C}$, $\Delta T_{sub}=25\ ^{\circ}\text{C}$, $Re = 5400$ and $w_H/w_N = 3$, is shown in Fig. 5.46 at four different locations from the stagnation point. It is evident from the figure that the velocity gradients (keeping no-slip on the wall) are consistently larger for the smaller standoff distance. This is also partially attributed to the presence of the confinement plate which facilitates acceleration of the fluid after impingement in the direction along the wall jet, thus further enhancing forced convection as compared to any similar unconfined cases. This observation is in-line with the literature on the investigation of single phase jet impingement heat transfer, such as in Martin [42], Zuckerman and Lior [43], and Lee and Lee [174]. Wolf et al. [175] showed that for surface temperatures beyond boiling incipience and within the partial nucleate boiling regime, boiling on the surface is limited to only a small number of vapor bubbles and the jet flow continues to strongly influence the heat transfer. The negligible difference in the boiling curves for the quenching and evaporative components of the total heat flux between $H = 2$, 6 and 8 in Figs. 5.45 (b-c) implies the very abstemious relationship between the standoff distance and the characteristics of fully developed nucleate boiling. It is also seen from the figures that the lithe effect of the standoff distance on quenching and evaporative heat fluxes is consistent irrespective of the heater size, for the range of representative parameters considered for the discussion. It is also seen from Fig. 5.45 (b) and Fig. 5.45 (c) that the effect of change in dimensionless standoff distance on the evaporative heat flux or production of vapor phase is independent of the heater size for the range of parameters considered. However, it is also observed that the change in the heater size from $w_H/w_N = 3$ to $w_H/w_N = 10$, *ceteris paribus*, is influential on the magnitude of quenching component of the total heat flux is prominent only in the fully developed nucleate boiling regime. It is also seen that the variation of the liquid phase convective heat flux in the partial nucleate boiling regime with change in standoff distance is larger for $w_H/w_N = 3$ as compared to $w_H/w_N = 10$, implying a larger influence of the standoff distance for smaller heaters.

5.2.4.5   Effect of Fluid Subcooling on Heat Flux Partitioning

To study the effect fluid subcooling on the partitioning of surface heat flux, simulations are carried out for two different values of ΔT_{sub} = 7.45 ^{o}C and 16.74 ^{o}C corresponding to two experimental data sets obtained from the present study. The two experimental data sets are for similar Reynolds numbers of Re = 9836 (for ΔT_{sub} = 7.45 ^{o}C) and 9046 (for ΔT_{sub} = 16.74 ^{o}C). Figures 5.47 (a-d) illustrate the boiling curves for the individual component heat fluxes as well as the total heat flux obtained from the present simulations for the aforementioned cases. In addition, the experimentally obtained boiling curves for the total heat flux are also included for

(a)

(b)

(c)

(d)
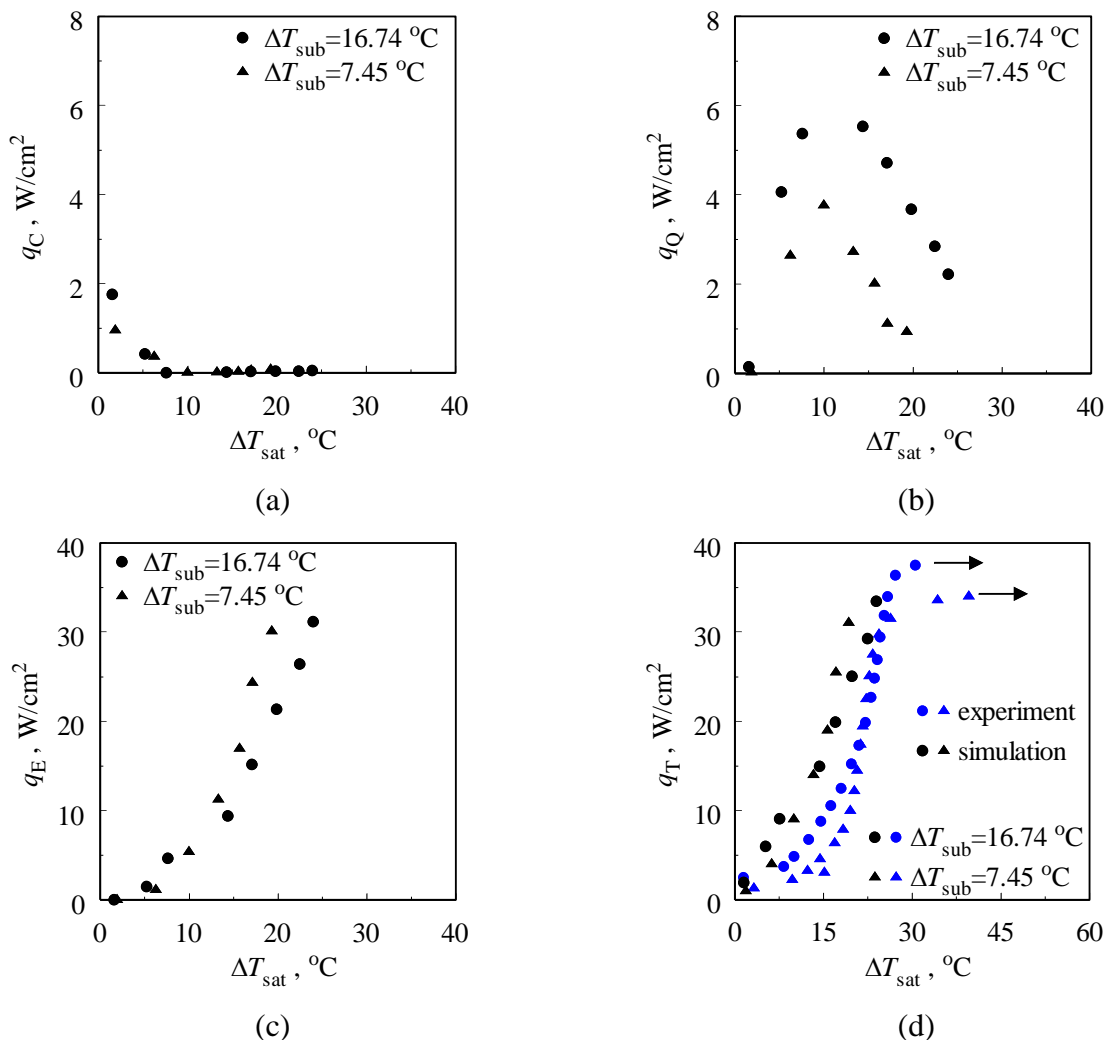
Figure 5.47: Comparison of boiling curves between ΔT_{sub} = 7.45 ^{o}C and 16.74 ^{o}C for similar jet Reynolds numbers Re = 9836 and 9046, respectively, pertaining to cases from the present experimental studies; ⟶ indicates critical heat flux

comparison purposes. It is pointed out that although there is a slight but consistent underprediction of the surface temperature for each heat flux in the numerical simulations, the trends are in good agreement with the experimental boiling curve, which is deemed sufficient for the following discussion put forth, for the qualitative dependence of the component heat fluxes on the degree of inlet subcooling. It is seen from the figures that the total surface heat flux remains uninfluenced by change in degree of subcooling through most of the boiling curve, but for low degree of surface superheats, indicating a weak dependence of the liquid temperature on nucleate boiling regime. Several studies in the literature [176-178] on similar confined jet impingement configurations using a variety of fluids including R113, water and FC-72 have reported that the degree of subcooling has no notable effect on the boiling curve. However, Ma and Bergles [179,180] found that the boiling curve slightly shifted towards the left for relatively lower degrees of superheat during the initial stages of nucleate boiling, with an increase in subcooling. This observation could be attributed to the fact that while the magnitude of the evaporative component of the total heat flux is still low in the initial stages of nucleate boiling (see Fig. 5.47 (c)), the quenching heat flux component is substantially larger in magnitude for $\Delta T_{sub} = 16.74$ ^{o}C as compared to that for $\Delta T_{sub} = 7.45$ ^{o}C. However, as the boiling regime transcends farther into the fully developed nucleate boiling regime, quenching is deteriorated due to relatively denser vapor fraction that suspends the quantity of fluid

(a)   (b)
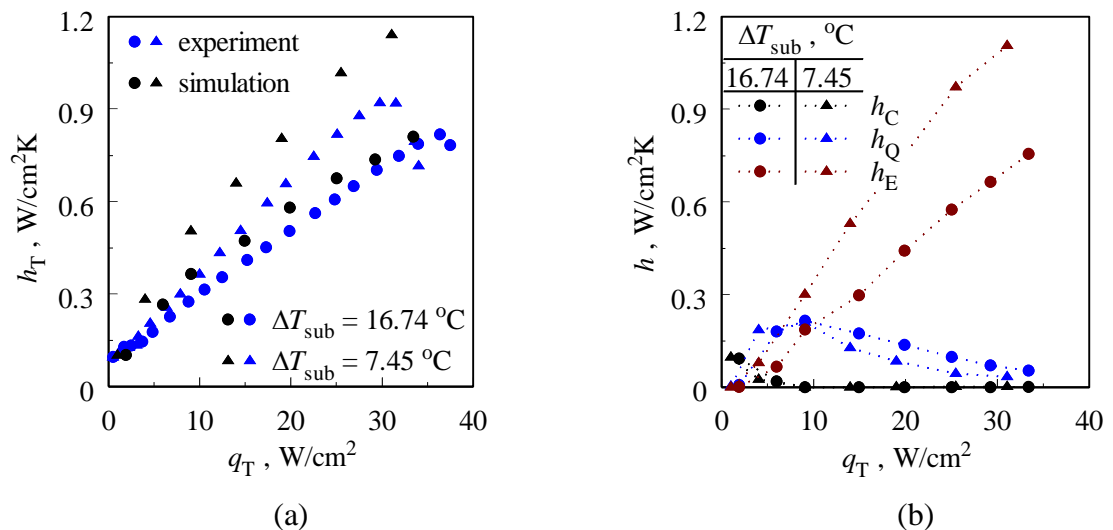
Figure 5.48: Comparison of total and component heat transfer coefficients obtained between $\Delta T_{sub} = 7.45$ ^{o}C and 16.74 ^{o}C for similar jet Reynolds numbers $Re = 9836$ and 9046, respectively, pertaining to cases from the present experimental studies

fed to the heated surface, consequently resulting in no significant difference in the segment of the boiling curves pertaining to relatively larger superheats. The relatively larger quenching heat flux for the larger subcooling could be substantiated with the photographic evidence shown in Cardenas [17] from a similar submerged jet impingement boiling study using FC-72. Cardenas [17] pointed out that the occupation of heater surface by vapor bubbles was substantially larger for saturated conditions as compared to subcooled conditions for heat fluxes sufficiently below CHF, implying that the impinging jet significantly enhanced the supply of colder fluid for lower subcoolings during the relatively initial stages of nucleate boiling. It is however beneficial to operate at lower subcoolings as the heat transfer coefficients are comparatively larger for $\Delta T_{sub} = 7.45$ ^{o}C as compared to that for $\Delta T_{sub} = 16.74$ ^{o}C as seen in Fig. 5.48 (a). It is also observed from Fig. 5.48 (b) that the evaporative phase change from the absorption of latent heat and a relatively reduced sensible heating required to reach saturation in the case of for $\Delta T_{sub} = 7.45$ ^{o}C as compared to for $\Delta T_{sub} = 16.74$ ^{o}C results in the consistently larger total heat transfer coefficients observed in Fig. 5.48 (a).

5.2.5   Summary of Key Findings

A comprehensive set of simulations using the Eulerian multiphase model were carried out to study the influence of the various controlling parameters *viz.* jet Reynolds number, dimensionless heater size, dimensionless standoff distance, degree of subcooling, type of heating used on confined and subcooled jet impingement boiling in a confined configuration. The study included two fluids- water and FC-72 which have substantially different fluid properties.

- A rigorous grid independence test was carried out for each geometric configuration studied particularly to ensure the wall $y+$ to be small enough (< 5) to resolve the viscous sublayer of the turbulent boundary layer, keeping in mind the requirements posed by the turbulence models employed.

- As the geometry for the computational domain involves a confined outflow, which partially consists of a wall-jet and partially reverse flow (re-circulation), the length of the domain beyond the heater was determined by studying the predictions from successively longer sections of the confined region far from

heater, to ensure that the outlet boundary condition does not affect the flow features in the region of interest.

- Several multiphase turbulence models *viz.* RNG-k-ε-EWT, Std. k-ω-SFC, k-ω-SST + Low Re and RSM- linear pressure strain + EWT, were explored for their suitability in terms of computational accuracy and convergence stability for the simulation of the present multiphase heat transfer/ fluid flow problem under investigation. The RNG-k-ε-EWT multiphase turbulence model was deemed suitable.

- Several models for the prediction of the ebullition parameters such as bubble departure diameter and frequency were compared for their suitability for confined and submerged subcooled slot jet impingement boiling. Unal's model for the prediction of bubble departure diameter determined to be best suitable for the computations. While for bubble departure frequency, boiling curves from the use of Podowski et al.'s and Cole's (although not particularly developed for flow boiling) models conform well to experimental data in the literature. However, the predicted bubble departure frequencies had opposing relationships with the imposed surface heat flux. As there are published experimental evidences to show trends predicted by both models are plausible, a further investigation is suggested to ascertain the correct relationship between the parameters for jet impingement boiling problems of the type considered in the present research

- The steady state characteristics of boiling exhibited by the two types of heaters viz. isothermal and isoflux are nearly equivalent, irrespective of the heater size or Reynolds number, for the range of heat fluxes (or surface degree of superheats for isothermal heaters)

- The effects of the various controlling parameters on the partitioning of surface heat flux are characterised for various regimes of the boiling curve. The results of the parametric analysis are using the local as well as surface temperatures, heat fluxes, liquid-vapor phase change rates on the heater surface, isotherms, streamlines and vapor-phase contours.

5.3   EXPERIMENTAL STUDY OF PULSATING SINGLE PHASE AND BOILING JET IMPINGEMENT HEAT TRANSFER

5.3.1   Pulsating Single Phase Liquid Jet Impingement Heat Transfer

This section of the chapter delineates the results from experimental investigations carried out to study the effect of jet pulsation frequency and amplitude on the heat transfer characteristics of single phase submerged and confined slot jet impingement cooling using de-ionized water as the working fluid, and aluminium alloy 5083 as the material for the heater block. The effectiveness of jet pulsating over the range of pulsation frequencies and amplitudes were determined from comparison against baseline steady state experimental data obtained from the present study. The details of the experimental setup for the following discussion on steady and pulsating jet impingement heat transfer are detailed in Section-4.2.1.

5.3.1.1   Base Line Steady State Single Phase Jet Impingement

For evaluating the thermal effectiveness of pulsating jet impingement, base line steady state jet impingement cooling experiments were carried out for three different inlet temperatures of T_N = 34.83 ^{o}C, 39.68 ^{o}C and 44.54 ^{o}C and for Reynolds numbers in the range 800-7000 as detailed in Table-5.3. As a consequence of the variation in the thermophysical properties of the working fluid (in this case de-ionized water), particularly the dynamic viscosity, which is susceptible to change in operating temperature, the Prandtl number of the fluid also changed substantially over the range of operating conditions studied. The fluid Prandtl number evaluated based on the bulk fluid temperature (defined as T_{bulk} = $(T_N+T_w)/2$) was observed to vary in the range $3.0 \leq Pr \leq 5.0$. Figure 5.49 illustrates the experimentally obtained

Table 5.3: Ranges of single phase jet impingement experimental parameters

	Steady jet	Pulsed jet
Re (-)	800 – 7000	500 – 3400
T_N (^{o}C)	34.83, 39.68, 44.54	39.66
p (Pa)	101325	101325
A (-)	-	0.5, 1
f (Hz)	-	0.25, 0.5
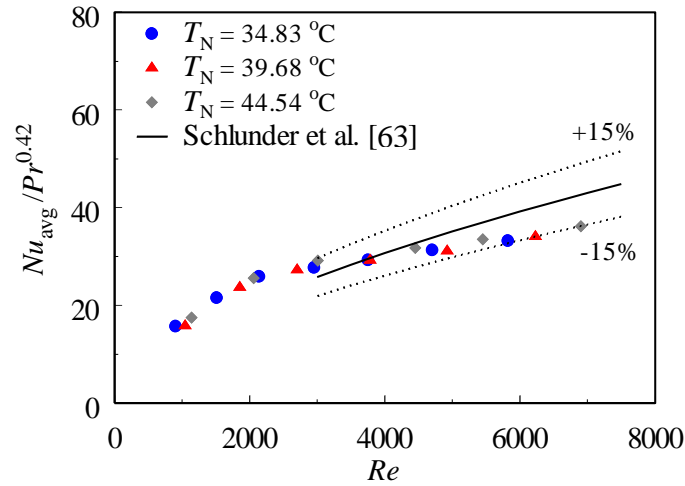
Figure 5.49: Variation in the experimentally obtained steady state Nusselt numbers with jet Reynolds number for different inlet jet temperatures

surface average Nusselt number (expressed in terms of $Nu_{avg}/Pr^{0.42}$) over the range of jet Reynolds numbers for the three different jet inlet temperatures. The standard correlation for the surface averaged Nusselt number proposed by Schlunder et al. [63]:

$$\frac{Nu_{avg}}{Pr^{0.42}} = \frac{Sh_{avg}}{Sc^{0.42}} = \left(\frac{1.53}{w_H/B + H/B + 1.39}\right) Re^{0.695 - \left[w_H/B + (H/B)^{1.33} + 3.06\right]^{-1}} \tag{5.4}$$

which was developed from heat-mass transfer analogy of the experimental Sherwood number data of [27,62,63] is also included in the figure for comparison with the present experimental data. The preceding correlation is valid in the range $3000 \leq Re \leq 90000$, $2 \leq w_H/B \leq 25$ and $2 \leq H/B \leq 10$ with 85% confidence [63]. It is seen from the figure that the present data for average Nusselt number obtained for all three inlet temperatures collapse into a single curve, in-line with the dependence of Nusselt number on the fluid Prandtl number reported in the literature [42,43, 63]. It is also seen that the maximum deviation between the present experimental data and that predicted by Schlunder et al.'s correlation is about ±15%, which is within the confidence level of the correlation for the range of the operating conditions studied.

5.3.1.2   Influence of Jet Pulsations on Thermal Characteristics

Recalling the consistency in the relationship between surface-averaged Nusselt number and Prandtl number (see Eq. (5.4)) over the range of operating temperatures considered in the present study with steady state jet impingement heat transfer
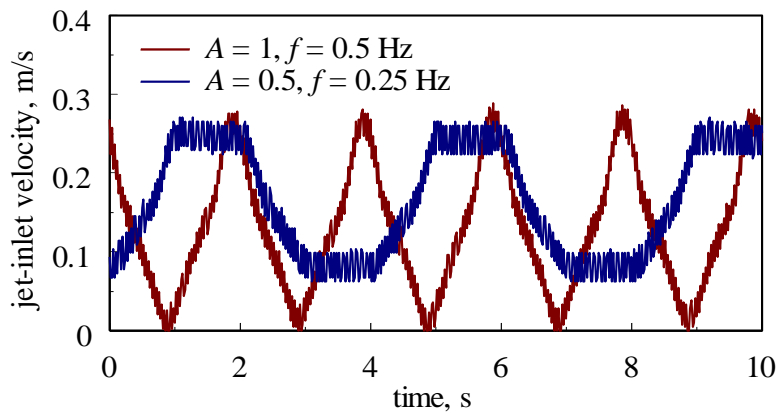
Figure 5.50: Sample inlet velocity profiles during pulsating jet impingement with de-ionized water

experiments, it was deemed sufficient to carry out pulsed jet impingement experiments for just one inlet temperature. The effect of jet pulsations on the heat transfer characteristics were studied for Reynolds numbers in the range $500 \leq Re \leq 3400$, amplitudes of 50% and 100% of mean flow rate, and for low frequencies 0.25 and 0.5 Hz and a given jet inlet temperature of 39.66 ^{o}C, as detailed in Table-5.3. As the flow pulsations were introduced using solenoid control valves it was observed that the amplitude of the pulse was consistently reduced when larger frequencies (beyond 1-2 Hz) were attempted for any flow rate, because of the time involved (about 0.35 seconds) in the opening/ closing of the solenoid control valve, besides the natural consequence of fluid inertia in the piping. Perhaps, by introduction of the flow pulsations using a fully rotational ball valve as used in Sheriff and Zumbrunnen [21] and Azevedo et al. [104], the effects of large pulsation amplitudes at higher frequencies could be explored. Figure 5.50 illustrates a two typical pulsating jet velocity profiles obtained using the present technique. It can be seen that irrespective of the flow rate, amplitude or frequency, the time period between the two end states remain almost constant (see slope of the curve), thus tending the wave-form more triangular at 0.5 Hz (and for any larger frequency; not shown in the present paper) as compared to that at 0.25 Hz where it is more trapezoidal.

To study the effect of pulsation frequency on the transient surface temperature oscillations an area-averaged normalized temperature was defined in terms of the instantaneous temperature, time averaged mean temperature (over the last 120 seconds of the oscillating steady state) and the jet inlet temperature as
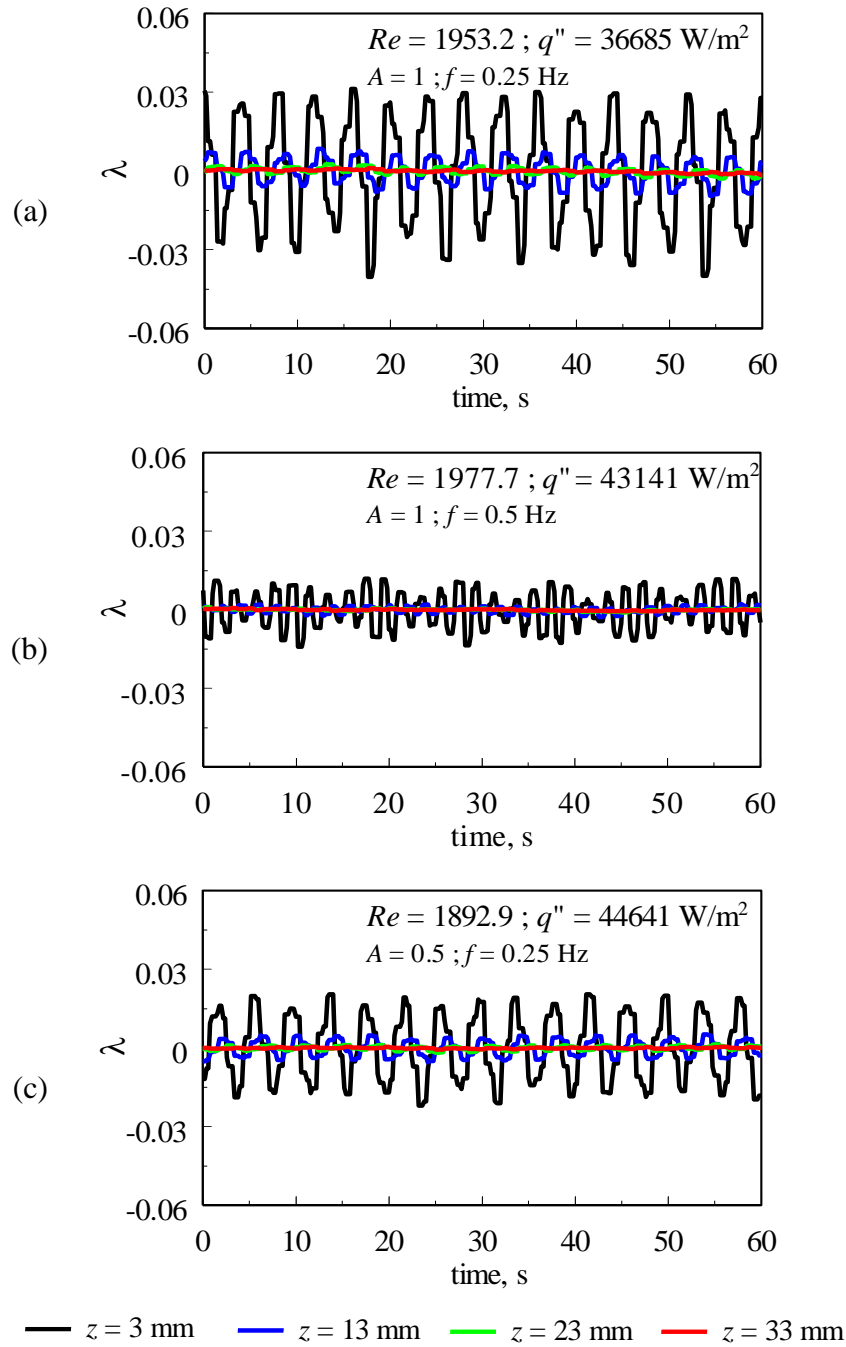
Figure 5.51: Comparison of area-averaged normalized temperature oscillations at different locations beneath the impingement surface in the heater block, during the last 60 seconds of oscillating steady state, between $f = 0.25$ and 0.5 Hz

$$\lambda = \frac{T_{w,\,mean} - T}{T_{w,\,mean} - T_N}$$ (5.5)

The normalized temperature oscillations at four different locations beneath the impingement surface in the heater block obtained for different frequencies and amplitudes is illustrated in Figs. 5.51 (a-c). The comparison of these oscillations

between f = 0.25 Hz and 0.5 Hz for similar mean jet Reynolds numbers Re = 1953.2 and 1977.7 is shown in Figures 5.51 (a,b). It is seen that the amplitude of temperature oscillations decreases with depth in the heater block (where 1D conduction is applicable), *ceteris paribus*, because of the thermal inertia of the heater block. It is also seen that at any given location beneath the impingement surface in the heater block (which is also applicable for surface temperature), the amplitude of the temperature oscillations substantially decreases with increase in the frequency of the jet pulsation although the amplitude of jet pulsations is kept constant (A = 1) for both cases shown in the figure. From a computational analysis of a similar pulsed liquid impingement cooling system (for frequencies in the range 0.03 - 4Hz), Narumanchi et al. [102] pointed out that the heated surface ceases to respond to the jet pulsations when the time period of the jet pulsations is less than the response time of the heater (in their case, a 0.25 mm thick silicon with a Biot number of the order of 0.0004). Hence, it is possible that higher pulsation frequencies, which would invariably involve a larger input power for operation, might not result any substantial influence on the heater's transient thermal characteristics. As expected, it is seen from comparison of Fig. 5.51 (a) and Fig. 5.51 (c) for f = 0.25 Hz that a change in jet pulsation amplitude from A = 1 to A = 0.5 has a direct consequence on the amplitude of normalized temperature oscillation on the heater, due to cyclic renewal of thermal boundary layer on the heater surface.
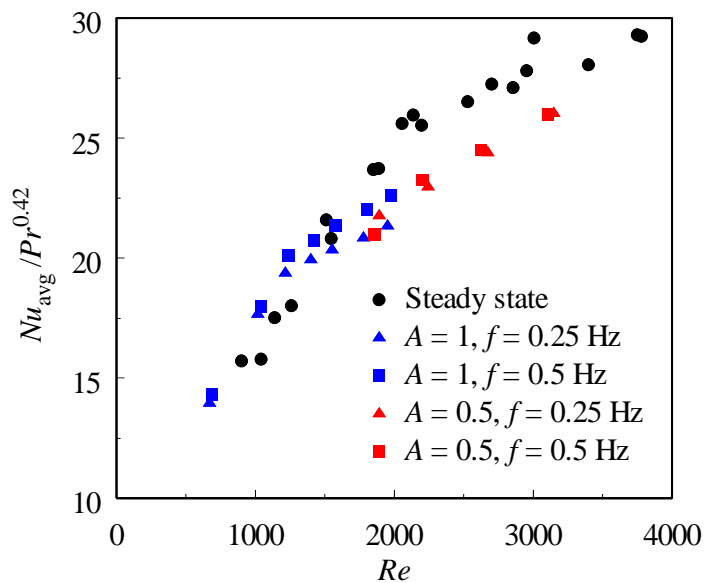
Figure 5.52: Comparison of average Nusselt numbers between different pulsation frequencies and amplitudes

The time and space averaged Nusselt numbers (in terms of Nu_{avg} / $Pr^{0.42}$, following the discussion in the previous paragraph) for two different frequencies (f = 0.25 Hz and 0.5 Hz) each for two different amplitudes (A = 0.5 and 1), along with the base line steady state case are shown in Fig. 5.52 over the range of Reynolds numbers studied in the present research. It is seen that for Reynolds numbers upto about 1000, there is no significant difference between the thermal performance during steady and pulsed jet impingements. For relatively larger Reynolds numbers a slight attenuation in the time averaged Nusselt number is observed for both frequencies and amplitudes (upto 12%) as compared to steady state jet impingement over the same range of Reynolds numbers. While the Nusselt numbers are relatively lower (about 6%) in magnitude for f = 0.25 Hz as compared to f = 0.5 Hz for the interrupted jet case (A = 1), no significant difference is seen for A = 0.5 with change in jet pulsation frequency. Hence, it is reasonable to mention that for the range of Reynolds numbers and pulsation characteristics studied in the present research using water as the base fluid, no substantial difference is observed in the time averaged heat transfer characteristics between steady and pulsed jet impingement cases. This is also in qualitative agreement with the suggestions of Narumanchi et al. [102] from their theoretical analysis of the effect of jet pulsations at lower Reynolds numbers (0-100). The unsubstantial difference between the time averaged Nusselt numbers obtained between the steady state and pulsed case can be attributed due to the fact that the frequencies are not large enough to sustain a significantly thinner or thicker thermal boundary layer over the impingement surface, as pointed out by Zumbrunnen and Aziz [105] from their study with interrupted free surface water jets.

5.3.2   Pulsating Boiling Jet Impingement Heat Transfer

As pointed out earlier in Chapter-2 jet pulsations have been found to have both enhancing as well as deteriorating heat transfer characteristics as compared to steady state jet impingement. While there is significant literature on the effect of jet flow oscillations on single phase impingement cooling systems, that discussing the influence on boiling characteristics of an impinging subcooled jet is very limited, particularly to self-oscillating jets. The following section presents results from an investigation the effect of low frequency externally induced jet pulsations on the associated transient as well as time-averaged heat transfer characteristics of boiling
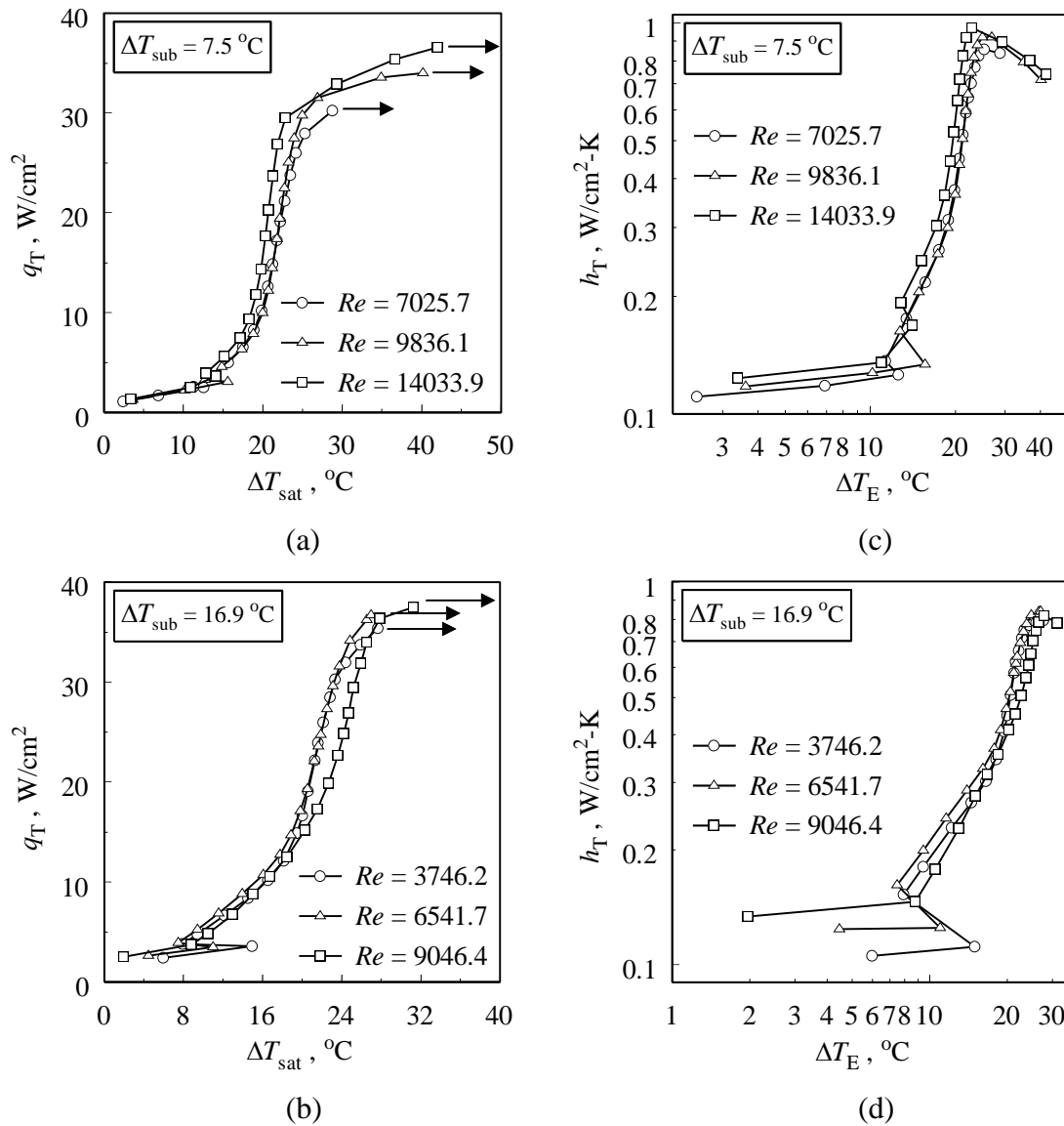
Figure 5.53: Comparison of area averaged boiling curves and heat transfer coefficients with change in Reynolds number for two different inlet jet subcoolings $\Delta T_{sub} = 7.5\ ^oC$ and $16.9\ ^oC$; $\longrightarrow$ indicates CHF

heat transfer using a subcooled jet of FC-72 in a submerged and confined geometry detailed in Section-4.2.1.

5.3.2.1   Base Line Steady State Jet Impingement Boiling

For estimating the effectiveness of jet pulsations and with a view to isolate the effect of the unsteady jet pulsations on the heat transfer characteristics during impingement boiling, base line steady state experiments were carried out for two different inlet

subcoolings of about 16.9 ^{o}C and 7.5 ^{o}C for jet Reynolds numbers in the range 3500–14000. as listed in Table-5.4. Figures 5.53 (a,b) illustrate the variation in the surface averaged boiling curves during steady state jet impingement with change in jet Reynolds number, for two different subcoolings, and Figs. 5.53 (c,d) illustrate the corresponding variations in the surface averaged heat transfer coefficients over the range of excess temperatures (ΔT_{E}) on the impingement surface. It is seen from the figures that irrespective of the Reynolds number, the boiling curves collapse to a single curve during most of fully developed boiling regime indicating the weak dependence of the jet velocity on the boiling characteristics in the regime for the geometric configuration considered. This observed trend of merger of the nucleate boiling data was previously demonstrated by several studies [17,71,172,173], and elucidated in the earlier section of this document (Section-5.2.4.3 using computational simulations. However, the critical heat fluxes are consistently larger for larger Reynolds numbers for both jet subcoolings studied. With an increase in Reynolds number, the strength of the jet on the impingement surface increases in terms of larger fluid acceleration from the stagnation point and larger shear velocities in the wall jet region. This results in enhanced removal of the bubbles from the heater surface by the fluid post-impingement, consequently leading to a to sustained bubble removal on the heated surface upto relatively larger heat fluxes by inversely affecting the bubble flooding on the surface, as compared to conditions with relatively lower Reynolds numbers. As pointed out by Cardenas [17], the effect of

Table 5.4: Experimental test matrix for steady and pulsed boiling jet impingement

Test number	ΔT_{sub} ^{o}C	Re –	f Hz	A %	q_{CHF} W/cm^2
1	17.06	3746.2	steady	steady	35.41
2	16.85	6541.7	steady	steady	36.73
3	16.74	9046.4	steady	steady	37.49
4	7.45	7205.7	steady	steady	30.25
5	7.45	9836.1	steady	steady	34.03
6	7.53	14033.9	steady	steady	36.58
7	17.00	3390.3	0.50	63.2	36.39
8	17.02	3553.2	0.25	61.1	35.58
9	17.02	3482.4	0.50	36.5	35.69

increase in jet velocity in the nucleate boiling regime can also be correlated to an enhanced fluid supply to the heat transfer surface thereby elevating CHF limits. It is interesting to note from 5.53 (a,b) that the slope of the boiling curve for heat fluxes close to CHF reduces slightly, and this reduction in slope is larger for larger Reynolds numbers and particularly for lower subcooling ($\Delta T_{sub} = 7.5$ ^{o}C as compared to 16.9 ^{o}C). Consequently the average heat transfer coefficient reduces for heat fluxes close to CHF as seen in 5.53 (c,d). As is the case for single phase jet impingement heat transfer, the heat transfer coefficients before the onset of nucleate boiling are significantly affected by the fluid velocity, and hence are consistently larger for larger Reynolds numbers as seen in Figs. 5.53 (c,d) for both subcoolings.

(a)   (b)
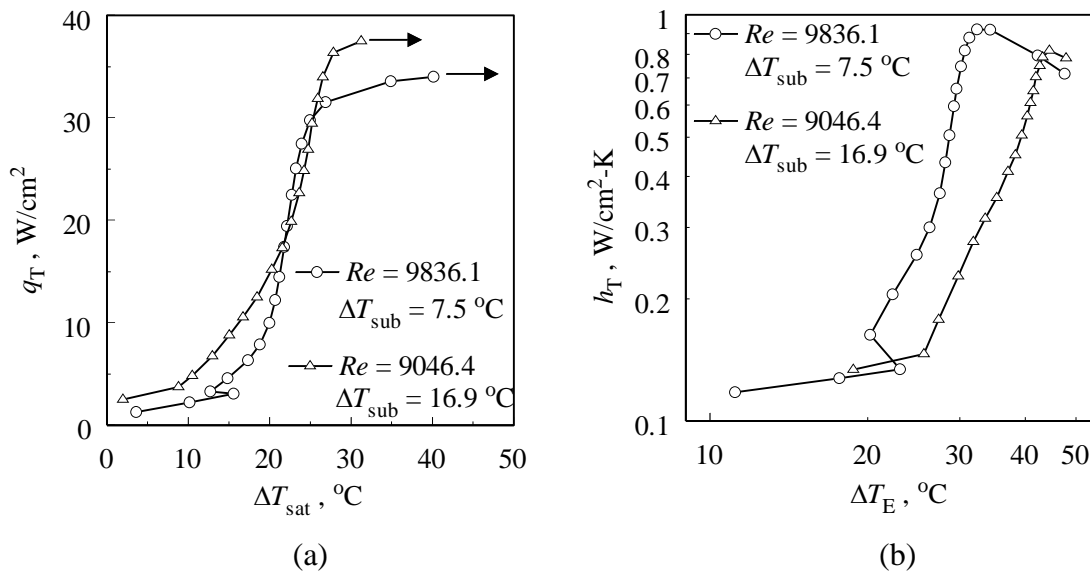
Figure 5.54: Comparison of area averaged boiling curves between two different inlet jet subcoolings $\Delta T_{sub} = 7.5$ ^{o}C and 16.7 ^{o}C for similar Reynolds numbers; $\longrightarrow$ indicates CHF

The effect of inlet subcooling on steady jet impingement boiling during similar Reynolds numbers is delineated by comparison of the associated boiling curves and variation of the corresponding heat transfer coefficients as shown in Fig. 5.54 for a representative experimental case. It is seen from the Fig. 5.54 (a) that the surface heat flux remains uninfluenced by change in degree of subcooling through most of the boiling curve, but for low degree of surface superheats, indicating a weak dependence of the liquid temperature in the fully developed nucleate boiling regime. Several studies [176-178] on similar confined jet impingement configurations using a

range of fluids including R113, water and FC-72 have reported that the degree of subcooling has no notable effect on the boiling curve. However, Ma and Bergles [179,180] found that the boiling curve was slightly shifter towards the left (for larger subcoolings) for relatively lower heat fluxes during the initial stages of nucleate boiling, with an increase in degree of subcooling. Cardenas [17] showed photographic evidence that the occupation of heater surface by vapor bubbles was substantially larger for saturated conditions as compared to subcooled conditions for heat fluxes sufficiently below CHF, implying that the impinging jet significantly enhanced the supply of colder fluid for lower subcoolings during the relatively initial stages of nucleate boiling. It was pointed out with computational simulations in Section-5.2.4.3, that during the partial nucleate boiling regime prevalent at low heat fluxes as the influence of the forced convection due to the jet is still significant due to the relatively small number of bubbles formed on the heated surface, the relatively colder impinging fluid results in a concomitant reduction in the surface temperature for any specified heat flux. It was also shown that the reduction in the surface temperature for larger subcoolings was largely due to the contribution of liquid quenching occurring due to the occupation of colder fluid in the void of departed bubbles, in addition to the enhanced forced convection on the fraction of the impingement surface where bubble nucleation did not occur.
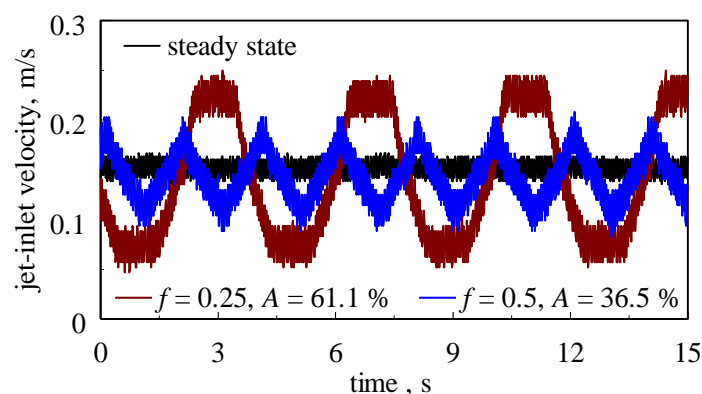
Figure 5.55: Typical velocity profiles at the nozzle outlet during steady state and pulsed jet impingement of FC-72

5.3.2.2 Influence of Jet Pulsations on Thermal Characteristics

The effect of jet pulsations on jet impingement boiling heat transfer characteristics were studied for a given subcooling $\Delta T_{sub} = 17\ ^{\circ}$C and similar Reynolds numbers, for

two different pulsation frequencies and amplitudes, as shown in Table-5.4. It is once again pointed out that as the flow pulsations were introduced using solenoid control valves it was observed that the amplitude of the pulse was consistently reduced when larger frequencies (beyond 1-2 Hz) were attempted for any flow rate, because of the time involved (about 0.35 seconds) in the opening/ closing of the solenoid control valve, besides the natural consequence of fluid inertia in the piping. Figure 5.55 illustrates a two typical pulsating jet velocity profiles obtained using the present
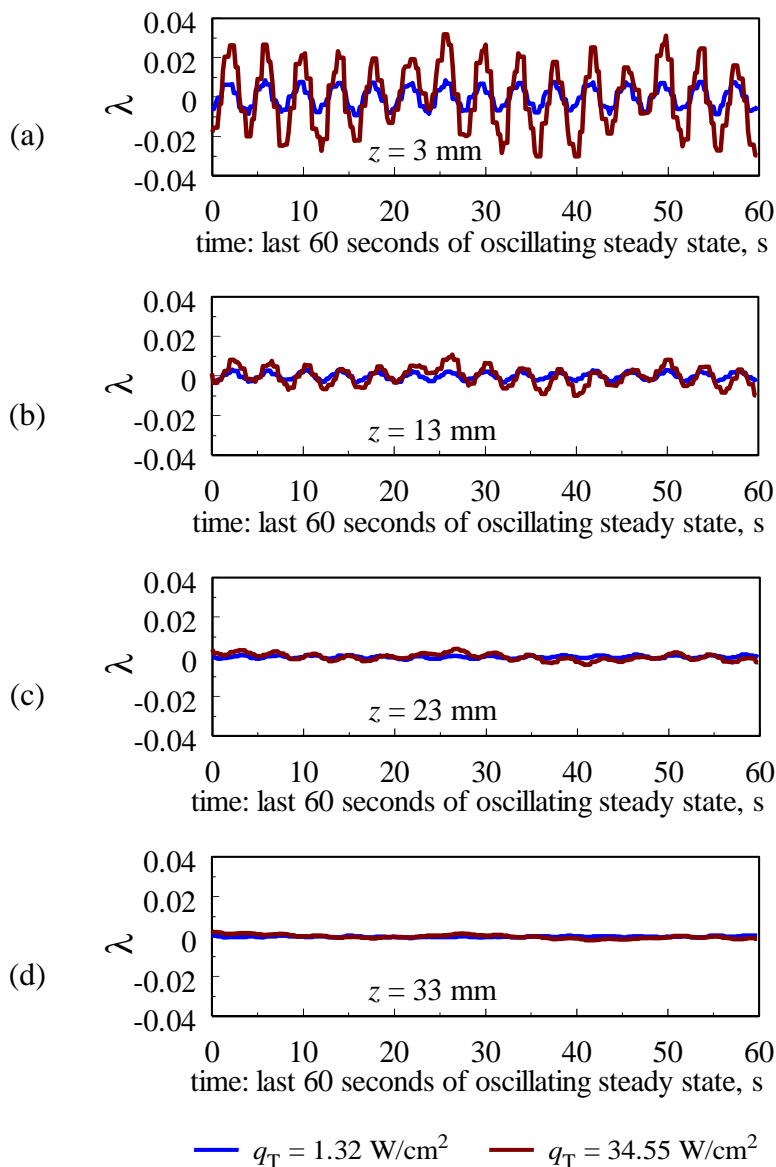
Figure 5.56: Comparison of area averaged normalized temperature oscillations at different locations (represented by z) beneath the impingement surface during the last 60 seconds of the oscillating steady state, for two different vales of time averaged heat fluxes; $A = 61.1$ %, $f = 0.25$ Hz and $Re = 3553.2$

methodology; a steady state velocity profile is also shown for comparison. It can be seen that irrespective of the flow rate, amplitude or frequency, the time period between the two end states remain almost constant (see slope of the curve), thus tending the wave-form more triangular at 0.5 Hz (and for any larger frequency; not shown in the present paper) as compared to that at 0.25 Hz where it is more trapezoidal.

To study the effect of pulsation frequency on the transient surface temperature oscillations an area-averaged normalized temperature was defined in terms of the instantaneous temperature, time averaged mean temperature (over the last 120 seconds of the oscillating steady state) and the jet inlet temperature as shown in Eq. 5.5. The oscillations in the normalized temperature (λ) at four different locations (z) beneath the impingement heat transfer surface, obtained for two different heat fluxes 1.32 W/cm^2 and 34.55 W/cm^2, representative of the convection dominant and nucleate boiling dominant regimes, respectively, are shown in Figs. 5.56 (a-d) for a given pulsation frequency f = 0.25 Hz, amplitude A = 61.1 %, and for mean Reynolds number Re = 3553.2. From comparison of Figs. 5.56 (a-d), it is seen that the amplitude of temperature oscillations beneath the impingement surface is largest close to the impingement surface. It is also seen that the amplitude decreases monotonically with distance beneath the impingement surface (where time averaged 1D conduction is applicable) irrespective of the prescribed average heat flux, due to the thermal inertia of the heater block. Extension of this observed trend to z = 0 (implying the plane of the impingement surface) indicates that the unsteady pulsating jet velocity influences the instantaneous heat transfer characteristics of the heated surface in both single phase convection dominant as well as the nucleate boiling dominant regimes. Visual observation during the experiment revealed a periodic renewal of the boiling process where the bubbles on the heater surface were cyclically flushed downstream of the stagnation point almost in phase with the pulsating jet. While an extrapolative judgement on the amplitude of temperature oscillations is derived from Figs. 5.56 (a-d), the exact values are not be determined from the present methodology as the instantaneous (cross-section averaged) temperatures distribution in the heater block would be nonlinear at any instant of time, and a precise extrapolation would only be possible with sufficiently large
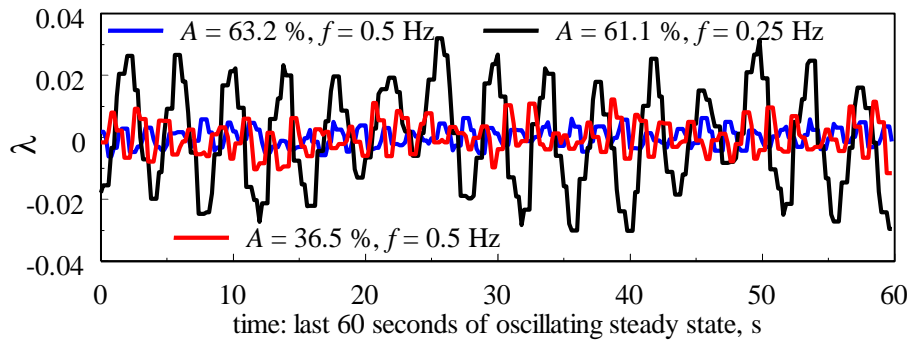
Figure 5.57: Effect of pulsation amplitude and frequency on the area averaged normalized temperature oscillations at $z = 3$ mm beneath the impingement surface

number of temperature measurements close to the impingement surface at small length intervals to reconstruct the nonlinear instantaneous temperature distribution.

Figure 5.57 illustrates the comparison of temperature oscillations at $z = 3$ mm beneath the impingement surface between the three different jet pulsations studied in the present research, for similar time averaged heat flux $q_T \approx 34$ W/cm^2. As indicated in the earlier paragraph, the temperature oscillations are almost in phase with the imposed jet pulsations. It is also notable that the amplitude of the normalized temperature oscillations are considerably reduced for $f = 0.5$ Hz as compared to 0.25 Hz. It was pointed out in the earlier investigation (Section 5.3.1.2) on single phase pulsating liquid jet impingement cooling using de-ionized water that the transient characteristics of the heater surface becomes unresponsive to jet pulsations at large frequencies if the time period of the jet pulsations is less than the response time of the heater, although it was realized that it is possible for the time-averaged thermal boundary layer thickness to be different from that during steady state jet impingement. It is also seen that the amplitude of temperature oscillations are reduced with a reduction in the amplitude of jet pulsations as a natural consequence of the reduction in kinetic energy.

Figure 5.58 (a) illustrate the comparison of the time-averaged boiling curves between the different pulsating jet impingement cases considered for the present study against the steady state boiling curve for a similar mean Reynolds number, and Fig. 5.58 (b) illustrates the corresponding comparisons of the time averaged heat transfer coefficients. It is seen that the boiling curves are predominantly unaffected by jet pulsations over the range of controlling parameters studied. It is however

(a)   (b)
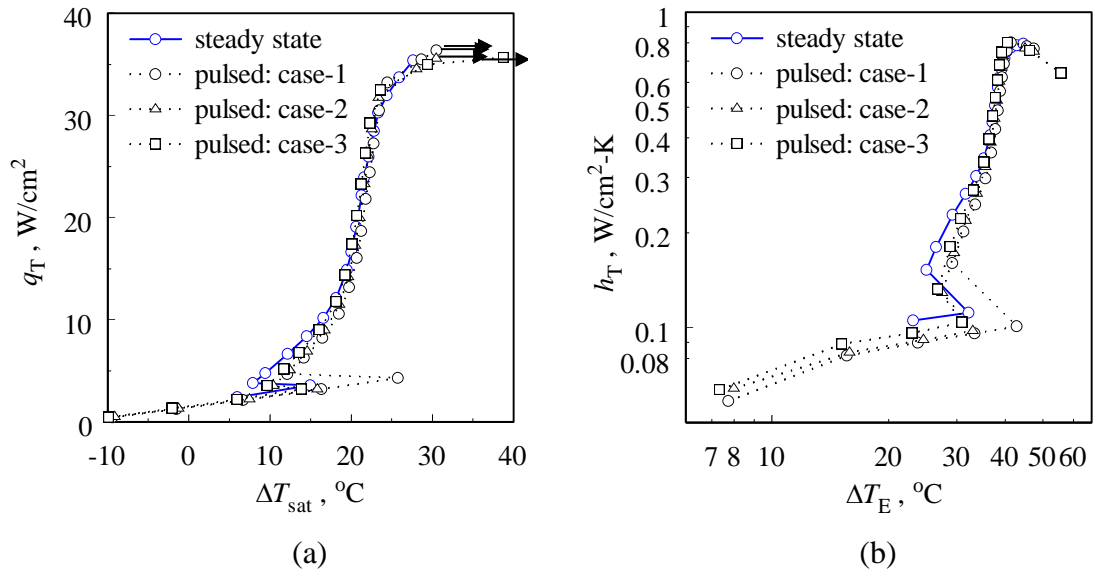
| Case | ΔT_{sub} | Re | f | A | q_{CHF} |
	^oC	-	Hz	%	W/cm^2
steady	17.06	3746.2	0	0	35.41
pulsed-1	17.00	3390.3	0.50	63.2	36.39
pulsed-2	17.02	3553.2	0.25	61.1	35.58
pulsed-3	17.02	3482.4	0.50	36.5	35.69

Figure 5.58: Comparison boiling curves between steady state and pulsating
impinging jets for similar mean Reynolds numbers; ⟶ indicates CHF

observed that there is a slight deterioration of the heat transfer coefficients for low
heat fluxes in the single phase convection and partial nucleate boiling regime. It can
be recalled from Section 5.3.2.2 that a similar result was obtained in with single
phase pulsating liquid jet impingement heat transfer using de-ionized water in a
similar geometry. As the influence of jet velocity is minimal in the fully developed
nucleate boiling regime, and as the time scale of mean flow (jet) pulsations are orders
of magnitude larger than the timescale of the bubble nucleation ebullition process, it
is indicative that low frequency jet pulsations do not provide any enhancement to
traditional steady jet impingement boiling for the operating conditions studied in the
present research. It is however possible that at much larger pulsation frequencies
comparable with the frequency of bubble nucleation/ departure (typically of the order
of several 10s or 100s Hz), pulsating jets could enhance the time averaged boiling
heat transfer characteristics. In a recent study using a vibration induced jet generated
from under a metallic diaphragm controlled by a piezoelectric actuator at 7 kHz
frequency (with a threshold diaphragm displacement of 12 μm), Tillery et al. [22]

showed that boiling heat transfer was enhanced over 200 % due to a cyclic flushing of the heat transfer surface off nucleating bubbles.

5.3.3   Summary of Key Findings

(i)   Single Phase Experiments

- For evaluation of the effect of jet pulsations, baseline experiments were carried out for three different inlet jet temperatures T_N = 34.83 ^{o}C, 39.68 ^{o}C and 44.54 ^{o}C, and $800 \leq Re \leq 7000$, and the Nusselt number data were validated against a standard correlation in the literature. Subsequently, the effect of low frequency pulsations on the associated impingement heat transfer was investigated experimentally using de-ionized water as the working fluid, for controlling parameters in the ranges $500 \leq Re \leq 3400$, f = 0.25 Hz and 0.5 Hz, and A = 0.5 and 1 and a fixed liquid temperature T_N = 39.66 ^{o}C.

- It was found that the amplitude of temperature oscillations on the heater decreases with an increase in jet pulsation frequency, indicating that the surface temperature could become insensitive to applied jet pulsations beyond a threshold pulsation frequency. However, it is possible for the time averaged thermal boundary layer thickness to attain a thickness different from that during steady state jet impingement.

- The change in the magnitude of amplitude of temperature oscillations on the heater are almost the same as the prescribed change in the amplitude of jet pulsations.

- For the range of parameters studied, it was found that the effects of jet pulsations are only marginal on the time averaged heat transfer characteristics.

- While the effect of jet pulsations was negligible for Reynolds numbers upto 1000, a slight decrease (upto 12%) was observed in the Nusselt number for larger Reynolds numbers.

(ii)   Boiling Experiments

- For evaluation of the effectiveness of jet pulsations, base line steady state

experiments were carried out using FC-72 as the working fluid, for two different inlet subcoolings of about 16.9 ^{o}C and 7.5 ^{o}C for jet Reynolds numbers in the range 3500–14000. Subsequently, low frequency pulsating jet impingement heat transfer was studied for two different frequencies 0.25 Hz and 0.5 Hz, and amplitudes of about 36 % and 62 % of mean jet velocity, for a given mean Reynolds number and jet subcooling. Complete boiling curves from single phase convection (including temperature overshoot) through partial and fully developed nucleate boiling were covered upto critical heat flux condition for both steady as well as pulsating jet impingement cases.

- A periodic renewal of the boiling process where the bubbles on the heater surface were cyclically flushed downstream of the stagnation point almost in phase with the pulsating jet was observed during the experiments.

- The amplitude of temperature oscillations beneath the impingement surface was largest close to the impingement surface, while the amplitude decreased monotonically with distance beneath the impingement surface irrespective of the heat flux, indicating that the unsteady pulsating jet velocity influences the instantaneous heat transfer characteristics of the heated surface in both single phase convection dominant and nucleate boiling dominant regimes.

- The amplitude of the normalized temperature oscillations are considerably reduced for f = 0.5 Hz as compared to 0.25 Hz and the amplitude of temperature oscillations were reduced with a reduction in the amplitude of jet pulsations.

- The boiling curves including critical heat fluxes were predominantly unaffected by jet pulsations over the range of controlling parameters studied. The variation in the critical heat flux between steady and pulsating jet impingement boiling was less than 5%.

- A slight deterioration of the heat transfer coefficients was seen for low heat fluxes in the single phase convection and partial nucleate boiling regimes.

- As the influence of jet velocity is minimal in the fully developed nucleate boiling regime, and as the time scale of mean flow (jet) pulsations are orders of magnitude larger than the timescale of the bubble nucleation ebullition process, it is indicative that low frequency jet pulsations does not provide any enhancement to traditional steady jet impingement boiling for the operating conditions studied.

CHAPTER 6

CONCLUSIONS

The preceding chapters presented a detailed description of the present research including the need for the present research, the methodology adopted for accomplishing the objectives and discussion of the results obtained from the extensive experimental and computational analyses. The research distinctly focussed on three different types of confined slot jet impingement cooling *viz.* (i) steady state laminar air jet impingement accounting for effects of buoyancy and surface radiation, (ii) steady state turbulent subcooled jet impingement boiling, and (iii) pulsating single phase (liquid) and boiling jet impingement. The steady state analyses focussed on a fundamental investigation on the mechanisms of heat transfer, through parametric investigations, on the significance and strengths of the contributing mechanisms to the overall heat transfer under different operating conditions. The total heat transfer rate from the heated surface during laminar air jet impingement was attributed to the simultaneous interactions of mixed convection and surface radiation, and during boiling jet impingement to simultaneous turbulent convection, quenching and latent heat transfer. The experimental investigation on pulsating jet impingement focussed on evaluating the effectiveness of jet pulsations under both, single phase as well as boiling jet impingement, on heat transfer augmentation in confined liquid jet impingement systems. The following sections of this chapter present the summary of major conclusions from the present research, highlights of the present study, and recommendations for further research on the subject.

6.1   RESEARCH SUMMARY AND HIGHLIGHTS

(i)   Confined Single Phase Laminar Air Jet Impingement Accounting for Buoyancy and Surface Radiation

A mathematical model and computational code is developed for the analysis of confined and submerged jet impingement flow and heat transfer of a radiatively non-participating gas (air), accounting for effects of surface radiation. A thorough

parametric investigation on the flow and heat transfer is carried for an exhaustive range of controlling dimensionless parameters such as jet Reynolds number, dimensionless standoff distance, dimensionless surface temperature, dimensionless radiation-flow interaction parameter and Richardson number, using the developed computational methodology. The following conclusions are drawn from the research on the mixed convective laminar jet impingement accounting for surface radiation:

- The overall heat transfer in a confined air jet impingement system operating in the laminar Reynolds number regime can be significantly augmented to advantage by improving the surface radiation characteristics, such as surface emissivity. For the range of parameters studied, the improvement of emissivity of the heated surface from 0.05 to 0.85 resulted in the change in the contribution of surface radiation to the total heat transfer from nearly negligible to about 23 % in the stagnation region and over 50 % in the regions downstream.

- The presence of a confinement plate in the jet impingement configuration plays a larger role in the heat transfer process for large surface emissivity conditions, as compared to pure forced or mixed convective jet impingement. For low Reynolds numbers (≈ 100), higher temperatures on the confinement plate that result due to the radiation interaction (for high emissivities) leads to a slight convection suppression on the impingement surface in the wall-jet region, particularly for low standoff distances. For larger Reynolds numbers, larger standoff distances result in the reduction in both convection as well as radiation.

- The increase in the effect of buoyancy assisted fluid motion results in the augmentation of convective Nusselt number, but results in a slight suppression of radiative Nusselt number in the confined geometry.

- For a given surface emissivity of 0.85, the dimensionless radiation-flow interaction parameter was most influential in affecting the heat transfer characteristics. The total Nusselt number was substantially augmented by about 10-25 % in the stagnation region, while over 40-50 % in the wall jet region, for a change in radiation flow interaction parameter over the range considered.

- For sufficiently high Reynolds numbers or standoff distance, a recirculation region is formed on the impingement surface at a certain distance downstream of

the stagnation point, where the contribution of radiation to local Nusselt number reaches about 60 - 80 % for specific combinations of controlling parameters.

• The significance of surface radiation from the perspective of augmentation of heat transfer reduces with an increase in the jet Reynolds number over the range considered.

(ii)   Confined Submerged and Subcooled Turbulent Jet Impingement Boiling

A comprehensive modeling philosophy is developed for the computational analysis of confined and submerged turbulent jet impingement boiling. The necessary user defined functions for the estimation of ebullition parameters are formulated and integrated into the finite volume computational solver ANSYS FLUENT 14.0/14.5. A thorough and rigorous analysis is carried out to ascertain and establish the suitability of different ebullition models as well as multiphase turbulence models, through comparison of the computational predictions against experimental data. Using the comprehensive model, elaborate set of computational simulations are carried out study the effects of the various geometric, flow, thermal parameters on the fundamental mechanism of subcooled impingement boiling heat transfer, with particular focus on the partitioning of the total surface heat flux into convection, quenching and evaporation. The various controlling parameters are dimensionless standoff distance, dimensionless heater size, jet Reynolds number, degree of jet subcooling, type of heating (isothermal, isoflux of uniform generation), and degree of superheat on the heated impingement surface. Results are discussed with spatially averaged boiling curves for the individual component heat fluxes as well as total heat flux, and the local description of the flow and heat transfer characteristics such as distributions of surface temperatures, heat fluxes, liquid-vapor phase change rates, isotherms, streamlines and contours of vapor-phase volume fraction. The relative significance of the partitioned heat transfer mechanisms on the different regimes of the boiling curves are characterized under an exhaustive range of operating parametric conditions using two different fluids- water and FC 72. The following conclusions are drawn from the computational analysis of steady state confined subcooled jet impingement boiling:

- The Rensselaer-Polytechnic-Institute heat flux partitioning model with appropriately adapted boiling submodels can be used for efficient prediction of the flow field as well as estimation of the heat transfer characteristics during subcooled jet impingement boiling.

- Several Reynolds-averaged turbulence models *viz.* RNG-k-ε-EWT, Std. k-ω-SFC, k-ω-SST + Low Re and RSM- linear pressure strain + EWT, appropriately adapted for multiphase simulations were explored for their suitability to simulate boiling heat transfer under an impinging subcooled jet in a confined configuration. The RNG-k-ε-EWT multiphase turbulence model was deemed most suitable in terms of computational accuracy and convergence stability.

- Unal's model for the prediction of bubble departure diameter is determined to be best suitable for the simulation of jet impingement boiling of the type considered in the present research. While for bubble departure frequency, averaged boiling curves from the use of Podowski et al.'s and Cole's models conform well to available experimental data. However, the predicted bubble departure frequencies had opposing relationships with the imposed surface heat flux. As there are experimental evidences to support the trends predicted by both models, a further investigation is suggested to ascertain the correct relationship between the parameters for jet impingement boiling problems.

- The steady state surface averaged heat transfer characteristics under partial and fully developed nucleate boiling conditions exhibited by the different types of heating are nearly equivalent, for the range of parameters considered for the present research. This reassures the validity of the present computational approach by corroborating the fact that the type of heating significantly affects the boiling curves only beyond critical heat flux.

- The contribution of the liquid phase convection to the overall heat transfer reduces monotonically from 100% prior to the onset of nucleate boiling with increase in degree of superheat on the surface. The contribution of quenching heat flux increases initially until the vapor fraction on the surface of the heater reaches a threshold value and consequently attenuates with further increase in the surface superheat. The percentage contribution of latent heat transfer to the overall heat

transfer increases monotonically with increase in surface superheat to almost 100 % near critical heat flux.

- For any prescribed degree of superheat on the impingement surface, liquid phase convection, quenching as well as the evaporative component of the total heat flux are higher for relatively smaller heaters, implying a larger effectiveness of jet impingement boiling for localized heated regions.

- The standoff distance influenced the characteristics of boiling only in the partial nucleate boiling regime, while the boiling curves in the fully developed nucleate boiling regime were unaffected. Besides, in the partial nucleate boiling regime, only on the liquid phase convective component was affected by a change in standoff distance. The liquid phase convective heat flux, and hence, the total heat flux in the partial nucleate boiling regime are consistently larger for smaller standoff distances, irrespective of the heater size. The increase in convective heat flux with change in standoff distance was larger for smaller heaters.

- The observed collapse of boiling curves into a single curve in the nucleate boiling regime for different Reynolds numbers is attributed to the lesser influence of the flow field on the ebullition for the range of parameters considered. However, the heat flux obtained for a specified degree of superheat is consistently larger for larger Reynolds numbers in partial nucleate boiling regime due to the domination of turbulent convection in the regime.

- For a given surface superheat, the magnitude of quenching heat flux is larger for larger Reynolds numbers, and this is attributed to two factors: (i) relatively cooler fluid occupying the void of a departed bubble departure due to the thinner thermal boundary layer for larger Reynolds numbers, and (ii) the bubble dwelling being larger for larger Reynolds numbers. Nevertheless, the relative contribution of quenching heat flux to the total heat flux remains negligibly affected by a change in Reynolds numbers for the range of parameters studied.

- For a given change in jet subcooling, the boiling curve (plotted against degree of superheat) shifts (to the right or left) by the same degree of change prescribed to the jet temperature. The quenching component of the total heat flux is larger for larger subcoolings. In any case, the total heat transfer coefficients obtained are consistently lager for lower subcoolings, implying a beneficial operational mode

for impingement boiling applications.

(iii)   Confined and Submerged Pulsating Single Phase and Boiling Jet Impingement

An experimental facility and test rig are designed and fabricated for the study of confined submerged liquid jet impingement heat transfer under both boiling and non-boiling conditions, with and without jet pulsations. A novel flow pulsation generation and monitoring mechanism is designed to facilitate the control of jet pulsation amplitude and frequency for the pulsating impingement studies. Two different fluids are used for the investigation; de-ionized water is used for single phase pulsating jet impingement studies, and a low boiling point dielectric coolant FC 72 is used for the pulsating jet impingement boiling studies. Baseline steady state jet impingement experiments are carried out prior to the introduction of jet pulsations to evaluate the effectiveness of pulsating jet impingement on the heat transfer characteristics against steady impinging jets. Besides, some of the steady state data obtained from the present experiments are also used for the effective validation of the present computational employed for the boiling jet impingement simulations (discussed in the previous section). The experiments were carried out for a range of operating control parameters including jet temperature (or jet subcooling for boiling experiments), jet Reynolds number, pulsation amplitude and frequency, and surface heat flux. Boiling jet impingement experiments under both steady as well as pulsating jets were carried out from the forced convection regime to critical heat flux including the partial and fully developed nucleate boiling regimes. The following conclusions are drawn from the experimental studies on steady and pulsating single phase (liquid) and boiling jet impingement:

- Temperature oscillations of the heated surface due to jet pulsations are an important factor to be considered during design of pulsating impingement cooling systems. This is because large temperature oscillations could result in potentially damaging transient thermal stresses, particularly when applied in direct cooled electronic applications. Hence the importance of a detailed understanding of the transient behaviour of the heated module is highlighted, besides the time averaged heat transfer characteristics that explicate the effectiveness of the pulsating impingement cooling system.

- The present study showed that the temperature of the heated block oscillates almost in phase with the prescribed cycle of jet pulsations. The change in the magnitude of pulsation amplitude resulted in a concomitant change in the amplitude of temperature oscillations on the heated impingement block under both single phase as well as boiling conditions.

- Under both boiling as well as single phase conditions, the amplitude of temperature oscillations decreases with distance beneath the impingement surface (irrespective of the applied heat flux), suggesting that the presence of an appropriately chosen (thermal diffusivity) spacer between an electronic module and the impinging fluid could help in reduce the temperature oscillations on the hot electronic module.

- The amplitude temperature oscillations on the heated surface decreases with an increase in jet pulsation frequency, indicating that the surface temperature could become insensitive to applied jet pulsations beyond a threshold pulsation frequency. It is however possible for the time averaged thermal boundary layer thickness to attain a thickness different from that during steady state jet impingement.

- During pulsating boiling jet impingement experiments, a periodic renewal of the boiling process was observed, where the bubbles on the heater surface were cyclically flushed downstream of the stagnation point almost in phase with the pulsating jet.

- For the range of parameters studied, it was found that the effects of jet pulsations are only marginal on the time averaged heat transfer characteristics of single phase jet impingement. While the effect of jet pulsations was negligible for Reynolds numbers upto 1000, a slight decrease (upto 12%) was observed in the Nusselt number for higher Reynolds numbers.

- Likewise, under boiling conditions, the boiling curves and critical heat fluxes were predominantly unaffected by jet pulsations over the range of parameters studied. The critical heat flux varied by a maximum of about 5 % between pulsating and steady state jet impingement for similar mean Reynolds numbers and degree of subcoolings.

- As the influence of jet velocity is minimal in the fully developed nucleate boiling regime, and as the time scale of mean flow (jet) pulsations considered for the present study are orders of magnitude larger than the timescale of the bubble nucleation ebullition process, it is indicative that perhaps frequencies with time scales comparable with the bubble growth/ departure are required to efficiently influence the boiling heat transfer characteristics.

- Considering that pulsating jet impingement boiling has not been investigated before, the present research would provide benchmark heat transfer data for further research in the field.

6.2   RECOMMENDATIONS FOR FURTHER WORK

The present research addresses some unresolved issues on three different types of jet impingement cooling systems. Continued research is required to expand on the work presented in this thesis; some recommendations and directions for extended research are presented hereunder:

Laminar jet impingement study accounting for effects of surface radiation was carried out for air, a radiatively-non participating medium. The study could be extended to include the influence of a radiatively participating fluid, and for different Prandtl numbers, to broaden the field of applicability from just impingement cooling to applications such as flame heating, or higher temperature applications (when the absorptivity of air cannot be ignored). As micro-jet impingement systems predominantly operate in the laminar flow regime, the present study could be extended to account for the micro-scale flow effects and thus identify the influence of radiation in augmentation of heat transfer in air cooled micro heat exchangers.

The computational analysis jet impingement boiling, or in general, any flow boiling phenomena is extensively dependant on empirical or semi-mechanistic models for the prediction of the complex ebullition characteristics as well as the liquid-bubble interactions. Most of the available models are not extendable to any general flow boiling phenomena and are highly constrained to the operating conditions, geometry or fluid for which they have been developed. More so, the flow field under an impinging jet is significantly different from that during tube boiling or

parallel flow scenarios, which make the use of boiling submodels developed under such conditions extremely difficult to extend to impingement boiling. A great deal of research is required in the directions of determining exact relationships between the flow and thermal conditions of the systems and the local bubble dynamics during impingement boiling. The presence of bubbles (during bubble growth, and sliding) on the surface as well as near the surface (after departure) significantly affects the turbulence characteristics in the near wall region. Extension of the general turbulence log-law of the wall to such multiphase systems with the introduction of phasic volume fractions may not always present the realistic estimation of the near wall multiphase flow field. The present understanding of turbulent multiphase boundary layers over a surface where boiling takes place is sparse; and further research is required in this front, particularly to help improve the computational framework for more accurate prediction of the physics. Although it would be impractical to accurately model all the surface cavities and nucleation sites on any general surface, the advancements and the growing capability of high speed computing could be exploited to move towards much higher resolved flow boiling simulations accounting for accurate interface capturing, and reducing the need for empirical closures for bubble-liquid momentum, heat and mass transfers. In any case, further controlled experiments are required for the local characterization of bubble dynamics under jet impingement boiling.

The effects of pulsations on impingement boiling is unexplored so far, and an attempt has been made in the present research to study the effects of low frequency jet pulsations on the boiling heat transfer characteristics. The effects of jet pulsations were studied for low frequencies predominantly due to the constraints imposed by the operating mechanism of the solenoid valves, and the fluid inertia in the tubing. Higher frequencies inevitably resulted in reduced jet pulsation amplitudes. A further research is required towards the identification of alternative mechanisms for the production of jet pulsations at frequencies comparable with the time-scale of the bubble dynamics to understand the influence of flow oscillations on the ebullition characteristics. The advancements in fabrication of transparent heaters (transparent aluminium heater) could be exploited for high-speed as well as clear thermal characterization of the local ebullition process on the impingement surface under the influence of jet pulsations.

REFERENCES

[1] C.J.M. Lasance, 2005, Advances in High-Performance Cooling for Electronics, Electronics Cooling, http://www.electronics-cooling.com/2005/11/advances-in-high-performance-cooling-for-electronics/, Retrieved 09/2013.

[2] http://www.genewscenter.com/Press-Releases/GE-Cooling-Technology-As-Thin-As-A-Credit-Card-Enables-Ultra-thin-Tablets-Laptops-3cf6.aspx#downloads, Retrieved 09/2013.

[3] T. Acikalin, S. Wait, S. Garimella, A. Raman, 2004, Experimental Investigation of the Thermal Performance of Piezoelectric Fans, Heat Transfer Engineering, Vol. 25, pp. 4-14.

[4] M. Peterson, T. Fisher, S. Garimella, D. Schlitz, 2003, Experimental Characterization of Low Voltage Field Emission from Carbon-Based Cathodes in Atmospheric Air, Proceedings of IMECE'03, Paper Number: 41775.

[5] N. Beratlis, M. Smith, 2003, Optimization of Synthetic Jet Cooling for Micro-electronics Applications, Proceedings of 19th SemiTherm Symposium, San Jose, CA, pp. 66-73.

[6] L.L. Vasiliev Jr., A.G. Kulakov, 2010, Development of Advanced Miniature Copper Heat Pipes for a Cooling System of Mobile PC Platform, Heat Pipe Science and Technology, Vol 1(1), pp. 59–70.

[7] D.B. Tuckerman, R.F. Pease, 1981, High Performance Heat Sinking for VLSI, IEEE Electron Device Letters, Vol. 2 (5), pp. 126-129.

[8] S. Mohapatra, D. Loikitis, 2005, Advances in Liquid Coolant Technologies for Electronics Cooling, Proceedings of 21st SemiTherm Symposium, San Jose, CA, pp. 354-360.

[9] D. DeSilva, 1973, Cooling Components by Forced Fluorochemical Boiling, Electromech Des, Vol. 17 (5), pp. 24-25.

[10]   S.C. Yao, S. Deb, N. Hammouda, 1989, Impacting Spray Boiling for Thermal Control of Electronic Systems, Heat Transfer in Convective Flows; Philadelphia, PA, USA, American Society of Mechanical Engineers, Heat Transfer Division (Publication), Vol. 111, pp. 129-134.

[11]   S.V.J. Narumanchi, A. Troshko, D. Bharathan, V. Hassani, 2008, Numerical Simulations of Nucleate Boiling in Impinging Jets: Applications in Power Electronics Cooling, International Journal of Heat and Mass Transfer, Vol. 51, pp. 1–12.

[12]   J.H.V. Leinhard, A.M. Hounsary, 1997, Liquid Impingement Cooling in Conjunction with Diamond Substrates for Extremely High Heat Flux Applications, High Heat Flux Engineering II, Bellingham, WA: Society of Photo-Optical Instrumentation Engineers, pp. 29-43.

[13]   X. Liu, J.H.V. Leinhard, 1993, Extremely High Heat Fluxes Beneath Impinging Liquid Jets, ASME Journal of Heat Transfer, Vol. 115 (2), pp. 472-476.

[14]   J. Hall, N. Gao, D. Ewing, 2002, Effect of Confinement on the Heat Transfer from Impinging Round Jets, American Physical Society, Division of Fluid Dymanics 55th Annual Meeting, Paper Number: JM.007.

[15]   C.G. Rao, C. Balaji, S.P. Venkateshan, 2001, Conjugate Mixed Convection with Surface Radiation from a Vertical Plate with a Discrete Heat Source, ASME Journal of Heat Transfer, Vol. 123, pp. 698–702.

[16]   S. Nukiyama, 1934, Film Boiling Water on Thin Wires, Society of Mechanical Engineering, Japan, Vol. 37.

[17]   R. Cardenas, 2011, Submerged Jet Impingement Boiling Thermal Management, Ph.D. Thesis, Oregon State University, Corvalis, OR, USA.

[18]   N. Kurul and M.Z. Podowski, 1991, On the Modeling of Multi-dimensional Effects in Boiling Channels, Proceedings of the 27th National Heat Transfer Conference, Minneapolis, USA.

[19]   R.C. Behera, P. Dutta, K. Srinivasan, 2007, Numerical Study of Interrupted Impinging Jets for Cooling of Electronics, IEEE Transactions on Components and Packaging Technologies, Vol. 30 (2), pp. 275-284.

[20]   H.M. Hofmann, D.L. Movileanu, M. Kind, H. Martin, 2007, Influence of a Pulsation on Heat Transfer and Flow Structure in Submerged Impinging Jets, International Journal of Heat and Mass Transfer, Vol. 50 (17,18), pp. 3638–3648.

[21]   H.S. Sheriff, D.A. Zumbrunnen, 1994, Effect of Flow Pulsations on the Cooling Effectiveness of an Impinging Jet, ASME Journal of Heat Transfer, Vol. 116 (4), pp. 886-895.

[22]   S.W. Tillery, S.N. Heffington, M.K. Smith, A. Glezer, 2006, Boiling Heat Transfer Enhancement using a Submerged Vibration-Induced Jet, Journal of electronic packaging, Vol. 128 (2), pp. 145-149.

[23]   R.A. Daane, S.T. Han, 1961, An Analysis of Air Impingement Drying, Tappi, Vol. 44 (1), pp. 73-80.

[24]   D.E. Metzger, 1962, Spot Cooling and Heating of Surfaces with High Velocity Impinging Air Jets, Technical Report No. 52, Department of Mechanical Engineering, Stanford University, 1962.

[25]   W. Tabakoff, W. Clevenger, 1972, Gas Turbine Blade Heat Transfer Augmentation by Impingement of Air Jets Having Various Configurations, ASME Journal of Engineering Power, Vol. 94, pp. 51-58.

[26]   R. Gardon, J.C. Akfirat, 1965, Heat Transfer Characteristics of Impinging Two-Dimensional Air Jets, ASME AIChE Heat Transfer Conference and Exhibit, Los Angeles, California, Paper number: 65-HT20, re-published in ASME Journal of Heat Transfer, Vol. 88 (1), pp. 101-107.

[27]   R. Gardon, J.C. Akfirat, 1965, The Role of Turbulence in Determining the Heat Transfer Characteristics of Impinging Jets, International Journal of Heat and Mass Transfer, Vol. 8, pp. 1261-1272.

[28]   E.M. Sparrow, T.C. Wong, 1975, Impingement Transfer Coefficients due to Initially Laminar Slot Jets, International Journal of Heat and Mass transfer, Vol. 18, pp. 597-605.

[29]   Z.H. Lin, Y.J. Chou, Y.H. Hung, 1997, Heat Transfer Behaviors of a Confined Slot Jet Impingement, International Journal of Heat and Mass Transfer, Vol. 40, pp. 1095-1196.

[30]   A.R.P. Heiningen, A.S. Mujumdar, W.J.M. Douglas, 1975, Numerical Prediction of the Flow Field and Impingement Heat Transfer due to a Laminar Slot Jet, American Society of Mechanical Engineers, 75-WA/HT-99.

[31]   A.R.P. Heiningen, W.J.M. Douglas, A.S. Mujumdar, 1976, A Study of Two Finite Difference Schemes and Matrix Inversion Technique to Solve the Vorticity Stream Function Equations, Numerical/ Laboratory Computer Methods in Fluid Mechanics, Winter Annual Meeting, New York, American Society.

[32]   A.D. Gosman, W.M. Pun, A.K. Runchal, D.B. Spalding, M. Wolfshtein, 1969, Heat and Mass Transfer in Recirculating Flows, Academic Press, New York.

[33]   H. Miyazaki, E. Silberman, 1971, Flow and Heat Transfer on a Flat Plate Normal to a Two-dimensional Laminar Jet Issuing from a Nozzle of Finite Height, International Journal of Heat and Mass Transfer, Vol. 15, pp. 2097-2107.

[34]   T.D. Yuan, J.A. Liburdy, T. Wang, 1988, Buoyancy Effects on Laminar Impinging Jets, International Journal of Heat and Mass Transfer, Vol. 31 (10), pp. 2137-2145.

[35]   D. Sahoo, M.A. R. Sharif, 2004, Mixed-Convective Cooling of an Isothermal Hot Surface by Confined Slot Jet Impingement, Numerical Heat Transfer-Part A, Vol. 45, pp. 887-909.

[36]   M. Corcione, E. Habib, G. Ruocco, 2006, Heat Transfer Features of a Horizontal Slot Jet Impinging in Mixed Convection, Proceedings of IMECE

2006, ASME International Mechanical Engineering Congress and Exposition, pp. 333-340.

[37]   D. Sahoo, M.A.R. Sharif, 2003, Mixed-Convective Cooling of a Surface by Two-Dimensional Slot Jet Impingement, Proceedings of HT 2003, ASME Summer Heat Transfer Conference, USA, pp. 817-826.

[38]   R. Siegel, M. Perlmutter, 1962, Convective and Radiant Heat Transfer for Flow of a Transparent Gas in a Tube With a Gray Wall, International Journal of Heat Mass Transfer, Vol. 5, pp. 639-660.

[39]   L. Buller, B. McNelis, 1988, Effects of Radiation on Enhanced Electronic Cooling, IEEE Transactions on Components, Hybrids and Manufacturing Technology, Vol. 11 (4), pp. 538-544.

[40]   E.G. Keshock, R. Siegel, 1964, Combined Radiation and Convection in an Asymmetrically Heated Parallel Plate Flow Channel, ASME Journal of Heat Transfer, Vol. 86, pp. 341-350.

[41]   C.G. Rao, C. Balaji, S.P. Venkateshan, 2002, Effect of Surface Radiation on Conjugate Mixed Convection in a Vertical Channel With a Discrete Heat Source in Each Wall, International Journal of Heat and Mass Transfer, Vol. 45, pp. 3331-3347.

[42]   H. Martin, 1977, Heat and Mass Transfer between Impinging Gas Jets and Solid Surfaces, Advances in Heat Transfer, Vol. 13, pp. 1-60.

[43]   N. Zuckerman, N. Lior. 2006, Jet Impingement Heat Transfer: Physics, Correlations, and Numerical Modeling, Advances in Heat Transfer, Vol. 39, pp. 565-631.

[44]   N. Zuckerman, N. Lior, 2005, Impingement Heat Transfer: Correlations and Numerical Modeling, ASME Journal of Heat Transfer, Vol. 127 (5), pp. 544-552.

[45]   A. Dewan, R. Dutta, B. 2012, Srinivasan, Recent Trends in Computation of Turbulent Jet Impingement Heat Transfer, Heat Transfer Engineering, Vol. 33 (4-5), pp. 447-460.

[46]   K. Jambunathan, E. Lai, M.A. Moss, B.L. Button, 1992, A Review of Heat Transfer Data for Single Circular Jet Impingement, International Journal of Heat and Fluid Flow, Vol. 13 (2), pp. 106-115.

[47]   A. Sarkar, N. Nitin, M.V. Karwe, R.P. Singh, 2004, Fluid Flow and Heat Transfer in Air Jet Impingement in Food Processing, Journal of Food Science, Vol. 69 (4), CRH113-122.

[48]   S. Gupta, A. Chaube, P. Verma, 2012, Review on Heat Transfer Augmentation Techniques: Application in Gas Turbine Blade Internal Cooling, Journal of Engineering Science and Technology Review, Vol. 5 (1), pp. 57-62.

[49]   B. Han, R.J. Goldstein, 2001, Jet-Impingement Heat Transfer in Gas Turbine Systems, Annals of the New York Academy of Sciences, Vol. 934 (1), pp. 147-161.

[50]   S. Chander, A. Ray, 2005, Flame Impingement Heat Transfer: A Review, Energy Conversion and Management, Vol. 46 (18), pp. 2803-2837.

[51]   D. Schafer, F.P. Incropera, S. Ramadhyani, 1991, Planar Liquid Jet Impingement Cooling of Multiple Discrete Heat Sources, Journal of Electronic Packaging, Vol. 113, pp. 359-366.

[52]   C.F. Ma, Y.P. Gan, Y.C. Tian, D.H. Lei, T. Gomi, 1993, Liquid Jet Impingement Heat Transfer with or without Boiling, Journal of Thermal Science, Vol. 2 (1), pp. 32-49.

[53]   D.C. Wadsworth, I. Mudawar, 1990, Cooling of a Multichip Electronic Module by means of Confined Two-Dimensional Jets of Dielectric Liquid, Journal of Heat Transfer, Vol. 112, pp. 891- 898.

[54] B.W. Webb, C.F. Ma, 1995, Single-Phase Liquid Jet Impingement Heat Transfer, Advances in Heat Transfer, Vol. 26, pp. 105-217.

[55] M.A. Ebadian, C.X. Lin, 2011, A Review of High-Heat-Flux Heat Removal Technologies, Journal of Heat Transfer, Vol. 133, pp. 110801-1-11.

[56] D.H. Wolf, F.P. Incropera, R. Viskanta, 1993, Jet Impingement Boiling, Advances in Heat Transfer, Vol. 23 (1), pp. 1-132.

[57] M.M. Rahman, R. Ponnappan, 2001, A Review of Thermal Management Techniques and some Recent Developments on Jet Impingement Cooling, 4th International Conference on Mechanical Engineering, December 26-28, Dhaka, Bangladesh, pp.79-96, Keynote Paper 79.

[58] S.V. Garimella, 1999, Heat Transfer and Flow Fields in Confined Jet Impingement, Annual Review of Heat Transfer, Vol. 11, pp. 413-494.

[59] Y.L. Shi, M.B. Ray, A.S. Mujumdar, 2003, Effects of Prandtl Number of Impinging Jet Heat Transfer under a Semi-Confined Laminar Slot Jet, International Communications in Heat and Mass Transfer, Vol. 30 (4), pp. 455-464.

[60] C.Y. Li, S.V. Garimella, 2001, Prandtl-Number Effects and Generalized Correlations for Confined and Submerged Jet Impingement, International Journal of Heat and Mass Transfer, Vol. 44 (18), pp. 3471-3480.

[61] E.U. Schlunder, P. Krotzsch, F.W. Hennecke, 1970, Gesetzmäßigkeiten der Wärme-und Stoffübertragung bei der Prallströmung aus Rund-und Schlitzdüsen, Chemie Ingenieur Technik, Vol. 42 (6), pp. 333-338.

[62] M. Korger, F. Krizek, 1966, Mass-Transfer Coefficient in Impingement Flow from Slotted Nozzles, International Journal of Heat and Mass Transfer, Vol. 9 (4), pp. 337-344.

[63] W.M. Rohsenow, 1985, Boiling, Handbook of Heat Transfer Fundamentals, 2nd ed. (W.M. Rohsenow et al., eds.), Chapter 12, McGraw-Hill, New York.

[64] K.A. Joudi, D.D. James, 1981, Surface Contamination, Rejuvenation, and the Reproducibility of Results in Nucleate Pool Boiling, Journal of Heat Transfer, Vol. 103, pp. 453-458.

[65] V.V. Fisenko, V.I. Baranenko, L.A. Belov, V.A. Korenevskiy, 1988, Effect of Dissolved Gas on Nucleate Boiling and Critical Heat Flux, Heat Transfer-Soviet Research, Vol. 20, pp. 294-299.

[66] G. Guglielmini, E. Nannei, 1976, On the Effect of Heating Wall Thickness on Pool Boiling Burnout, International Journal of Heat Mass Transfer, Vol. 19, pp. 1073-1075.

[67] V.V. Klimenko, S.Y. Snytin, 1990, Film Boiling Crisis on a Submerged Heating Surface, Experimental Thermal and Fluid Science, Vol. 3, pp. 467-479.

[68] W.R. Houchin, J.H. Lienhard, 1966, Boiling Burnout in Low Thermal Capacity Heaters, ASME Paper Number 66-WA/HT-40.

[69] A.E. Bergles, W.G. Thompson Jr, 1970, The Relationship of Quench Data to Steady State Pool Boiling Data, International Journal of Heat and Mass Transfer, Vol. 13, pp.55-68.

[70] C.H. Shin, S.J. Wu, K.M. Kim, H.H. Cho, 2008, Effect of Planar Jet Impingement on Single Phase and Boiling Heat Transfer Characteristics, JP Journal of Heat and Mass Transfer, Vol. 2 (1), pp. 55-71.

[71] I. Mudawar, D.C. Wadsworth, 1991, Critical Heat Flux from a Simulated Chip to a Confined Rectangular Impinging Jet of Dielectric Liquid, International Journal of Heat and Mass Transfer, Vol. 34 (6), pp. 1465-1479.

[72] D.C. Wadsworth, I. Mudawar, 1992, Enhancement of Single-Phase Heat Transfer and Critical Heat Flux from an Ultra-High-Flux Simulated Microelectronic Heat Source to a Rectangular Impinging Jet of Dielectric Liquid, ASME Journal of Heat Transfer, Vol. 114 (3), pp. 764-768.

[73] C.T. Chang, G. Kojasoy, F. Landis, S. Downing, 1995, Confined Single-and Multiple-Jet Impingement Heat Transfer-II, Turbulent Two-Phase Flow, International Journal of Heat and Mass Transfer, Vol. 38 (5), pp. 843-851.

[74] C.T. Chang, G. Kojasoy, F .Landis, S. Downing, 1995, Confined Single-and Multiple-Jet Impingement Heat Transfer-I, Turbulent Submerged Liquid Jets, International Journal of Heat and Mass Transfer, Vol. 38 (5), pp. 833-842.

[75] W. Nakayama, M. Behnia, H. Mishima, 2000, Impinging Jet Boiling of a Fluorinert Liquid on a Foil Heater Array, ASME Journal of Electronic Packaging, Vol. 122 (2), pp. 132-137.

[76] C.H. Shin, K.M. Kim, S.H. Lim, H.H. Cho, 2009, Influences of Nozzle-Plate Spacing on Boiling Heat Transfer of Confined Planar Dielectric Liquid Impinging Jet, International Journal of Heat and Mass Transfer, Vol. 52 (23-24), pp. 5293-5301.

[77] I. Mudawar, 2001, Assessment of High-Heat-Flux Thermal Management Schemes, IEEE Transactions on Components and Packaging Technologies, Vol. 24(2), pp. 122-141.

[78] W. Nakayama, 1997, Liquid-Cooling of Electronic Equipment: Where does it Offer Viable Solutions?, Advances in Electronic Packaging, Vol. 2, pp. 2045-2052.

[79] M.K. Jensen, G.J. Memmel, 1986, Evaluation of Bubble Departure Diameter Correlations, Heat Transfer: 8th International Conference, Vol. (4), pp. 1907-1912.

[80] V.I. Tolubinsky, D.M. Kostanchuk, 1970, Vapor Bubbles Growth Rate and Heat Transfer Intensity at Subcooled Water Boiling, 4th International Heat Transfer Conference, Paris, France, Paper number: B2.8.

[81] G. Kocamustafaogullari, M. Ishii, 1983, Interfacial Area and Nucleation Site Density in Boiling Systems, International Journal of Heat and Mass Transfer, Vol. 26 (9), pp. 1377-1387.

[82]   H.C. Unal, 1976, Maximum Bubble Diameter, Maximum Bubble-Growth Time and Bubble-Growth Rate During Subcooled Nucleate Flow Boiling of Water up to 17.7 M N/m^2, International Journal of Heat and Mass Transfer, Vol. 19, pp. 643-649.

[83]   H.J. Ivey, 1967, Relationships Between Bubble Frequency, Departure Diameter and Rise Velocity in Nucleate Boiling, International Journal of Heat and Mass Transfer, Vol. 10, pp. 1023-1040.

[84]   I.G. Malenkov, 1971, Detachment Frequency as a Function of Size for Vapor Bubbles, Journal of Engineering Physics, Vol. 20 (6), pp. 704-708.

[85]   R. Cole, 1960, A Photographic Study of Pool Boiling in the Region of the Critical Heat Flux, A.I.Ch.E. Journal, Vol. 6 (4), pp. 533-538.

[86]   N. Basu, G.R. Warrier, V.K. Dhir, 2005, Wall Heat Flux Partitioning During Subcooled Flow Boiling: Part 1- Model Development, ASME Journal of Heat Transfer, Vol. 127, pp. 131-140.

[87]   R.M. Podowski, D.A. Drew, R.T. Lahey Jr., M. Z. Podowski, 1997, A Mechanistic Model of the Ebullition Cycle in Forced Convection Subcooled Boiling, Proc. 8th International Topical Meeting on Nuclear Reactor Thermal-Hydraulics, Kyoto, Japan, Vol. 3, pp. 1535-1542.

[88]   R. Situ, M. Ishii, T. Hibiki, J.Y. Tu, G.H. Yeoh, M. Mori, 2008, Bubble Departure Frequency in Forced Convective Subcooled Boiling Flow, International Journal of Heat and Mass Transfer, Vol. 51, pp. 6268-6282.

[89]   R. Situ, J.Y. Tu, G.H. Yeoh, T. Hibiki, G.C. Park, 2007, Assessment of Effect of Bubble Departure Frequency in Forced Convective Subcooled Boiling, Proceedings of the 16th Australian Fluid Mechanics Conference, December 2-7, Gold Coast, Australia, pp. 848-855.

[90]   M.Z. Podowski, 2012, Towards Mechanistic Modeling of Boiling Heat Transfer, Nuclear Engineering and Technology, Vol. 44(8), pp. 889-896.

[91] N.R. Snyder, D.K. Edwards, 1956, Post Conference Comments-Summary of Conference of Bubble Dynamics, Jet Propulsion Lab, Pasadena, CA, pp. 20-137.

[92] D. Wang, E. Yu, A. Przekwas, 1999, A Computational Study of Two-Phase Jet Impingement Cooling of an Electronic Chip, 15th IEEE Semi-therm Symposium, IEEE, pp. 10-15.

[93] S. Narumanchi, A. Troshko, V. Hassani, D. Bharathan, 2006, Numerical Simulations of Boiling Jet Impingement Cooling in Power Electronics, In Thermal and Thermomechanical Phenomena in Electronics Systems, ITHERM-06, IEEE, pp. 204-214.

[94] Y.Y. Li, Z.H. Liu, 2012, Theoretical Research of Critical Heat Flux in Subcooled Impingement Boiling on the Stagnation Zone, International Journal of Heat and Mass Transfer, Vol. 55, pp. 7544–7551.

[95] W. Timm, K. Weinzierl, A. Leipertz, 2003, Heat Transfer in Subcooled Jet Impingement Boiling at High Wall Temperatures, International Journal of Heat and Mass Transfer, Vol. 46, pp. 1385–1393.

[96] A.M.T. Omar, M.S. Hamed, M. Shoukri, 2009, Modeling of Nucleate Boiling Heat Transfer under an Impinging Free Jet, International Journal of Heat and Mass Transfer, Vol. 52, pp. 5557–5566.

[97] N. Karwa, T.G. Roisman, P. Stephan, C. Tropea, 2011, A Hydrodynamic Model for Subcooled Liquid Jet Impingement at the Leidenfrost Condition, International Journal of Thermal Sciences, Vol. 50 (6), pp. 993-1000.

[98] W. Lee, G. Son, 2013, Numerical and Analytical Study of Film Boiling in a Planar Liquid Jet, International Communications in Heat and Mass Transfer, Vol. 46, pp. 42-48.

[99] K. Kim, G. Son, 2013, Numerical Analysis of Film Boiling in Liquid Jet Impingement, Numerical Heat Transfer-Part A: Applications, Vol. 64 (9), pp. 695-709.

[100] A. Pavlova, M. Amitay, 2006, Electronic Cooling Using Synthetic Jets, ASME Journal of Heat Transfer, Vol. 128, pp. 897-907.

[101] C. Cengiz, H. Frank, 2002, Forced Convection Heat Transfer Enhancement Using a Self-Oscillating Impinging Planar Jet, ASME Journal of Heat Transfer, Vol. 124, pp. 770-782.

[102] S.K. Narumanchi, C.H. Amon, J.Y. Murthy, 2003, Influence of Pulsating Submerged Liquid Jets on Chip-level Thermal Phenomena, ASME Journal of Heat Transfer, Vol. 125, pp. 354-361.

[103] E.C. Mladin, D.A. Zumbrunnen, 1997, Local Convective Heat Transfer to Submerged Pulsating Jets, International Journal of Heat and Mass Transfer, Vol. 40 (14), pp. 3305-3321.

[104] L.F.A. Azevedo, B.W. Webb, M. Queiroz, 1994, Pulsed Air Jet Impingement Heat Transfer, Experimental Thermal and Fluid Science, Vol. 8 (3), pp. 206-213.

[105] D.A. Zumbrunnen, M. Aziz, 1993, Convective Heat Transfer Enhancement Due to Intermittency in an Impinging Jet, ASME Journal of Heat Transfer, Vol. 115, pp. 91-98.

[106] R. Zulkifli, K. Sopian, 2007, Studies on Pulse Jet Impingement Heat Transfer: Flow Profile and Effect of Pulse Frequencies on Heat Transfer, International Journal of Engineering and Technology, Vol. 4 (1), pp. 86-94.

[107] E.C. Mladin, D.A. Zumbrunnen, 1994, Nonlinear Dynamics of Laminar Boundary Layers in Pulsatile Stagnation Flows, Journal of Thermophysics and Heat Transfer, Vol. 8 (3), pp. 514-523.

[108] R. Zulkifli, E. Benard, S. Raghunathan, A. Linton, 2004, Effect of Pulse Jet Frequency on Impingement Heat Transfer, AIAA 42nd Aerospace Sciences Meeting & Exhibit, Reno, Paper number: AIAA 2004-1343.

[109] H.D. Haustein, G. Tebrügge, W. Rohlfs, R. Kneer, 2012, Local Heat Transfer Coefficient Measurement Through a Visibly-Transparent Heater under Jet-

Impingement Cooling, International Journal of Heat and Mass Transfer, Vol. 55 (23-24), pp. 6410-6424.

[110] R.M. Curet, J.P. Girard, 1973, Visualization of a Pulsating Jet, Proceedings of The Joint Meeting of the Fluids Engineering Division-Fluid Mechanics of Mixing, June 20-22, Atlanta, Georgia, pp. 173-180.

[111] R.B. Farrington, S.D. Claunch, 1994, Infrared Imaging of Large-Amplitude, Low Frequency Disturbances on a Planar Jet, AIAA Journal, Vol. 32, pp. 317-323.

[112] A. Glezer, 1988, The Formation of Vortex Rings, Physics of Fluids, Vol. 31, pp. 3532-3542.

[113] H.S. Sheriff, D.A. Zumbrunnen, 1997, Improvements in Heat Transfer Characteristics of Jet Arrays by Incorporating Convergent Nozzles with and without Flow Pulsations, HTD-Vol. 347 National Heat Transfer Conference, Vol. .9, pp. 83-94.

[114] Z. Zhao, Y. Peles, M.K. Jensen, 2013, Water Jet Impingement Boiling from Structured-Porous Surfaces, International Journal of Heat and Mass Transfer, Vol. 63, pp. 445-453.

[115] E. Demir, A. Kosar, T. Izci, O.Y. Perk, M. Sesen, W. Khudhayer, T. Karabacak, 2012, Multiphase Submerged Jet Impingement Cooling Utilizing Nanostructured Plates, ASME 2012 10th International Conference on Nanochannels, Microchannels, and Minichannels, Rio Grande, Puerto Rico, USA, July 8-12, Paper number: ICNMM2012-73062, pp. 49-56.

[116] R.W. Hyland, A. Wexler, 1983, Formulations for the Thermodynamic Properties of Dry Air from 173.15 K to 473.15 K and of Saturated Moist Air from 173.15 to 372.15 K at Pressures to 5 M Pa. Transactions of ASHRAE, Vol. 89 (2a), pp.520–35.

[117] R. Siegel, J.R. Howell, 1992, Thermal Radiation Heat Transfer, 3rd ed., Taylor & Francis, Washington and London.

[118] N. Kurul, M.Z. Podowski, 1990, Multidimensional Effects in Forced Convection Subcooled Boiling, Proceedings of the 9th International Heat Transfer Conference, Jerusalem, Israel, Vol. 1, pp. 21-26.

[119] W.E. Ranz, W.R. Marshall Jr., 1952, Evaporation from Drops, Part 1 and Part 2, Chemical Engineering Progress, Vol. 48 (4), pp. 173-180.

[120] M. Ishii, N. Zuber, 1979, Drag Coefficient and Relative Velocity in Bubbly, Droplet or Particulate Flows, AIChE Journal, Vol. 25 (5), pp. 843-855.

[121] F.J. Moraga, F.J. Bonetto, R.T. Lahey, 1999, Lateral Forces on Spheres in Turbulent Uniform Shear Flow, International Journal of Multiphase Flow, Vol. 25, pp. 1321-1372.

[122] T. Frank, J. Shi, A.D. Burns, 2004, Validation of Eulerian Multiphase Flow Models for Nuclear Reactor Safety Applications, 3rd International Symposium on Two-phase Flow Modelling and Instrumentation, Pisa.

[123] F.J. Moraga, A.E. Larreteguy, D.A. Drew, R.T. Lahey, 2003, Assessment of Turbulent Dispersion Models for Bubbly Flows in the Low Stokes Number Limit, International Journal of Multiphase Flow, Vol. 29, pp. 655-673.

[124] P.M. Carrica, D.A. Drew, R.T. Lahey, 1999, A Polydisperse Model for Bubbly Two-Phase Flow Around a Surface Ship, International Journal of Multiphase Flow, Vol. 25, pp. 257-305.

[125] A. Behzadi, R.I. Issa, H. Rusche, 2001, Effects of Turbulence on Interphase Forces in Dispersed Flow, Proceedings of ICMF-2001, 4th International Conference in Multiphase Flow, New Orleans, LA, USA, pp. 1-12.

[126] A.D. Gosman, C. Lekakou, S. Politis, R.I. Issa, M.K. Looney, 1992, Multidimensional Modeling of Turbulent Two-Phase Flows in Stirred Vessels, AIChE Journal, Vol. 38 (12), pp. 1946-1956.

[127] A.D. Burns, T. Frank, I. Hamill, J. Shi, 2004, The Favre Averaged Drag Model for Turbulence Dispersion in Eulerian Multi-Phase Flows,

Proceedings of ICMF-2004, 5th International Conference in Multiphase Flow, Yokohama, Japan, Paper number: 392, pp. 1-12.

[128] J. Shi, T. Frank, A.D. Burns, 2004, Turbulent Dispersion Force-Physics, Model Derivation and Evaluation, 2nd Joint Workshop - Multiphase Flow: Simulation, Experiment and Application, F.Z. Rossendorf & Ansys Germany GmbH, pp. 28-30.

[129] V. Yakhot, S.A. Orszag, S. Thangam, T.B. Gatski, C.G. Speziale, 1992, Development of Turbulence Models for Shear Flows by a Double Expansion Technique, Physics of Fluids-A, Vol. 4 (7), pp. 1510-1520.

[130] V. Yakhot, S.A. Orszag, 1986, Renormalization - Group Analysis of Turbulence, Physical Review Letters, Vol. 57 (14), pp. 1722-1724.

[131] V. Yakhot, S.A. Orszag, 1986, Renormalization - Group Analysis of Turbulence I: Basic theory, Journal of Scientific Computing, Vol. 1 (1), pp. 3-51.

[132] V. Yakhot, L.M. Smith, 1992, The Renormalization-Group, The e{open}-Expansion and Derivation of Turbulence Models, Journal of Scientific Computing, Vol. 7 (1), pp. 35-61.

[133] M.S. Khalid, S.A. Hossam, A.W. Mazlan, M.S. Mohsin, 2009, Numerical Simulation of Confined Vortex Flow Using a Modified k-ε Turbulence Model, CFD-Letters, Vol. 1 (2), pp. 87-94.

[134] A.A. Troshko, Y.A. Hassan, 2001, A Two-Equation Turbulence Model of Turbulent Bubbly Flows, International Journal of Multiphase Flow, Vol. 27, pp. 1965-2000.

[135] Y. Egorov, F. Menter, 2004, Experimental Implementation of the RPI Wall Boiling Model in CFX-5.6, Technical Report ANSYS/TR-04-10, ANSYS Germany GmbH.

[136] V.H. Del Valle, D.B.R. Kenning, 1985, Subcooled Flow Boiling at High Heat Flux, International Journal of Heat and Mass Transfer, Vol. 28, pp. 1907-1920.

[137] M. Lemmert, L.M. Chawla, 1977, Influence of Flow Velocity on Surface Boiling Heat Transfer Coefficient, in Heat Transfer in Boiling, E. Hahne and U.Grigull, Eds., Academic Press and Hemisphere, New York, NY, USA.

[138] R. Cardenas, V. Narayanan, 2012, Heat Transfer Characteristics of Submerged Jet Impingement Boiling of Saturated FC-72, International Journal of Heat and Mass Transfer, Vol. 55, pp. 4217-4231.

[139] M. Monde, Y. Katto, 1978, Burnout in a High Heat-Flux Boiling System with an Impinging Jet, International Journal of Heat Mass Transfer, Vol. 21, pp. 295-305.

[140] Z. Liu, T. Tong, Y. Qiu, 2004, Critical Heat Flux of Steady Boiling for Subcooled Water Jet Impingement on the Flat Stagnation Zone, ASME Journal of Heat Transfer, Vol. 126 (2), pp. 179-183.

[141] M.K. Jensen, G.J. Memmel, 1986, Evaluation of Bubble Departure Diameter Correlations, Heat Transfer: 8th International Conference, Vol. (4), pp. 1907-1912.

[142] H. Li, S.A. Vasquez, H. Punekar, R. Muralikrishnan, 2011, Prediction of Boiling and Critical Heat Flux using an Eulerian Multiphase Model, Proceedings of the ASME 2011 International Mechanical Engineering Congress & Exposition IMECE2011, Denver, Colorado, USA, Paper number: IMECE2011-65539.

[143] J.Y. Tu, G.H. Yeoh, 2002, On Numerical Modelling of Low-Pressure Subcooled Boiling Flows, International Journal of Heat and Mass Transfer, Vol. 45, pp. 1197-1209.

[144] E. Krepper, B. Koncar, Y. Erogov, 2007, CFD Modelling of Subcooled Boiling - Concept, Validation and Application to Fuel Assembly Design, Nucleate Engineering Design, Vol. 237, pp. 716-731.

[145] ANSYS® Academic Research Release 14.5, Help System, ANSYS-FLUENT Theory Guide, October 2012, ANSYS, Inc., Southpointe, USA.

[146] A.S. Perkins, J.W. Westwater, 1956, Measurements of Bubbles Formed during Boiling Methanol, AIChE Journal, Vol. 2 (4), pp. 471-476.

[147] R.G. Deissler, 1954, Columbia University Heat Transfer Symposium, New York, USA.

[148] J.W. Westwater, 1958, Boiling Heat Transfer, American Scientist, Vol. 47, pp. 427-446.

[149] H.B. Clark, P.S. Strenge, J.W. Westwater, 1959, Active Sites for Nucleate Boiling, Chemical Engineering Progress and Symposium, Vol. 55, pp. 103-110.

[150] P. Griffith, J.D. Wallis, 1960, The Role of Surface Conditions in Nucleate Boiling, Chemical Engineering Progress and Symposium, Vol. 56, pp. 49-63.

[151] Y.Y. Hsu, 1962, On the Size Range of Active Nucleation Cavities on a Heating Surface, ASME Journal of Heat Transfer, Vol. 84, pp. 207-216.

[152] S.G. Kandlikar, P.H. Spiesman, 1998, Effect of Surface Finish on Flow Boiling Heat Transfer, American Society of Mechanical Engineers, Heat Transfer Division, (Publication) HTD 361-1, pp. 157-163.

[153] R. Cardenas, V. Narayanan, 2012, Submerged Jet Impingement Boiling of Water under Subatmospheric Conditions, ASME Journal of Heat Transfer, Vol. 134 (2), article number: 020909.

[154] S.J. Kline, F.A. McClintock, 1953, Describing the Uncertainties in Single Sample Experiments, Mechanical Engineering, pp. 3-8.

[155] R.J. Moffat, 1988, Describing the Uncertainties in Experimental Results, Experimental Thermal and Fluid Science, Vol. 1 (1), pp.3-17.

[156] D.C. Wilcox, 1988, Re-assessment of the Scale-Determining Equation for Advanced Turbulence Models, AIAA Journal, Vol. 26 (11), pp. 1299-1310.

[157] D.C. Wilcox, 2004, Turbulence Modeling for CFD, ISBN 1-928729-10-X, 2nd Ed., DCW Industries, Inc.

[158] F.R. Menter, 1993, Zonal Two Equation k-ω Turbulence Models for Aerodynamic Flows, AIAA Paper, pp. 1993-2906.

[159] F.R. Menter, 1994, Two-Equation Eddy-Viscosity Turbulence Models for Engineering Applications, AIAA Journal, Vol. 32 (8), pp. 1598-1605.

[160] D. Cokljat, M. Slack, S.A. Vasquez, 2003, Reynolds-Stress Model for Eulerian Multiphase, Proceedings of the 4th International Symposium on Turbulence Heat and Mass Transfer, pp. 1047-1054.

[161] W.R. Chang, C.A. Chen, J.H. Ke, T.F. Lin, 2010, Subcooled Flow Boiling Heat Transfer and Associated Bubble Characteristics of FC-72 on a Heated Micro-pin-finned Silicon Chip, International Journal of Heat and Mass Transfer, Vol. 53, pp. 5605-5621.

[162] C. Ramaswamy, Y. Joshi, W. Nakayama, W.B. Johnson, 2002, High-Speed Visualization of Boiling from an Enhanced Structure, International Journal of Heat and Mass Transfer, Vol. 45, pp. 4761-4771.

[163] G.L. Medavaram, S.H. Bhavnani, R.C. Jaeger, 2005, Ebullition Characteristics of an Isolated Surface Microstructure for Immersion Cooled Heat Sinks, IEEE Transaction on Components and Packaging Technologies, Vol. 28 (2), pp. 263-271.

[164] C. Hutter, D.B.R. Kenning, K. Sefiane, T.G. Karayiannis, H. Lin, G. Cummins, A.J. Walton, 2010, Experimental Pool Boiling Investigations of FC-72 on Silicon with Artificial Cavities and Integrated Temperature Microsensors, Experimental Thermal and Fluid Science, Vol. 34, pp. 422-433.

[165] C. Hutter, K. Sefiane, T.G. Karayiannis, A.J. Walton, R.A. Nelson, D.B.R. Kenning, 2012, Nucleation Site Interaction between Artificial Cavities during Nucleate Pool Boiling on Silicon with Integrated Micro-Heater and

Temperature Micro-sensors, International Journal of Heat and Mass Transfer, Vol. 55, pp. 2769-2778.

[166] P. Mani, 2012, Local Heat Transfer Rate and Bubble Dynamics during Jet Impingement Boiling, Ph.D. Thesis, Oregon State University, USA.

[167] V.P. Carey, 1992, Liquid-Vapor Phase-Change Phenomena: An introduction to the Thermophysics of Vaporization and Condensation Process in Heat Transfer, 2nd ed., Hemisphere Publishing Corporation, Taylor and Francis Group, Washington, USA.

[168] N. Basu, G.R. Warrier, V.K. Dhir, 2005, Wall Heat Flux Partitioning During Subcooled Flow Boiling: Part II-Model Validation, ASME Journal of Heat Transfer, Vol. 127, pp. 141-148.

[169] P. Mani, R. Cardenas, V. Narayanan, 2012, Comparison of Area-Averaged and Local Boiling Curves in Pool and Jet Impingement Boiling, International Journal of Multiphase Flow, Vol. 42, pp. 115–127.

[170] N.M. Seiler, J.M. Seiler, O. Simonin, 2004, Transition Boiling at Jet Impingement, International Journal of Heat and Mass Transfer, Vol. 47, pp. 5059-5072.

[171] R.W. Bowring, 1962, Physical Model based on Bubble Detachment and Calculation of Steam Voidage in the Subcooled Region of a Heated Channel, HPR-10, Institute for Atomenergi, Halden, Norway.

[172] W.H. McAdams, W.E. Kennel, C.S. Minden, C. Rudolf, J.E. Dow, 1949, Heat Transfer at High Rates to Water with Surface Boiling, Industrial Engineering Industrial & Engineering Chemistry, Vol. 41, pp. 1945-1953.

[173] A.E. Bergles, W.M. Rohsenow, 1964, The determination of forced convection surface-boiling heat transfer, ASME Journal of Heat Transfer, Vol. 86, pp. 365-372.

[174] J. Lee, S.J. Lee, 1999, Stagnation Region Heat Transfer of a Turbulent Axisymmetric Jet Impingement, Experimental Heat Transfer, Vol. 12, pp. 137-156.

[175] D. Wolf, F.P. Incropera, R. Viskanta, 1996, Local Jet Impingement Boiling Heat Transfer, International Journal of Heat and Mass Transfer, Vol. 39, pp. 1395-1406.

[176] R.J. Copeland, 1970, Boiling Heat Transfer to a Water Jet Impinging on a Flat Surface (-l g), Ph.D. Thesis, Southern Methodist University, Dallas, TX

[177] S. Ishigai, S. Nakanishi, T. Ochi, 1978, Boiling Heat Transfer for a Plane Water Jet Impinging on a Hot Surface, Proceedings of the 6th International Heat Transfer Conference, Vol. 1, Paper number: FB-30, pp. 445-450.

[178] D.T. Vader, F.P. Incropera, R. Viskanta, 1992, Convective Nucleate Boiling on a Heated Surface Cooled by an Impinging, Planar Jet of Water, ASME Journal of Heat Transfer, Vol. 114, pp. 152-160.

[179] C.F. Ma, A.E. Bergles, 1983, Boiling Jet Impingement Cooling of Simulated Microelectronic Chips, in Heat Transfer in Electronic Equipment-1983 (S. Oktay and A. Bar-Cohen, eds.), Heat Transfer Division, Vol. 28, pp. 5-12.

[180] C.F. Ma, A.E. Bergles, 1986, Jet Impingement Nucleate Boiling, International Journal of Heat and Mass Transfer, Vol. 29, pp. 1095-1101.

[181] 3M Fluorinert Electronic Liquid FC-72, Product Information data sheet.

[182] Thermophysical Properties of Fluid Systems, NIST Standard Reference Database, webbook.nist.gov/chemistry/fluid, Retrieved 09/2013.

Appendix A-1: Design Considerations for the Choice of Components in the Development of the Experimental Facility
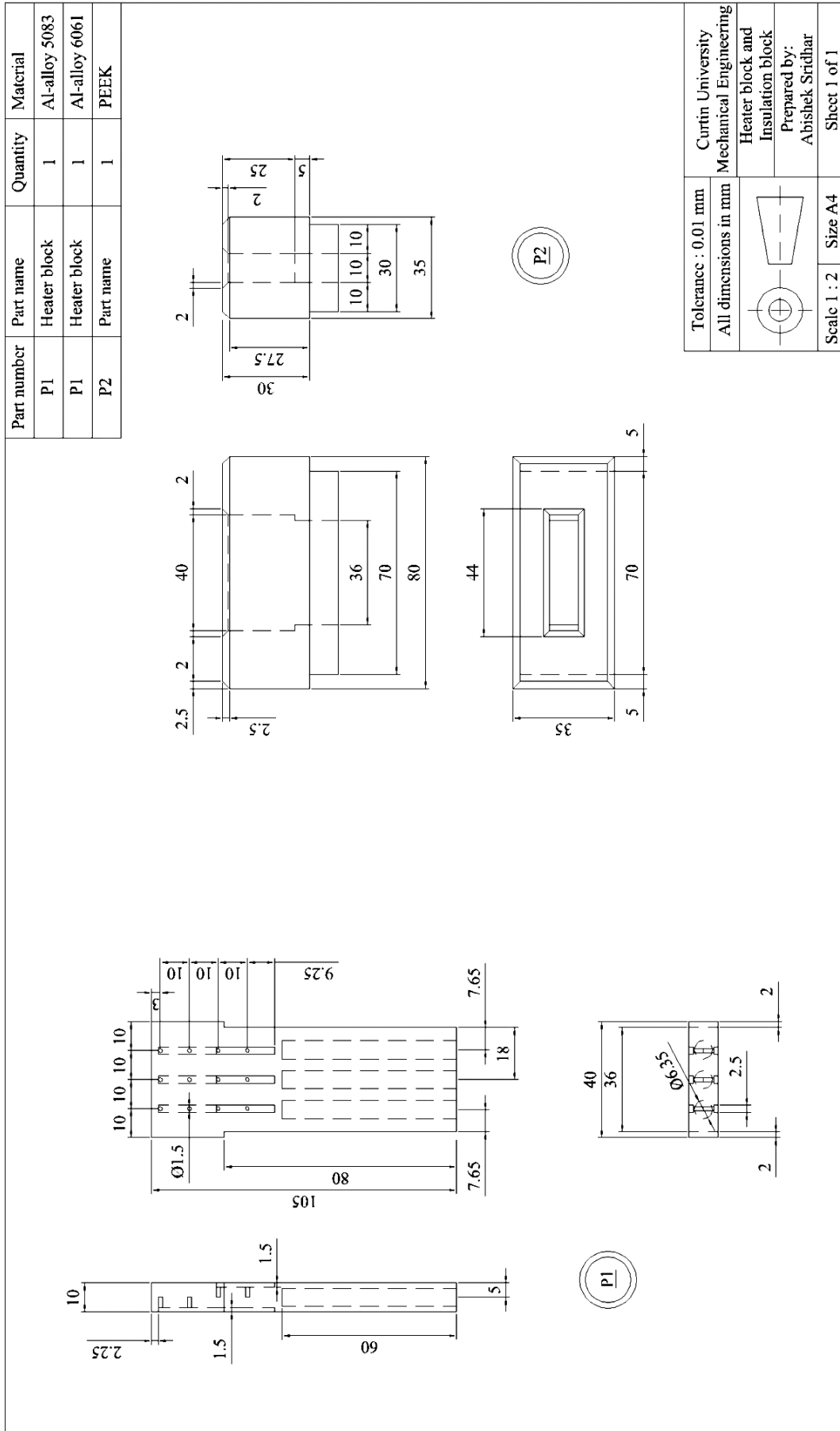
pump	pump flow steadiness; operating range: flow rates, temperatures, pressures; electrical power requirements; compatibility with working fluids
needle valves	operating range: flow rates, temperatures, pressures; compatibility with working fluids
nozzle / slot duct	length (for fully developed flow at nozzle outlet); nozzle width; cross-sectional area
solenoid control valve	operating range: flow rates, temperatures, pressures; open/close cycle time; electrical power requirements; compatibility with working fluids
solid state relays	range of input frequencies; circuitry control voltages; controlled (output) voltage to be consistent with solenoid valve's operating voltages
function generator	signal waveforms; frequencies; voltage output (to be consistent with relay's operating voltages); electrical power requirements
thermal bath	operating range: pressure, temperature control range; internal circulation flow rate; electrical power requirements; compatibility with working fluids
cartridge heaters	power density; operating range: temperature; electrical power requirements
heater block	material and thermophysical properties; operating range: temperature/ stress; geometry and size
power supply transformer	voltage control range
degasser with thermostat controlled heater	degasser dimensions; power density of immersion heater (consistent with flow rate in loop); operating temperature range of heater
pressure relief valve	operating pressure range
graham condenser and cooling water jacket/ circuit	condenser size and coolant/ water flow rate
water/ fc 72	Prandtl number; boiling point
polycarbonate confinement blocks	geometry and size; material compatibility with working fluids; operating temperature range
nozzle (duct) housing	geometry and size; material compatibility with working fluids; operating temperature range
insulation around heater block	geometry and size; material compatibility with working fluids; operating temperature range

Piping	material; nominal size (compatible with equipment and instrumentation connections)
pipe connections	brazing compatibility where applicable; fittings sizes (compatible with piping, equipment and instrumentation connections)
seals and adhesives and fasteners	compatibility with working fluid; operating temperature range; O-ring sizes; bolts and washer sizes and spacings required
flow meter	length of piping before flow meter; accuracy of flow meter; electrical power requirements
in line thermocouple	temperature range; precision; time constant
bank of thermocouples	temperature range; precision; time constant; number of thermocouples; location of thermocouples
dissolved gas sensor	Precision; only oxygen content measured; compatibility with working fluid
oscilloscope	electrical power requirements
thermocouple data logger	data sampling range; number of thermocouples that can be connected

Appendix A-2: Photograph of the Jet Impingement Experimental Facility

Appendix A-3: Part-Drawings for the Jet Impingement Test Cell

Part number	Part name	Quantity	Material
P1	Heater block	1	Al-alloy 5083
P1	Heater block	1	Al-alloy 6061
P2	Part name	1	PEEK

Curtin University
Mechanical Engineering
Heater block and
Insulation block

Prepared by:
Abishek Sridhar

Sheet 1 of 1

Tolerance : 0.01 mm
All dimensions in mm

Scale 1 : 2   Size A4

Part number	Part name	Quantity	Material
P3	Base plate	1	Acryllic

Tolerance : 0.01 mm
All dimensions in mm

Curtin University
Mechanical Engineering

Acryllic base plate

Prepared by:
Abishek Sridhar

Sheet 1 of 1

Scale 1 : 3 | Size A4

Part number: P4
Part name: Confinement block part-1
Quantity: 1
Material: Acryllic

Curtin University
Mechanical Engineering
Confinement block part-1 of 2
Prepared by: Abishek Sridhar
Sheet 1 of 1

Tolerance : 0.01 mm
All dimensions in mm

Scale 1 : 3 | Size A4

Part number	Part name	Quantity	Material
P5	Confinement block part-2	2	Acryllic
P6	slot tube / nozzle	1	Copper

Curtin University
Mechanical Engineering
Confinement block part-2 of 2 and slot tube
Prepared by: Abishek Sridhar
Sheet 1 of 1

Tolerance : 0.01 mm
All dimensions in mm

Scale 1 : 3 | Size A4

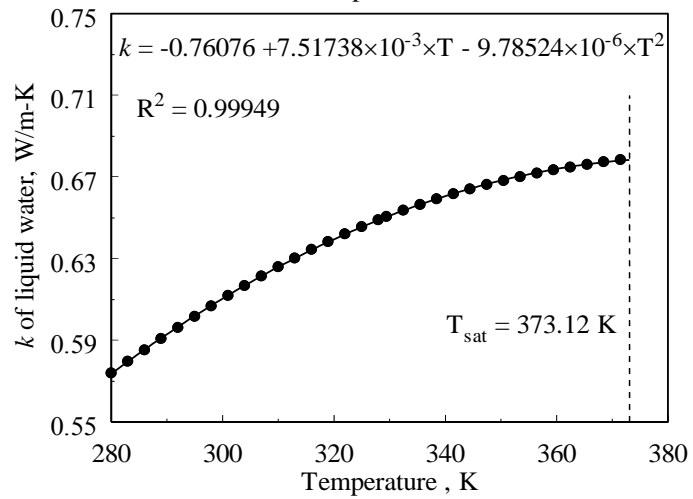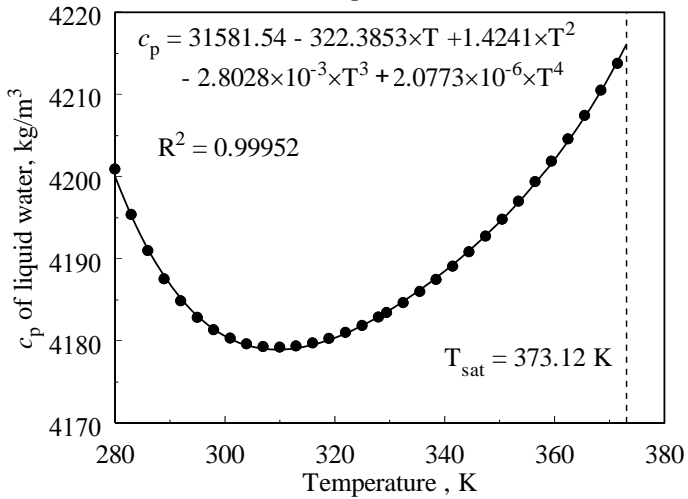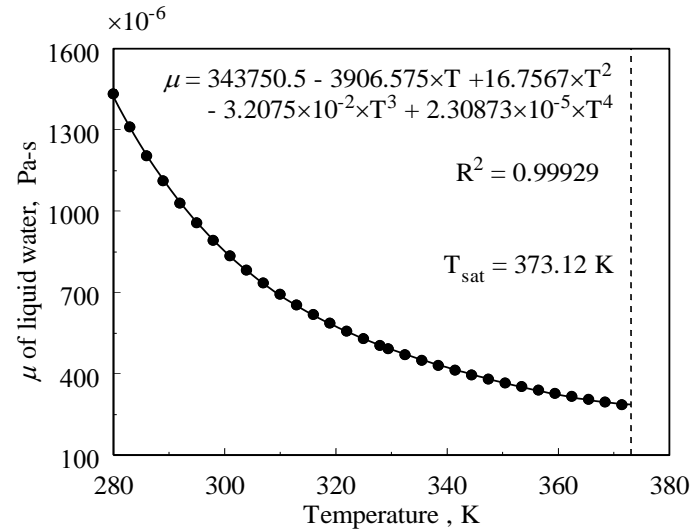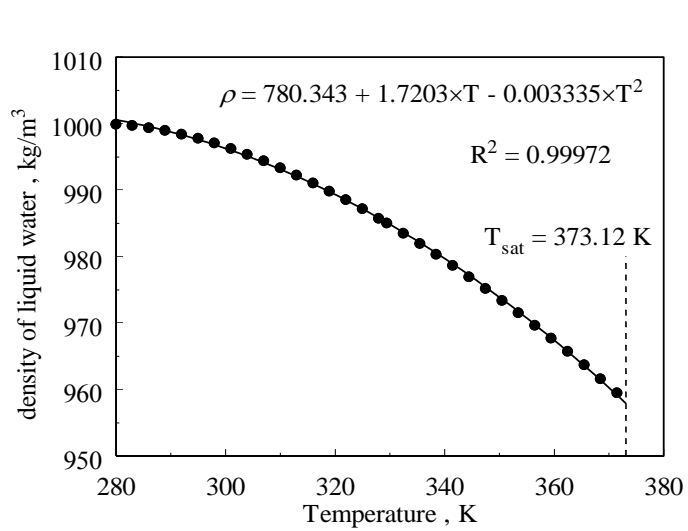## Appendix A-4: Thermophysical Properties of Liquid and Vapor Phases of FC-72 and Water

(i)   Thermophysical properties of FC-72 at 101.325 k Pa

Property	Units	FC-72 liquid	FC-72 vapor (at T_{sat})
ρ	kg/m3	$2452.84 - 2.61 \times T$	13.43
μ	Pa-s	$5.202 \times 10^{-3} - 2.438 \times 10^{-5} \times T + 3.004 \times 10^{-7} \times T2$	1.81×10^{-5}
k	W/m-K	$9.005 \times 10^{-2} - 1.1 \times 10^{-4} \times T$	0.02
cp	J/kg-K	$589.57 + 1.554 \times T$	500
$Tsat$	K	329.12	
L	J/kg-K	88000	
σ	N-m	$40.4609 \times (1 - T/T_C)^{1.2382}$; where $T_C = 451.33$ K	
Molar mass	g/mol	338	

In the above table, the temperature (T) is represented in K. Data is taken from References [17,181].

(ii)   Thermophysical properties of water (liquid and vapor) at 101.325 k Pa

$\rho = 780.343 + 1.7203 \times T - 0.003335 \times T^2$

$R^2 = 0.99972$

$T_{sat} = 373.12$ K

$\mu = 343750.5 - 3906.575 \times T + 16.7567 \times T^2 - 3.2075 \times 10^{-2} \times T^3 + 2.30873 \times 10^{-5} \times T^4$

$R^2 = 0.99929$

$T_{sat} = 373.12$ K

$c_p = 31581.54 - 322.3853 \times T + 1.4241 \times T^2 - 2.8028 \times 10^{-3} \times T^3 + 2.0773 \times 10^{-6} \times T^4$

$R^2 = 0.99952$

$T_{sat} = 373.12$ K

$k = -0.76076 + 7.51738 \times 10^{-3} \times T - 9.78524 \times 10^{-6} \times T^2$

$R^2 = 0.99949$

$T_{sat} = 373.12$ K

Water vapor properties at T_{sat}		
ρ	kg/m^3	0.59765
μ	Pa-s	1.2268×10^{-5}
c_p	J/kg-K	2079.94
k	W/m-K	0.0251

Other properties		
T_{sat}	K	373.12
L	J/kg-K	2256472
σ	N-m	0.059 at T_{sat}
Molar mass	g/mol	18.0153

Data obtained from NIST
Standard reference database
[182]